



Ministério da  
**Ciência, Tecnologia  
e Inovação**



sid.inpe.br/mtc-m21b/2014/10.17.18.30-TDI

**ANALYSIS OF THE POTENTIAL OF IN SITU  
HYPERSPETRAL OPTICAL DATA AND HIGH  
SPATIAL RESOLUTION SATELLITE IMAGERY TO  
MAP BOTTOM TYPES IN THE ABROLHOS CORAL  
REEF BANK (BRAZIL)**

Maria Laura Zoffoli

Doctorate Thesis Course Graduate  
in Remote Sensing, guided by Drs.  
Milton Kampel, and João Antônio  
Lorenzetti, approved in August,  
29, 2014.

URL of the original document:

<<http://urlib.net/8JMKD3MGP5W34M/3H8T2PL>>

INPE  
São José dos Campos  
2014

**PUBLISHED BY:**

Instituto Nacional de Pesquisas Espaciais - INPE

Gabinete do Diretor (GB)

Serviço de Informação e Documentação (SID)

Caixa Postal 515 - CEP 12.245-970

São José dos Campos - SP - Brasil

Tel.:(012) 3208-6923/6921

Fax: (012) 3208-6919

E-mail: pubtc@sid.inpe.br

**BOARD OF PUBLISHING AND PRESERVATION OF INPE INTELLECTUAL PRODUCTION (RE/DIR-204):****Chairperson:**

Marciana Leite Ribeiro - Serviço de Informação e Documentação (SID)

**Members:**

Dr. Gerald Jean Francis Banon - Coordenação Observação da Terra (OBT)

Dr. Amauri Silva Montes - Coordenação Engenharia e Tecnologia Espaciais (ETE)

Dr. André de Castro Milone - Coordenação Ciências Espaciais e Atmosféricas (CEA)

Dr. Joaquim José Barroso de Castro - Centro de Tecnologias Espaciais (CTE)

Dr. Manoel Alonso Gan - Centro de Previsão de Tempo e Estudos Climáticos (CPT)

Dr<sup>a</sup> Maria do Carmo de Andrade Nono - Conselho de Pós-Graduação

Dr. Plínio Carlos Alvalá - Centro de Ciência do Sistema Terrestre (CST)

**DIGITAL LIBRARY:**

Dr. Gerald Jean Francis Banon - Coordenação de Observação da Terra (OBT)

**DOCUMENT REVIEW:**

Maria Tereza Smith de Brito - Serviço de Informação e Documentação (SID)

Yolanda Ribeiro da Silva Souza - Serviço de Informação e Documentação (SID)

**ELECTRONIC EDITING:**

Maria Tereza Smith de Brito - Serviço de Informação e Documentação (SID)

André Luis Dias Fernandes - Serviço de Informação e Documentação (SID)



Ministério da  
**Ciência, Tecnologia  
e Inovação**



sid.inpe.br/mtc-m21b/2014/10.17.18.30-TDI

**ANALYSIS OF THE POTENTIAL OF IN SITU  
HYPERSPETRAL OPTICAL DATA AND HIGH  
SPATIAL RESOLUTION SATELLITE IMAGERY TO  
MAP BOTTOM TYPES IN THE ABROLHOS CORAL  
REEF BANK (BRAZIL)**

Maria Laura Zoffoli

Doctorate Thesis Course Graduate  
in Remote Sensing, guided by Drs.  
Milton Kampel, and João Antônio  
Lorenzetti, approved in August,  
29, 2014.

URL of the original document:

<<http://urlib.net/8JMKD3MGP5W34M/3H8T2PL>>

INPE  
São José dos Campos  
2014

## Cataloging in Publication Data

---

Zoffoli, Maria Laura.

Z73a      Analysis of the potential of in situ hyperspectral optical data and high spatial resolution satellite imagery to map bottom types in the Abrolhos Coral Reef Bank (Brazil) / Maria Laura Zoffoli. – São José dos Campos : INPE, 2014.  
xxvi + 182 p. ; (sid.inpe.br/mtc-m21b/2014/10.17.18.30-TDI)

Thesis (Doctorate in Remote Sensing) – Instituto Nacional de Pesquisas Espaciais, São José dos Campos, 2014.

Guiding : Drs. Milton Kampel, and João Antônio Lorenzzetti.

1. Water column correction. 2. Biological diversity.  
3. Worldview-2. 4. Bottom reflectance. 5. Remote sensing.  
I.Título.

CDU 528.88

---



Esta obra foi licenciada sob uma Licença [Creative Commons Atribuição-NãoComercial 3.0 Não Adaptada](https://creativecommons.org/licenses/by-nc/3.0/).

This work is licensed under a [Creative Commons Attribution-NonCommercial 3.0 Unported License](https://creativecommons.org/licenses/by-nc/3.0/).

Aprovado (a) pela Banca Examinadora  
em cumprimento ao requisito exigido para  
obtenção do Título de **Doutor(a)** em

**Sensoriamento Remoto**

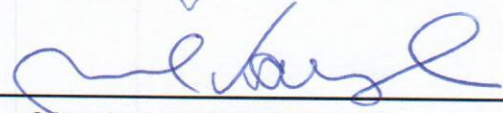
Dra. Evelyne Márcia Leão de Moraes Novo



---

**Presidente / INPE / SJC Campos - SP**

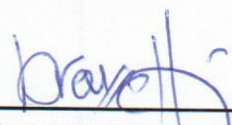
Dr. Milton Kampel



---

**Orientador(a) / INPE / SJC Campos - SP**

Dr. João Antonio Lorenzetti



---

**Orientador(a) / INPE / SJC Campos - SP**

Dr. Cláudio Clemente Faria Barbosa



---

**Membro da Banca / INPE / SJC Campos - SP**

Dr. Carlos Alexandre Domingos Lentini



---

**Convidado(a) / UFBA / Salvador - BA**

Dr. Ricardo Coutinho



---

**Convidado(a) / IEAPM / Rio de Janeiro - RJ**

**Este trabalho foi aprovado por:**

maioria simples

unanimidade

Aluno (a): **Maria Laura Zoffoli**

**São José dos Campos, 29 de Agosto de 2014**



*“Assim como você não conhece o caminho do vento, nem como o corpo é formado no ventre de uma mulher, também não pode compreender as obras de Deus, o Criador de todas as coisas.”*

*Eclesiastes 11:5, A Bíblia*



## AGRADECIMENTOS

Agradeço aos meus orientadores, Dr. Milton Kampel, Dr. João Antônio Lorenzetti e Dr. Robert Frouin, pela oportunidade de realizar este doutorado, por acreditar em mim, pela confiança plena e por todos os aprendizados que me ajudaram a adquirir neste curso.

Ao Programa de Estudantes-Convênio de Pós-Graduação (PEC-PG) e à Coordenação de Aperfeiçoamento de Pessoal de Nível Superior (CAPES), pelo apoio financeiro e concessão de bolsa durante o curso de doutorado. Ao INPE e Programa de Pós-graduação em Sensoriamento Remoto que me deram toda a estrutura e condições de realizar o curso, e a todos os professores, secretárias e funcionários que sempre se disponibilizaram para ajudar frente a qualquer dificuldade.

Agradeço ao pessoal da Rede Abrolhos por me permitir realizar o trabalho de campo na região de Abrolhos e fornecer todo o apoio logístico necessário para a realização da amostragem. Em especial ao Dr. Rodrigo de Leão Moura, pelo auxílio no campo e discussões e ensinamentos sobre a área de estudo. Obrigada a todos os mergulhadores que me acompanharam nas duas saídas de campo, sempre com ótima disposição: Linda, Fernando G., Diana, Pablo, Daniel, Arthur, Guilherme e Fernando M. Agradeço ao Rodrigo, Arthur e Augusto, pela ajuda para a identificação de espécies nas fotografias do substrato bentônico.

Ao Dr. Salvador Ayrtton Gaeta e à Mayza Pompeu que me permitiram realizar as análises laboratoriais. Especialmente à Mayza, João Felipe, Vadim, Pedro, Rafael, Matheus e Julia que me ajudaram a processar todas as amostras.

À Digital Globe que forneceu sem custo um imageamento do satélite Worldview-2, coincidente com uma das campanhas na área de estudo.

A todos os meus colegas e amigos do INPE. À Aline, Gabriel, Lucas, Larissa, Leandro, Johny, Marília, Matheus, Cibele, Thiago, que me ajudaram desinteressadamente em várias etapas do trabalho.

Aos meus queridos amigos e família de São José dos Campos: Nati, Fran, Liana, Luiz, Jairo, Dani, Rodrigo. Fran, Nati, Liana: obrigada por seu apoio e carinho sempre, pelos momentos de distensão e pelos momentos de partilha e suporte emocional e espiritual. Nati, você merece um capítulo à parte. Obrigada por toda sua ajuda no trabalho, discussões e correções do inglês.

Ao Gabriel, que sempre me apoiou, me incentivou e me acompanhou com paciência nas horas difíceis. Você tem sido um suporte inestimável e insubstituível desde que cheguei

ao INPE e nunca deixou que me sentisse sozinha. Obrigada por seu profundo amor e sua companhia permanente.

A toda minha família. Obrigada por sua confiança cega em mim, seu apoio incondicional, seu ânimo constante, seu amor imenso. Obrigada por estar tão perto de mim, mesmo estando longe.

Acima de todas as coisas a Deus, minha única e verdadeira fonte de inspiração, fortaleza, alegria e paz.

## ABSTRACT

Human activity and natural climate trends constitute a major threat to coral reefs worldwide. Models predict a significant reduction in reef spatial extension together with a decline in biodiversity in the relatively near future. In this context, monitoring programs to detect changes in reef ecosystems are essential. In recent years, coral reef mapping using remote sensing data has benefited from instruments with better resolutions and computational advances in storage and processing capabilities. However, the water column represents an additional complexity when extracting information from submerged substrates by remote sensing, which demands a correction of its effect. Another limitation arises when focusing in complex benthic substrates, with a mixture of different taxonomic and/or functional types with the aim to detect alterations. In the first part of this work a deep study about water column correction methods was proposed, showing some inter-comparisons of different algorithms and evaluating the uncertainties associated with the determination of bottom reflectance from above water radiometry. An inter-comparison of three methods was carried out using simulated spectra and remote sensing data of the Worldview-2 (WV02) sensor over the Abrolhos Coral Reef Bank (ACRB), Brazil. The results showed that the available methods were not able to completely eliminate the water column effect, but they minimized its influence. Uncertainties in retrieving the bottom reflectance from above-water spectra increase with depths and the concentration of optically water constituents. In clear waters with low colored dissolved organic matter (CDOM) concentration, uncertainties augmented towards the red spectral bands. While in environments with high CDOM concentration, uncertainties increased both towards the blue and the red spectral ends. Choosing the best method depends on the marine environment, available input data and desired outcome for the scientific application. In the second part of this study, hyperspectral above-water radiometry sampled over natural benthic communities in the ACRB were analyzed to: (i) evaluate the ability of a water column algorithm to retrieve accurate bottom reflectance spectra from above-water radiometric measurements; and (ii) assess the separability of submerged benthic communities with subtle differences based on their reflectance spectra. Despite of the good performance to retrieve bottom reflectance from above-water radiometric measurements, benthic communities in the ACRB, whose waters were characterized as Case-2, were not spectrally separable. This implies that effective monitoring programs in the ACRB able to detect insightful alterations in the benthic coverage, necessarily have to include both complementary approaches: remote sensing and field campaigns. In the last part of this work, an area belonging to the ACRB was mapped for the first time into benthic classes using high spatial resolution orbital imagery of the WorldView-2 (WV02) sensor. This sensor has 6 bands in the visible region, but only one band at 478 nm was used because of the low performance to correct the water column effect, which represented one of the main challenges in this work. The produced map had an accuracy of 88.2% and a Kappa index of 0.81 using four classes (Reef, Sand, Macroalgae, Inter-reef areas), however new validation points are required to validate the entire scene. The isolated reefs covered an area of approximately 22 km<sup>2</sup> that correspond to 12.4% of the total area. *Chapeirões* were distributed almost in all the studied area, formed by patches with different sizes. Macroalgae were the most

abundant class in the scene and was concentrated around the Archipelago and inter-reef areas. Further works regarding extensive *in situ* data collection to properly describe the benthic communities and their spectral behavior, as well as the water column constituents and depths surveys are recommended to improve satellite mapping of the bottoms types in the Abrolhos Coral Reef Bank.

**ANÁLISE DO POTENCIAL DE DADOS HIPERESPECTRAIS ÓPTICOS  
OBTIDOS *IN SITU* E DE IMAGENS DE SATÉLITE DE ALTA RESOLUÇÃO  
ESPACIAL PARA MAPEAR TIPOS DE FUNDO DOS RECIFES DE CORAIS  
DO BANCO DOS ABROLHOS (BRASIL)**

**RESUMO**

Atividades antrópicas e mudanças climáticas são as maiores ameaças aos recifes de corais no mundo inteiro. Modelos preveem uma redução significativa na extensão espacial dos recifes acompanhado por um declínio na biodiversidade num futuro relativamente próximo. Neste contexto, programas de monitoramento de detecção de mudanças em ecossistemas de recifes de corais são essenciais. Nos anos recentes, o mapeamento de recifes de corais usando dados de sensoriamento remoto tem se beneficiado com o advento de instrumentos com melhores resoluções e avanços computacionais em termos de capacidade de armazenamento e processamento de dados. No entanto, a coluna de água representa uma complexidade adicional quando se quer extrair informação dos substratos submersos por sensoriamento remoto, o que demanda a correção deste efeito. Outra limitação advém quando se tratam de substratos bentônicos complexos, com mistura de diferentes grupos taxonômicos e/ou tipos funcionais, quando o objetivo é detectar alterações. Na primeira parte deste trabalho foi proposto um estudo aprofundado sobre métodos de correção da coluna de água, com a comparação de diferentes algoritmos e a avaliação das incertezas associadas à determinação da reflectância de fundo da radiometria acima da água. A inter-comparação de três métodos foi realizada usando espectros simulados e dados de sensoriamento remoto do sensor Worldview-2 (WV02) sobre os Recifes de Corais do Banco de Abrolhos (RCBA), Brasil. Os resultados mostram que os métodos disponíveis não foram capazes de eliminar totalmente o efeito da coluna de água, mas minimizaram a sua influência. As incertezas na determinação da reflectância de fundo de espectros obtidos acima da água aumentam com a profundidade e concentração dos constituintes opticamente ativos. Em águas claras com baixas concentrações de matéria orgânica dissolvida colorida (MODC), as incertezas foram maiores para as bandas espectrais do vermelho. Enquanto que em águas com alta concentração de CDOM, as incertezas aumentaram tanto para as bandas do azul como do vermelho. A escolha do melhor método vai depender do ambiente marinho, da disponibilidade dos dados de entrada e da saída desejada para a aplicação científica. Na segunda parte deste estudo, dados radiométricos hiperespectrais medidos acima da água, sobre comunidades bentônicas naturais do RCBA, foram analisados para: (i) avaliar a habilidade de um algoritmo de

correção da coluna de água em obter espectros de reflectância de fundo acurados, das medidas radiométricas acima da água; e (ii) verificar a separabilidade de comunidades bentônicas submersas com diferenças sutis, com base nos espectros de reflectância de fundo. Apesar do bom desempenho para a obtenção da reflectância de fundo das medidas radiométricas acima da água, as comunidades bentônicas do RCBA, com águas caracterizadas do tipo Caso-2, não foram espectralmente separáveis. Isso implica que programas de monitoramento no RCBA, eficientes para detectar alterações importantes na cobertura bentônica, necessariamente têm que incluir técnicas complementares com coleta de dados *in situ* e de satélite. Na última parte deste trabalho, uma área pertencente ao RCBA foi mapeada pela primeira vez em classes bentônicas, usando uma imagem de alta resolução espacial do sensor WorldView-2 (WV02). O sensor possui 6 bandas espectrais na região do visível, mas somente a banda centrada em 478 nm foi usada devido ao baixo desempenho da correção da coluna de água, que foi um dos maiores desafios encontrados no presente trabalho. O mapa resultante apresentou uma acurácia de 88,2% e um índice Kappa de 0,81 com 4 classes (Recifes, Areia, Macroalga, Áreas inter-recifais), no entanto, novos pontos de validação são necessários para cobrir a cena inteira. Os recifes isolados cobriram uma área de aproximadamente 22 km<sup>2</sup> que corresponderam a 12,4% da área total. Os chapeirões foram distribuídos em quase toda a área de estudo, formando manchas (ou agregados) de diferentes tamanhos. A classe mais abundante em toda a cena foi de Macroalgas, concentrada no entorno no Arquipélago e das áreas inter-recifais. Trabalhos futuros com coletas intensivas de dados *in situ* para descrever melhor as comunidades bentônicas e seu comportamento espectral, bem como os constituintes da coluna de água e mapeamentos batimétricos, são recomendados para melhorar o mapeamento dos tipos de fundo dos Recifes de Corais do Banco de Abrolhos, por meio de imagens de satélite

## LIST OF FIGURES

	<u>Pag.</u>
Figure 3.1 – Diagram representing main processes that contribute to signal measured by a passive remote sensor above shallow waters.....	6
Figure 3.2 – Absorption coefficients spectra measured in a productive oceanic environment.....	9
Figure 3.3 – Light decay modeled along water column expressed as percentage of incident light as function of depth.....	13
Figure 3.4 – (a) Reflectance of different substrates at 0 m depth, as function of wavelength. (b-d) Reflectance above water versus wavelength simulated for the same substrates in clear Case-1 waters at different depths. (e-g) Reflectance above water versus wavelength simulated for the same substrates in Case-2 waters at different depths .....	15
Figure 3.5 – Different strategies proposed to obtain diffuse attenuation coefficient from a remote sensing image .....	19
Figure 3.6 – Different strategies proposed to obtain bottom reflectance from a remote sensing image above shallow waters.....	24
Figure 3.7 – Graphic representation of the approach using Look Up Table matching to generate bottom type map without effect of water column.....	34
Figure 3.8 – (a) Diagram to obtain of gain and offset values to normalized image as function of a previous one .....	39
Figure 4.1 – Landsat TM-5 Image of the study area and its location in South America.. .....	42
Figure 4.2 – Cross-section scheme of the main reef types in the study area showing the coral reefs in the coastal and external arcs .....	42
Figure 4.3 – Localization of the main stations sampled in the first and second field campaigns.....	44
Figure 4.4 – Random points on a submerged picture of benthic communities in the ACRB using the CPCe software. ....	49
Figure 4.5 – Flowchart of the main activities of data collection, processing and analysis .....	52
Figure 5.1 – Diffuse attenuation coefficient and $z_{90}$ simulated in WASI for water-a to -d as a function of wavelength.....	59
Figure 5.2 – Quasi-true color composition of a portion of the Abrolhos Coral Reef Bank, Brazil, around the archipelago, captured by WV02 sensor and distribution of depth points in the area.....	60
Figure 5.3 – Diffuse attenuation coefficient versus wavelength measured quasi-concomitant with WV02 imagery in ACRB, Brazil .....	61
Figure 5.4 – Water optical properties estimated nearly concomitantly with the time of WV02 imagery around the archipelago in ACRB, Brazil.....	62
Figure 5.5 – Bottom reflectance below water versus wavelength for the same type of substrate and depth .....	65
Figure 5.6 – Sensitivity analyses for parameters of Maritorena et al.’ model.....	67
Figure 5.7 – Sensitivity analyses for parameters of Lee et al.’ model .....	68

Figure 5.8 – Simulated remote sensing reflectance above water as a function of wavelength in shallow waters .....	70
Figure 5.9 – Maximum range of wavelength in which a substrate located at different depths can be detected with remote sensing techniques. ....	72
Figure 5.10 – (a) Zoom in different portions of WV02 image in quasi-true color. (b) Reflectance below water versus wavelength captured by WV02 sensor above the four points located in (a) and above deep water. (c-d) Bottom reflectance below water versus wavelength retrieved by Maritorena et al. and Lee et al.'s algorithms, respectively. ....	73
Figure 5.11 – Bottom reflectance retrieved using Lee et al.'s algorithm versus Maritorena et al.'s algorithm retrieval from WV02 image .....	75
Figure 6.1 – Ternary diagram representing the percentage of the absorption coefficients of each optical constituent (CDOM, detritus and phytoplankton) at 440 nm .....	95
Figure 6.2 – Absorption coefficients at 440 nm obtained <i>in situ</i> as a function of longitude and the depths of the sites in meters. The area of the circles is directly proportional to their value.....	96
Figure 6.3 – Absorption coefficients measured in the field at all stations and sites in the ARCH and PAB reefs .....	97
Figure 6.4 – Absorption coefficients measured in the field at all stations and sites in PL and PA reefs .....	98
Figure 6.5 – Absorption coefficients measured in the field at all stations and sites in the TIM reef .....	99
Figure 6.6 – Retrieved bottom reflectance as a function of wavelength .....	100
Figure 6.7 – Measured and modeled $R_{\infty}(0)$ as a function of wavelength .....	100
Figure 6.8 – Retrieved bottom reflectance as a function of wavelength using the third approach with the parameters retrieved using Lee et al.' inversion scheme (1999).....	102
Figure 6.9 – Relative composition of benthic communities in the ACRB considering the average of abundance between all sites.....	103
Figure 6.10 – Relative percentage of coverage of each category to the benthic communities for the 20 sites analyzed in the ACRB. ....	104
Figure 6.11 – Photographs of the benthic community taken at four sites within the ACRB during the field campaign of 2013 .....	105
Figure 6.12 – Retrieved bottom reflectance as a function of wavelength.....	107
Figure 6.13 – First-derivative of the retrieved bottom reflectance as a function of wavelength .....	108
Figure 6.14 – Bottom reflectance simulated in WASI for combinations of different proportions of red, green and brown algae.....	109
Figure 6.15 – Spectra absorption of the main pigments encountered in benthic communities versus wavelength.....	109
Figure 6.16 – Cluster analysis for the coverage of benthic communities and the percentage of coverage of each benthic category.....	113
Figure 6.17 – Cluster analysis for the SAM matrix applied to bottom reflectance spectra and the percentage of coverage of benthic categories at each site .....	113

Figure 6.18 – Cluster analysis for bottom reflectance in all visible region and the percentage of coverage of benthic categories in each site .....	114
Figure 6.19 – Decision tree obtained from data mining processing for normalized bands between 450 and 650 nm and different band ratios .....	115
Figure 7.1 – Visibility as a function of Aerosol Optical Thickness (at 550 nm) according to Vermote et al.'s model (2002). .....	127
Figure 7.2 – Scatterplot of surface reflectance values at the visible bands against reflectance in the NIR region from samples extracted in deep waters....	129
Figure 7.3 – Average of $R_{\infty}(0)$ corrected for sunglint and extracted over deep waters within the WV02 image. ....	132
Figure 7.4 – Result of the segmentation process that was considered satisfactory, in a subset image of a portion of the <i>Parcel dos Abrolhos</i> .....	137
Figure 7.5 – Mean values extracted from the WV02 image in deep waters, as a function of wavelength .....	139
Figure 7.6 – Water reflectance as a function of wavelength collected <i>in situ</i> in three different sites around the Archipelago .....	141
Figure 7.7 – Water reflectance before and after application of sunglint correction for the different bands of the WV02 sensor.....	142
Figure 7.8 – Vertical stripes in the WV02 image at 478 nm, enhanced after sunglint correction.....	143
Figure 7.9 – Bathymetric map of the Archipelago and <i>Parcel dos Abrolhos</i> , in the ACRB, Brazil, obtained through the application of the Stumpf et al. (2003) algorithm to a WV02 scene .....	144
Figure 7.10 – Zooms over the bathymetric map of the Archipelago and <i>Parcel dos Abrolhos</i> , in the ACRB, Brazil.....	145
Figure 7.11 – WV02 image at 478 nm in different portions of the ACRB .....	148
Figure 7.12 – Bottom type map of the ACRB produced from the WV02 image.....	151
Figure 7.13 – Patches with different patterns of spatial distribution of coral reefs in the ACRB. ....	153
Figure 7.14 – Zooms over different portions of the bottom type map of the ACRB, that correspond with different spatial patterns of reef distribution. ....	154
Figure 7.15 – Portion of the WV02 image at 478 nm northern to the islands and the same feature identified in the image, showed in a subaquatic picture ....	157



## LIST OF TABLES

	<u>Pag.</u>
Table 3.1 – Summary of models reviewed in this paper considering methodological approach, data spectral resolution, data required, model results and other observations.....	29
Table 4.1 – Main characteristics of the Worldview2 orbital sensor and specificities of the used scene: spectral and spatial resolutions, solar and off-nadir angles and percentage of cloud cover.....	51
Table 5.1 – Water characteristics of the four different types of water used to simulate surface reflectance above shallow areas.....	55
Table 5.2 – Water column characteristics in coral reefs areas Worldwide reviewed from literature. ....	57
Table 5.3 – Confusion matrix obtained for CRISTAL method using the SAM classification algorithm. ....	70
Table 6.1 – Confusion matrix for the cross-validation after the decision tree creation.	115
Table 6.2 – Pearson correlation index between band depth and different substrate type coverage .....	118
Table 7.1 – Equations used to perform sunglint correction in each band, based in Hedley et al.’ model (2005). ....	130
Table 7.2 – $K_d$ obtained around PAB and ARCH stations in the ACRB during the summer of 2012 and 2013 for the five bands of WV02 in the visible region.....	131
Table 7.3 – $\beta_1$ and $\beta_0$ coefficients used for the calibration of the bathymetry map, $R^2$ and RMSE obtained for different data sets .....	134
Table 7.4 – Illustration of the thematic classes used for the bottom mapping in the <i>Parcel dos Abrolhos</i> , ACRB. ....	135
Table 7.5 – $\beta_1$ and $\beta_0$ coefficients, $R^2$ and RMSE obtained for the validation of different data sets of the bathymetric map .....	147
Table 7.6 – Area and percentage of occupation of each class of bottom type. ....	152
Table 7.7 – Confusion matrix for the classified WV02 image.....	155



## LIST OF ACRONYMS AND ABBREVIATIONS

AAHIS	Advanced Airborne Hyperspectral Imaging Sensors
ACRB	Abrolhos Coral Reef Bank
ALUT	Adaptive Look-Up Trees
AOP	Apparent Optical Property
AOT <sub>547</sub>	Aerosol optical thickness at 574 nm
ARCH	Archipelago
ASTER	Advanced Spaceborne Thermal Emission and Reflection Radiometer
AVIRIS	Airborne Visible/Infrared Imaging Spectrometer
BD	Band depth
BRUCE	Bottom Reflectance Un-mixing Computation of the Environment model
BSP	Binary Space Partitioning
CASI	Compact Airborne Spectrographic Imager
CDOM	Coloured Dissolved Organic Matter
chl- <i>a</i>	Chlorophyll- <i>a</i> concentration
CPCe	Coral Point Count software
CRISTAL	Comprehensive Reflectance Inversion based on Spectrum matching and Table Lookup
CRR	Continuum removed Reflectance
DMF	N,N-Dimethylformamide
DN	Digital Number
ETM+	Enhanced Thematic Mapper Plus
FOV	Field of View
G1	Group 1
G2	Group 2
GCP	Ground Control Point
GF/F	Whatman Glass Fiber Filters
HRV	High Resolution Visible
IFOV	Instantaneous Field of View
IHS	Intensity-Hue-Saturation

IOP	Inherent Optical Properties
IOUSP	<i>Instituto Oceanografico, Universidade de São Paulo</i>
LIDAR	Light Detection And Ranging
LQM	Least Squares Minimum
LUT	Look-Up Tables
MNF	Minimum Noise Fraction
MSS	Multispectral Scanner
NIR	Near Infrared
OAC	Optically Active Constituents
OBIA	Object-Based Image Analysis
ONA	Off-Nadir-Angle
PA	<i>Parcel das Paredes</i>
PAB	<i>Parcel dos Abrolhos</i>
PAN	Panchromatic
PCA	Principal Components Analysis
PHILLS	Portable Hyperspectral Imager For Low Light Spectroscopy
PIF	Pseudo-Invariant Feature
PL	<i>Pedra de Leste</i>
QAAv5	Quase-Analytical Algorithm
RGB	Red-Green-Blue
RMSE	Root Mean Square Error
RPC	Rational Polynomial Coefficients
SAM	Spectral Angle Mapper
SAMBUCA	Semi-Analytical Model for Bathymetry, Un-mixing and Concentration Assessment
SDI	Substratum Detectability Index
SG	<i>Sebastião Gomes</i>
SPOT	<i>Satellite Pour l'Observation de la Terre</i>
SST	Sea Surface Temperature
TIM	<i>Timbebas</i>
TM	Thematic Mapper
TOA	Top-of-Atmosphere

TSM	Total Suspended Matter
UV	Ultraviolet Radiation
WV02	WorldView-2 sensor
XS	Multi-spectral
WASI	The Water Colour Simulator



## LIST OF SYMBOLS

$a$	Total absorption coefficient
$a_{CDOM}$	Absorption coefficient of CDOM
$a_d$	Absorption coefficient of detritus
$a_g$	Absorption coefficient of CDOM and detritus
$a_p$	Absorption coefficient of particulate fraction
$a_{phyto}$	Absorption coefficient of phytoplankton pigments
$a_w$	Absorption coefficient of pure water
$b$	Scattering coefficient
$b_b$	Backscattering coefficient
$b_{bp}$	Backscattering coefficients of suspended particles
$b_{b \text{ pure water}}$	Backscattering coefficient of pure water
$b_{bw}$	Backscattering coefficients of seawater
$b_p$	Particles scattering coefficient
$B_{ba}$	Substrate weighting coefficients for brown algae
$B_{sg}$	Substrate weighting coefficients for seagrass
$B_{sd}$	Substrate weighting coefficients for sediments
$c$	Beam attenuation coefficient
chl- $a$	Chlorophyll- $a$ concentration
$d$	Distance Sun-Earth at the day of imagery
$d_0$	Mean distance Sun-Earth
$d_{SAM}$	Difference between pair of spectra estimated from the Spectral Angle Mapper analysis
$D_u^B$	Length optical path factor from substrate
$D_u^C$	Length optical path factor from water column
$e$	Coefficient published in Morel and Maritorena (2001)
$E_d$	Downwelling irradiance
$E_{do}$	Downwelling irradiance below surface
$E_{dz}$	Sub-aquatic downwelling irradiance at bottom depth
$E_{SUN}$	Solar downward irradiance
$E_u$	Upward irradiance

$f$	Average of the cosine of the scattering angle for phase scattering function
$F_c$	Calibration factor of the white reference
$g_{bm,sand}$	Fractional cover of substrates brown mud and sand within each pixel
$k$	Attenuation coefficient (Lee et al. 1998, 1999)
$k_B$	Upward attenuation coefficient originated by substrate
$K_{BAND}$	Absolute calibration factor
$k_C$	Upward attenuation coefficients originated by water column
$K_d$	Diffuse attenuation coefficient of downward irradiance
$K_w$	Absorption value of pure water
$L$	Radiance
$L_b$	Bottom radiance
$L_g$	Radiance reflected from a horizontal reference white panel
$L_w$	Water-leaving radiance for shallow waters
$L_u$	Upward radiance
$L_{TOA}$	Radiance at the Top-of-Atmosphere
$L_\infty$	Water-leaving radiance for deep water
$MIN_{NIR}$	Minimum value of the samples over deep waters, in the NIR band.
$n$	Exponent of backscattering by small particles
$N$	Number of spectral bands
$q$	Geometric factor that considers length path in water column
$Q$	Ratio of the subsurface upward irradiance to radiance conversion factor
$R$	Irradiance reflectance
$R_i$	Irradiance reflectance in band $i$ of shallow water
$R_{ba}$	Brown algae irradiance reflectance
$R_{sd}$	Sediments irradiance reflectance
$R_{sg}$	Seagrass irradiance reflectance
$R_w$	Irradiance reflectance of shallow water
$R_1$	Photons that do not strike the bottom
$R_2$	Photons that strike the bottom once
$R_\infty$	Irradiance reflectance of deep water
$s$	ratio of the number of photons that strike the bottom twice by the number striking once, cited in Gordon and Brown 1974

$t$	Atmospheric transmittance
$z$	Depth
$Z$	Derivation of real depth $z$
$z_m$	Mean depth
$z_{90}$	Effective penetration depth of imagery
$[z - 0]$	Thickness of water layer between depth ( $z$ ) and surface (0)
$\beta_0$	Offset for a depth of 0 m
$\beta_1$	Tunable constant to scale the above ratio to obtain bathymetry information
$\tilde{\beta}_A, \tilde{\beta}_B, \tilde{\beta}_C$	Scattering phase functions, cited in Gordon and Brown 1974
$\beta_w(90^\circ, \lambda_0)$	Volume scattering function for pure water, at the reference wavelengths 350 and 600 nm (Morel 1974)
$\Delta z$	Intrinsic methodological depth error, Bierwirth et al. (1993)
$\Delta\lambda_{BAND}$	Effective bandwidth
$\rho_b$	Bottom reflectance
$\rho_b^{RS}$	Remote sensing reflectance of bottom
$\rho_B^{RS}$	Derived from the real remote sensing reflectance of bottom
$\rho_\infty^{RS}$	Remote sensing reflectance of deep water
$\rho_{b,i}$	Bottom reflectance in band $i$
$\rho_w$	Reflectance of shallow water
$\rho^{RS}$	Remote sensing reflectance
$\rho_{sky}$	Above-water reflectance factor for radiance
$\rho_{TOA}$	Reflectance at the Top-of-Atmosphere
$\rho_\infty$	Reflectance of optically deep water
$\rho_w$	Reflectance of shallow water
$\rho'_w(0^+)$	Above-water sunglint corrected reflectance
$\theta_v$	Water-sensor angle
$\theta_s$	Solar zenith angle
$\lambda$	Wavelength
$\lambda_0$	Wavelength selected from the reference wavelength table (Morel 1974)
$\lambda'$	Excitation wavelength of fluorescence
$\tau_B$	Optical depth (Gordon and Brown 1974)
$\Phi_a$	Absorbed radiant flux

$\Phi_i$	Incident radiant flux
$\Phi_{F^*CDOM}$	Fluorescence radiant flux by CDOM
$\Phi_{F^*phyto}$	Fluorescence radiant flux by phytoplankton pigments
$\Phi_r$	Radiant flux reflected by water sea surface
$\Phi_s$	Elastic scattered radiant flux
$\Phi_{sRaman}$	Raman scattered radiant flux
$\Phi_t$	Transmitted radiant flux
$\psi_1$	Scattering angle between the forward direction of the incident beam and the straight line connecting the detector and the scattering point $C_1$ . $C_1$ corresponds to intersect between water layer surface and beginning of sensor swath, which depends on field of view (FOV)
$\psi_2$	Scattering angle between the forward direction of the incident beam and the straight line connecting the detector and the scattering point $C_2$ . $C_2$ corresponds to intersect between water layer surface and end of sensor swath, which depends on FOV
$\omega_0$	Single scattering albedo
$0^-$	Below surface
$0^+$	Above surface
$\chi$	Coefficient published in Morel and Maritorena (2001)

## SUMMARY

1 INTRODUCTION .....	1
2 OBJECTIVES.....	3
3 THEORETICAL BACKGROUND .....	5
3.1. Some concepts in ocean color remote sensing .....	5
3.1.1. Top-of-atmosphere signal components .....	5
3.1.2. Physical processes in water column .....	8
3.1.3. Light penetration in the water column .....	10
3.1.4. Surface and bottom reflectance relation .....	13
3.2. Water column correction algorithms.....	16
3.2.1. Band combination algorithms .....	16
3.2.2. Model-based algebraic algorithms .....	22
3.2.3. Optimization/Matching algorithms .....	33
3.2.4. Water column corrections for multi-temporal studies.....	38
3.2.5. Bertels et al.'s approach (2008).....	39
4 MATERIALS AND METHODS .....	41
4.1. Study area.....	41
4.2. Field work .....	44
4.2.1. Under-water radiometry .....	45
4.2.2. Above-water radiometry .....	46
4.2.3. Bio-optical parameters .....	47
4.2.4. Environmental characterization.....	48
4.2.5. Benthic community .....	48
4.3. Remote sensing data: Worldview-2 .....	50
5 WATER COLUMN CORRECTION STUDY.....	53
5.1. Introduction.....	53
5.2. Materials and methods .....	54
5.2.1. Application and comparison of selected methods: simulated spectra .....	54
5.2.2. Application and comparison of selected methods: remote sensing data .....	59
5.3. Results and discussion.....	62
5.3.1. Simulated spectra .....	62
5.3.2. Remote sensing data.....	71
5.4. Final considerations.....	76

6	HYPERSPECTRAL ANALYSES OF BENTHIC COMMUNITIES .....	81
6.1.	Introduction .....	81
6.2.	Materials and methods .....	84
6.2.1.	Bio-optical characterization .....	84
6.2.2.	Above-water radiometric measurements.....	84
6.2.3.	Water column correction.....	85
6.2.4.	Benthic community composition.....	89
6.2.5.	Hyperspectral $\rho_{\text{bottom}}$ vs. benthic communities composition.....	90
6.3.	Results and discussion.....	93
6.3.1	Bio-optical characterization .....	93
6.3.2.	Retrieved bottom reflectance.....	97
6.3.3.	Benthic community composition.....	103
6.3.4.	Analyzing the bottom reflectance in light of the benthic community .....	105
7	REMOTE SENSING DATA FOR CORAL REEF MAPPING IN THE ACRB.....	121
7.1.	Introduction .....	121
7.2.	Materials and Methods.....	125
7.2.1.	Pre-processing of the WV02 scene .....	125
7.2.2.	Bottom mapping in the <i>Parcel dos Abrolhos</i> , ACRB .....	134
7.3.	Results and discussion.....	138
7.3.1.	Performance of the pre-processing steps.....	138
7.3.2.	ACRB Mapping.....	149
8	CONCLUDING REMARKS, RECOMENDATIONS AND FINAL CONSIDERATIONS .....	159
	REFERENCES .....	163
	APPENDIX A .....	181

## 1 INTRODUCTION

Coral reefs are the most biodiverse and productive ecosystems in marine environments (CONNELL, 1978). Several studies have shown that these ecosystems appear to be the first to respond to global climate changes, such as increasing sea surface temperature (SST) and ultraviolet radiation, and the acidification of seawater that results from higher levels of atmospheric CO<sub>2</sub> concentration (HOLDEN; LEDREW, 1998; HOEGH-GULDBERG, 1999). SST increases can lead to the loss of symbiotic relationships between corals and zooxanthells and cause coral bleaching events. In response to ocean acidification, a decrease in the biodiversity of these ecosystems can be expected (HOEGH-GULDBERG et al., 2007). Additionally, variation in sedimentation rates caused especially by deforestation can also result in negative feedbacks for these ecosystems. Because of its sensitivity, coral reefs are considered biological indicators of global climate change (HOLDEN; LEDREW, 1998). In this context, monitoring programs to detect changes in coral reef biodiversity and coral bleaching are essential.

As in other environments, remote sensing approaches for acquiring data in coral reef ecosystems are the most cost-effective, allowing for the synoptic monitoring of large areas, including places with difficult access (MUMBY et al., 1999). In recent years, remote sensing studies on coral ecosystems have increased considerably because of the greater availability of orbital sensors with better spatial and spectral resolutions, as well as the development of different techniques for digital classification processes. Orbital high spatial resolution sensors, such as IKONOS and Quickbird (4 and 2.4 m, respectively), as well as high spectral resolution sensors (e.g., *Airborne Visible/Infrared Imaging Spectrometer* –AVIRIS) and other airborne sensors with both high spatial and spectral resolutions (e.g., *Compact Airborne Spectrographic Imager - CASI*, *Portable Hyperspectral Imager For Low Light Spectroscopy* - PHILLS, *Advanced Airborne Hyperspectral Imaging Sensors* -AAHIS) have been successfully used in coral reef studies (ANDRÉFOUËT et al., 2003; LOUCHARD et al., 2003; HOCHBERG; ATKINSON, 2003; PHINN et al., 2012, among many others). These technologies have improved mapping accuracy compared to other multispectral sensors traditionally used.

Even though remote sensing has the potential to map pure bottom types in submerged reef environments, the next challenge would be to monitor biodiversity to detect

changes in the benthic communities along time. Literature shows that most of the works using this technology in coral reefs were conducted in the Caribbean Sea, in Polynesia and the Great Barrier Reef in Australia, where water is very clear, the biological communities show high diversity and geomorphology presents distinctive zones. Some limitations arise when focusing in complex benthic substrates, with a mixture of different taxonomic and/or functional types, with the aim to detect alterations. The water column above these targets introduces additional complexity and the performance in removing its effect needs to be known to obtain adequate conclusions about the environmental shifts.

In the present work, some of these constraints are addressed for the Abrolhos Coral Reef Bank (ACRB), Brazil, which is an unexplored geographic area from the remote sensing of the bottom point of view. Chapter 3 includes a theoretical background and a revision of the proposed methods correct the water column effect. Chapter 4 describes main characteristics of the ACRB, *in situ* and remote sensing data used in this work. In chapter 5, a deep study about water column correction methods was performed, showing some inter-comparisons of different methods and evaluating the uncertainties associated with the determination of bottom reflectance from above water radiometry. In chapter 6, the spectral separability of hyperspectral above water radiometry sampled over natural benthic communities was analyzed for the ACRB. The water column effect was not neglected for the radiometric measurements and demanded a correction of its distortion. In chapter 7, an area belonging to the ACRB was mapped into benthic classes using high spatial resolution orbital imagery of the WorldView-2 (WV02) sensor. Finally, in chapter 8, some recommendations for future works and concluding remarks are addressed.

## **2 OBJECTIVES**

### **General**

The general objective of this work was to evaluate the potential of remote sensing to map coral reef areas and monitor changes in submerged benthic communities in coastal waters of the Abrolhos Coral Reef Bank, Brazil.

### **Specific**

As specific objectives the following were proposed:

- To evaluate the evaluate the performance of the algorithms in the retrieval of bottom reflectance associated with (i) different optical active constituents (OAC) concentrations in the water, (ii) bathymetry gradient, and (iii) types of bottom substrate, using simulated spectra, multispectral remote sensing data and *in situ* above-water radiometric hyperspectral measurements collected at the ACRB;
- To analyze the spatial variability of OAC in waters of the ACRB, collected during two summer campaigns;
- To assess the potential to detect subtle changes in the submerged benthic community composition by above water radiometry and detect possible diagnostic spectral features of these changes;
- Finally, to achieve the first bottom type map of the external arc of the ACRB using remote sensing data collected with the WV02 orbital sensor.



### 3 THEORETICAL BACKGROUND

#### 3.1. Some concepts in ocean color remote sensing

##### 3.1.1. Top-of-atmosphere signal components

Although remote technologies have a great potential in studies of the sea bottom, extracting the reflectance spectrum from the data of orbital optical sensors is complex. Several processes affect satellite signals which include four main contributions that should be properly treated: (i) photons that interact with the atmosphere but do not reach the water surface. This is an inherent problem for any type of terrestrial target studied by remote sensing. Nevertheless, in oceanic environments, atmospheric interference should be carefully considered because Rayleigh scattering caused by gas molecules that constitute the atmosphere is higher in shorter wavelengths where light has a higher penetration in the water; (ii) photons directly or diffusely reflected by the air-sea interface according to Fresnel laws. The specular reflection of direct sunlight is commonly referred to as the sunglint effect. The amount of energy reflected by the surface depends on the sea state, wind speed and observation geometry (solar and view angles), and in images with very high spatial resolution (lower than 10 m), it causes a texture effect that introduces bottom confusion and distortions in reflectance spectrum (HOCHBERG et al., 2004; HEDLEY et al., 2005; LYZENGA et al., 2006; KAY et al., 2009); (iii) photons that penetrate the ocean and interact with water molecules and other constituents of the water column, but do not reach the bottom; and (iv) photons that have interacted with the bottom and contains information about its reflectance properties. Removing the interference of the atmosphere and surface, the first two contributions, to arrive at the signal backscattered by the water body and bottom requires applying specific procedures (atmospheric correction schemes) to the satellite imagery.

A passive optical sensor in space measures the top-of-atmosphere reflectance ( $\rho_{TOA}$ ) (adimensional) (Figure 3.1), defined as:

$$\rho_{TOA} = \frac{\pi L_{TOA}}{E_{SUN} \left(\frac{d}{d_0}\right)^2} \quad (3.1)$$

where  $L_{TOA}$  corresponds to the radiance (in  $W\ m^{-2}\ sr^{-1}\ \mu m^{-1}$ ) received by an orbital optical sensor,  $E_{SUN}$  is the solar downward irradiance at TOA (in  $W\ m^{-2}\ \mu m^{-1}$ ),  $d$  is the distance between the Sun and Earth at the day the image was captured and  $d_0$  is the mean distance between the Sun and Earth. Various processes affect the TOA signal, namely scattering and absorption by the atmosphere (Figure 3.1, Number 1), Fresnel reflection (Figure 3.1, Number 2), backscattering by the water body (Figure 3.1, Number 3), and bottom reflection (Figure 3.1, Number 4).

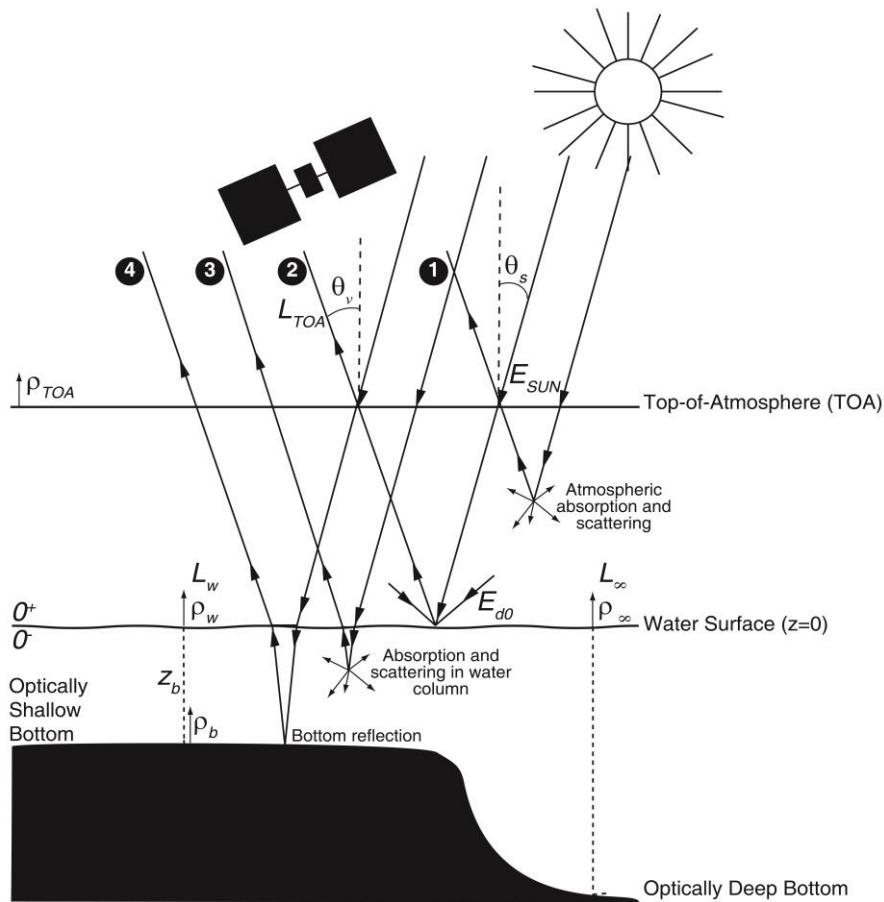


Figure 3.1 – Diagram representing main processes that contribute to signal measured by a passive remote sensor above shallow waters

After crossing the atmosphere to the surface, two distinctions can be made between optically deep water that correspond to water that does not have an influence of the bottom and optically shallow water that is where the remote sensing signal integrates the contribution of the bottom and water column. Analogously, we can define water

reflectance (or surface reflectance) of the optically deep ( $\rho_\infty$ ) and shallow water ( $\rho_w$ ), which are both adimensional, according to equations 3.2 and 3.3:

$$\rho_\infty = \frac{\pi L_\infty}{E_{SUN} \left(\frac{d}{d_0}\right)^2 t(\theta_s)} = \frac{\pi L_\infty}{E_{d0}} \quad (3.2)$$

$$\rho_w = \frac{\pi L_w}{E_{SUN} \left(\frac{d}{d_0}\right)^2 t(\theta_s)} = \frac{\pi L_w}{E_{d0}} \quad (3.3)$$

where  $L_\infty$  and  $L_w$  correspond to water-leaving radiance (in  $\text{W m}^{-2} \text{sr}^{-1} \mu\text{m}^{-1}$ ) in water without and with bottom influence, respectively,  $t(\theta_s)$  is the atmospheric transmittance for the solar zenith angle  $\theta_s$  and  $E_{d0}$  is the downward solar irradiance at the water surface (in  $\text{W m}^{-2} \mu\text{m}^{-1}$ ). These reflectances correspond to the signal from the ocean after atmospheric correction. The differences between equation 3.2 and 3.3 are that  $L_\infty$  only corresponds to the interaction between photons and water constituents in the water column, and  $L_w$  includes, in addition, the effects of bottom reflectance ( $\rho_b$ ). Note that the definitions of  $\rho_w$  and  $\rho_\infty$  (e.g., Equations 3.2 and 3.3) assume that the water body is Lambertian, e.g., they represent true reflectances only in this case.  $\rho_b$  can be formally defined as:

$$\rho_b = \frac{\pi L_b}{E_{dz}} \quad (3.4)$$

where  $L_b$  is the radiance from the bottom and  $E_{dz}$  is the irradiance at the bottom depth  $z$ , and it is also considered as Lambertian. Note that to avoid considering anisotropy of the reflected light field, a commonly used quantity is the remote sensing reflectance ( $\rho^{RS}$ ), expressed in  $\text{sr}^{-1}$ . It is defined as:

$$\rho^{RS} = \frac{L_w}{E_{d0}} \quad (3.5)$$

$\rho^{RS}$  is not *strict sensu* a reflectance because it has units of  $\text{sr}^{-1}$ . If the water body is Lambertian, then  $\rho_w$  and  $\rho^{RS}$  differ by a factor of  $\pi$ .

Reflectance may also be expressed in terms of irradiance. In this case, it is called the irradiance ratio or irradiance reflectance ( $R$ ) (adimensional) and is formally defined as:

$$R = \frac{E_u}{E_d} \quad (3.6)$$

where  $E_u$  and  $E_d$  are upward and downward irradiances, respectively. Depending on the atmospheric correction model applied, results will be in terms of radiance (e.g., water-leaving radiance) or reflectance (e.g., surface reflectance or remote sensing reflectance).

### 3.1.2. Physical processes in water column

In the path between the water surface and marine bottom, electromagnetic radiation interacts with optically active constituents (OAC) by absorption and scattering processes. Both processes occur simultaneously in the water column and can be expressed by the beam attenuation coefficient ( $c, \text{m}^{-1}$ ) as the sum of the absorption ( $a, \text{m}^{-1}$ ) and the scattering ( $b, \text{m}^{-1}$ ) coefficients. The  $c$  value can be easily obtained; however, it is difficult to obtain the relative contribution of absorption and scattering to the total attenuation (KIRK, 2003). The coefficients  $a$ ,  $b$  and  $c$  are Inherent Optical Properties (IOP) that depend on the water column characteristics and do not depend on the geometric structure of light field (MOBLEY, 1999).

In natural environments, other OAC are present in addition to water molecules and cause the attenuation of light throughout the water column. The OAC can be classified as: (i) colored dissolved organic matter (CDOM), that is a fraction of the dissolved organic matter ( $<0.2 \mu\text{m}$ ); (ii) total suspended matter (TSM), defined for ocean color purposes as the material retained in a  $0.7 \mu\text{m}$  (nominal) pore-sized filter; and (iii)

phytoplankton pigments, in which chlorophyll-*a* (chl-*a*) is the most studied (KIRK, 1983).

Each OAC has typical and different spectral behavior (Figure 3.2). Water molecules absorb little quantity of radiation in the blue and green regions, but its absorption increases towards wavelengths in the red. CDOM strongly absorbs energy in the UV and blue regions, showing an exponential behavior that results in low or null absorption in the red (BRICAUD et al., 1981). In comparison with CDOM and water molecules, TSM do not show strong absorption, however, it presents significative contribution to scattering processes (MUMBY; EDWARDS, 2000). Absorption by phytoplankton depends on their pigments presence and concentration, as well as size and shape of phytoplanktonic cells or colonies. The spectrum of chl-*a*, which is present in all vegetal cells, shows absorption peaks in the blue and red regions.

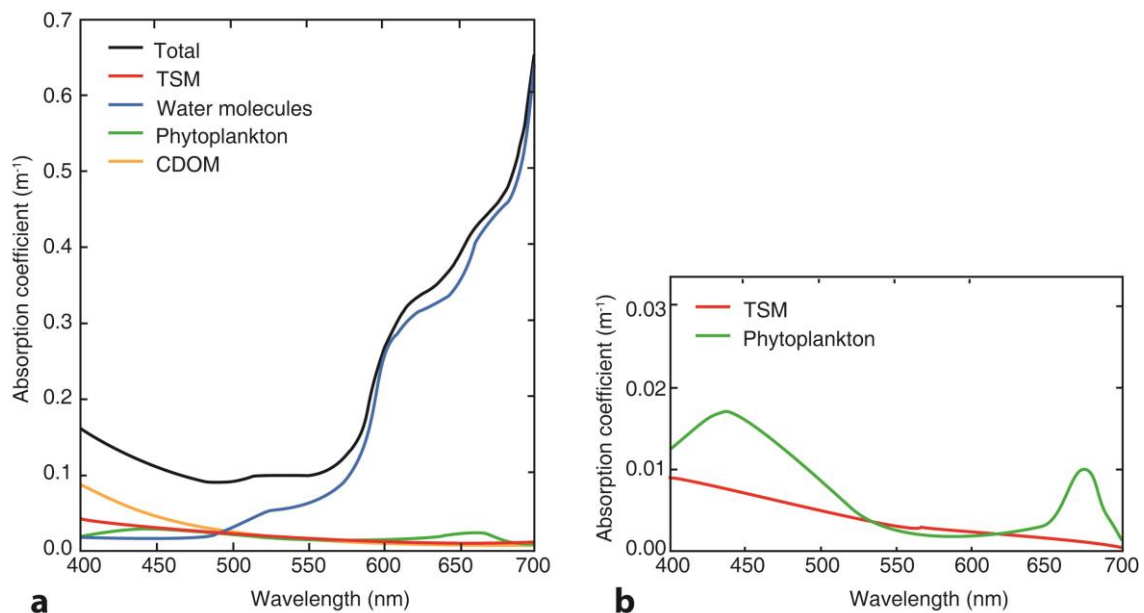


Figure 3.2 – (a) Absorption coefficients spectra ( $m^{-1}$ ) measured in a productive oceanic environment ( $1 \text{ mg m}^{-3}$  chl-*a*): Total absorption (black), TSM absorption (red), water molecules (blue), phytoplankton (green), and CDOM (yellow). (b) Absorption spectra of phytoplankton (green) and TSM (red) are plotted, for a better visualization.

Source: Kirk (2011)

In a simplified manner and through conservation of energy, transmitted light that reaches the benthic community is the incident light in the surface water minus the absorbed and scattered energy within the water column minus the reflected energy of the water surface:

$$\begin{aligned} \Phi_t(\lambda) = & \Phi_i(\lambda) - \Phi_a(\lambda) - \Phi_s(\lambda) - \Phi_r(\lambda) + \Phi_{F^*phyto}(\lambda) \\ & + \Phi_{F^*CDOM}(\lambda) + \Phi_{sRaman}(\lambda) \end{aligned} \quad (3.7)$$

where  $\Phi_t(\lambda)$ ,  $\Phi_i(\lambda)$ ,  $\Phi_s(\lambda)$  and  $\Phi_r(\lambda)$  (W) correspond to transmitted, incident, elastic scattered and reflected by water sea radiant flux, respectively. Inelastic scattering implies changes in the wavelength and/or polarization of scattered photons (MOBLEY, 1994).  $\Phi_a(\lambda)$  accounts for OAC absorption and photons lost in inelastic scattering in  $\lambda$ .  $\Phi_{F^*phyto}(\lambda)$  and  $\Phi_{F^*CDOM}(\lambda)$  refer to the fluorescence by phytoplankton pigments and CDOM, respectively, and  $\Phi_{sRaman}(\lambda)$  refers to Raman scattering by water molecules. In these terms, lost in wavelength  $\lambda'$  (excitation wavelength) acts as source of  $\lambda$  (emission wavelength in cases of inelastic scattering). Chlorophyll-*a* fluorescence emission band is approximately 685 nm, CDOM fluorescence emission is within a broad range, and Raman scattering by water molecules influences the underwater light between 550 and 650 nm (HUOT et al., 2007; ZIMMERMAN; DEKKER, 2006).

### 3.1.3. Light penetration in the water column

Once solar irradiance reaches the water surface, the simplest model that describes the light attenuation in the water column considers that  $E_{d0}$  decays exponentially with depth ( $z$ ) as the Beer-Lambert Law and is a function of wavelength ( $\lambda$ ):

$$E_{dz} = E_{d0}e^{-K_d z} \quad (3.8)$$

where  $E_{dz}$  and  $E_{d0}$  are the downwelling irradiance at depth  $z$  and the water surface, respectively.  $K_d$  ( $m^{-1}$ ) is the diffuse attenuation coefficient of the downward irradiance defined in terms of the decrease of the ambient downwelling irradiance ( $E_d$ ) with depth

that comprises photons heading in all downward directions (MOBLEY et al., 1994);  $K_d(\lambda)$  varies vertically with depth, but in ocean color remote sensing it is generally used as an average over the first attenuation depth, that is referred to in this work. Unlike  $a$ ,  $b$  and  $c$ ,  $K_d$  is an Apparent Optical Property (AOP) that depends on water column characteristics (scattering and absorption properties) and the geometric structure of light fields.

$$K_d = -\frac{d \ln E_d}{dz} = -\frac{1}{E_d} \frac{dE_d}{dz} \quad (3.9)$$

From *in situ* measurements of the vertical profile of  $E_d$ ,  $K_d$  also can be estimated as the slope of the linear regression in a plot of  $(\ln E_d)$  versus  $z$  over the depth range of interest. Other approaches that more accurately obtain  $K_d$  values may be encountered in Kirk (2003). Nevertheless, some approximation of  $K_d$  can be estimated from remote sensing data. For example, Lee et al. (2005) provide an algorithm for its estimation that performed well even in Case-2 waters (those waters influenced not just by phytoplankton and related particles, but also by other substances that vary independently of phytoplankton, notably inorganic particles in suspension and yellow substances (MOREL; PRIEUR, 1977; GORDON; MOREL, 1983; IOCCG, 2000). The algorithm is based in estimates of certain IOP,  $a$  and backscattering ( $b_b$ ) coefficients obtained from remote sensing from the Quasi-Analytical Algorithm (QAAv5) (LEE et al., 2002).

The depth of light penetration is compromised when the concentration of OAC in the water column is high. Because of the  $E_d$  that reaches the water column, bottom detection decreases as the water constituent concentration increases, and,  $K_d$  increases as OAC increase.

As a result of light in the water column interacting with OAC,  $K_d$  is also affected by the OAC concentration. Figure 3.3a shows the light attenuation in Case-1 waters with very low chl- $a$  concentration ( $0.01 \text{ mg m}^{-3}$ ) for different wavelengths: 450 nm (a) 500 nm (b) 550 nm (c) 600 nm (d) and 650 nm (e). Attenuation increases with  $\lambda$  such that light in

the red region has a low penetration in which, only 1% of the surface radiance penetrates to 20 and 13 m for the 600 and 650 nm wavelengths, respectively. As a result of the low light penetration for wavelengths greater than 700 nm, in submerged substrate mapping by remote sensing, only the sensors that operate in the visible region are used. Figure 3.3b compares the curves of light penetration in different environments at 400 nm: Case-1 waters with a chl-*a* concentration of 0.1 mg m<sup>-3</sup> (a); coral reef environments using the  $K_d$  value of 0.14 m<sup>-1</sup> found in French Polynesia (MARITORENA, 1996) (b); Abrolhos Coral Reef Bank (ACRB), Brazil with a  $K_d$  of 0.18 m<sup>-1</sup> (c); Case-1 waters with a chl-*a* concentration of 1 mg m<sup>-3</sup> (d); and Case-2 waters with a chl-*a* concentration of 0.5 mg m<sup>-3</sup>, CDOM absorption at 400 nm of 0.3 m<sup>-1</sup> and mineral concentration of 0.5 g m<sup>-3</sup> (e). In these natural coral reef ecosystems, particulate and dissolved matter occurs along with phytoplankton biomass. In low chl-*a* concentration waters (0.1 mg m<sup>-3</sup>) at 100 m depths, 3.8% of the water surface irradiance penetrates. If chl-*a* concentrations experience rise a 10 fold, attenuation increases disproportionately and this light percentage reaches only the first 14 m in depth. It is known that total pigments concentration increases at low irradiance levels as result of ontogenetic chromatic acclimation processes (WAALAND et al., 1974; ROSENBERG; RAMUS, 1982; HANNACH, 1989; DAWES, 1998). It means that if for example a macroalgae specie occurs in two different depths, it is expected to be found higher pigments content in the deepest one.

In optically deep waters, the effective penetration depth of imagery (commonly called  $z_{90}$ ) is the layer thickness from which 90% of the total radiance originates; this depth is approximately:

$$z_{90} \cong \frac{2.3}{K_d} \quad (3.10)$$

Therefore, if the target of interest is located below  $z_{90}$ , the water column correction would be severely compromised or not able to correct the water column effect. This would be caused by not enough photons reaching to the bottom and returning to the surface. If  $K_d$  decays, the maximum depth in which a substrate can be detected increases. If the objective is to map a substrate, for example, at 10 m depth,  $K_d$  should

be equal or lower than  $0.10 \text{ m}^{-1}$ . To map deeper areas, the water should be clearer. In clear waters, the maximum depth in which reef bottoms can be mapped by optic remote sensing varies between 20 m (ISOUN et al., 2003) to 25 m (GREEN et al., 2000). These depths are further reduced in turbid Waters.

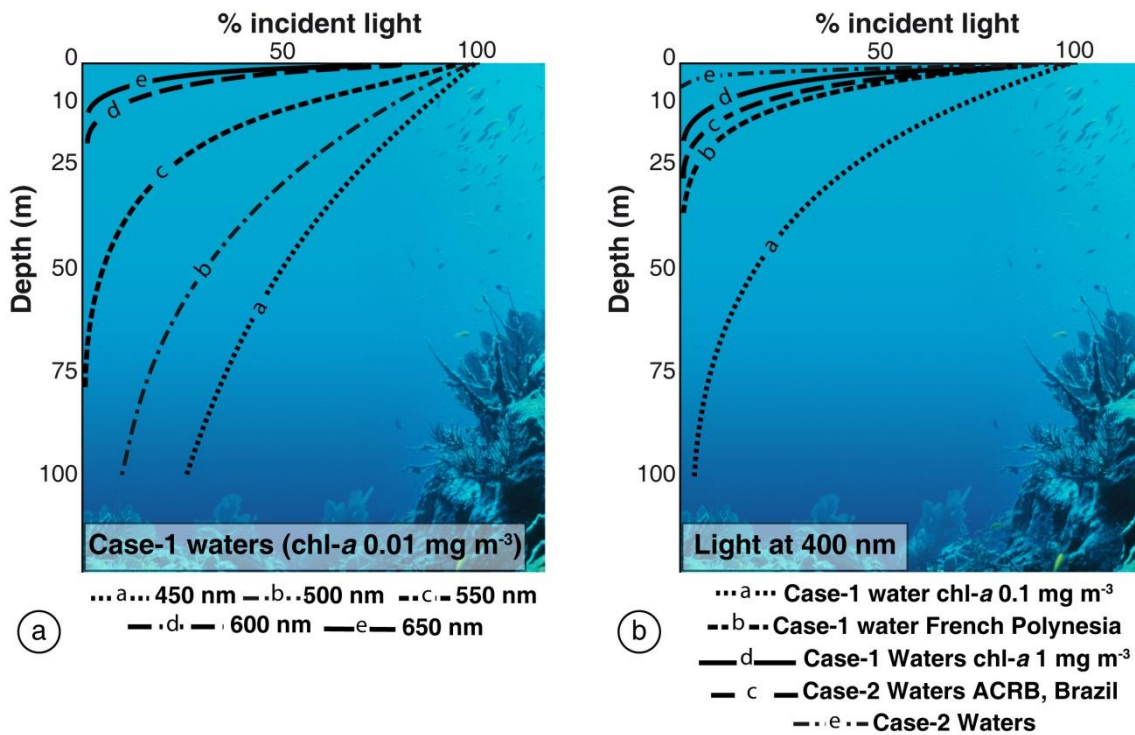


Figure 3.3 – Light decay modeled along water column expressed as percentage of incident light as function of depth (m). (a) Curves represent different wavelengths (nm) in an environment considered as Case-1 water, where chl-*a* concentration is  $0.01 \text{ mg m}^{-3}$ . (b) All curves represent light at 400 nm but in different kind of environment: Case-1 waters (chl-*a*= $0.1 \text{ mg m}^{-3}$ ); French Polynesia Case-1 waters ( $K_d=0.14 \text{ m}^{-1}$ ); Case-2 waters in ACRB, Brazil ( $K_d=0.18 \text{ m}^{-1}$ ); Case-1 waters (chl-*a*= $1 \text{ mg m}^{-3}$ ); Case-2 waters (chl-*a*= $0.5 \text{ mg m}^{-3}$ ,  $a_{CDOM}(400)=0.3 \text{ m}^{-1}$ , minerals concentration= $0.5 \text{ g m}^{-3}$ ).

### 3.1.4. Surface and bottom reflectance relation

The reflectance ( $\rho_w$ ) measured at surface with  $\rho_b$  may be related to the water column reflectance following expression 3.11 (BIERWIRTH et al., 1993):

$$\rho_w = \rho_\infty(1 - e^{-2K_d z}) + \rho_b e^{-2K_d z} \quad (3.11)$$

where  $\rho_\infty$  refers to the remote sensing reflectance from optically deep water that does not influence the bottom and can be used as a proxy of water columns above shallow substrates, assuming that its characteristics are depth independent. The influence of different water columns in the above water reflectance of shallow bottom types are illustrated below. Different substrates (e.g., coral sand, brown algae and green algae) can be easily distinguishable from each other by their spectral behavior when they are at the surface (Figure 3.4a). Coral sand has a high reflectance in the visible spectra, which increases with wavelength. Both algae types have a lower reflectance with an absorption band at approximately 680 nm that responds to accessory pigments and increments towards the infrared region, where reflectance is high and caused by high scattering within the vegetal tissue. These two curves are also easily differentiated by their reflectance peak, at approximately 550 nm in the case of green algae and displaced to the red region (at approximately 600 nm) in brown algae.

Different simulations were performed using WASI v.4 software (GEGE, 2012) to assess the impact caused by the above water reflectance as a result of different water columns upon the substrate. In all simulations, the same environmental conditions were considered. In the first simulations, the set depth was altered using Case-1 water models at low chl-*a* concentrations ( $0.05 \text{ mg m}^{-3}$ ), that covaried with the CDOM ( $a_{\text{CDOM}}(440) = 0.004787 \text{ m}^{-1}$ ) according to Morel and Gentili (2009) (Figure 3.4b-d). When the substrate was placed under a water column of 1 m thickness, the reflectance decreased across the spectra and was even high at longer wavelengths. This situation was exacerbated with the bottom depth increment. At 20 m, it was possible to differentiate the substrate type at wavelengths smaller than 570 nm. In the second set of modeled bottoms, the water column characteristics were changed to Case-2 waters (chl-*a*:  $1 \text{ mg m}^{-3}$ ;  $a_{\text{CDOM}}(440) = 0.3 \text{ m}^{-1}$ ; minerals:  $1 \text{ g m}^{-3}$ ). In this case, at a 1 m depth, the three spectra showed lower reflectance than in Case-1 waters; however the substrate types were easily separable (Figure 3.4e).

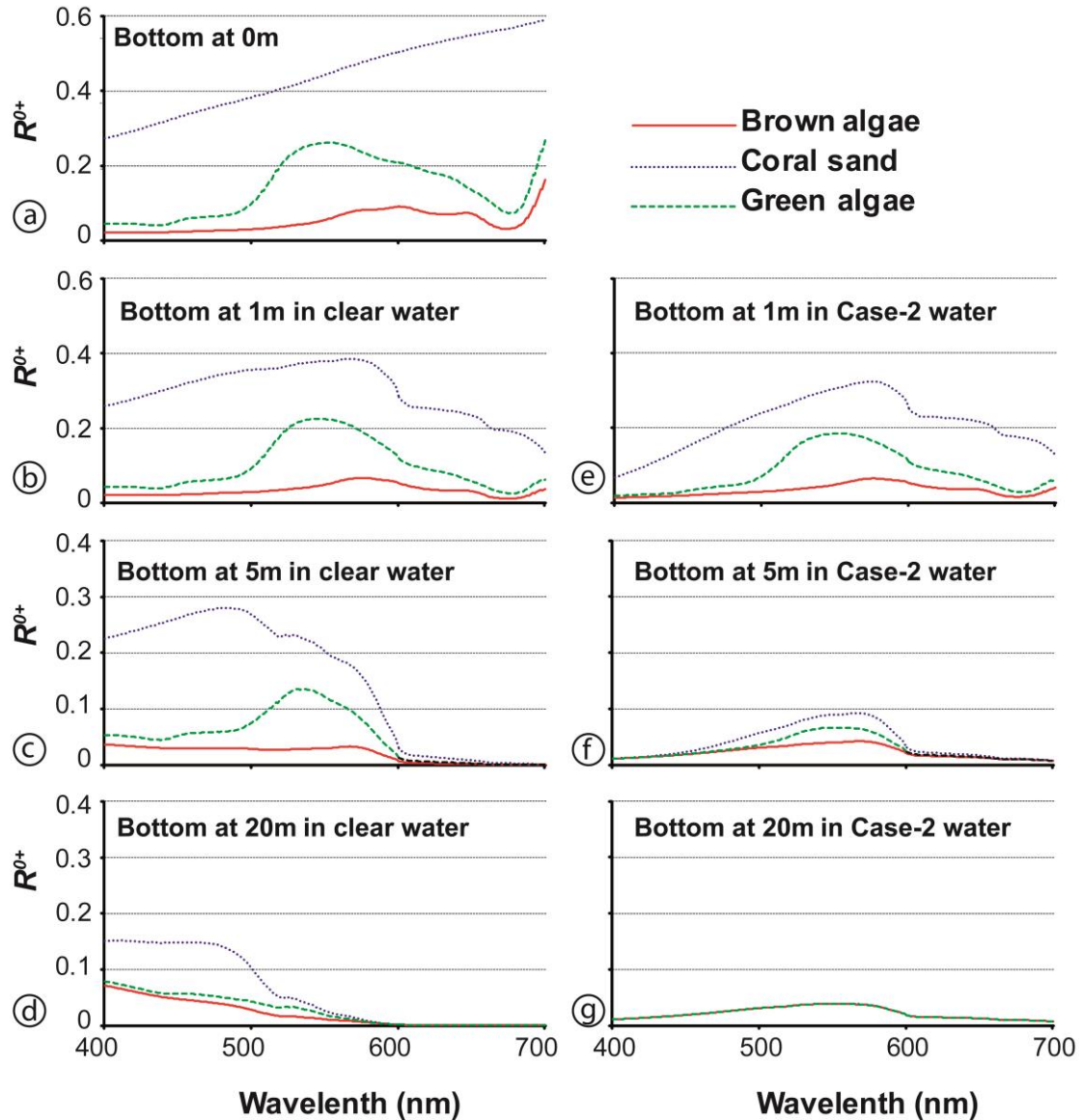


Figure 3.4 – (a) Reflectance of different substrates at 0 m depth, as function of wavelength (in nm): coral sand (blue), brown algae (red) and green algae (green) (Maritorena et al. 1994). (b-d) Reflectance above water versus wavelength (nm) simulated for the same substrates in clear Case-1 waters ( $chl-a = 0.05 \text{ mg m}^{-3}$ ) at different depths: 1, 5 and 20 m, respectively. (e-g) Reflectance above water versus wavelength (nm) simulated for the same substrates in Case-2 waters ( $chl-a: 1 \text{ mg m}^{-3}$ ;  $a_{CDOM}(440) = 0.3 \text{ m}^{-1}$ ; minerals:  $1 \text{ g m}^{-3}$ ) at different depths: 1, 5 and 20 m, respectively.

In contrast to the same depth for clear waters, it was possible to see a decrease in reflectance in the blue region in the coral sand spectrum (400-500 nm), which was related to the presence of CDOM that strongly absorbs in this region. When substrates were situated at 5 m or deeper, if differentiation was possible, it was in the green region.

If the three bottoms were at 20 m depth, they showed exactly the same curve, which indicate that this water constitution prevented the bottom detection and can be considered optically deep (Figures 3.4f-g). Curves at 20 m did not have the higher above water reflectance in the blue region; however, they do have a reflectance at approximately 550 nm because of the chl-*a* present in the water and CDOM absorption at 400-500 nm. A higher reflectance can be detected at approximately 600 nm compared to clear water be caused of the TSM scatterings. Therefore, the remote sensing reflectance should be corrected for the column water effect to minimize the confusion between bottom types.

### **3.2. Water column correction algorithms**

All the water correction algorithms reviewed in the following require data that have been radiometrically corrected/calibrated and masked for land and clouds. Most of them also require previous atmospheric corrections. The algorithms consider the bottom as a Lambertian reflector and the terms of reflectance and albedo of the bottom are used interchangeably. They also consider that the signal measured at the surface (being  $L$ ,  $R$ ,  $\rho^{RS}$ ) can be separate into two additive components: the water column and the bottom.

Algorithms differ in their ways of estimating partial contributions to the surface signal and we propose grouping them according to their methodological approach. The models are summarized in Table 3.1, including the approach, characteristics, input data, main equations and output.

#### **3.2.1. Band combination algorithms**

Algorithms in this group can be applied to multispectral data and assume that bottom radiance ( $L_b$ ) is a linear function of bottom reflectance and an exponential function of its depth. Therefore, these algorithms attempt to linearize the relation between radiance and water depth (LYZENGA, 1978). The first algorithm was proposed by Lyzenga (1978) and other derivations have been made and are presented here. Some of these algorithms use  $K_d$ , and although the best estimations of this parameter are obtained from *in situ* data, different approaches to estimate  $K_d$  from satellite data have been made (Figure 3.5).

These algorithms start with  $L_{TOA}$  in shallow areas and the subtraction of the term  $L_{\infty}$  accounts for the influence of the atmosphere based on the dark pixel correction method. Validity of this procedure for atmospheric correction is limited and sometimes the image to be corrected does not include optically deep waters. For some methods, an alternative to this restriction could be performing an atmospheric correction independently and replace terms  $(L_{TOA} - L_{\infty})$  by  $L_w$ .

### 3.2.1.1. Lyzenga's algorithm

Lyzenga's algorithm (LYZENGA, 1978; 1981) is currently one of the most popular approaches (e.g., ANDREFOUËT et al., 2003, MUMBY et al., 1997; MUMBY; EDWARDS, 2002; VANDERSTRAETE et al., 2006; BENFIELD et al., 2007; GAGNON et al., 2007; CALL et al., 2003; CIRAOLO et al., 2006; VALESINI et al., 2010; PU et al., 2010; ZHANG et al., 2013, among others) and the use of this methodology for water column correction has resulted in increased mapping accuracy (MUMBY et al., 1998; GREEN et al., 2000; ACLKESON; KLEMAS, 1987; ZAINAL et al., 1994). This is a relatively simple algorithm in which the local depth of the entire scene is not required. The main assumptions of this model are that: (i) differences in radiances between different pixels for the same substrate are due to differences in depth, and (ii)  $K_d$  is constant for each band. The first step is to select pixel samples for the same bottom at different depths and plot  $(\ln L_{w,i})$  versus  $(\ln L_{w,j})$ , where  $L_{w,i}$  and  $L_{w,j}$  are water-leaving radiances in each band  $i$  and  $j$ , respectively. Depths of these samples must be known, accurate and corrected for the tidal height. The slope of the regression corresponds to a proxy of the attenuation coefficient ratio  $K_{d,i}/K_{d,j}$  that is a constant value for any substrate because it only depends on the band wavelength. As result, a new image composition of depth-independent bands  $i$  and  $j$  (pseudo-color band) is generated. Figure 3.5a shows an adaptation of Mumby and Edwards' scheme (2000) and Yamano's diagram (2013) that represents the method proposed by Lyzenga (1978). This algorithm does not retrieve substrate reflectance, instead, and the results are a relation between radiances in two spectral bands without a depth effect. The result will be in  $(N - 1)$  bands. The algorithm assumes vertical and horizontally homogeneous optical properties and a small variability in the bottom reflectance considering the same type of substrate. This method is applicable only in waters with high transparency, and

its performance depends on the wavelength. Into the entire visible region, this algorithm produces accurate results until 5 m depth and may be suitable until 15 m depth for bands in the blue and green wavelengths (LYZENGA, 1981). Lyzenga (1981) applied his algorithm to airborne multispectral data and spaceborne Multispectral Scanner (MSS)/LANDSAT data. The validation did not include comparisons with measured reflectance using a radiometer but with percentage of reflectance estimated from color intensity, in pictures registered in 9 homogeneous areas between 3 and 5 m in depths. The author found that the remote sensing data corrected with his algorithm estimates reflectances with a standard error between 0.018 and 0.036 for the airborne data and MSS/LANDSAT data, respectively.

Mumby et al. (1998) applied the Lyzenga model in CASI data and in Thematic Mapper (TM)/LANDSAT, MSS/LANDSAT and Multi- /Satellite Pour l'Observation de la Terre sensors (XS/SPOT) images and then classified the images with and without water column corrections. They recognized that in the CASI image, the water column correction improved the accuracy of the bottom map by 13% in the detailed habitat discrimination, but not in the coarse discrimination. For TM/LANDSAT images the map accuracy was significantly increased in both, the coarse and fine discriminations. Nevertheless, for MSS/LANDSAT and XS/SPOT, the method produced only a single band index using both bands in the visible. The loss of one dimension could not improve the accuracy, even when it was corrected for the deep effect. In contrast, Zhang et al. (2013) tested the effect of application of Lyzenga's algorithm in an orbital hyperspectral image of AVIRIS sensor but no accuracy improvement was observed in the map of habitat types. The authors suggested that the low performance of the procedure is because their study area does not present the same substrate in a wide range of depth, which is necessary to obtain accurate values of  $K_{d,i}/K_{d,j}$ . Therefore, this technique could not be adequate for application in any kind of reef environment. In cases like this, where the same type of substrate only occurs in a narrow range of depths another possibility could be the estimation of  $K_{d,i}/K_{d,j}$  using downward irradiance profiles registered *in situ* (CALL et al., 2003).

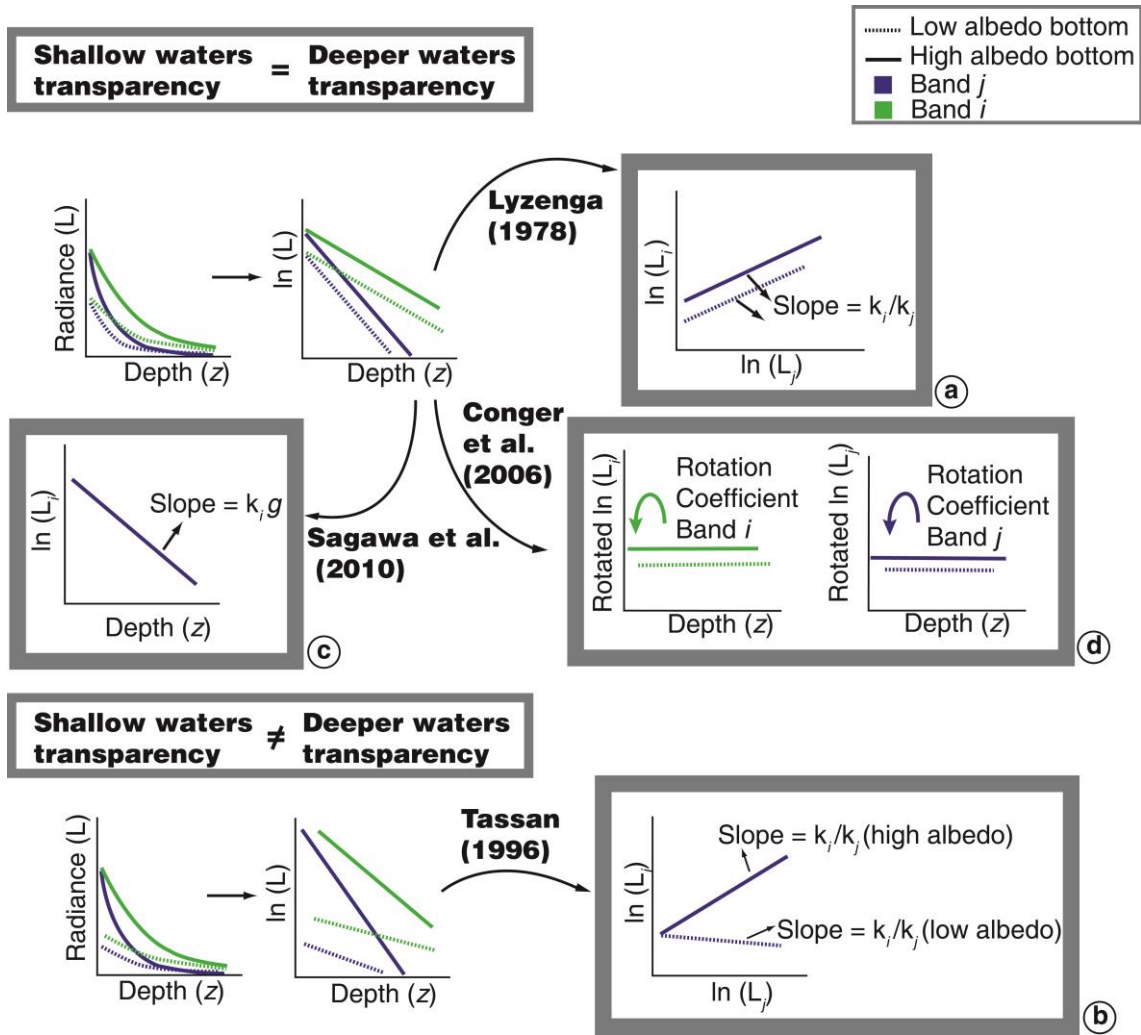


Figure 3.5 – Different strategies proposed to obtain diffuse attenuation coefficient ( $K_d$ ) from a remote sensing image. These methodologies work with samples of radiance in pixels where depth is known. (a) Lyzenga (1978). (b) Tassan (1996). (c) Sagawa et al. (2010). (d) Conger et al. (2006).

Hamylton (2011) applied Lyzenga's algorithm to a CASI image with 15 spectral bands. She used 28 different band combinations, and even though the optimal band combination depended on depths and characteristics of each area, she suggested to:

- Maximize the distance between spectral bands used to obtain the  $Index_{ij}$  (for description of this index see Table 3.1);
- Use bands where the light penetrates in all depths range and avoid using bands beyond 600 nm as a result of the low light penetration in this region;

- Use bands with a certain degree of attenuation in the considered depths range to obtain an accurate  $K_{d,i}/K_{d,j}$

### 3.2.1.2. Spitzer and Dirks's algorithm

Spitzer and Dirks (1987) developed three algorithms analogous to Lyzenga's (1981) specifically for MSS-TM/LANDSAT and High Resolution Visible/SPOT (HRV/SPOT) data. The bands in the visible region of these satellites were renamed as:

(i) Band 1 (Blue region): Band 1/TM (450-520 nm)

(ii) Band 2 (Green region): Band 4/MSS (500-600 nm), Band 2/TM (520-600 nm), and Band 1/HRV (500-590 nm)

(iii) Band 3 (Red region): Band 5/MSS (600-700 nm), Band 3/TM (630-690 nm), and Band 2/HRV (610-680 nm)

The sensitivity of the algorithm to the water column composition, bottom depth and bottom composition was tested. The  $index_{b1}$  which relates Bands 2 and 3 was limited to shallow waters because bands in the green and red bands in this algorithm have smaller penetration in water. Both  $index_{b2}$  (that consider Bands 1, 2 and 3) and  $index_{b3}$  (which uses Bands 1 and 2) can be used in deeper regions because they consider the blue band. While both  $index_{b1}$  and  $index_{b2}$  can be applied in substrates composed of sandy mud, the  $index_{b3}$  can be used in substrates composed of vegetation and sand. In the three cases, the main limiting factor was water turbidity (MUMBY et al., 1998). Similar to Lyzenga's algorithm, they do not retrieve substrate reflectance, but the results relate the radiances in two or three spectral bands without a depth effect.

### 3.2.1.3. Tassan's algorithm

Tassan (1996) modified Lyzenga's method through numerical simulations for application in environments with important gradients in turbidity between shallow and deep waters. Its sequential application can be described according to the following steps:

- Estimate  $X'_i = \ln[L_{TOA,i} - L_{TOA,\infty,i}]$ , for two bands  $i, j$  in pixels from two different substrates (e.g., sand and seagrass or high and low albedo, respectively).  $L_{TOA,\infty,i}$

corresponds to optically deep TOA radiance, with low turbidity, and  $L_{TOA,i}$  corresponds to shallow TOA radiance, with high turbidity;

- Plot  $X'_i$  versus  $X'_j$  for the two substrates and estimate the slope of the linear regressions. Because the slopes of the two lines are different, they did not express a ratio  $(K_{d,i}/K_{d,j})$  (Figure 3.5b);

- Perform statistical analysis  $X'_{ij} = X'_i - [(K_{d,i}/K_{d,j})(low\ albedo)]X'_j$  to separate the sand pixels in the shallow waters of seagrass and deep waters pixels;

- Perform statistical analysis  $X'_{ij} = X'_i - [(K_{d,i}/K_{d,j})(high\ albedo)]X'_j$  to separate the seagrass pixels.

The result of the algorithm is a relation between two bands; however the real reflectance spectrum is not retrieved. In this work, the author did not apply his algorithm to real data, so no quantification of its performance was provided.

#### **3.2.1.4. Sagawa et al.'s algorithm**

Sagawa et al. (2010) developed an index to estimate bottom reflectance based on Lyzenga's method (1978; 1981) that could be applied in environments with low water transparency. For its application, the depth and attenuation coefficient are required. Depth data of various pixels on a homogeneous substrate (sand) allowed estimation of the attenuation. The regression between the radiance and depth of these pixels was calculated (Figure 3.5c) and the slope of the linear equation corresponded to  $[K_d q]$ , where  $q$  is a geometric factor that considers the path length in the water column. Because  $q$  can be geometrically estimated from the view and zenithal angles, it is possible to obtain the attenuation coefficient.

The reliability of this algorithm depends directly on the reliability of Lyzenga's algorithm (SAGAWA et al., 2010) in which the attenuation coefficient is constant over the entire scene and independent of the substrate type, which may be valid only within small areas. The authors emphasize that the accuracy of the bathymetric map is important for obtaining reliable results. The algorithm application in Case II and III waters (JERLOV, 1951) increased the accuracy of the classification from 54-61.7 % to 83.3-90 %. However, the work of Sagawa et al. (2010) does not produce an estimation of algorithm efficiency for retrieving bottom reflectance.

### **3.2.1.5. Conger et al.'s algorithm**

Although Lyzenga's algorithm allows for the removal of the depth effect, after its application, it is difficult to interpret the physics of the generated pseudo-color images. Conger et al. (2006) proposed linearizing the spectral bands with depth using principal component analysis (PCA) to estimate the coefficient that allows each spectral band to be rotated (Figure 3.5d). The first component explains the higher variability and in this case, represents the signal attenuation that results from increasing depth. The second component provides a coefficient that allows the logarithm of spectral band  $i$  to be rotated. This procedure generates depth independent data while maintaining the variability caused by small bottom differences.

The algorithm was applied to a multispectral Quickbird image. As result, depth independent pseudo-color bands were obtained that can be calibrated to obtain the bottom albedo, which was done by Hochberg and Atkinson (2008). Since the application was individually performed for all bands, there was no limitation on their number or width. However, as a result of the low penetration in water of the red wavelengths, this method was not effective for long visible wavelength bands. This algorithm assumes vertical and horizontal homogeneity in the water column optical properties and small albedo variability between samples of the same substrate. Only a visual inspection of the three visible bands of the scene before and after application of the method was performed to evaluate the technique's performance.

### **3.2.2. Model-based algebraic algorithms**

Algorithms in this group require measurements of different water body parameters (e.g., absorption and scattering coefficients) which determine the behavior of light within a water column. Most of the models in this group were not developed to estimate bottom reflectance from surface reflectance measurements, and in general, no such validations are provided. Nevertheless, they could be inverted if all other parameters are known.

These algorithms propose distinctive characteristics of the water column, and parameters used in each method are represented in Figure 3.6. In the equations of these models, the parameters are wavelength dependent; for brevity, argument  $\lambda$  was omitted.

For the water column correction of multi-spectral satellite images, *in situ* hyperspectral data used to estimate the parameters required by any model (e.g.,  $K_d$ ,  $a$ ,  $b_b$ , etc.) must be transformed to correspond to the spectral bands of the sensors (MARITORENA, 1996). In most cases, the bottom depth is also required. Passive remote sensing in visible bands can be useful when deriving a bathymetric map in shallow clear waters (LYZENGA et al., 2006; STUMPF et al., 2003; KANNO; TANAKA, 2012, among others]. Also, estimations of the bathymetry using airborne LIght Detection And Ranging (LIDAR) in the blue-green wavelengths can provide highly resolved bathymetric surfaces and offer much greater depth penetration than passive technologies (BROCK; PURKIS, 2009).

### 3.2.2.1. Gordon and Brown's algorithm

Gordon and Brown (1974) proposed an empirical algorithm based in the path of photon. The algorithm uses three main parameters:  $R_1$ , that corresponds to photons that do not reach the bottom;  $R_2$  is the contribution of photons to  $R_i$  that strike the bottom once for  $\rho_b = 1$ ; and  $s$  was the ratio of the number of photons that strike the bottom twice by the number that strike once for  $\rho_b = 1$  (Figure 3.6a). They depended on the optical depth ( $\tau_B = \int_0^{z_B} c(z)dz$ ), single scattering albedo ( $\omega_0 = b/c$ ) and scattering phase functions  $\tilde{\beta}_A$ ,  $\tilde{\beta}_B$  or  $\tilde{\beta}_C$  and were provided in Gordon and Brown's work (1973). Phase functions were defined according to the photon path in a water body using Monte Carlo simulations. This algorithm requires some knowledge of the medium characteristics, such as  $c$  and  $b$ , however, it was not tested to retrieve the bottom reflectance and its performance was not provided.

### 3.2.2.2. Maritorena et al.'s algorithm

Maritorena et al. (1994) developed an algorithm to model the water surface reflectance in shallow waters ( $R_w$ ) that can be inverted to derivate substrate albedo ( $\rho_b$ ) from surface measurements. Unlike Gordon and Brown's model (1974) that is based on the photon life history, Maritorena et al. (1994) proposed a more convenient method based on measurable properties of the water column (Figure 3.6b). In their algorithm, the irradiance reflectance of shallow waters ( $R_w$ ) below the surface is equal to the deep water reflectance ( $R_\infty$ ) plus substrate contrast ( $\rho_b - R_\infty$ ) after correction for the depth effect (using the term  $e^{[-2K_d z]}$ ). The algorithm's ability to model  $R_w$  was satisfactorily

validated with both Monte Carlo simulations and *in situ* measurements. Nevertheless, it was not tested in an inverse manner to obtain the  $\rho_b$ .

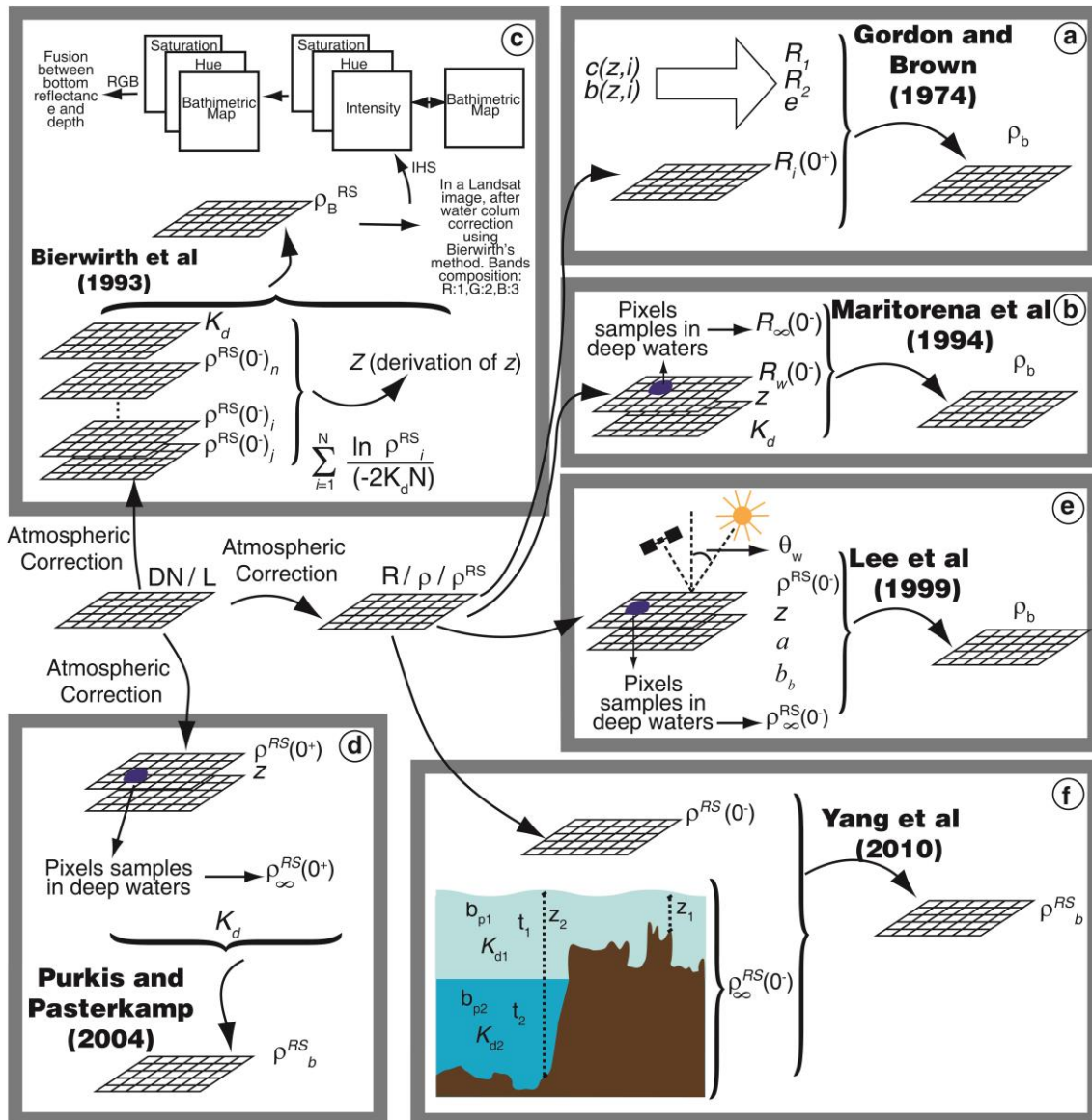


Figure 3.6 – Starting from a remote sensing image above shallow waters, several algorithms can be applied to obtain bottom reflectance. Note that each approach uses distinct inputs. Different boxes represent different algorithms (a) Gordon and Brown (1974). (b) Maritorena et al. (1994). (c) Bierwirth et al. (1993) (d) Purkis and Pasterkamp (2004) (e) Lee et al. (1999). (f) Yang et al. (2010).

### 3.2.2.3. Bierwirth et al.'s algorithm

In contrast with other methods in this group, Bierwirth et al.'s algorithm (1993) does not require  $z$  as input, but only needs  $\rho^{RS}(0^-)$  and  $K_d$ . The results of the model are  $\rho_B^{RS}$  and  $Z$ , that correspond to derivations of the real bottom reflectance and depth, respectively. Therefore, this methodology corrects for the depth effect in each pixel; however, it does not retrieve the real bottom reflectance. Derived and real bottom reflectances ( $\rho_B^{RS}$  and  $\rho_b^{RS}$ ) can be related by a factor ( $e^{\Delta z}$ ), where  $\Delta z$  corresponds to an intrinsic methodological depth error. This error is different between pixels but constant between different bands of the same pixel. This means that the properties of the real reflectance can be staggered by the same constant for each band, which varies between pixels.

Thus, the spectral hue for each pixel will be preserved, regardless of variations in depth. The authors estimated  $\rho_B^{RS}$  for the visible bands of a TM/LANDSAT image. For visualization, the  $\rho_B^{RS}$  values were resampled between 0 and 255. In a composition red-green-blue (RGB) system of  $\rho_{B,3}^{RS}:\rho_{B,2}^{RS}:\rho_{B,1}^{RS}$ , the observed colors are depth independent. The algorithm was tested successfully and represents a valuable tool for management and analysis of coastal regions and submerged substrates. The authors note that accurate estimates of water column parameters are required and that the model assumes horizontal homogeneity, which may not be valid for certain regions.

If a bathymetric map of the reef is available, this methodology offers an additional utility by producing a fusion to both images. The  $\rho_{B,3}^{RS}:\rho_{B,2}^{RS}:\rho_{B,1}^{RS}$  composition can be transformed to an intensity-hue-saturation (IHS) color system. The intensity can be replaced by the bathymetric map, and the layers composition must be transformed again to the RGB system. As result, a fusion image is produced where the bottom reflectance color is preserved and the intensity shows the depth structure of the image (Figure 3.6c). The orbital image and bathymetric map should be of the same spatial resolution.

### 3.2.2.4. Purkis and Pasterkamp's algorithm

Unlike the other models discussed here, Purkis and Pasterkamp's algorithm considers the direct effect of the water surface (corrected by the multiplicative factor  $1/0.54$ ). Hence, the remote sensing data is evaluated above the surface ( $0^+$ ) (Figure 3.6d). The

algorithm validation was performed with the radiometric data measured above and below the water over a sand seafloor. The model was able to reproduce *in situ* data with a root mean square error (RMSE) equal to 0.017. The water column model was applied to a TM/LANDSAT sensor image with different processing levels: homogeneous depth for the entire reef assuming a flat topography (i), with a modeled topographic profile (ii), and depths measured in field (iii). The digital classification showed a higher accuracy for the third case, because of the higher quality of the depth data. Thus, the authors concluded that a bathymetric survey with the spatial resolution compatible with the image spatial resolution is required to produce a map of benthic habitats with sufficient accuracy to be used in quantitative analyses, management or time series studies.

#### 3.2.2.5. Lee et al.'s algorithm

Maritorena et al. (1994) proposed a simplification where different attenuations could be reduced to a unique factor  $K_d$ . Lee et al., however, considered that the attenuation coefficients for the upward and downward direction were different and suggested a simple method of estimating them as a function of their inherent optical properties. In this algorithm, which was developed for hyperspectral data, Lee and colleagues (LEE et al., 1998; LEE et al., 1999) proposed a model to estimate  $\rho^{RS}$  in shallow waters with bottom influence in the surface signal. This model was based on the quasi-single scattering theory (GORDON, 1976). Therefore, it considers that the forward scattering is negligible and water attenuation is only dependent on total absorption ( $a$ ) and backscattering ( $b_b$ ) (Figure 3.6e). If hyperspectral data are available, the method proposes an inversion scheme to retrieve some information of water column and bottom from spectral data: absorption coefficients at 440 nm of phytoplankton ( $a_{phyto}(440)$ ), and gelbstoff and detritus ( $a_g(440)$ ), particle backscattering coefficient at 400 nm ( $b_{bp}(400)$ ), bottom reflectance at 550 nm ( $B$ ) and  $z$ . However, in this work the authors did not compare *in situ* bottom reflectance with those retrieved by the algorithm, but they only used *in situ* values to validate the model for coefficients  $a_{phyto}(440)$ ,  $a_g(440)$  and  $z$ .

Some studies have applied an inversion scheme of Lee et al.'s algorithm to obtain the bottom reflectance, depth and water column properties simultaneously (LEE et al.,

2001; LEE et al., 2007; GOODMAN et al., 2008). In this scheme, the bottom reflectance ( $\rho_b$ ) is defined as  $\rho_b = B\rho_{sh}$ , where  $\rho_{sh}$  is the albedo shape normalized at 550 nm. In their works, Lee et al. (2007) only considered the shape of the sand albedo; Lee et al. (2001) also considered the spectral shape of seagrass; whereas Goodman et al. (2008) used four types of bottom: sand, coral, algae and a flat spectrum. Nevertheless, validations of bottom reflectance included in these studies were limited. Lee et al. (2001; 2007) only showed the retrieved bottom reflectances at 550 nm in the form of a histogram or map without comparing them with the ground truth. Goodman et al. (2008) Goodman and Ustin (2007) combined inversion and the forward schemes of Lee's model. First, they used an inversion of the model to obtain the bathymetry and water constituents for all of the pixels from an AVIRIS image. In this step, the bottom reflectance was only the sand spectrum. Nevertheless, they found that the results were similar, regardless of the bottom reflectance spectra considered as the input. Once the water constituents and bathymetry were obtained, the authors used this information in a second step as input for the Lee model in the forward method together with the reflectance curves of the coral, sand and algae to create endmembers to apply an unmixing model. The unmixing model results were evaluated from depths of 0-3 m and the map accuracy was 80%. The bottom reflectance was also validated at 550 nm for 16 homogeneous sites, and the offset was +10%.

Mishra et al. (2005) applied Lee et al.'s model (1999) to correct a multi-spectral IKONOS image. Because of the limited number of spectral bands of this sensor, the original algorithm was simplified. The algorithm application was effective and showed that the differences in radiance between deeper and shallow areas were minimized. The corrected image showed all areas dominated by sand with approximately the same albedo. Only a visual examination of the image after the water column correction was performed. After classification of the corrected image, the map accuracy was 80.7 %.

#### **3.2.2.6. Mumby et al.'s algorithm**

Mumby et al. (2004) applied a simple model to correct a CASI image of the French Polynesian values. Their model only considered the reflectance at the surface ( $R_w$ ),  $K_d$  and depth for each point of the image, and was obtained as  $\rho_b = R_w e^{-K_d z}$ . The  $K_d$  was obtained by same approach as Lyzenga's, by using the slope of the natural logarithm of

reflectance for a uniform substratum (sand) against the depth from ground-truth maps. Derivative analyses were applied to  $\rho_b$  spectra, but a validation of the model performance to correct the water column was not provided in their work.

#### **3.2.2.7. Yang et al.'s algorithm**

Yang et al. (2010) recently developed an algorithm in which the water column is considered as a multi-layered. This algorithm can be applied to hyperspectral data and considers water column attenuation and scattering components, both of the water molecules and other OAC (e.g., phytoplankton and CDOM). In their work, the authors applied the algorithm to radiometric data collected *in situ*. To be applied to orbital or airborne images, a bathymetric map is required. Modeled values by this algorithm were consistent with *in situ* measured data (fit between modeled and measured data of  $R^2 = 0.9395$ ). Thus, the algorithm proved to be a robust tool applicable for natural heterogeneous environments that can properly remove the water column influence. However, its application is not simple because thorough knowledge of the environment under study is required to determine the attenuation and scattering coefficients of the OAC and volume scattering functions in each layer of the water column. In addition, it can be a computationally expensive method depending on the number of layers used. This methodology is suggested for application in environments with strong water column stratification, as for example in places affected by coastal upwelling events, which frequently leaves a chlorophyll peak associated with a thermocline (Figure 3.6f).

Table 3.1 – Summary of models reviewed in this paper considering methodological approach, data spectral resolution, data required, model results and other observations

Model	Methodical approach	Spectral resolution	Required input and main equations	Assumptions/applicability	Algorithm output
Lyzenga (1978)	Band combination	Multispectral	<p><math>L_w</math> in at least, in two bands. Pixels samples of the same substrate (homogeneous) depth known, occurring in a wide range of depths.</p> $Index_{ij} = \ln(L_{TOA,i} - L_{TOA,\infty,i}) - \left[ \left( \frac{K_{d,i}}{K_{d,j}} \right) \ln(L_{TOA,j} - L_{TOA,\infty,j}) \right]$	Water column vertically and horizontally homogeneous; small variability in bottom reflectance for the same type of substrate. Applicable in high transparency waters. The model cannot be applied to very shallow waters.	Composition of bands $i,j$
Spitzer and Dirks (1987)	Band combination	Multispectral (MSS-TM/LANDSAT, HRV/SPOT)	<p><math>L_{TOA}, L_{TOA,\infty}</math> in at least two spectral bands in the visible region, obtained by MSS-TM/LANDSAT or HRV/SPOT sensors.</p> $Index_{b1} = \ln(L_{TOA,2} - L_{TOA,\infty,2}) - 0.3 \ln(L_{TOA,3} - L_{TOA,\infty,3}) + h_{b1}$ $Index_{b2} = \ln(L_{TOA,1} - L_{TOA,\infty,1}) + \ln(L_{TOA,2} - L_{TOA,\infty,2}) - 0.6 \ln(L_{TOA,3} - L_{TOA,\infty,3}) + h_{b2}$ $Index_{b3} = \ln(L_{TOA,2} - L_{TOA,\infty,2}) - 1.05 \ln(L_{TOA,1} - L_{TOA,\infty,1}) + h_{b3}$	Same assumptions of Lyzenga's model. Applicable only for LANDSAT and SPOT satellites.	Composition of two or three bands
Tassan (1996)	Band combination	Multispectral	<p><math>L_{TOA}, L_{TOA,\infty}</math> in at least two spectral bands. Pixels samples (depth known) of two homogeneous substrates: high and low bottom albedo, occurring in a wide range of depths.</p> $X'_i = \ln[L_{TOA,i} - L_{TOA,\infty,i}]$ $X'_{ij} = X'_i - [(K_{d,i}/K_{d,j})(low\ albedo)]X'_j$ $X'_{ij} = X'_i - [(K_{d,i}/K_{d,j})(high\ albedo)]X'_j$	Can be able to be applied in scenes with turbidity gradients between shallow and optically deep waters. Assumes vertically homogeneity. The application of this method is sequential.	Composition of bands $i,j$
Sagawa et al. (2010)	Band combination	Multi and hyperspectral	<p><math>L_{TOA,i}; L_{TOA,\infty,i}; k_i, q</math> and <math>z</math></p> $Index_i = \frac{(L_{TOA,i} - L_{TOA,\infty,i})}{e^{(-K_d q z)}} = m_i \rho_{b,i}$	Vertical and horizontal homogeneity. Can be applied in environments with low water transparency. Accuracy in bathymetric map is important to obtain a reliable result.	Index proportional to $\rho_{b,i}$

Conger et al. (2006)	Band combination	Multi and hyperspectral	$L_{TOA,i}$ , pixel samples of the same homogeneous substrate, depth known, $L_{TOA,\infty,i}$		Assumes vertical and horizontal homogeneity and small albedo variability of the substrate samples. This method is not effective in the red band.	Pseudo-color band, depth independent
Gordon and Brown (1974)	Model-Based Algebraic	Multi and hyperspectral	$R_i, c, b$	$R_i(0^+) = R_1 + [\rho_b R_2 / (1 - s \rho_b)]$	Vertical and horizontal homogeneity. Empirical estimation of model parameters.	$\rho_b$
Maritorena et al. (1994)	Model-Based Algebraic	Multi and hyperspectral	$R_w, R_\infty, z$ in each pixel of the scene, $K_d$	$R_w = R_\infty + (\rho_b - R_\infty)e^{[-2K_d z]}$	Assumes a vertical and horizontal homogeneity and high water transparency.	$\rho_b$
Bierwirth et al. (1993)	Model-Based Algebraic	Multispectral	$\rho^{RS}, K_d$ , two or more spectral bands are required, $N$ corresponds to number of spectral bands used	$\rho_B^{RS} = \rho^{RS}(0^-) e^{(2K_d Z)}$ $Z = \sum_{i=1}^N \frac{\ln \rho^{RS}(0^-)}{(-2K_d N)}$ $\rho_B^{RS(1/2K_d)} = \rho_b^{RS(1/2K_d)} e^{\Delta z}$	Model must be applied in clear water environments. Bathymetric map can be combined with model results and an image with bottom reflectance and depth structure is obtained.	Derivation of the real bottom reflectance.

Purkis and Pasterkamp (2004)	Model-Based Algebraic	Multi and hyperspectral	$\rho^{RS}(0^+), \rho_{\infty}^{RS}(0^+), K_d, z$ $\rho_b^{RS} = \frac{1}{0.54} \rho^{RS}(0^+) - \frac{(1 - e^{-2K_d z}) \rho_{\infty}^{RS}(0^+)}{e^{-2K_d z}}$	Water-leaving reflectance does not need previous correction for sea-air interface. Accurate bathymetric data are required. Model must be applied in clear water environments.	$\rho_b^{RS}$
Lee et al. (1999)	Model-Based Algebraic	Multi and hyperspectral	$\rho^{RS}, \theta_v, \theta_w, b_b, a, z$ in each pixel of the scene $\rho^{RS}(0^-) = \rho_{\infty}^{RS}(0^-) \left( 1 - e^{\left[ -\left( \frac{1}{\cos \theta_s} + \frac{D_u^C}{\cos \theta_v} \right) k z \right]} \right) + \frac{1}{\pi} \rho_b e^{\left[ -\left( \frac{1}{\cos \theta_s} + \frac{D_u^B}{\cos \theta_v} \right) k z \right]}$ $D_u^C \approx 1,03(1 + 2,4u)^{0,5}$ ; $D_u^B \approx 1,04(1 + 5,4u)^{0,5}$ $u = \frac{b_b}{(a+b_b)}$ ; $k = a + b_b$	Assumes vertical and horizontal homogeneity. The model uses detailed information of the optical properties of the water column. Semi-analytic model.	$\rho_b$
Yang et al. (2010)	Model-Based Algebraic	Multi and hyperspectral	For each water layer: $\rho^{RS}, K_d, z, b_p, f, \beta_w(90^\circ, \lambda_0), \psi_1$ and $\psi_2$ $\rho_b^{RS} = \rho^{RS}(0^-) - \rho_{\infty}^{RS}(0^-)$ $\rho_{\infty}^{RS}(0^-) = Q \left[ \frac{e^{[-2K_d][z-0]} - 1}{-2K_d} \right] \left[ -2\pi\beta_w(90^\circ, \lambda_0) \left( \frac{\lambda_0}{\lambda} \right)^{4.32} \left( \cos \psi + \frac{0.835}{3} \cos^3 \psi \right) - \frac{b_p}{2f} \frac{1 - f^2}{(1 + f^2 - 2f \cos \psi)} \right]_{\psi_1}^{\psi_2}$	Can be used if the water column is vertically heterogeneous and composed by multiple layers. Within each layer, the optical properties are homogeneous. Analytical model.	$\rho_b^{RS}$
Louchard et al. (2003)	Optimization/ Matching	Hyperspectral	Measurements of optical properties, range of depths in area and substrate reflectance occurring in the scene. Data of the geometric conditions of the illumination and image acquisition. Any software that can generate the spectra for the spectral library.	For the first application in an area, it can take long time to generate the spectral library.	Categorical map of bottom type, OAC concentration, z
CRISTAL	Optimization/ Matching	Hyperspectral	Measurements of all bottom reflectance occurring in the scene. Any software that can generate the spectra for the spectral library.	For the first application in an area, it can take long time to generate the spectral library.	Categorical map of bottom type, OAC concentration, z

BRUCE	Optimization/ Matching	Hyperspectral	$\rho^{RS}$ , substrate reflectance of the main types occurring in the scene $\rho_b = B_{sd}R_{sd} + B_{sg}R_{sg} + B_{ba}R_{ba}$	Long processing time to generate spectral library. The result is not categorical but a simplification of the main types of substrates occurring in the area. Useful for areas with low diversity.	$\rho_b$ , OAC concentration, z
SAMBUCA	Model-Based Algebraic	Hyperspectral	$\rho^{RS}$ , substrate reflectance of main substrate types occurring in the scene In Lee et al.'s equation, $\rho_b$ corresponds to: $\rho_b = g_{bm,sand} \rho_{bm} + (1 - g_{bm,sand}) \rho_{sand}$	Modification of inversion scheme of Lee et al. but consider that bottom is a linear combination of two types of substrates.	$\rho_b$ , OAC concentration, z
ALUT	Optimization/ Matching	Hyperspectral	$\rho^{RS}$	ALUT algorithm optimizes the processing time to subdivide the parameters space.	Categorical map of bottom type, OAC concentration, z
Pseudo-Invariant feature (PIF)	Multi-temporal Analysis	Multi and hyperspectral	DN, images of the same sensor and area for different dates perfectly co-registered. Samples of low and high albedo for all dates.	Model assumes the samples are constant in time.	Normalized time series of images
Bertels et al. (2008)	Geomorphology	Multi and hyperspectral	$\rho^{RS}$ , previous geomorphologic analysis	Useful in reefs where the substrate types and geomorphologic zones are strongly related.	Categorical map of bottom type

### 3.2.3. Optimization/Matching algorithms

Hyperspectral data provides information almost continuous in the visible region, which can help to differentiate among submerged substrates. However, when any of the previous procedures to correct water column effect is applied to images with high spectral resolution, the results are computationally heavy. Another approach that can be used involves simulating the spectra for different water column characteristics and mapping the spectra similarities with the simulated spectral library. The result is a substrate map independent of the water column effect (Figure 3.7). In other words, the water column effect is “added” to the substrate’s underwater spectra and is used for different environmental conditions. Further, classification is performed by assigning to each pixel a substrate type that corresponds to the spectrum in the library that best fits with those in the image. Depending on the proposed model, OAC concentration and bathymetric map are simultaneously derived. To generate the spectral library, all of these methods require actual bottom reflectance measured *in situ*. For this reason, all types of substrate reflectances in all possible combinations occurring in the scene that can be registered by the spatial resolution of the sensor must be accurately represented.

Other approach able to be applied only to hyperspectral data is the inversion scheme in which using successive runs, it is looking to minimize errors between a simulated spectrum and a spectrum arriving from the image. Environmental conditions (in this case absorption and backscattering coefficients, depth, bottom reflectance), for which the errors are minimal, are considered as the real ones. For either LUT or inversion methods, the simultaneous retrieval of all the properties (bottom reflectance, depth and water constituents) does mean that the accuracy of each estimated property is highly dependent on the retrieval results of each of the other properties (DEKKER et al., 2011). The relative effect of each of them depends on the water depth and clarity.

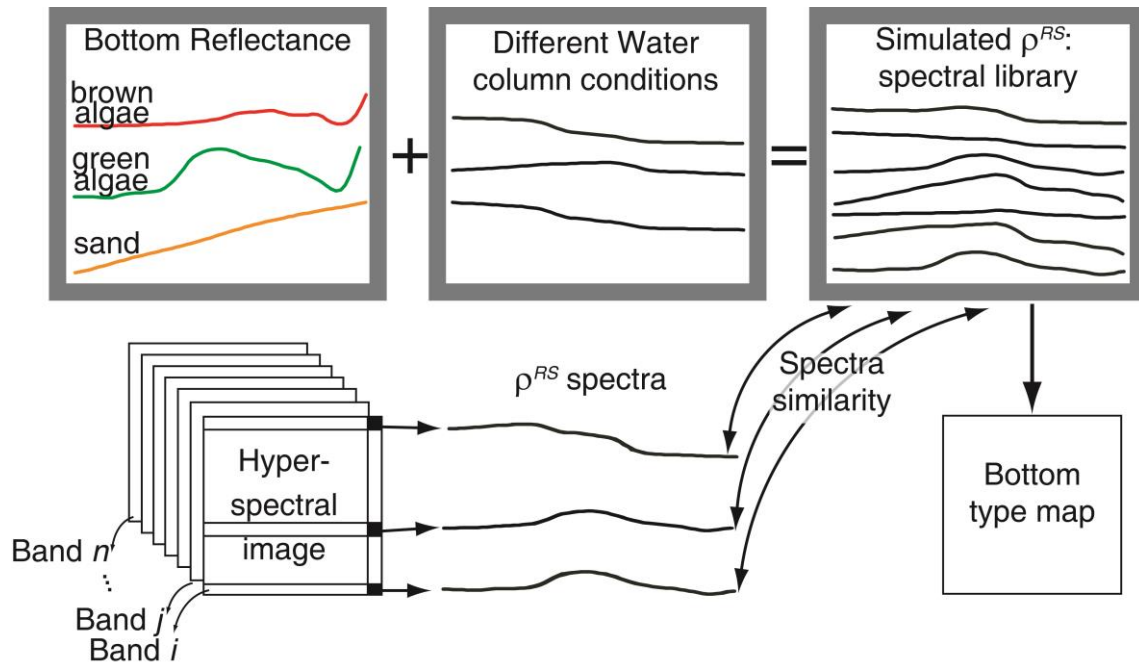


Figure 3.7 – Graphic representation of the approach using Look Up Table matching to generate bottom type map without effect of water column.

### 3.2.3.1. Louchard et al.’s approach

Louchard et al. (2003) created the spectral library simulated in Hydrolight software using the reflectance of the main bottom types present in the study area, estimations of IOP, *in situ* measurements of upward radiance ( $L_u$ ) and downward irradiance ( $E_d$ ), geometric data of the conditions of illumination, image acquisition and range of depth found in the area. The authors also considered Raman scattering. They then applied a minimum distance method to relate the simulated spectra with the spectra of a PHILLS image. This classification methodology generated a thematic map of the substrate without the effects caused by the water column. The authors noted that a good correspondence was found between the classification result and ground truth map, but they did not provide an objective quantification of the accuracy of the substrate type map. This method failed to differentiate the pavement from dense seagrass in areas deeper than 8 m.

### 3.2.3.2. Comprehensive Reflectance Inversion based on Spectrum matching and Table Lookup (CRISTAL)

In contrast to Louchard et al.'s approach, Mobley et al.'s (2005) approach does not require field data and *a priori* assumptions regarding the water depth, IOPs, or bottom reflectance do not have to be made, rather, they are simultaneously extracted from the hyperspectral image. In this approach, pre-computed look-up tables (LUT) are used that include simulated spectral databases generated in HydroLight software for different pure substrates and several combinations of them, in varying depths, OAC in the water column, IOPs, sky conditions and geometry of data acquisition. A total of 41,590 spectra were simulated. The authors only evaluated the method performance by visual interpretation and found that it was successfully applied to a PHILLS image because all variables extracted from the LUT application were consistent with the ground truth. This methodology assumes that the  $\rho^{RS}$  spectrum is accurately calibrated and the spectral library represents all of the environmental variability found in the image. Unlike most of the methodologies, the simulated spectra include inelastic scattering (Raman). If this is not the case, retrieval errors may be large.

### 3.2.3.3. Bottom Reflectance Un-mixing Computation of the Environment model (BRUCE)

Klonowski et al. (2007) proposed an adaptation of Lee et al.'s inversion method (1999) to simultaneously retrieve the substrate type and depth from the reflectance collected by the airborne HyMap imaging system (126 bands and 3.5 m of spatial resolution), on the Australian West Coast. In their work, they expressed  $\rho_b$  as a linear combination of sediments ( $R_{sd}$ ), seagrass ( $R_{sg}$ ) and brown algae reflectances ( $R_{ba}$ ). Spectral curves of 10 substrate types were used as the input to the model: the six pure substrates most frequent in the area (two types of sediments, two types of seagrass and two types of brown algae) and four combinations of them.

For each pixel, the seven unknown parameters  $a_{phyto}(440)$ ,  $a_g(440)$ ,  $b_{bp}(440)$ ,  $B_{sd}$ ,  $B_{sg}$ ,  $B_{ba}$  and  $z$  assumed to be the actual conditions were those that minimized the residual between the simulated and measured spectra (spectra from the image). As result three substrate weighting coefficients ( $B_{sd}$ ,  $B_{sg}$ ,  $B_{ba}$ ) are obtained. These coefficients are reflectance scaling factors that represent, after normalization, the proportional

coverage by an individual substrate class (FEARNS, 2011). They were used to assign the color composition:  $B_{ba}$  to channel red,  $B_{sg}$  to channel green and  $B_{sd}$  to channel blue. The performance validation was performed visually by comparing the substrate mapped with the video records for 25 points of the image, and the authors found a high level of consistency. Although 10 bottom reflectance spectra originating in pure and mixed substrates were considered in the validation only 5 classes were considered according to color in the composed image, so different resultant colors might mean the same combination of bottom types and vice-versa. One requirement of this model is that the bottom types must be spectrally different from one to the other. This point implies a restriction for using this approach in areas with a high diversity of bottom types because it could not provide a good separability between types.

Fearns et al. (2011) applied the BRUCE method in an image collected by the airborne hyperspectral HyMap sensor in a shallow area, whose substrate contained sand, seagrass and macrophyte species. They retrieved proportions of each of these classes in each pixel. Map validation was performed to one section of one of the flight lines, and levels of classification success varied according to type of coverage: sand = 52 %, seagrass = 48 % and brown algae = 88 %. The authors suggested that the presence of seagrass at low to medium densities in sand areas could swamp the sand signal and be responsible for low accuracy achieved for sand class. Higher success to classify brown algae could be related to lower depths where algal habitats were located.

#### **3.2.3.4. Semi-Analytical Model for Bathymetry, Un-mixing and Concentration Assessment (SAMBUCA)**

Brando et al. (2009) modified the inversion scheme proposed by Lee et al. (1999) to retrieve the bathymetry together with the OAC concentration (chl-*a*, CDOM and suspended particles) and bottom type. Contrary to Lee et al.'s algorithm, SAMBUCA model accounts for the linear combination of two substrate types. When solving for more than two cover types, SAMBUCA cycles through a given spectral library, retaining those two substrata and their estimated fractional cover which achieve the best spectral fit. In this work, the authors were interested in retrieving bathymetric information and some parameters of the water column were fixed in advance using information collected in field. Based on the types of bottom present in the study area,

they only considered brown mud and bright sand. Thus,  $g_{bm,sand}$  is the proportion of each of the bottom covers: brown mud and white sand. The authors used either least squares minimum (LQM), spectral shape matching function or a hybrid formulation of them to estimate the optimization residuum. Their paper proposed a novel method to improve the bathymetry retrieval by combining the optimization residuum with a substratum detectability index (SDI). Therefore, their focus was to retrieve depths, and they did not provide measurements of the performance of the method in retrieving substrate composition.

### **3.2.3.5. Adaptive Look-Up Trees (ALUT)**

Hedley et al. (2009) proposed an algorithm that optimizes both the inversion scheme and matching between the simulated and measured spectra to reduce the time required for its application. The Adaptive Look-Up Trees (ALUT) algorithm proposed a more efficient subdivision of the parameter space (any parameter of interest) once the real range of variability is known. This is simpler to understand using an example. Considering changes in the reflectance as a function of depth, it can be observed that in the first meters of the water column small changes can lead to greater diminution in measured reflectance. However, at greater depths, small changes lead to lesser impacts in the measured reflectance. Therefore, the ALUT algorithm proposes a more detailed subdivision of the depth in shallow areas than in deeper ones. Additionally, Hedley et al. used the matching algorithm Binary Space Partitioning (BSP) tree, which is more efficient than an exhaustive search algorithm.

They used the ALUT approach with the inversion method L99 [58] considering that bottom reflectance spectrum could be one of 78 different curves resulting from the linear mixture of 13 most common substrate types (sand, live and dead coral, algae and seagrass). Considering that they obtained high accuracy when retrieving depths from satellite images, the method appears to be a promising alternative for rapidly running the water column correction. Nevertheless, in that work Hedley et al. only compared depths retrieved by the model with depths measured by sonar, and they did not provide an estimation of the efficiency of retrieving bottom reflectance or substrate type compositions. The authors indicated that their method could have a high level of error when many parameters are derived together.

### 3.2.4. Water column corrections for multi-temporal studies

To detect changes in images from the same sensor in different periods, an inter-calibration between the images is needed. As in all of the temporal studies, co-registration between images must be rigorous since the spatial misregistration can introduce false indications of change. These methods are advantageous because they are inexpensive and require little processing time and data availability. According to Equation 3.1, if the reflectance of the same invariant target shows differences between two dates, these differences might be caused by the acquisition geometry of a scene, water column and/or atmospheric effects. Therefore, contrary to the previously reviewed methods, prior atmospheric corrections are not required. One option is the application of a “pseudo-invariant feature” (PIF) technique (SCHOTT et al., 1988; ELVIDGE et al., 2004) wherein bright and dark pixels (e.g., white beach sand and seagrass substrate, respectively) called PIF pixels are extracted from all images. Any image can be selected as the reference (Image a) and the other image (Image b) is normalized to be compatible radiometrically with Image a. For this conversion, the digital number (DN) of PIF pixels of Image b are plotted versus those of Image a (Figure 3.8a) in each band. Fitting a linear equation to this plot will define a gain and offset to normalize Image b. This method works under the assumption that PIF pixels are constant over time.

A similar normalization was used by Michalek et al. (1993) where the image used as the reference (Image a) showed the highest and widest data range in its histogram. Image b was modified to be compatible radiometrically with Image a (Figure 3.8b). The authors examined pixel samples that appeared similar in natural color in both images, such as bare soil, mangrove forest and deep water.

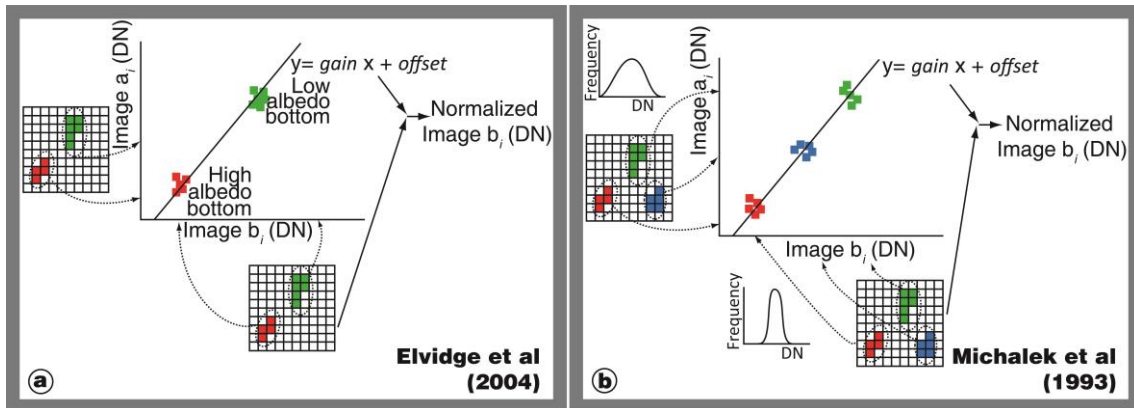


Figure 3.8 – (a) Diagram to obtain of gain and offset values to normalized image as function of a previous one, according to Elvidge et al. (2004) approach. (b) Diagram to obtain of gain and offset values to normalized an image as function of a previous one, according to Michalek et al. (1993) approach.

### 3.2.5. Bertels et al.’s approach (2008)

After the unsuccessful application of Lee et al.’s algorithm, Bertels et al. (2008) selected another approach to minimize the class confusion caused by the depth effect in CASI images of a coral reef area. In this work, they classified an image previously divided into five geomorphological zones found in the scene. For the geomorphologic zone mapping, they applied a minimum noise fraction (MNF) analysis to remove redundant spectral information and used the first five bands. Then, independent classifications according to its geomorphology were applied under the assumption that each geomorphologic zone has different depth and associated benthic communities. A post-processing was finally performed to merge the classes between the different zones. The authors only validated their method in the fore reef and obtained an accuracy of 73 %. This approach did not generate reflectance spectra and can only be used in reefs with a determined configuration where the substrate types and geomorphologic zones are strongly related.



## 4 MATERIALS AND METHODS

In this section, a general characterization of the study area, field work, data collection and remote sensing data using in the present work are described. More detailed information regarding data processing is provided in the correspondent chapters.

### 4.1. Study area

The Abrolhos Coral Reef Bank (ACRB) extends 60 km, along the coastal zone in the south of Bahia State (Brazil), between approximately 17°20''-18°10''S and 38°35''-39°20''O (Figure 4.1). It is considered the largest and richest coral reef area in the South Atlantic Ocean and probably one of the world oceans' major biodiversity hot spots. The biologic relevance of this area boosted the creation of the first Marine National Park in Brazil, besides being an environmental protected area and a marine extractive reserve. The ACRB is located in the largest continuous rhodoliths bed all over the world and its total annual CaCO<sub>3</sub> production is comparable to that of the largest biogenic CaCO<sub>3</sub> deposits in the world (AMADO-FILHO et al., 2012)

In this region, the geomorphology of the reefs is characterized by the type of growth in vertical columns. Such structures are called "*chapeirões*" and their shapes are similar to mushrooms with tops that have a circular or elongated shape. The reefs are formed parallel to the coastline, distributed in the form of two arcs, largely exposed during low tide (Figure 4.1) (LEIPE et al., 1999). Both arcs are separated by the Abrolhos Channel, 15 km wide. The inner, or coastal, arc is located 10-20 km from the coastline and is formed by a complex structure of reef banks and isolated *chapeirões* with variable dimensions. The reef banks are formed by several *chapeirões* that are in close proximity to each other and whose tops are merged. The external, or outward, arc is located in the surroundings of the Abrolhos Archipelago, which is composed of small islands located approximately 60 km from the coast. The reefs in the external arc are disposed as isolated enormous *chapeirões*, in areas up to 25 m deep (LEÃO, 1999). Figure 4.2 represents a cross-section of both arcs, showing the differences in the geomorphology and depths between them.

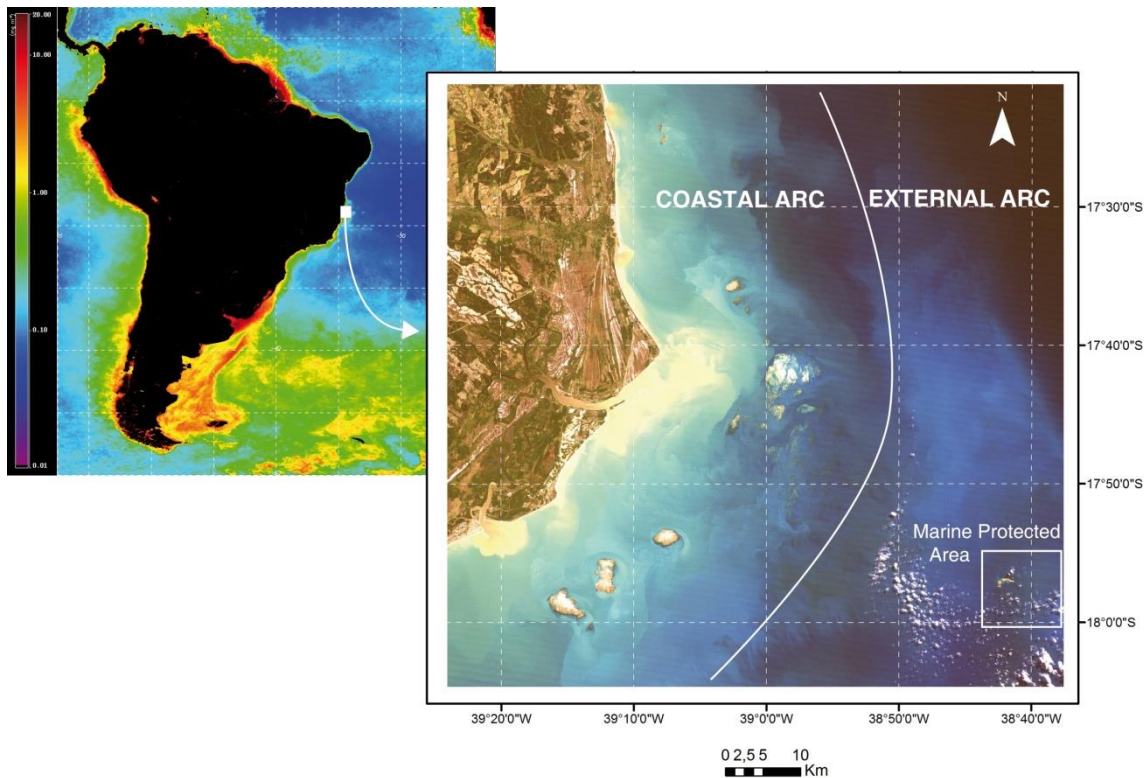


Figure 4.1 – Landsat TM-5 Image (RGB) of the study area (right) and its location in South America, indicated in a MODIS-Aqua Chlorophyll image (left)

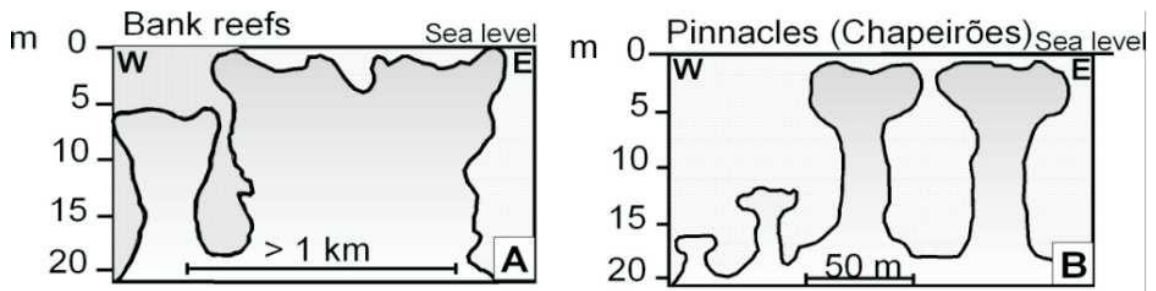


Figure 4.2 – Cross-section scheme of the main reef types in the study area showing the: coral reefs in the coastal (A) and external (B) arcs.

Source: Dutra et al. (2006)

The coastal arc is affected by processes acting in the mainland and bottom sediments near the coastline, which are characterized by 30 to 70% of quartz grains, rare micas and terrigenous mud. At the external arc, siliciclastic sediments represent less than 10%, whereas carbonate sediments dominate, mainly composed of reef derived constituents (SILVA et al., 2013). Reef banks with wide lateral dimensions are located closer to the

shoreline and they function as a physical barrier that block the water flows towards the open sea, acting as a sediment trap from continental sources. This explains the transition from dominant siliciclastic components along and near the coastline to pure carbonate sediments in the middle and outer continental shelf (LEÃO, 1982). Thus, while the external arc is influenced by the tropical waters of the Brazil Current and resuspended bioclastic marine sediments, the coastal arc also receives some contribution from continental discharges (KNOPPERS et al., 1999; LEIPE et al., 1999; SEGAL et al., 2008, SILVA et al., 2013). Among the terrestrial discharges, the most important is from the Doce River, which has a mean annual discharge of  $1,140 \text{ m}^3 \text{ s}^{-1}$  (Source: ANA, 2010). The greatest river discharge season is from November to April due to the rainfall regime along its catchment area, with the maximum between December and February (SEGAL et al., 2008). Sedimentation rates in the Abrolhos Bank are relatively higher than other recifal areas (SEGAL-RAMOS, 2003). The deposition flux is greater during the austral winter due to polar fronts crossing the area, when surface winds from SE, S and SW are predominant and produce turbulent processes increasing sediment resuspension (SEGAL et al., 2008). The circulation with direction North-South is induced by the along-shore winds with a seasonal cycle: Southward in spring-summer and Northward in fall-winter (TEIXEIRA et al., 2013). The cross-shore circulation is mainly forced by tides, and the sub-inertial flow is weak and restricted by the local topography. The passage of cold fronts that arrive in ACRB or that arrive in Cabo Frio and have a remote effect in the region, is also important. Long-period shelf waves created thousands kilometers south of ACRB that propagate into the region also affect the local circulation.

The Abrolhos reefs have also other peculiarities related to the biologic communities. The benthic community in ACRB is dominated mainly by cnidarian and seaweeds, and in lesser proportion, by sponges and mollusks. Three characteristics distinguish the cnidarian fauna of Abrolhos from other coral reefs: the low diversity, high degree of endemism and absence of branching scleractinian. Two factors can be appointed as responsible for this: (i) the isolation from the Caribbean Sea reefs; and (ii) some environmental conditions such as the high turbidity and low geomorphology variability that limit the availability of reef habitats (LEÃO, 1999). Regarding the algae populations, they constitute one of the most abundant elements in the Abrolhos coral

reefs, and are found throughout the entire reef ecosystem, particularly covering inter-reef areas.

#### 4.2. Field work

The field work conducted as part of the present work was framed in the "*Rede Abrolhos*", a cooperative network between several institutions. Two field campaigns were done in the ACRB as part of this work, both during the austral summer, which corresponds to the rainy season. The first was done between 02/06/2012 and 03/03/2012 and the reefs visited were: *Sebastião Gomes* (SG), *Parcel das Paredes* (PA), the Archipelago (ARCH), and the *Parcel dos Abrolhos* (PAB) (Figure 4.3). The second field work was carried out between 03/06/2013 and 03/26/2013. In this case, the sampled areas were: SG, PA, ARCH, PAB, PL (*Pedra de Leste*) and *Timbebas* (TIM) (Figure 4.3).

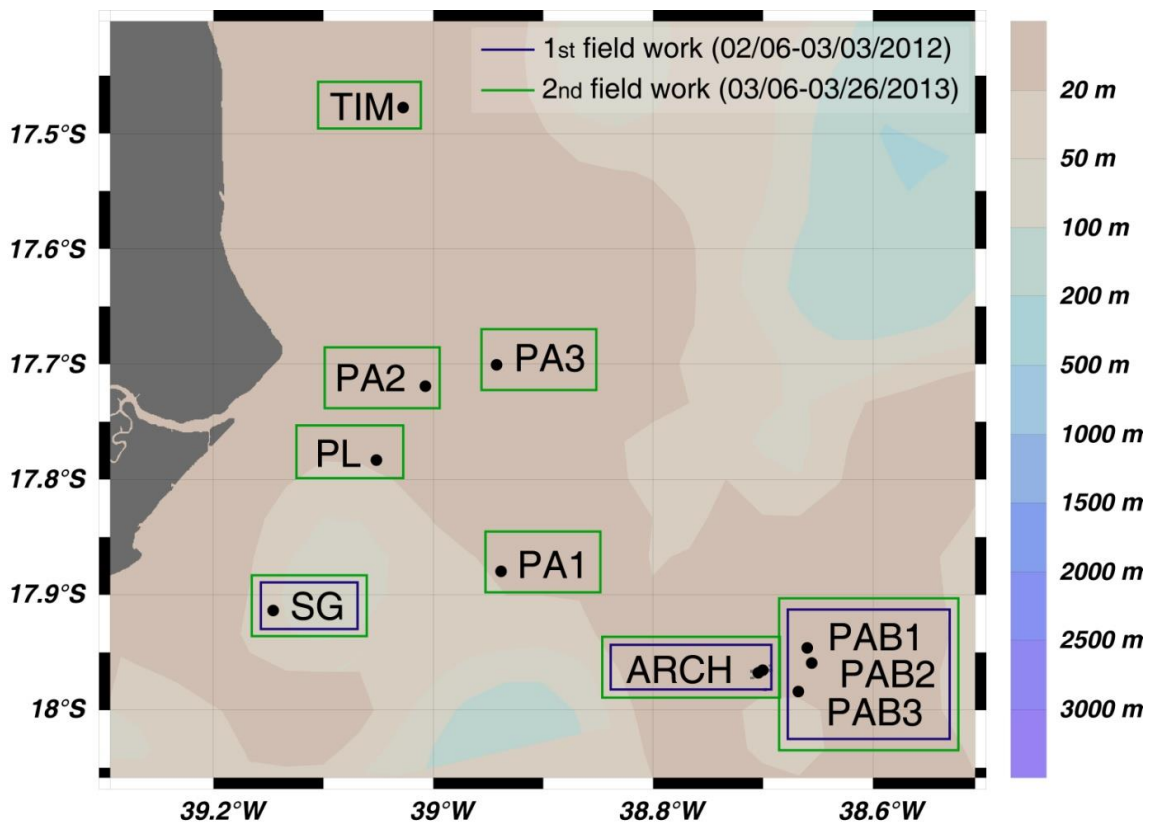


Figure 4.3 – Localization of the main stations sampled in the first and second field campaigns: *Sebastião Gomes* (SG), *Parcel das Paredes* (PA), Archipelago (ARCH), *Parcel dos Abrolhos* (PAB) and *Timbebas* (TIM). The bathymetry data was extracted from the ETOPO2 data base.

The daily sampling plan consisted basically in arriving at a main station and anchoring the vessel for the surveys. Two to six sites above the reefs located in the surroundings of the station, were sampled each day using a small boat due to the shallow depths. In this work, the term “station” is referred only to the main station sampled from the ship and “sites” are referred to the places visited with the small boat in the surrounding reefs. At the main stations the measurements consisted of: above and in-water radiometry, bio-optical properties and environmental factor records. At the shallow sites covered by the small boat, the measurements were: above-water radiometry, water surface collection for bio-optical properties, environmental factors and underwater photographs for the characterization of the benthic community.

#### 4.2.1. Under-water radiometry

Hyperspectral profiles of  $E_d$  ( $\mu\text{W cm}^{-2} \text{ nm}^{-1}$ ) and  $L_u$  ( $\mu\text{W cm}^{-2} \text{ nm}^{-1} \text{ sr}^{-1}$ ) were collected underwater from 349.6 to 802.6 nm using HyperOCR PRO sensors connected to a Satlantic Profiler II (Satlantic Inc.). The  $E_{d0}$  ( $\mu\text{W cm}^{-2} \text{ nm}^{-1}$ ) deck sensor was maintained at the topmost level of the ship superstructure. The Satlantic Profiler was only deployed from the ship in deeper waters letting the instrument drift more than 50 m away before logging to avoid contamination in the measurements caused by shadows of the ship or additional reflection. Profiles were registered between the surface and bottom, with 2-3 casts per station. The data were processed using Prosoft 7.7.16 software to estimate: the profiles of underwater remote sensing reflectance  $\rho^{RS}(z)$  and  $K_d(z)$ .

Prosoft software estimates remote sensing reflectance profiles using the ratio of the upwelling radiance ( $L_u$ ) with the downwelling irradiance ( $E_d$ ), measured at each depth ( $z$ ) (Equation 4.1).

$$\rho^{RS}(z) = \frac{L_u(z)}{E_d(z)} \quad (4.1)$$

The  $K_d(z)$  was estimated following the standard method of Smith and Baker (1986), as the local slope of measured  $\ln(E_d(z))$  within a depth interval centered on  $z_m$  (Equation 4.2). In this work, depth intervals of 50 cm were chosen to determine the local slope.

$$\ln(E_d(z)) \cong \ln(E_d(0^-)) - (z - z_m)K_d(z_m) \quad (4.2)$$

To choose the best depth interval used to determine  $K_d$ , the  $E_d$  profiles at each station were carefully examined. In the first meters of water column,  $E_d$  showed a noisy behavior. Thus, the  $K_d$  values were determined solely at depths where  $E_d$  presented an approximately exponential decay, generally at depths greater than 6 m.

#### 4.2.2. Above-water radiometry

Radiance measurements ( $L$ ,  $\mu\text{W m}^{-2} \text{sr}^{-1}$ ) were made using an ASD Fieldspec Handheld (ASD Inc.) radiometer, which collects radiance between 350 and 1100 nm (bandwidth 1 nm) and with a field-of-view of  $25^\circ$ . The sensor was used to measure signals proportional to the sea surface radiance ( $L_w$ ), sky radiance ( $L_{sky}$ ) and the radiance reflected from a horizontal reference white panel Spectralon ( $L_g$ ). The azimuth angle with respect to the Sun plane was  $137^\circ$  to avoid shadows and sunglint contamination in the measurements (MOBLEY, 1999; FOUGNIE et al., 1999; HOOKER; MOREL, 2003). The zenith angle of the sensor was set to  $45^\circ$  for correspondent water and sky measurements. Measurements were done in the following sequence: WATER - WHITE REFERENCE - SKY, repeating each set 4 to 11 times. For each set of measurements,  $\rho^{RS}(0^+)$  (above-water remote sensing reflectance) was estimated following Expression 4.3:

$$\rho^{RS}(0^+) = \frac{L_w - \rho_{sky} * L_{sky}}{L_g / \rho_g * F_c * \pi} \quad (4.3)$$

where  $\rho_{sky}$  is an above-water reflectance factor for radiance,  $\rho_g$  is the reflectance of the white reference with a value of 0.99 and  $F_c$  is the calibration factor of the white reference.  $F_c$  refers to the calibration between the reference used in the field and a Spectralon panel that remains in the laboratory.  $\rho_{sky}$  was estimated according to Mobley (1999) as a function of the viewing and solar zenith angles and wind speed.

Due to the high light attenuation in the water column for wavelengths shorter than 400 nm and longer than 700 nm only the visible portion of the spectrum was analyzed. Despite this, a residual correction was performed for each each  $\rho^{RS}(0^+)$  spectrum following the procedure suggested by Rudorff et al. (2014) for turbid waters, which uses values in the near IR. For that, the cast with the lowest value at 800 nm (averaged between 790-810 nm) was used as the baseline to correct for the positive white offset of the other casts, measured at each site and station. Equation 4.1 and the residual correction were applied to correct the spectra from noises and biases due to contaminations from the viewing geometry and environmental factors (such as the sky condition and sea surface state) and to allow for an intercomparative analysis between the spectra. Finally, for each station the  $\rho^{RS}(0^+)$  was determined with the average of all casts.

#### 4.2.3. Bio-optical parameters

At each station and site, 5-10 liters of seawater were collected at the surface for the estimation of the main OAC: absorption coefficients of CDOM ( $a_{CDOM}$ ), detritus ( $a_d$ ) and phytoplankton pigments ( $a_{phyto}$ ) and chlorophyll-*a* concentration (chl-*a*). Water was filtered on board up to 3 hours after collection following NASA's protocols (MITCHELL et al., 2002) and the conversion coefficients to estimate the particulate absorption ( $a_p$ ) were taken from Mitchell (1990). Two replicates were filtered for  $a_p$  with samples of 1-2 liters for each replicate, according to the water clarity. Water was filtered using Whatman Glass Fiber Filters (GF/F) with porosity of 0.7  $\mu\text{m}$  and the filters with retained material were stored in liquid nitrogen until their analysis at the mainland laboratory. Particulate absorption spectra were measured using a Shimadzu UV-2450 spectrometer. After the  $a_p$  measurements, the sample filters were soaked with Sodium Hypochlorite for 24 hs to remove the chemicals and pigments from the material retained on the filter, and the absorption spectra were measured once again in the filters to obtain  $a_d$ .  $a_{phyto}$  was estimated as  $a_{phyto} = a_p - a_d$ . To estimate  $a_{CDOM}$ , water samples were filtered through membrane filters with 0.2  $\mu\text{m}$  pore size. Samples were preserved in dark at around 4°C until their measurements using a Hitachi spectrophotometer at the main laboratory. For  $a_{CDOM}$ , a single replica was measured for

station. All measurements of the absorption coefficients were analyzed at the *Instituto Oceanográfico, Universidade de São Paulo* (IOUSP, Brazil).

For the chl-*a* concentration, 500 to 750 ml of water samples were filtered using Whatman GF/F with 0.7  $\mu\text{m}$  of porosity. N,N-Dimethylformamide (DMF) was used to extract pigments (SUZUKI; ISHIMARU, 1990). Duplicates for each station and site were analyzed using a spectrofluorimeter (LUTZ et al., 2009). The  $a_p$  and chl-*a* duplicates were either averaged.

Profiles of the backscattering coefficient measured at 700 nm were collected at the main stations with an ECO BB3 sensor connected to the Satlantic Profiler. The data was processed using Prosoft 7.7.16 software to estimate the particle backscattering coefficient of particles at 700 nm ( $b_{bp}(700)$ ). The spectral  $b_{bp}(\lambda)$  was derived with the QAAv5 model (LEE et al., 2002) using  $\rho^{RS}(0^-)$  at 440 and 550 nm determined with the Satlantic Profiler II. The spectral  $b_{bp}(\lambda)$  model was validated comparing the modeled and measured  $b_{bp}(700)$ .

#### **4.2.4. Environmental characterization**

The depths at each site were recorded using a handle ecobatimeter measured at surface or by a diver using underwater pressure gauge. At each station, depth was measured by the ecobatimeter installed in the ship. The geographic position was always registered using a Garmin GPS unit (mean error  $\pm 5$  m).

At the same time of the above-water radiometric measurements, the following environmental factors were registered: wind velocity, percentage of clouds and sea state. This information aided for the estimation of  $\rho_{sky}$  in Equation 4.3.

#### **4.2.5. Benthic community**

At each site, underwater photographs were taken by a diver for the characterization of the benthic communities. Benthic photos were taken at a distance of about 30 cm from the bottom, and covered an area of about 60 x 60 cm for each picture. These photos were used for a detailed description and quantification of the main benthic classes present in the sites.

Between 2 and 9 benthic photos were analyzed for each site, depending on the heterogeneity of its benthic community. Photos were initially processed to adjust their contrast and histograms in the three channels (red, blue and green), which allowed a better identification of the classes. In each picture, 100 random points were collected and the class (up to the maximum taxonomical level as possible to be identified in an underwater picture) of each of them was registered (Figure 4.4). This processing was performed using the Coral Point Count (CPCe) software.

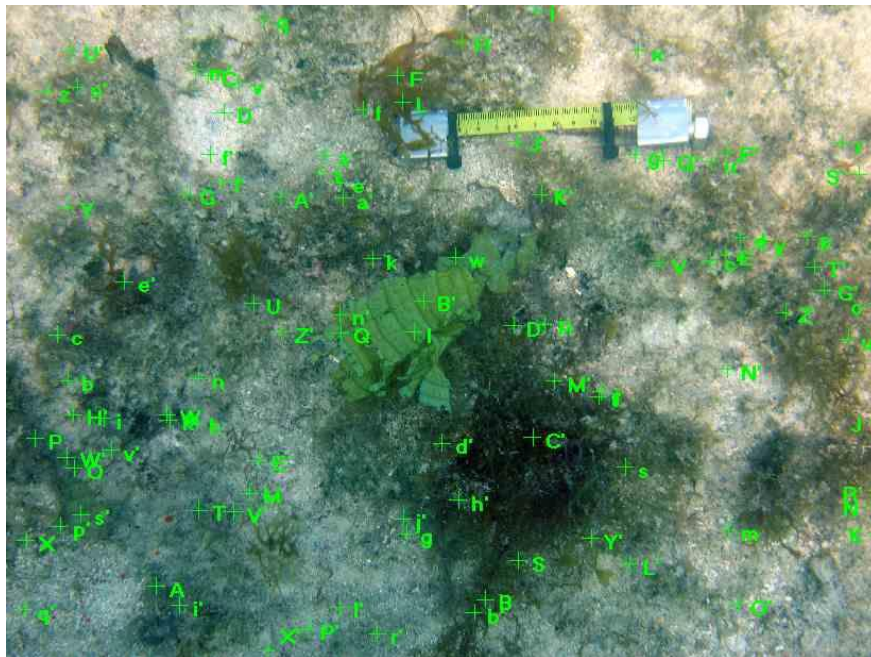


Figure 4.4 – Random points on a submerged picture of benthic communities in the ACRB using the CPCe software.

The benthic characterization included the following categories:

- Seaweeds:
  - Phyllamentous green algae (Chlorophyta)
  - Fleshy green algae (Chlorophyta)
  - Brown algae (Phaeophyceae)
  - Fleshy red algae (Rhodophyta)
  - Non-Fleshy calcareous algae (Rhodophyta)

- Algal turfs (often a mixture of Chlorophytes, Cyanophytes, Phaeophytes, and Rhodophytes -BERNER, 1990-)
- Seagrass
- Corals:
  - Millepora sp.
  - Bleached Millepora sp.
  - Mussismilia sp.
  - Bleached Mussismilia sp.
  - Montastraea sp.
  - Bleached Montastraea sp.
  - Other corals
  - Other bleached corals
- Sponge (Porifera)
- Sediment
- Sand
- Zoanthids:
  - Palythoa sp.
  - Other Zoanthids
- Other organisms
- Shadows

The percentage of coverage for each class was estimated in each photo. For each site, the mean percentage of coverage between pictures was calculated.

#### **4.3. Remote sensing data: Worldview-2**

In this work, very high spatial resolution data registered by the WorldView-2 (WV02) orbital sensor was used. The imagery (free of clouds) was captured on 02/14/2012 at 10:06 local time, during our first field campaign, between the coordinates of 17°54'9.38''-18°3'22.71''S / 38°35'43.25''- 38°45'38.17''W. The WV02 sensor has eight multispectral bands (MS) in the visible and near-infrared regions and one panchromatic band (PAN). Its spatial nominal resolution at nadir is 2 m for the multispectral bands and 0.5 m for the panchromatic band and its radiometric resolution is 11-bits, stored as a 16-bits integer. The nominal swath width is 16.4 km. The orbit of

WV02 is nearly circular, sun-synchronous, with an altitude of approximately 770 km with a descending nodal crossing time of approximately 10:30 a.m. (DIGITAL GLOBE, 2010). WV02 is a commercial sensor that captures images only under request and the imagery can be done at nadir or off-nadir-angles, due to its off-nadir pointing capability.

Table 4.1 – Main characteristics of the Worldview2 orbital sensor and specificities of the used scene: spectral and spatial resolutions, solar and off-nadir angles and percentage of cloud cover.

<b>Sensor specifications and ancillary information of the WV02 imagery</b>			
Spectral Resolution (Center Wavelength and 50% Band Pass Band, in nm)	Panchromatic	632	464 – 801
	Coastal	427	401 – 453
	Blue	478	448 – 508
	Green	546	511 – 581
	Yellow	608	589 – 627
	Red	659	629 – 689
	Red Edge	724	704 – 744
	NIR1	831	772 – 890
	NIR2	908	862 – 954
Spatial resolution (m)	PAN	0.5	
	MS	2	
Solar zenith angle		64.8°	
Solar azimuth angle		82.8°	
Off-Nadir-Angle (ONA)		15.6°	
Cloud cover		0%	

The image used was delivered in the 2A Standard processing level. This level includes sensor radiometric and geometric corrections, and data are projected to a plane using a map projection and datum, in this case UTM Datum WGS-84. Sensor corrections account for the internal detector geometry, optical distortion, scan distortion, any line-rate variations, and registration of the panchromatic and multispectral bands. Radiometric correction is performed to minimize dark and light vertical stripes caused by non-uniform responses between the detectors, the variability in electronic gain and offset, lens falloff, and particulate contamination on the focal plane. Since the WV02 is a pushbroom system, data in every column of an image come from the same detector causing this artifact. Additionally, radiometric correction scales all image pixels to top-of-atmosphere spectral radiance allowing to apply a unique absolute calibration factor to



## 5 WATER COLUMN CORRECTION STUDY

### 5.1. Introduction

Bottom reflectance ( $\rho_b$ ) is the central parameter in the remote sensing of coral reefs and, depends on the physical structure and chemical substrate composition (HOCHBERG et al., 2004).  $\rho_b$  in coral reef studies has been mainly used for the following:

- Identification of coral bleaching events, which are frequently used as a proxy for coral reef health (ELDVIDGE et al., 2004). Bleached corals can be differentiated from healthy corals in their reflectance spectrum because the zooxanthells that are lost are associated with pigment depletion and color change (CLARK et al., 2000; HOLDEN; LEDREW, 1998; 1999). Despite its potentiality, it can be complicated to observe by remote sensing and depends on the prompt imagery of the area because dead corals are rapidly colonized by algae, with a spectral behavior similar to zooxanthells;
- Mapping of different assemblages of benthonic species by using different techniques, such as methods based on spectra similarities or Object-Based Image Analysis (OBIA) (PHINN et al., 2012; KOBRYN et al., 2013; BOTHA et al., 2013; BENFIELD et al., 2007; ZHANG et al., 2013; among others). In the latter, knowledge of reflective bands can be introduced, which has resulted in improved mapping accuracy;
- Application of spectral mixed indexes to resolve benthic mixtures. This technique has been used in terrestrial environments where the three main fractions considered were vegetation, shadow and soil. In reef environments, it was applied with some success using the fractions algae, coral and sand (HOCHBERG; ATKINSON, 2003; HEDLEY et al., 2004; GOODMAN; USTIN, 2007);
- Application of methods such as derivative analysis in quasi-continuous spectra allowing detection of diagnostic features for discriminating between bottom types (HOLDEN; LEDREW, 1998; HOCHBERG et al., 2003; KUTSER et al., 2006).

However, in some situations, the actual bottom reflectance spectra are not required. These situations occur when the objective of the work is solely produce a map of a coral reef from an individual image using either supervised or unsupervised classification

algorithms. In these cases, spectra arising from each mapped class are not valid for descriptive and/or comparative purposes.

Although remote technologies have a great potential in studies of the sea bottom, extracting the reflectance spectrum from the data of orbital optical sensors is complex. Several interferences affect the solar irradiance before it reaches underwater substrates which were referred to in section 3. This chapter left aside the problem of atmospheric correction and water surface reflection, and it was focused on the separation between the signals from the water column and seabed.

Different methods have been proposed to minimize water column correction and were detailed in Chapter 3. The objective of this chapter was to perform an inter-comparison of methods to retrieve the bottom reflectance, evaluating their performance and uncertainties associated with different OAC concentration in water, depth and kind of bottom. The inter-comparison was accomplished using simulated spectra and multispectral data obtained from the WorldView-2 (WV02) sensor in the ACRB. Three methods were chosen for the inter-comparative analysis: Maritorena et al. (1994), Lee et al. (1999) and CRISTAL (2005), with the first two belonging to the second group and the last one to the third group. No method included in the first group was tested because they produce an index that involves two spectral bands instead of reflectance, which produces a non-viable performance comparison with methods in the other groups. Methods proposed by Maritorena et al. and Lee et al. seemed similar, but they differed in that Maritorena uses an AOP ( $K_d$ ) to characterize the water column while Lee uses two IOPs ( $a$  and  $b_b$ ). It was wondered if using these methods for bottom retrieval would not provide distinct results. These two methods were created to simulate  $R(0^-)$  or  $\rho^{RS}(0^-)$  in shallow waters. Nevertheless, they were not tested previously to obtain  $\rho_b$  from  $\rho^{RS}(0^-)$  or  $R(0^-)$  as is done here. The last method (CRISTAL) is a new approach that appears to have the potential to correct the water column. This method was chosen as a representative of the third group.

## **5.2. Materials and methods**

### **5.2.1. Application and comparison of selected methods: simulated spectra**

Simulations were performed using the WASI v.4 software (GEGE, 2012). Three types of bottoms were used in the simulations: coral sand, brown algae and green algae

(MARITORENA et al., 1994). Four depths were considered: 3, 5, 10 and 15 m. Four types of water were defined as representative of the variation of conditions in the water column in coral reefs (Table 5.1). To define the water constituents, the literature was reviewed to determine the range of variation of chl-*a*, CDOM absorption ( $a_{CDOM}$ ) and sediments concentration in the coral reefs environments (Table 5.2). These parameters vary between chl-*a*: 0.01-9.21 mg m<sup>-3</sup>;  $a_{CDOM}(440)$ : 0.0017-0.24 m<sup>-1</sup>; and sediments: 0.8-2.2 mg l<sup>-1</sup>. Zenith and view angles were set at nadir (0°). In total, 48 situations were considered from the combination of 3 bottoms, 4 depths and 4 waters (3 · 4 · 4). In WASI, the  $R(0^-)$ ,  $R_\infty(0^-)$ ,  $K_d$ ,  $\rho^{RS}(0^+)$ ,  $\rho_\infty^{RS}(0^+)$  and  $a$  coefficients were simulated.

Table 5.1 – Water characteristics of the four different types of water used to simulate surface reflectance above shallow areas.

Water type	chl- <i>a</i> (µg l <sup>-1</sup> )	$a_{CDOM}(440)$ (m <sup>-1</sup> )	Suspended particles Type I (mg l <sup>-1</sup> )	Suspended particles Type II (mg l <sup>-1</sup> )	$a_d(440)$ (m <sup>-1</sup> )	<i>n</i>
Water-a	0.01	0.0017	0.01	0	0	-1
Water-b	1	0.0316	1	0.8	0	-1
Water-c	3	0.15	3.5	2.2	0.2	0
Water-d	9	0.3	10	1	0.5	0

Maritorena et al.'s algorithm was applied to the 48 simulated spectra of  $R(0^-)$  using Equation 5.1. The cases where  $\rho_b$  did not contribute to  $R(0^-)$  (Equation 5.2) or when  $\rho_b$  retrieved behaved exponentially were excluded from the analysis. In all cases, a bottom contribution to the  $R(0^-)$  modeled signal could be found even when the bottom was deeper than  $z_{90}$ .

$$\rho_{b \text{ retrieved}} = \frac{R(0^-) - R_\infty(0^-)}{e^{-2K_d z}} + R_\infty(0^-) \quad (5.1)$$

$$\% \text{ of bottom contribution} = \frac{(\rho_{b \text{ retrieved}} - R_\infty(0^-)) e^{-2K_d z}}{R(0^-)} \cdot 100 \quad (5.2)$$

Uncertainties in retrieving the bottom reflectance for each wavelength were estimated as:

$$Uncertainty = \frac{\rho_{b \text{ retrieved}} - \rho_b}{\rho_b} \cdot 100 \quad (5.3)$$

The second applied method as the algorithm proposed by Lee et al. (Equation 5.4). In Equation 5.4,  $D_u^C$  and  $D_u^B$  are the optical path-elongation factors for scattered photons from the water column and bottom, respectively. They can be estimated from the  $a$  and  $b_b$  coefficients (see Table 3.1).  $\rho^{RS}(0^+)$ ,  $\rho_\infty^{RS}(0^+)$  and  $a$  coefficients spectra were used.  $\rho^{RS}(0^+)$  and  $\rho_\infty^{RS}(0^+)$  were converted to below water using expression 5.5.

$$\rho_{b \text{ retrieved}} = \frac{\pi \left[ \rho^{RS}(0^-) - \rho_\infty^{RS}(0^-) \left( 1 - e^{[-(1+D_u^C)kz]} \right) \right]}{e^{[-(1+D_u^B)kz]}} \quad (5.4)$$

$$\rho^{RS}(0^-) = \frac{\rho^{RS}(0^+)}{0.5 + 1.5 \rho^{RS}(0^+)} \quad (5.5)$$

The backscattering coefficient is not an output of WASI software. Hence, the  $b_b$  coefficients were estimated according to Gege (2012):

$$b_b(\lambda) = 0.00144 \text{ m}^{-1} \left( \frac{\lambda}{500} \right)^{-4.32} + Chl\_a(0.0006 \text{ m}^2 \text{ g}^{-1} \cdot Chl\_a^{-0.37}) + C_{Mie} 0.0042 \text{ m}^2 \text{ g}^{-1} \left( \frac{\lambda}{500} \right)^n \quad (5.6)$$

Table 5.2 – Water column characteristics in coral reefs areas Worldwide reviewed from literature.

Coral Reef	$a_{\text{CDOM}}(443)$ ( $\text{m}^{-1}$ )	chl- <i>a</i> ( $\text{mg m}^{-3}$ )	Sediments concentration ( $\text{mg l}^{-1}$ )	Approach	Source
Bahamas	0.006-0.030	0.031-0.21		Remote sensing	Otis, 2012
Bali	0.01-0.05	0.088-0.58		Remote sensing	Otis, 2012
GBR (lagoon)	0.016-0.075	0.078-0.38		Remote sensing	Otis, 2012
GBR (reef matrix)	0.008-0.040	0.088-0.58		Remote sensing	Otis, 2012
Florida Keys	0.008-0.050	0.058-0.38		Remote sensing	Otis, 2012
Maldives	0.006-0.045	0.078-0.58		Remote sensing	Otis, 2012
Palau and Yap	0.003-0.011	0.031-0.21		Remote sensing	Otis, 2012
Panama (Gulf of Panama (Chiriqui))	0.02-0.18	0.17-2.67		Remote sensing	Otis, 2012
Philippines	0.004-0.030	0.049-0.81		Remote sensing	Otis, 2012
Thailand (Andaman)	0.011-0.24	0.160-9.21		Remote sensing	Otis, 2012
Thailand (Gulf of)	0.012-0.15	0.11-2.39		Remote sensing	Otis, 2012
Lee Stocking Islands, Bahamas	0.0017-0.067 (at 440nm)	0.01-0.32		<i>In situ</i> data	Zaveneld and Boss, 2003
Moreton Bay, Australia		0.4-1	1-3.3	<i>In situ</i> data	Dekker et al., 2011
French Polynesia		~ 0.3-0.9	~ 0.8-2.2	<i>In situ</i> data	Maritorena and Guillocheau, 1996
GBR	0.08-0.15 (at 400 nm)	0.05-0.7		<i>In situ</i> data	Liston et al., 1992; Furnas et al., 1990; Kutser et al., 2006
Curaçao La Parguera Natural Reserve, Puerto Rico		0.26-1.1		<i>In situ</i> data	Van Duyl et al., 2002
		0.13-1.7		<i>In situ</i> data	Otero and Carbery, 2005

Uncertainties in retrieving the bottom reflectance for each wavelength were estimated according to Equation 5.3.

Because estimating the parameters used as input in any model involve errors, there are other output uncertainties related to this source. A sensitivity analysis can measure the impact of uncertainties for a parameter on a model result. This type of analysis shows the parameters for which more attention should be paid, because errors in their estimation can cause a significant and non-proportional response in the results. In the analysis,  $\rho_{b\text{ retrieved}}$  estimated using Maritorena's and Lee's models from  $R(0^-)$  or  $\rho^{RS}(0^-)$  modeled in WASI constituted the baseline retrieval. Each parameter ( $z$ ,  $K_d$ ,  $R_\infty$ ,  $\rho_\infty^{RS}(0^-)$ ,  $a$  and  $b_b$ ) was then varied between -95 and +100% to evaluate the impact on the  $\rho_{b\text{ retrieved}}$ . Sensitivity was estimated according to equation 5.8:

$$\text{Sensitivity (\%)} = \frac{|\rho_{b1} - \rho_{b2}|}{\rho_{b1}} 100 \quad (5.8)$$

where  $\rho_{b1}$  corresponds to each value obtained from baseline retrieval, with original parameters while  $\rho_{b2}$  are the values obtained after modifying the parameters. This analysis was performed for some extreme cases: water-a and water-c; sand and brown algae; 3 and 10 m depth. Results were evaluated at 450, 550 and 650 nm.

Finally, the CRISTAL method was applied. 5% of uncorrelated noise was added to the 48  $\rho^{RS}(0^+)$  spectra to be corrected, and other  $\rho^{RS}(0^+)$  spectra were simulated, considering different combinations of the three bottoms (coral sand, green algae and brown algae) at 16 depths (1-16 m) and water column constituents (chl- $a$ : 0.01, 0.02, 0.1, 0.2, 0.3, 0.9, 1, 1.1, 2.5, 2.8, 3, 3.1, 3.2, 8, 8.5, and 9  $\mu\text{g l}^{-1}$ ;  $a_{\text{CDOM}}(440)$ : 0.0017, 0.00269, 0.0074, 0.1, 0.15, 0.2, and 0.25  $\text{m}^{-1}$ ; concentration of suspended particles Type II: 0, 0.5, 0.8, 1, 2, 2.2, and 2.5  $\text{mg l}^{-1}$ ). In total, 26,352 spectra were generated and included in the spectral library. The classification technique SAM (KRUSE et al., 1993) based on the geometric proximity of two spectra was applied.

Figure 5.1a shows the  $K_d$  coefficients for the four waters. Increases in the OAC concentration produced increases in the  $K_d$ . Nevertheless, the minimum  $K_d$  value did

not always occur in the lowest wavelength. Water-a had a low concentration of constituents, and its  $K_d$  curve was similar with pure water and had a minimum at 400 nm. However, this minimum value was displaced to higher wavelengths when the OAC concentration increased. In the case of water-d, its CDOM concentration was so high that the  $K_d$  had a maximum at 400 nm. If  $z_{90}$  was estimated for the four waters (Equation 3.10); even in the clearest water,  $z_{90}$  was lower than 5 m for wavelengths greater than 600 nm (Figure 5.1b).

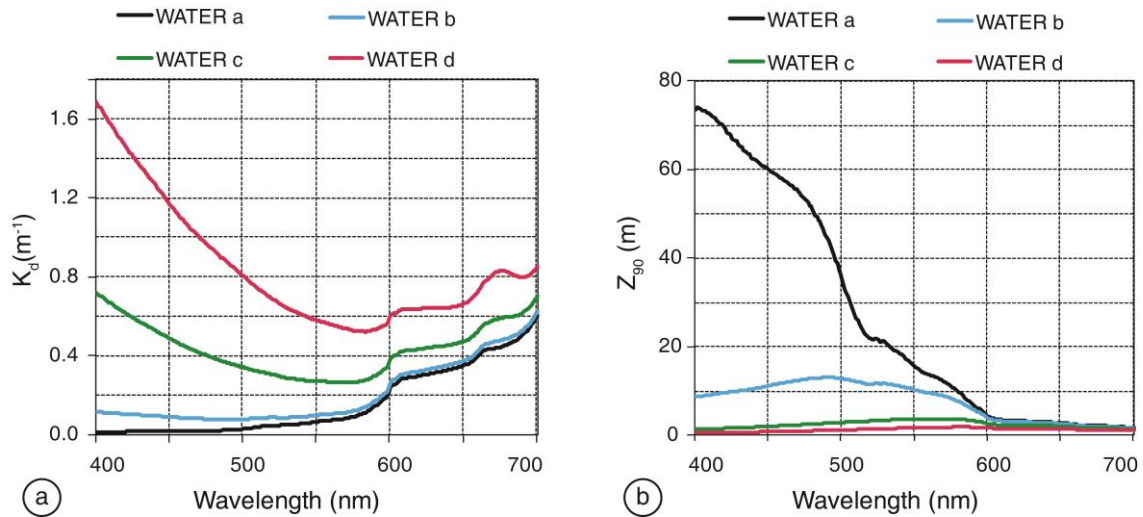


Figure 5.1 – (a) Diffuse attenuation coefficient ( $K_d$ ,  $m^{-1}$ ) as a function of wavelength (nm) simulated in WASI for water-a to -d. (b)  $z_{90}$  (m) versus wavelength (nm) for water- a to -d, that corresponds approximately to depth where radiance decay in 90%.

### 5.2.2. Application and comparison of selected methods: remote sensing data

In this section, some spectra extracted from a Worldview-2 (WV02) scene were intended to be corrected using Maritorena's and Lee's algorithms. The CRISTAL method was not used because of the lack of actual bottom reflectances, which are required to simulate the spectral library. The WV02 image corresponds to the *Parcel dos Abrolhos* and Archipelago, a portion of the ACRB (Figure 5.2). In this area depths vary between 2 and approximately 25 m and some reef structures show a typical

mushroom shape whose tops have a diameter between 20 and 300 m (FRANCINI-FILHO; MOURA, 2008).

The WV02 image was atmospheric corrected using the package ATCOR2 available in PCI Geomatica v.10.3.2, and visibility was set at 43 km. This value was obtained from the aerosol optical thickness at 574 nm ( $AOT_{574}$ ) of the MODIS-Aqua image on the same day, which was converted to a visibility value using the model proposed by Vermote et al. (2002). The scene was also corrected of sunglint effects (HEDLEY et al., 2005). Bathymetric information for 117 points inside the scene, was provided by the Brazilian Navy. These points were homogeneously distributed in the scene and depths were corrected to a tidal height at the time of the imagery. Spectral curves of the surface reflectance (adimensional) ( $\rho_w(0^+)$ ) were extracted in the same pixels where depth data was available. Several samples in deep areas were carefully selected, and mean values were calculated for each band. These values were used as input in both models to represent the deep water reflectances.

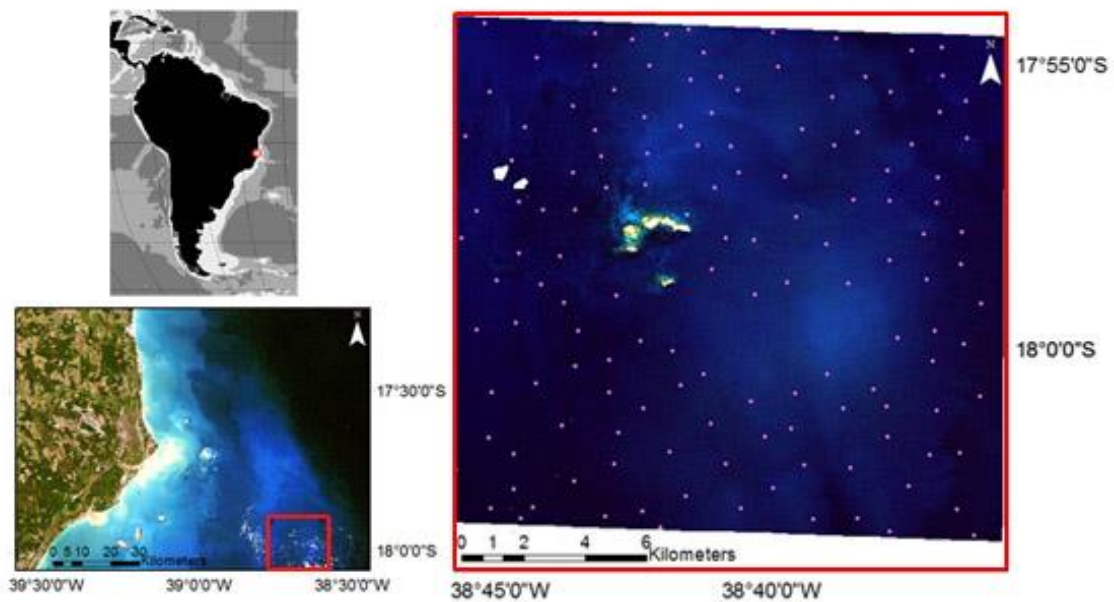


Figure 5.2 – Quasi-true color composition (R: 659 nm; G: 546 nm; B: 478 nm) of a portion of the Abrolhos Coral Reef Bank, Brazil, around the archipelago, captured by WV02 sensor in 2012/02/14. Pink dots show distribution of depth points in the area (Right). Red square in image Landsat TM-5 (R: 660 nm; G:560 nm; B:458 nm) captured in 2006/05/29 shows location of study area respect to coast (Left down). Location of study area in South America (Left up).

$K_d$  values used to correct the water column effect were estimated from in-water profiles, quasi-concomitant with the imagery (between 2012/02/27 and 2012/02/29). The hyperspectral  $K_d$  along the water column was averaged for each profile excluding measurements in the 5 first meters because the  $E_d$  showed a noisy pattern, mainly caused by waves and bubbles. Then, a mean  $K_d(\lambda)$  value of all profiles was obtained (Figure 5.3).

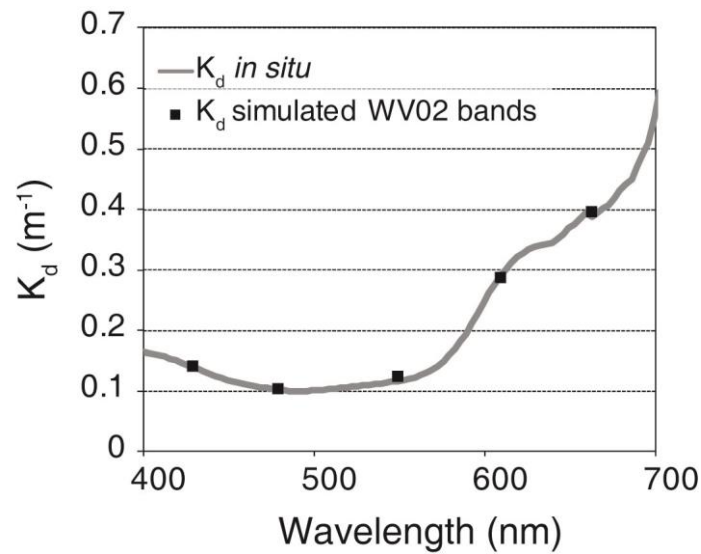


Figure 5.3 – In grey, diffuse attenuation coefficient ( $K_d$ , in m-1) versus wavelength (nm) estimated from  $E_d$  (m-1) profiles along water column measured quasi-concomitant with WV02 imagery in ACRB, Brazil. Black squares represent simulations of  $K_d$  for the bands of WV02 until 700 nm.

WASI software in the inverse manner was used to retrieve  $a_{CDOM}$ . In this sense, the  $K_d$  spectrum was used as an input and chl-*a* concentration was fixed at 0.48 mg m<sup>-3</sup> according to estimatives in the field. At last,  $a$  was obtained as the sum of  $a_{CDOM}$ ,  $a_d$ ,  $a_{phyto}$  and  $a_w$  (POPE; FRY, 1997).  $b_{bp}$  was derived through the QAAv5 method (LEE et al., 2002) using the  $\rho^{RS}$  at 440 and 550 nm registered with the Satlantic Profiler II. It was validated using  $b_{bp}$  at 700 nm measured *in situ*.  $b_b$  was estimated as the sum of  $b_{bp}$  and  $b_{bw}$  (MOREL, 1974) (Figure 5.4). The hyperspectral data of  $K_d$ ,  $b_b$  and  $a$  were simulated for the spectral bands of WV02 up to 700 nm.

117 spectra from the WV02 image for which depth information was available, were corrected. Maritorena and Lee's algorithms were applied using equations 5.1 and 5.4, respectively. The inputs for Maritorena's algorithm were  $z$ ,  $K_d$ ,  $\rho_w(0^-)$  and  $\rho_\infty(0^-)$ . Previously, the above surface reflectances were converted to below water reflectances using equation 5.5. The inputs for Lee's algorithm were  $z$ ,  $a$ ,  $b_b$ ,  $\rho^{RS}(0^-)$  and  $\rho_\infty^{RS}(0^-)$ . The above-water surface reflectances obtained from atmospheric corrections were divided by  $\pi$  to convert them to remote sensing reflectances, with the surface considered as Lambertian. Above remote sensing reflectances were also converted to below-water reflectances (Equation 5.5).

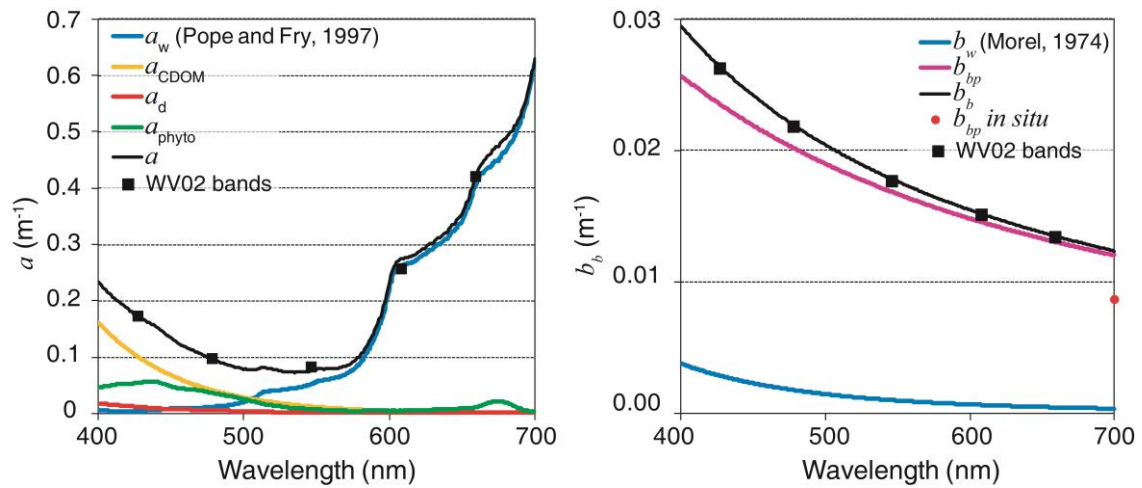


Figure 5.4 – Water optical properties estimated nearly concomitantly with the time of WV02 imagery around the archipelago in ACRB, Brazil. (a) Absorption coefficients (m<sup>-1</sup>). (b) Backscattering coefficients (m<sup>-1</sup>).

### 5.3. Results and discussion

#### 5.3.1. Simulated spectra

For the baseline retrievals using Maritorena et al. and Lee et al.'s models, a gradual loss in bottom contribution was observed for increases in the OAC concentration and depth. This occurred because when the depth increases, the optical path augments, and there are more chances for a photon reflected by the bottom to be absorbed before arriving to the surface. All types of water showed bottom contribution when they were located at 3 m depth. When the bottoms were located at 5 m in water-d, they only had a small contribution to surface reflectance (0.01-1.5% depending on the type of substrate) after

470-500 nm. In contrast, only the bottom at 10 m had contributions from the clearer waters (types a and b) and, in water-c, they were lower than 1% in certain portions of the spectrum. At 15 m, the bottom signal arrived to the surface in the entire visible spectrum only in water-a and water-b up to 600 nm. Additionally, the bottom contribution depends on the physicochemical and biologic characteristics of the substrate. If the bottom is more reflective, it is expected that more photons will come from the bottom and an additional quantity of them will have a chance of crossing the water column and arriving to the surface. For example, for a twice as reflective bottom, its contribution to the surface signal will be higher than for a less reflective bottom, although it will not be proportional.

At some depths, Maritorena's model retrieval showed an exponential growth, such as when the term  $e^{-2K_d z}$  tended to zero.  $e^{-2K_d z}$  was lower when  $K_d$  and  $z$  were higher. Therefore, in waters-a to c an exponential behavior was observed only in the red region. However, for water-d, this situation was observed also in the blue in response to increasing  $K_d$  by CDOM absorption. Compared to Maritorena's model, Lee's model retrieval showed an exponential decay in some cases. Generally, this behavior was found when the term  $e^{-(1+D_d^B)cz}$  was lower than 0.0002.

Note that in this section,  $K_d$ ,  $z$ ,  $b_b$ ,  $a$ ,  $\rho_\infty^{RS}(0^-)$ ,  $\rho_b$  and  $R_\infty(0^-)$  were known and fixed in advance. Therefore, if the WASI software had used the Lee or Maritorena's algorithms to estimate the water reflectance in the shallow water,  $\rho_b$  retrieved would have been exactly the same as  $\rho_b$  in the shallow and clearer waters. Differences between the real and retrieved bottom reflectance by both models are essentially due to differences between the model used by WASI and the tested models. In many cases, Maritorena's algorithm could retrieve the shape of the  $\rho_b$  spectra from the surface spectra simulated with WASI software (Figure 5.5). As expected, the algorithm had a better performance in shallower depths and clearer waters. For example, at 5 m depth, the model produced good results up to 700 nm with average of uncertainties of 6.5% (results are a bit degraded above 600 nm) but performance became degraded above 600 nm when the depth was 10 m (average of uncertainties 43.5%). The performance was further degraded in water-c and -d, being possible to retrieve  $\rho_b$  only in some section of the spectrum depending on the depth, with mean uncertainty of 35%. However, Lee's

model showed a slightly lower performance than Maritorena's (mean uncertainty at 10% for water-a, 5 m; 28% for water-a, 10m, between 600-699 nm) and tended to underestimate the bottom reflectance, especially after 600 nm (Figure 5.5). This algorithm was able to retrieve the shape of the algae spectra in most cases between 400 and 600 nm in water-a and -b at 5 m and below 600 nm in water-c at 10 m. If  $R(0^-)$  was used as the starting point for both models and if  $R(0^-)$  was divided by  $\pi$  to obtain  $\rho^{RS}(0^-)$  according to Lee et al.'s model (1999), closer values were obtained between the results of both models.

Reflectances, absorption and backscattering coefficients simulated by WASI software were slightly noisy. In cases where the water reflectance was very low (red and blue regions in the most turbid waters) this noise was magnified and explains some noisy behavior in the retrievals for certain waters and regions of the spectrum (Figure 5.5).

The Maritorena et al. (1994) algorithm yields errors up to 66% in the clearest waters (water-a) in the range from 400-499 nm, 62% in the range from 500-599 nm, and 91% in the range from 600-700 nm, depending on the bottom depth (between 3 and 15 m). The figures become 66%, 21%, and 36%, respectively, when using the Lee et al.'s algorithm, which indicates reduced uncertainties as a result of differences in radiative transfer modeling. When waters are more turbid (water-b, -c and -d), the errors generally increase. In the most extreme case (water-d), the errors could be as high as 300% for both models, depending on the portion of the spectrum and bottom depth. In general, no pattern associated with uncertainties was observed because they were simultaneously related to the optical path length ( $K_d \cdot 2 \cdot z$ ) and bottom reflectance in a non-linear way. For Maritorena's model, however, uncertainties at the shallowest depth appeared to be more sensitive to the variability of the optical path length for the three types of bottoms. For optical path length increases, uncertainties were more related to the reflectance at the water surface. Using Lee's algorithm, uncertainties were not sensitive to the unique input, optical path length,  $\rho_b$ ,  $\rho^{RS}(0^-)$  or  $\rho_{\infty}^{RS}(0^-)$ , and made it more difficult to predict the model performance in a particular environment. The pattern of uncertainties was dependent on the bottom reflectance. For example, for the brown algae bottom, uncertainties were not related to a sole factor. In contrast, uncertainties were explained mainly by the optical path length when the bottom was sand.

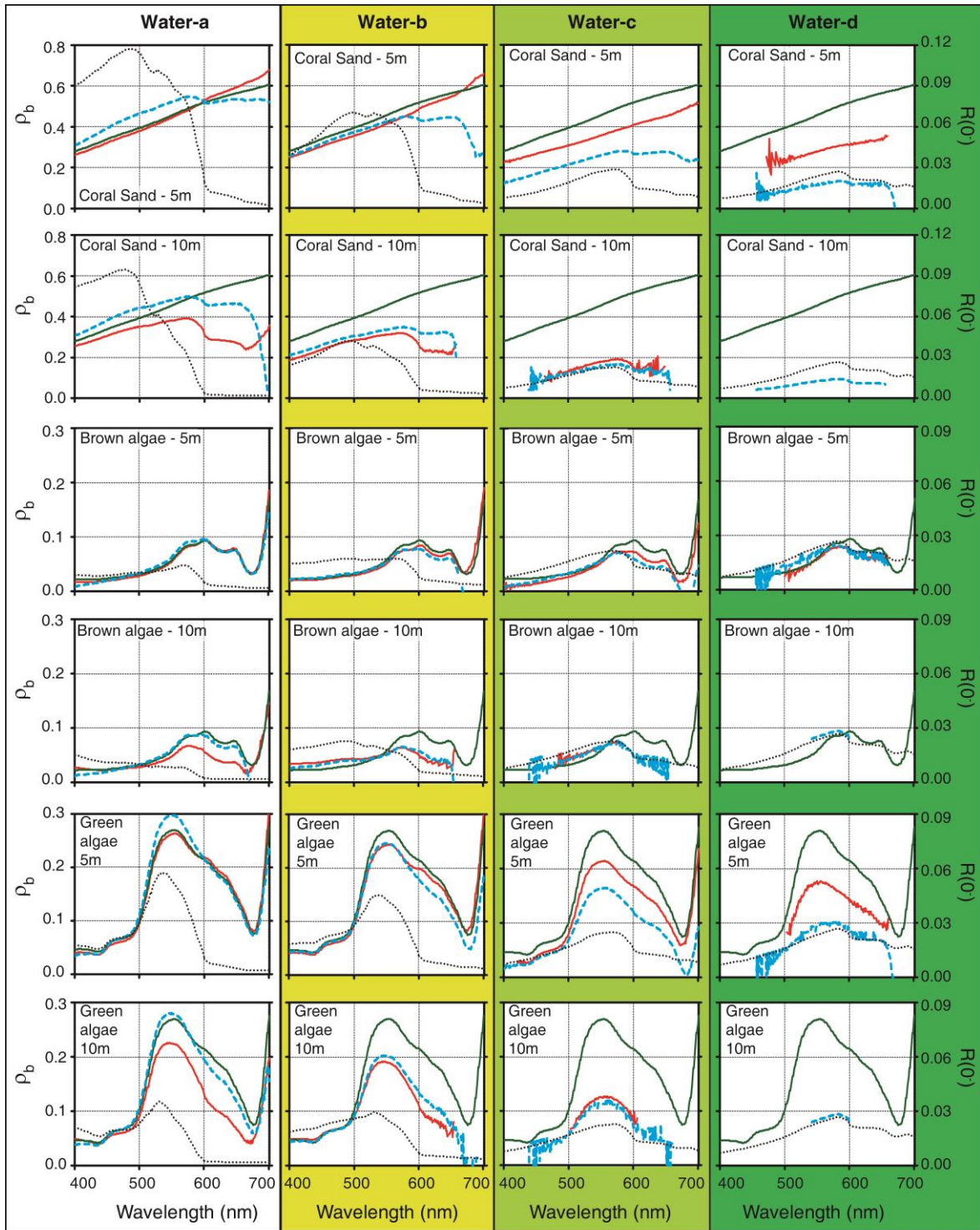


Figure 5.5 – Bottom reflectance below water versus wavelength (nm) for the same type of substrate and depth. In lines, there are results retrieved using Lee et al. (in blue) and Maritorena et al.'s (in red) algorithms, compared with real bottom reflectance. In columns, there are results for the same kind of water.

Both models showed similar sensitivity to variation in parameters (Figures 5.6 and 5.7). Lee's model exhibited a similar response pattern to  $a$  coefficient than Maritorena's model to the  $K_d$  because  $b_b$  was so low than its contribution to water attenuation seemed negligible in comparison with  $a$ . At 450 and 550 nm, models sensitivity showed a linear response in all of the parameters in the clearest water and shallowest situations (Figures 5.6 and 5.7). This response was symmetric at 450 nm considering either underestimation or overestimation in the parameters, and as length path increased, the models increased their sensitivity. In situations where substrates were located below a smaller path length in water (small  $K_d$  or  $a$ , and  $z$ ) models seemed insensitive to  $R_\infty$  or  $\rho_\infty$ . In contrast to deep water reflectance, attenuation and depth that are the parameters acting in the exponential term, showed an asymmetrical response according to underestimation or overestimation for long path length in waters (high attenuation and/or  $z$ ). It occurred because an increase on  $K_d$ ,  $a$  or  $z$  implied to modify denominator in Equations 5.1 and 5.4 of much lower values. Considering variations in either of them, the models showed an exponential behavior in their sensitivity to overestimations in the most turbid water (water-d). For example, overestimations lower than 50% impacts in more than 300% in the models results. At 650 nm, no one situation showed a linear behavior in sensitivity to  $K_d$  and  $z$ . The response patterns were similar than at 550 nm; however, at 650 nm models sensitivity was higher. Both algorithms were insensitive to  $R_\infty$  or  $\rho_\infty$  variations at 650 nm in the clear and shallowest water, while model sensitivity increased non linearly in deeper and more turbid waters.

Comparing the most reflective bottom (sand) with the lowest reflective bottom (brown algae), models were less sensitive to sand. In the clearest and shallowest situation (water-a, 3 m), both methods seemed to be robust. However, sensitivity is higher when length path in water increased. As the bottom contribution becomes larger, the effect of water column is less important reducing sensitivity. Analogously, according to OAC concentration or depth increase, contribution of bottom to surface reflectance decreases while water column contribution increases. It means that small errors in estimative of all parameters (attenuation, depth and deep water reflectance) incur in large errors in bottom retrieval in not clear and/or deeper environments.

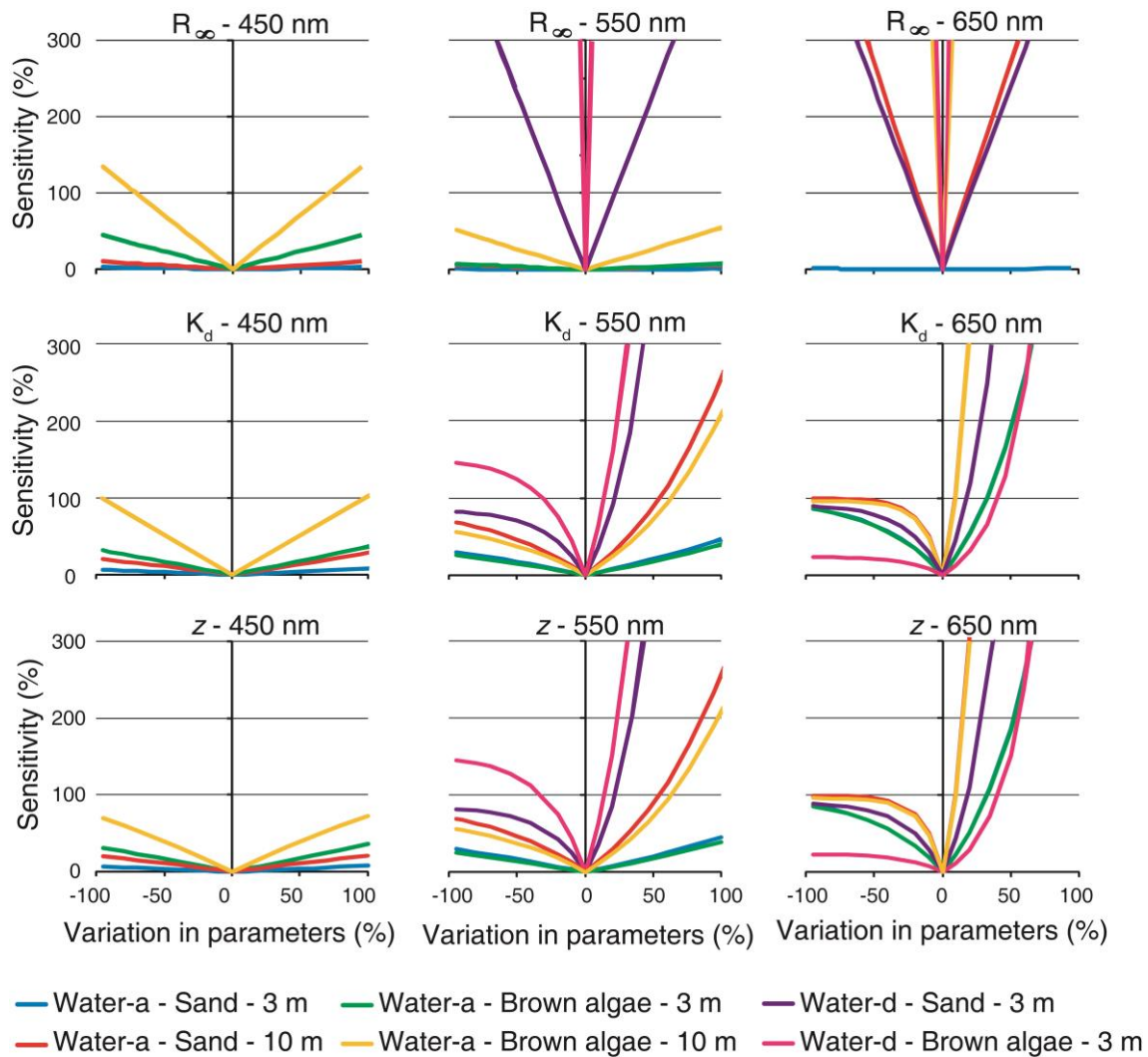


Figure 5.6 – Sensitivity analyses for parameters of Maritorena et al.' model:  $R_\infty$ ,  $K_d$  and  $z$ . Values correspond to sensitivity (in %) defined in equation 5.8. Results are arranged by parameter and wavelength (450, 550 and 650 nm).

Although errors in the modeling could be a large factor for accurate retrievals, some conclusions can be extracted. In general uncertainties are higher when optical path length is higher and sensitivity associated with both models is also higher in this case. Depending on depth and  $K_d$ , it is not always possible to retrieve a bottom signal or the retrieved signal might be subject to a great degree of uncertainty. This means that it is essential to know the environment under study to evaluate if the model is properly recovering the bottom reflectance or if it is creating an artifact. Validation of the water column correction is desirable when using *in situ* bottom reflectance; however, it can be

difficult to measure in the field. In addition, measurements of the bottom reflectance are normally performed very close to the target to minimize water interference, and the resulted Instantaneous Field of View (IFOV) is very small.

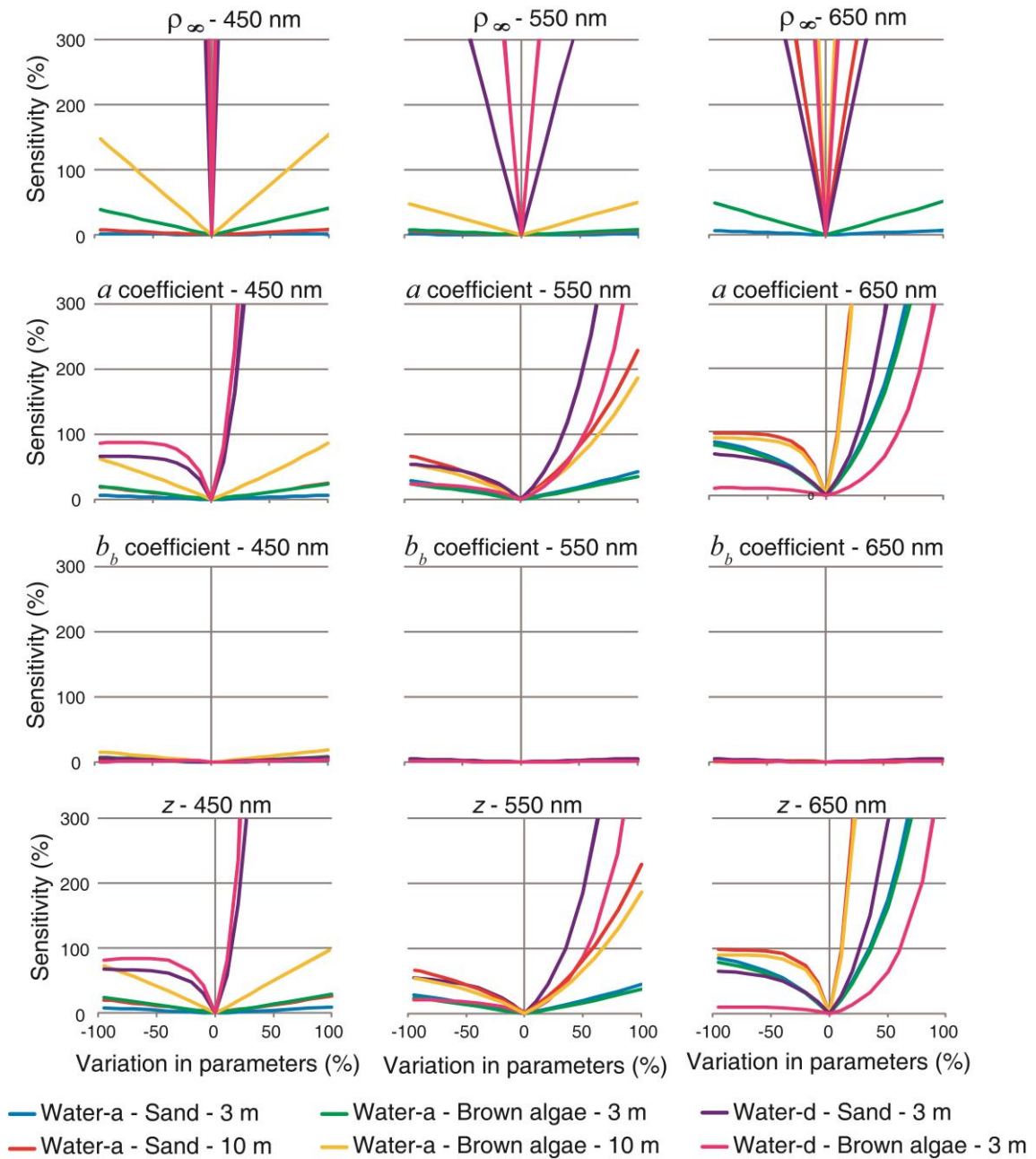


Figure 5.7 – Sensitivity analyses for parameters of Lee et al.' model:  $\rho_\infty$ ,  $a$ ,  $b_b$  and  $z$ . Values correspond to sensitivity (in %) defined in equation 5.8. Results are arranged by parameter and wavelength (450, 550 and 650 nm).

Considering that the substrate in coral reefs can be highly heterogeneous, punctual measurements are not representative of larger areas (1-900 m<sup>2</sup> depending on the configuration of the remote sensor); therefore, an understanding of the theory of the behavior of light in water as well as of the study area, such as the water column characteristics and real bottom reflectance at some locations, are required for interpreting such measurements.

Using the CRISTAL method, each of the 48  $\rho^{RS}(0^+)$  spectra was associated with the others in the spectral library whose SAM value was the minimum, and both spectra were considered as the same bottom. Therefore, the result of this method was a categorical classification. The accuracy obtained was: 81.25%, for brown algae, 87.50% for green algae and 93.75% for coral sand. Some confusion between the three classes was observed (Table 5.3), which occurred in water-c and -d, which were optical complex Case-2 waters.

This technique showed a satisfactory result, and it has the potential to be used to correct images. Nonetheless, several considerations are important. First, when the  $K_d$  and depth increase, the same spectra should be obtained at the surface for different bottoms. As example, in Figure 5.8 two  $\rho^{RS}(0^+)$  spectra were modeled in water-d at 5 m depth, for a sand bottom and the other for brown algae, with 5% uncorrelated noise for the latter. If it is neglected the noisy pattern of the brown algae spectrum, both curves showed the same shape. Second, the technique requires measurements of the bottom reflectance of all of the bottoms present in the area and in all combinations in which they might occur. If these inputs do not represent all of the variety present in the field, the technique will not retrieve the real type of bottom in a pixel. In this work, the exact same reflectance of pure substrates that was wanted to retrieve was used, which means that the most favorable conditions constructing the spectral library were used. The confusion could be higher if different combinations of substrates are used.

While the three methods tested here can be used to correct the water column effect, it is not simple to compare the performance between Maritorena and Lee's models with the CRISTAL model because the results are different. While the first two retrieve a numeric value of the bottom reflectance without the effect of the water column, the CRISTAL method produces a categorical result. When applied to an image, Maritorena and Lee's

model will result in a matrix with continuous values in each spectral band, whereas the CRISTAL method will produce a map with classes of bottoms. The choice of a method depends on different factors, such as the objective of the work, available input data, type of data (multi or hyperspectral), time of processing, etc. Whatever the chosen method, it must have some *in situ* data to perform the water column correction

Table 5.3 – Confusion matrix obtained for CRISTAL method using the SAM classification algorithm.

		Assigned Class			
		Sand	Green Algae	Brown Algae	
Real Substrate	Sand	15	0	1	16
	Green Algae	1	14	1	16
	Brown Algae	1	2	13	16
		17	16	15	48

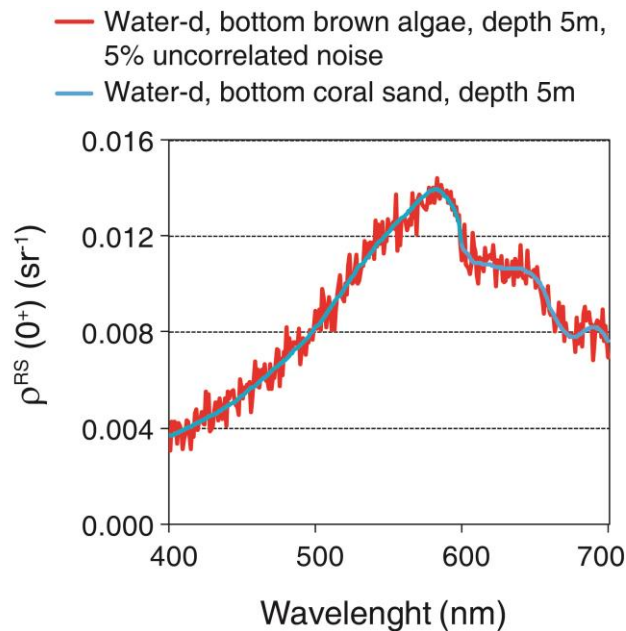


Figure 5.8 – Simulated remote sensing reflectance ( $\text{sr}^{-1}$ ) above water as a function of wavelength (nm) in shallow waters (5 m depth) with  $\text{chl-}a = 9 \mu\text{g l}^{-1}$ ,  $a_{\text{CDOM}}(440) = 0.3$ , suspended particles Type I =  $10 \text{ mg l}^{-1}$ , suspended particles Type II =  $1 \text{ mg l}^{-1}$  and  $a_{\text{detritus}}(440) = 0.5$ . The blue curve corresponds to brown algae substrate, while the red one represents coral sand substrate including 5% of uncorrelated noise.

### 5.3.2. Remote sensing data

To analyze the bottom retrieval for both methods, values where the algorithm was invalid ( $0 > \rho_{b \text{ retrieved}} > 1$ ) were excluded. Then, values where typically no bottom contribution to surface reflectance was expected were also removed. The bottom contribution to surface reflectance is dependent on bottom reflectance by itself. Due to real  $\rho_b$  in the study area was not available, other simulations were performed in the WASI software considering a standard bottom composed of 1/3 coral sand, 1/3 brown algae and 1/3 green algae. The bottom was simulated at 28 different depths between 1 and 28 m in a water medium with the same parameters estimated for the day of WV02 imagery. The bottom contribution was estimated through equations 5.2 and 5.7, and both models were slightly different in its estimation. For each depth, it was calculated the mean range of wavelength for which the bottom contribution at the surface was received. Figure 5.9 shows the shrinkage in wavelength range according to the depth increases. The water column characteristics in the study area were similar to the water-b simulated in section 5.2.1. Hence, values where exponential behavior was expected according to previous results were also neglected.

$\rho_{b \text{ retrieved}}$  by Lee's algorithm showed a higher percentage of invalid values at all depths. For example, between 9 and 11 m depth Maritorena's model retrieved 0-16% invalid values, whereas Lee's algorithm failed between 9 and 88%. Considering 13-16 m depth, the Maritorena model retrieved invalid values in 25-58% of the cases, whereas Lee's model retrieved 24-100% invalid results. Therefore, the Maritorena's model seemed to show a better performance than the Lee's algorithm.

Although all surface spectra in the shallow water seemed similar, they were influenced by the bottom because deep water showed a lower spectrum than shallow. As the bottom depth increased, the surface spectrum reduced its magnitude and approximated to the deep water spectrum. However, similar spectra for the surface water when the bottom was located at different depths can be explained by the differences in bottom reflectance. Indeed, depth points were clearly located above areas with different bottom characteristics (Figure 5.10a). These differences can be observed as slight discrepancies in  $\rho(0^-)$  spectra (Figure 5.10b).

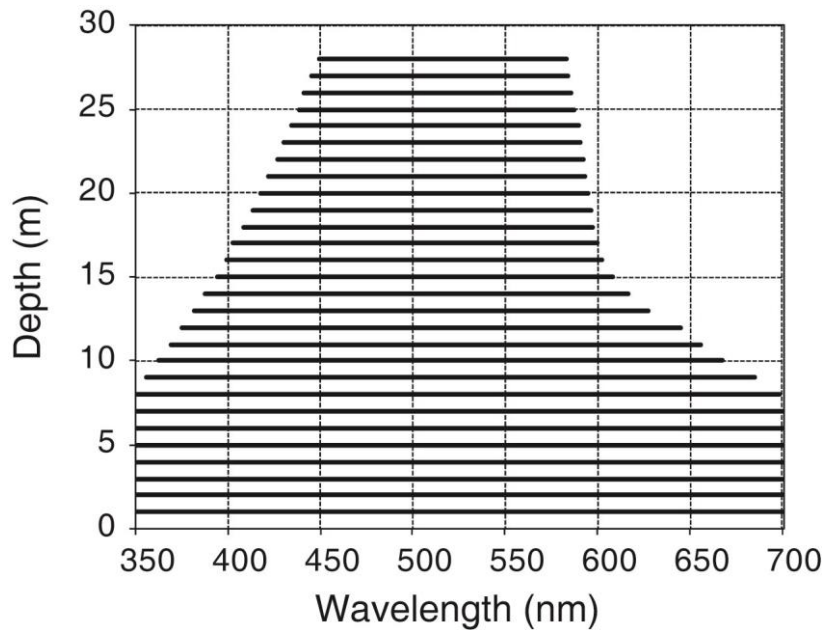


Figure 5.9 – Maximum range of wavelength in which a substrate (composed by coral sand, green and brown algae) located at different depths can be detected with remote sensing techniques.

If bottoms located at very distinct depths showed uniform reflectance patterns, it meant that they were not the same kind of bottom and exemplified the importance of applying water column corrections. After Maritorena's technique was applied, the  $\rho_b$  retrieved of these spectra showed a divergence, not only in their shape but in their magnitude (Figure 5.10b). Note that substrates at similar depths (at approximately 7 m) retrieved similar magnitudes in  $\rho_b$  retrieved. Moreover, substrates at 3.79 and 7.29 m in Figure 5.10 were located above the top of the reefs and were expected to have similar composition in a biological community dominated by corals, turf and crustose algae (VILLAÇA; PITOMBO, 1997; SEGAL; CASTRO, 2011; BRUCE et al., 2012). Likewise, according to a visual inspection, points at 7.39 and 10.09 m are expected to be composed by the same type of substrates: sand and macroalgae. In fact, retrieved spectra in each pair of locations showed the same shape, which suggested the same type of bottom. Nonetheless, it seems that the algorithm can properly retrieve the shape of a spectrum in some bands but fail to retrieve its correct magnitude.  $\rho_b$  retrieved through Lee's algorithm presented a peak in the shortest wavelength (427 nm) followed by an abrupt decay toward the longer wavelengths (Figure 5.10d).

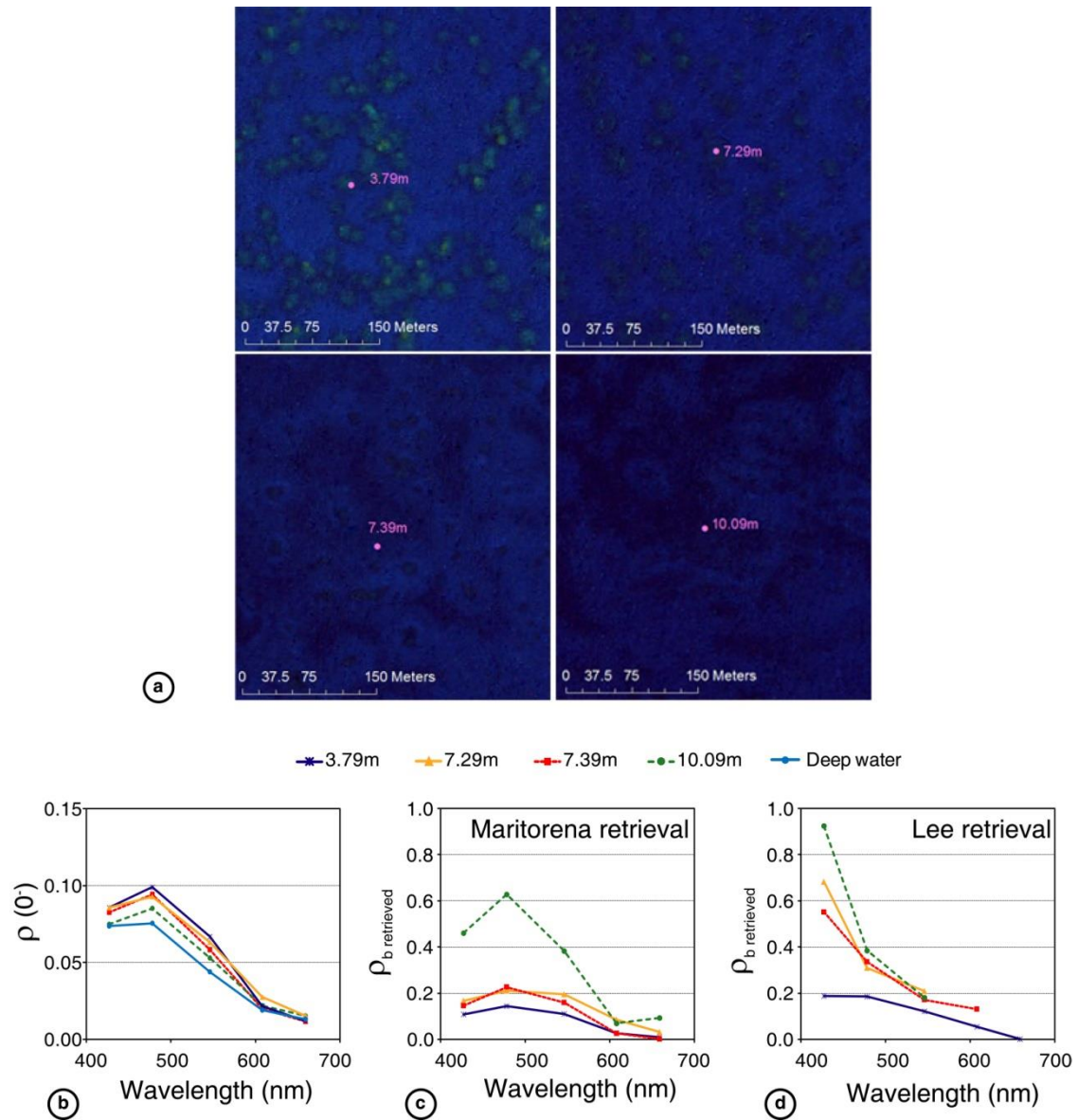


Figure 5.10 – (a) Zoom in different portions of WV02 image in quasi-true color (R: 659 nm; G: 546 nm; B: 478 nm). All images have exactly the same contrast and are in the same scale. Pink circles show location of depth points and their values are indicated. (b) Reflectance below water versus wavelength (nm) captured by WV02 sensor above the four points located in (a) and above deep water. (c-d) Bottom reflectance below water versus wavelength (nm) retrieved by Maritorena et al. and Lee et al.’s algorithms, respectively.

Only bottoms at the shallowest points exhibited a similar shape as the Maritorena retrieval. In this case, an increase in  $\rho_b$  retrieved was also observed according to bottom depth increases. Several uncertainty sources may cause increasingly large biases in retrieved bottom reflectance as depth increases. For example,  $K_d$ ,  $b_b$  and  $a$  were not estimated exactly at the time of the imagery, and this can introduce errors in results. As

observed in the sensitivity analyses in section 5.2.1, uncertainties in these inputs can have an important impact in retrievals and they can be related to the depth. Besides that, all models are based on the exponential decay of light. Nevertheless, in the first meters of the water column, the  $E_d$  profile showed a noisy pattern because of environmental factors such as waves, bubbles, OAC stratification, and fluctuations of the surface (STRAMSKI et al., 1992; FLATAU et al., 1999; FLATAU et al., 2000). It means that light could not perfectly decay exponentially, in particular considering shallow depths such in this analysis. If the light decay is not exactly exponential, the models will tend to retrieve skewed bottom reflectances as the depth increases.

The spectral shape of  $\rho_b$  retrieved from both models showed maximum values in shorter wavelengths, where the attenuation coefficient was lower. The natural substrates (e.g., sand, algae, corals, mud) do not have this type of reflectance curve, and it reveals that algorithms failed to retrieve the bottom reflectance below 500 nm. Above 600 nm, there are no differences between the shallow and deep water showing that there is no contribution of the bottom in these bands even in the lowest depth. It means that the absorption in the water is so high that it is not possible to retrieve bottom reflectance. Accordingly, the bands between 400 and 600 nm can contribute to the bottom differentiation. In this sense, the WV02 has an advantage over other orbital sensors with high spatial resolution because it has 4 bands inside this interval. Nonetheless, if the performance of the Maritorena's algorithm in retrieving bottom reflectance from the simulated spectra is considered (Section 5.2.1), it was able to retrieve a high reflectance value in water-b at 5 m, even above 600 nm. The models fail to simulate properly water reflectance at the surface above shallow bottoms and acting attenuation processes appear to be different in nature than in the simulations for models developed until now. Comparing the retrievals by both models, an overestimation by Lee's algorithm can be observed (Figure 5.11). Nevertheless, both retrieved exactly the same value at 546 nm in all depths, which was precisely in the band where there was the lowest percentage of invalid values. The overestimation by Lee's retrieval could correspond to an exponential behavior. Notice that N is higher at 546 nm because the invalid values were removed from the shorter and longer wavelengths.

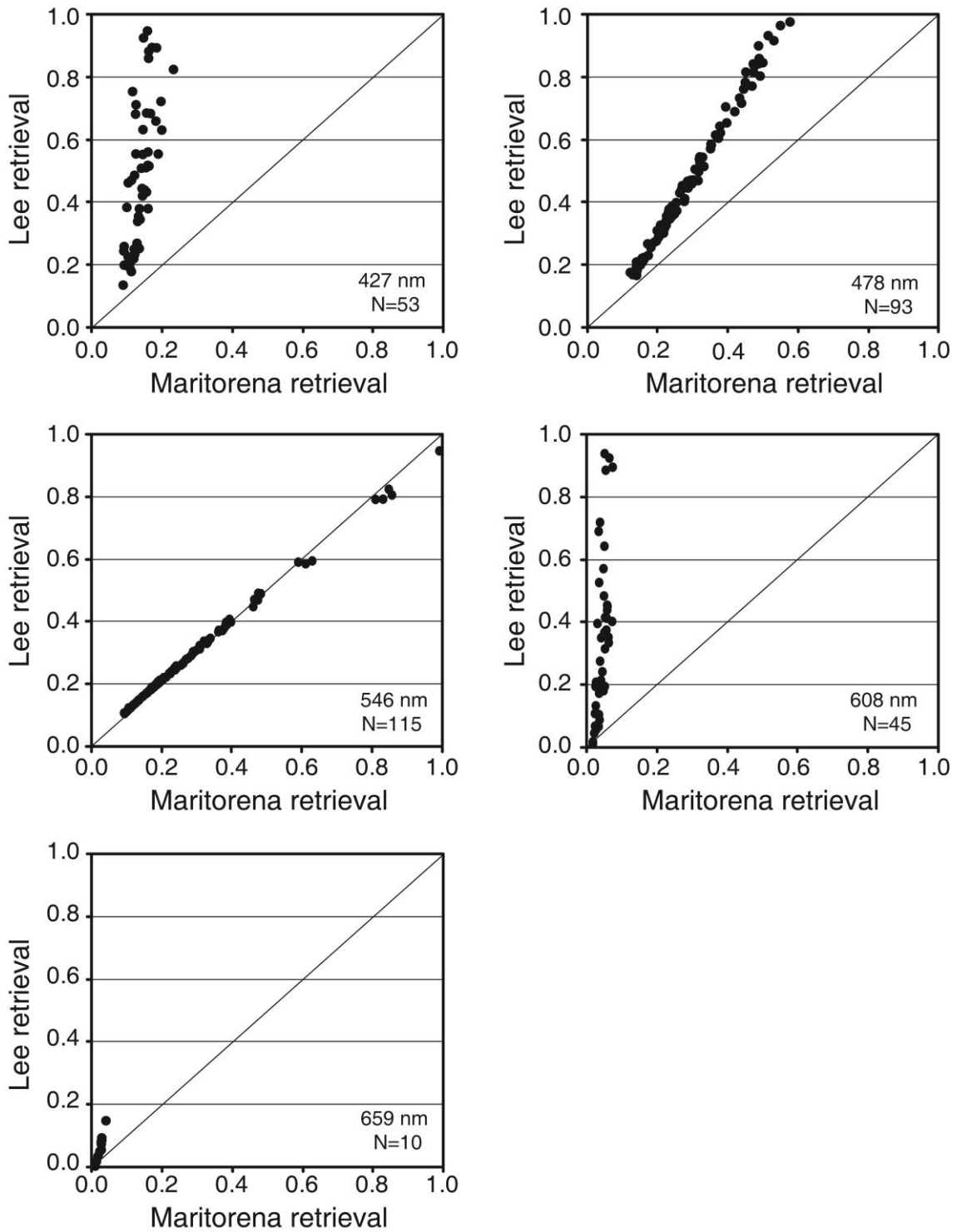


Figure 5.11 – Bottom reflectance retrieved using Lee et al.’s algorithm versus Maritorena et al.’s algorithm retrieval from WV02 image. Each plot corresponds to a different wavelength (427, 478, 546, 608 and 659 nm). Straight lines correspond to proportion 1:1.

To correct simulated spectra in an orbital multispectral image, Maritorena's was more efficient. It is also advantageous because it uses a lower quantity of inputs. Models with a high quantity of inputs frequently produced worse results because of uncertainties in estimating of each entrance parameter that propagated to the results. Goodman et al. (2008) noted that pre-processing steps, such as atmospheric and sunglint corrections, are important because they could have a large impact on the results of the Lee et al. model, especially when large amount of cross-track sunglint is present in an image. To obtain better results, the authors also suggested using a parameter  $Q$  in the equation for bottom reflectance ( $Q = E_u/L_u$ , the ratio of upwelling irradiance to upwelling radiance at nadir) instead of using  $\pi$ .

#### **5.4. Final considerations**

In recent years, the number of studies of coral reef ecosystems using remote sensing approaches has increased substantially. However, the characteristics of the medium of these ecosystems require the use of correction methods for the effects produced by the water column to compensate for those caused by the depth and optically active constituents. The application of an appropriate model for correcting the water column effects and accurately analyzing the input data, along with the development of new models, result in radiometric data with minimal water column effects that increase the accuracy of the mapping of reef ecosystems. Water column corrections minimize the confusing effects caused by different depths in scenes but do not eliminate this effect. At long wavelengths and high depths, it is difficult to retrieve the bottom reflectance due to the high light absorption by the water molecules.

Different models have been developed for passive sensors for both multi and hyperspectral resolutions. Simpler correction models have been applied for multi-spectral data of a few bands and consider clear water with vertical and horizontal homogeneity. For this reason, image correction fails when it is applied to deep or complex waters. However, these models have good potential since they only require a small amount of *in situ* data and may be useful in some regions. On the other hand, newer models allow considering higher environmental variability in water column related with depth. Although coral ecosystems are in clear water environments, horizontal heterogeneities in water transparency can often occur. This means that the

light attenuation may have some degree of spatial variability, especially in shallower areas. Thus, sometimes the use of a single attenuation coefficient in an entire scene, often obtained for deep water, can be inappropriate. It is for this reason that the assumption of horizontal homogeneity is a limitation for all of the models. New models for water column correction should consider this variability. A viable alternative would be to break the image into homogeneous areas for the application of different attenuation coefficients or different water correction models. Another input required in most models is the depth. For this reason, the availability of accurate bathymetry that is normalized by the tide height for the time of the image collection and with a spatial resolution match is a requirement to obtain a satisfactory result. Few models consider inelastic scattering (Raman) and none take into account the fluorescence of the phytoplankton and CDOM. However, in some situations, these scatterings may have important contributions in the light field, and their inclusion in the models can improve the fit.

The comparison between methods based in radiative transfer models showed that the model performance varied with depth, OAC concentration and type of bottom. Even considering the homogeneous water column in an image, different performance of water column correction models is expected between pixels according to the substrate and depth. It is an aspect that has to be included when mapping accuracy is developed. For example, validation points should be distributed in an area to be representative of all conditions found in a scene. Using simulated spectra, results showed that in clear waters and depth lower than 10 m it is possible to retrieve moderately accurate bottom reflectance, and are consistent with Dekker et al. findings (2011). When retrieving bottom reflectance from the WV02 image, results were degraded.

However, the lack of actual *in situ* bottom reflectance prevented a quantitative estimation of their accuracy. Although Lee et al.'s inversion scheme (1999) was previously applied with success to retrieve the water coefficients, it was developed considering a homogeneous reflective substrate. Its efficiency was lower for retrieving bottom reflectance. Even when Maritorena's model failed to retrieve the bottom reflectance at longer wavelengths, it showed a higher performance and can be easily applicable with just a few inputs. Algorithms are still not capable of completely separating the water from the bottom reflectance, and because the performance of

models is depth dependent, they do not obtain accurate bottom reflectances and do not eliminate completely the effect of depth.

After carefully investigating each method, the question that inevitably arises is what is the best method? The answer is not simple and each method has its advantages and limitations and can work properly in certain environments or potentially fail. For example, some methods assume homogeneity in the distribution of constituents of the water column while others can consider heterogeneities in the water between pixels. But inputs and outputs also differ between algorithms. Hence, the best choice for correction model depends on the environment and sensor characteristics, mapping purposes and availability of *in situ* data. When a new work is being planned, remote sensing images and field data collection can be designed. In this situation, water column corrections could be chosen in advance, for which a critical comparison of the performance of methods would be desired. Nevertheless, in an attempt to produce this comparison, certain restrictions were found. Most of the models did not provide a validation of their retrieval or each author validated their method in a different way. Some of them evaluated the adjustment between the simulated and measured bottom reflectance using different statistics parameters ( $R^2$ ,  $R$ , RMSE) or by visual comparison. Others scarcely visually inspected the scene after application of the water column correction model, whereas others did not show whether the water column correction application improved the mapping accuracy. Comparisons of map accuracy can also be subjective because it depends on a number of classes, sensor configurations, classification algorithms and environmental characteristics of the area, among others. For this reason, works such as Dekker et al.'s (2011) that produce an objective inter-comparison between different methods are required for the process of selecting an appropriate method and must be strongly encouraged.

With the availability of more *in situ* data from the water column, it is expected that a more realistic situation could be simulated and better results would be obtained. In the ideal condition, it would be desirable to know all of the IOPs from the water column, depth, and atmospheric conditions across the entire scene at the time of the image acquisition together with a significant quantity of points of bottom reflectance spectra to validate the results. Thus, what is the advantage in using remote sensing if so much data are required for reliable and accurate results? First, remote sensing offers an expansion

of spatial and simultaneous data collection that cannot be achieved with other approaches. Second, an initial effort is required at the beginning when a new area is explored; areas that are more well-known and for which higher quantities of data are available increase the reliability of a model and require fewer ground truth as model inputs. An endeavor to determine the water characteristics (e.g.,  $K_d$ , IOPs, OAC concentrations) in an area as a function of time should result in the successful application of water column corrections. Once these parameters are known, they can be used in other studies at the same season of year if they do not coincide with extreme weather or biological events, such as occurrence of hurricanes, phytoplankton bloom events or spawning events.

Coral reefs active remote sensing is a complement to passive remote sensing multispectral and hyperspectral data for bottom mapping in coral reefs because fluorescence signals from Light Detection And Ranging (LIDAR) measurements can be used to estimate the water column characteristics, bathymetry and habitat complexity (BROCK et al., 2004, BROCK; PURKIS, 2009). Fluorescence measurements also can provide information to differentiate between dead and healthy coral. In addition to retrieving bathymetry, active remote sensing offers the potential to estimate different AOPs and IOPs from fluorescence and polarization measurements from airborne platforms (HOGE et al., 1993; VASILKOV et al., 2001).



## 6 HYPERSPECTRAL ANALYSES OF BENTHIC COMMUNITIES

### 6.1. Introduction

At present, coral reef monitoring is a relevant topic in the global climate change context. If model predictions are confirmed, a depletion in biodiversity will be observed along with an increasing seaweed coverage in these ecosystems. Also, studies of benthic communities are relevant not only in the global change context. They have ecologically fundamental importance to determine the dynamics and functions in coral reef environments, productivity, rates of metabolism, biogeochemical cycles and indicates the reef status (KINSEY, 1985; CONNELL, 1997; HOCHBERG et al., 2003). This information is needed to establish guidelines of management and conservation of reef ecosystems.

Several maps of coral reef areas have been published in literature (HOLDEN; LEDREW, 1999; PURKIS, 2005; KUTSER et al., 2006; BENFIELD et al., 2007; BERTELS et al., 2008, FEARNIS et al., 2011; among others). These works have shown that it is possible to differentiate macroalgae from other types of benthic classes, even with a some degree of uncertainty. Evidence of this is that most of the mapping of coral reefs using remote sensing imagery considered at least one pure class of seaweed (e.g., brown algae or green algae or macroalgae) and showed some success of this discrimination with accuracy varying between 62 and 100%. Hence, if a benthic community was completely replaced by macroalgae according to model predictions (HOEGH-GULDBERG et al., 2007), it should be easily detected by remote sensing.

Until now, many works have used hyperspectral information collected *in situ*, very close to the targets, or in controlled laboratory conditions to understand the reflectance response of the benthic components of the communities (HOLDEN; LEDREW, 1999; HOCHBERG; ATKINSON, 2000; CLARK et al., 2000; FYFE, 2003; HOCHBERG et al., 2003; ANDRÉFOUËT et al., 2004; LIM et al., 2009; UHL et al., 2013). This kind of data has various advantages when compared with orbital information: (i) there is no influence of the atmosphere; (ii) the water column is minimal between the sensor and target, avoiding water column effects in the measurements, i.e., absorption and scattering; (iii) measurements are obtained for pure species in small areas, which allow the creation of spectral libraries; and (iv) with such small IFOV, spectral mixing is

negligible in the measured reflectance. These works showed that the spectral shape of individual benthic elements is mainly determined by the absorption of different pigments present in the biological community (HOCHBERG et al., 2003). Hedley and Mumby (2002) also highlighted the contribution of pigment fluorescence on the measured reflectance, and they encourage the inclusion of this effect in optical models. However, when using remote sensing information, such effects are still poorly known.

Some spectral features allow to perform an interspecific or intertaxa discrimination (FYFE, 2003). These characteristics must be evolutionally conservative so they may be maintained among different geographic regions (HOCHBERG et al., 2003). Notwithstanding, the optical similarity of some characteristic features result in some important restrictions for remote sensing purposes (LUCZKOVICH et al., 1993). It may seem contradictory that, on one hand, the spectral features are consistent and conservative and, on the other hand, a lot of spectral confusion exists between taxa. Hence, the question is if these spectral features are enough for the separation between bottom types? It seems that the absorption peaks are broadly conserved due to the presence of specific pigments in the different bottom types, which are evolutionally conserved, however, great variability in the reflectance spectra may be caused by distinct concentration of pigments, as well as, the influence of environmental noises which are difficult to remove and may still remain in measurements. Pigments are not constant between individuals, even being from the same species. Also, the reflectance is influenced not only by the characteristics of the target by itself, but also by the environmental conditions affecting the light field, such as the acquisition geometry (viewing and solar zenith angles), and in the case of marine environments, the sea surface and sky conditions (NICODEMUS et al., 1977; HEDLEY et al., 2012).

Besides of the complexities listed above, the actual benthic communities are not always formed by large patches occupied by pure substrates. Hence, when the target of interest is a habitat formed by the combination of different types, as usually occurs in nature, additional complexity is expected. In the first place, different taxa can produce the same pigments and only vary in their proportions (HEDLEY; MUMBY, 2002). In fact, analyzing the presence and concentration of pigments in samples of coral and algae tissues it is possible to see that it is necessary to unravel the mixture between optical signals from different organisms that occur in a benthic community to apply this

information for remote sensing purposes (MYERS et al., 1999). Second, epibiont foulers that are frequently found in seagrass and macroalgae as well as and zooxanthells, which occur within coral tissues, can also interfere in the reflectance spectra. Third, multiple scattering or multilayered structures also affect the reflectance spectra. Therefore, the tridimensional structure of the reef is another source of variability in the reflectance. For example, the morphology of corals can influence their reflectance spectrum, as massive and branching corals can present perspicacious but different characteristic features (HOLDEN; LEDREW, 1999). Fourth, the bottom of reef environments are submerged, and the water column above them will present different reflectance spectra according to the depth and OAC concentration. The water column will affect not only the bottom reflectance spectra acting as an "additive term", but also the light attenuation downward to the substrate and upward to the water surface. Models to correct the water column effect attend to remove the water reflectance from the surface spectra, as well as compensate for the light attenuation. However, such models do not work perfectly. The uncertainties in the bottom reflectance retrieval related to the algorithm performance and in the estimation of the parameters required by the models were discussed in the previous chapter.

The first works that applied remote sensing imagery to map coral reefs date from the 1970's. Four decades after, several questions still remain. For instance: Do the characteristic features of pure substrate still remain distinguishable in the spectra of complex benthic communities? Is it possible to detect subtle increases of seaweed coverage in coral reef environments by remote sensing? Acute variations in the proportion of macroalgae can be observed with differences in the reflectance spectra? Is it possible to distinguish benthic communities based only in their reflectance spectra? Is there any feature that alone helps to differentiate benthic communities? Is it possible to isolate the environmental factors (depth, solar zenith angle, IOPs, IFOV) from the biological factors (benthic species)? Or may it be that even when applying water column correction procedures, some environmental biases will still be included?

In this chapter, continuous *in situ* above-water spectra collected at shallow points in the ACRB were analyzed. Benthic communities at these sites were not dominated by just a few species and therefore, their spectra can be used to represent the real optical complexity found in a complex coral reef environment with high diversity. Contrary to

other works, the water column is included in the measured spectra, incorporating additional raveling to the study. It is actually, not feasible to evaluate the real potential of remote sensing for such applications, associating the reflectance spectra to submerged biological communities without including the water column. Since the *in-situ* sensor Field of View (FOV) is small, this implies that it must be used at a reasonable distance from the target. For example, a sensor with a FOV of 25° (such as the ASD) should be used at 1 m of distance from the bottom to integrate an area of 0.60 m<sup>2</sup>. The objective of this chapter was to address the following points: (i) to analyze the water column optical constituents estimated *in situ* in different sites of the ACRB belonging to both arcs; (ii) evaluate the ability of a water column algorithm to retrieve accurate bottom reflectance spectra from above-water radiometric measurements; and (iii) relate the bottom reflectance to the community composition, looking for spectral differentiation between communities through possible diagnostic features.

## **6.2. Materials and methods**

### **6.2.1. Bio-optical characterization**

In this section, all samples collected both in the stations and sites were analyzed, totalizing 62 samples. The absorption coefficients were used to classify the water type according to the Case-1 and Case-2 classification (MOREL; PRIEUR, 1977). A simple classification scheme was performed using the correlation coefficient between  $a_{CDOM}(440) + a_d(440)$  vs.  $a_{phyto}(440)$  to analyze the degree of dependence between the colored organic matter components with the local phytoplankton standing stock. To evaluate the percentage of contribution of  $a_{phyto}$ ,  $a_{CDOM}$  and  $a_d$  to the total biogenic absorption budget (the sum of the three components), a ternary diagram was also applied to the three components measured at 440 nm (GOULD; ARNONE, 2003; SYDOR et al., 2004).

### **6.2.2. Above-water radiometric measurements**

A total of 20 sampled sites were analyzed in this chapter, situated in different areas of the ACRB in both arcs, between the coordinates 17°20'-18°10'S and 38°35'-39°20'O. The sites belonging to the external arc were: *Parcel dos Abrolhos* (PAB), at 60 km from the coastline and Archipelago (ARCH); and belonging to the coastal arc were: *Timbebas* (TIM) at 18 km from the coast, *Pedra de Leste* (PL), at 12 km, and *Parcel*

*das Paredes* (PA). The sites were located above reef banks with different benthic communities and bottom depths, which varied between 0.3 - 5 m. The sites were chosen according to a previous inspection of the bottom, done by scuba diving, to attend the following conditions: (i) a homogenous benthic coverage, with an extended patch enough to avoid contaminations in the radiometric measurements from neighboring areas with different characteristics, and (ii) to have as much sites as possible covering the different biological communities found in the ACRB, to be included in the analysis.

Above-water radiometric measurements were collected every day during the campaign from 03/08/2013 - 03/26/2013, at 9:00-16:40, local time. Thus, the Sun zenith angles varied within 17-69°. Above-water radiance ( $L$ ) was measured when pointing the sensor to the ocean, sky and the white reference, as explained in Section 4.2.2. Above-water remote sensing reflectance ( $\rho^{RS}(0^+)$ ) was estimated according to Equation 4.3. All the spectra were filtered to eliminated noisy spikes using a moving average low-pass band of 25 points.

### 6.2.3. Water column correction

Similar to the processing performed to the surface spectra, the water column correction attempted to make the reflectance spectra independent of the effects of some environmental conditions, such as, the bathymetry, and the light attenuation caused by absorption and backscattering of the OAC present in different concentrations at each site. The  $\rho^{RS}(0^+)$  spectra collected *in situ* were first converted to  $\rho^{RS}(0^-)$  using expression 6.1 (LEE et al. 1999). Then, they were converted to below-water irradiance reflectance ( $R(0^-)$ ) assuming that the ocean is a Lambertian surface, following Equation 6.2.

$$\rho^{RS}(0^-) = \frac{\rho^{RS}(0^+)}{(0.5+1.5\rho^{RS}(0^+))} \quad (6.1)$$

$$R(0^-) = \pi * \rho^{RS}(0^-) \quad (6.2)$$

To retrieve bottom reflectance, the Maritorena et al. (1994) model was used since it showed better performance compared to other models for the retrievals (as shown in

Chapter 5, Equation 5.1). The term  $k = (a_{total} + b_b)$  was used instead of measured  $K_d$  (from the original model), since it was not possible to measure  $E_d$  profiles using the Satlantic Profiler at the sites with shallow depths (see Equation 6.3). In this expression,  $R_\infty(0^-)$  corresponds to the below-water irradiance reflectance of optically deep waters, and  $z$  is depth.

$$\rho_b \text{ retrieved} = \frac{R(0^-) - R_{deep\ water}(0^-)}{e^{-2kz}} + R_\infty(0^-) \quad (6.3)$$

In a first attempt to extract  $\rho_b$  from  $R(0^-)$ , the absorption coefficients measured from the *in situ* samples collected at each site (as detailed in section 4.2.3) were used in expression 6.3. The total absorption coefficient ( $a_{total}$ ) was determined as:

$$a_{total} = a_w + a_{CDOM} + a_{phyto} + a_d \quad (6.4)$$

being  $a_w$  the absorption coefficient of pure water measured by Smith and Baker (1981). The total backscattering coefficient ( $b_b$ ) was determined as:

$$b_b = b_{bp} + b_{b\ pure\ water} \quad (6.5)$$

where  $b_{b\ pure\ water}$  corresponds to the backscattering coefficient of pure water using the relation  $[b_{b\ pure\ water} = 0.00144 \text{ m}^{-1} * (\lambda/500 \text{ nm})^{-4.32}]$ , according to Morel (1974). Since no  $b_{bp}$  data was available for the shallow sites where Fieldspec measurements were done, the values of  $b_{bp}$  were estimated with the Quasi-Analytical Algorithm (QAAv5) (LEE et al., 2002) using below-water reflectance, as follows:

$$b_{bp}(\lambda) = b_{bp}(555) \left( \frac{555}{\lambda} \right)^Y \quad (6.6)$$

$$Y = 2.2 \left\{ 1 - 1.2 e^{\left[ -0.9 \frac{\rho^{RS(0^-)(440)}}{\rho^{RS(0^-)(555)}} \right]} \right\} \quad (6.7)$$

$$b_{bp}(555) = \frac{u(555)a(555)}{1-u(555)} - b_{b \text{ pure water}}(555) \quad (6.8)$$

$$a(555) = e^{(-2-1.4\alpha+0.2\alpha^2)} \quad (6.9)$$

$$\alpha = \ln \left( \frac{\rho^{RS(0^-)(440)}}{\rho^{RS(0^-)(555)}} \right) \quad (6.10)$$

$$u(\lambda) = \frac{-g_0 + [(g_0)^2 + 4g_1 \rho^{RS(0^-)(\lambda)}]^{1/2}}{2g_1} \quad (6.11)$$

where  $g_0$  and  $g_1$  are coefficients set to 0.084 and 0.17, respectively, since these values are recommended for coastal waters (LEE et al., 1999).

The determination of deep water marine reflectance ( $R_\infty$ ) for the shallow sites, was performed by assuming the same  $R(0^-)$  measured at other sites deeper than 7 m (assuming negligible bottom contribution), with approximate values of  $a$  and  $b_b$ . After applying the water column correction procedure, however, the  $\rho_b$  retrieved showed some anomalous behavior, with exponential values at the beginning of the blue spectral region and towards the red end. Because of the small depths of the sites, this behavior was not expected and a second approach was tested, as explained in the following.

In the second approach, modeled  $R_\infty$  using Equation 6.12 according to Lee (personal communication) was used instead of the measured values at deeper sites.

$$R_\infty(0^-) = 0.33 b_b / (a_{total} + b_b) \quad (6.12)$$

This approach gave better results for the  $\rho_b$  retrieved.

A third step was further performed in the correction scheme attempting to improve the retrievals of  $\rho_b$ . Here, the Lee et al. (1999) algorithm was first applied in the inversion form and then the Maritorena et al. (1994) algorithm in the forward way. This approach was similar to that adopted by Goodman and Ustin (2007) to correct for the water column using satellite orbital data of the AVIRIS sensor. The inversion/optimization scheme of Lee et al. (1999) was applied to derive  $a_{phyto}(440)$ ,  $a_g(440)$  (the sum of  $a_{CDOM} + a_d$ ),  $b_{bp}(400)$ , and  $z$  from the measured  $\rho^{RS}(0^+)$  spectra, at each station.  $a_{phyto}(\lambda)$  was estimated as:

$$a_{phyto} = [a_0 + a_1 \ln P]P \quad (6.13)$$

where  $P$  is  $a_{phyto}$  at 440 nm and  $a_0$  and  $a_1$  are empirical coefficients adjusted by Lee et al. (1999).  $a_g(\lambda)$  was estimated as:

$$a_g = G e^{[-0.015 \text{ nm}^{-1}(\lambda-440)]} \quad (6.14)$$

where  $G$  corresponds to  $a_g$  at 440 nm. And  $b_{bp}$  was determined as:

$$b_{bp} = X \left( \frac{400}{\lambda} \right)^Y \quad (6.15)$$

where  $X$  corresponds to  $b_{bp}$  at 400 nm. The slope  $Y$  was estimated using a ratio between  $\rho^{RS}(0^-)$  at 440 and 555 nm, according to the QAAv5 (Equation 6.7).

The inversion/optimization scheme of Lee et al. (1999) uses solely the measured  $\rho^{RS}$  as input to determine:  $a_{phyto}(\lambda)$ ,  $a_g(\lambda)$ , and  $b_{bp}(\lambda)$ . The modeled absorption and

backscattering coefficients were then used to estimate  $R_{\infty}(0^-)$  (Equation 6.12) and used as input for the Maritorena et al. (1994) algorithm to retrieve the bottom reflectance ( $\rho_b$ ). The  $\rho_b$  retrieved obtained using the measured and modeled coefficients were then compared and the best retrieval was used for the analysis of the relations between the bottom reflectance and benthic community.

#### **6.2.4. Benthic community composition**

To relate the retrieved bottom reflectance spectra with the benthic communities, benthic classes were grouped according to their characteristic  $\rho_b$  spectral shape. Non-fleshy calcareous algae groups were merged with algal turf and red fleshy algae, because they typically have similar spectral shapes (HOCHBERG et al., 2003). Although the reflectance amplitude signal for bleached coral is generally lower than for sand, the spectral shape of these bottom types is similar, hence both classes were also merged (HOCHBERG et al., 2003). Also, the reflectance curve of green fleshy algae and seagrass are characterized by a single broad feature around 550-560 nm and were joined in a unique class together with green phyllamentous algae (HOCHBERG et al., 2003). The 7 benthic classes considered were:

- Green bottom type = Green fleshy algae + Seagrass + Green phyllamentous algae
- Brown bottom type = Brown algae
- Red bottom type = Non-fleshy calcareous algae + Red fleshy algae + Algal turf
- High reflective bottom type = Sand + Bleached coral
- Live coral
- Sponge
- Zoanthids

Hedley et al. (2012) considered mixtures of pairs of substrates in different proportions and found that non-dominant classes restricted statistical separability, at least to sub-pixel proportions of 20%. Considering three classes of bottom types, i.e., sand, live coral and algae, Hochberg and Atkinson (2003) showed that linear mixtures frequently pushed the classification to the dominant type. Based on these findings, it is expected that the reflectance spectra should be dominated by the most abundant classes. In the

present work, some sites had biological communities with a balanced distribution between different classes and non-dominant classes added up 50 % of the total. For comparative purposes between the bottom reflectance and benthic communities, a threshold of a minimum 20% of dominance of a specific class within the defined bottom types was established to analyze its relations with  $\rho_b$ .

## 6.2.5. Hyperspectral $\rho_{bottom}$ vs. benthic communities composition

### 6.2.5.1. Spectral Derivative analysis

Derivative analysis is commonly applied to hyperspectral radiometric data (BUTLER; HOPKINS, 1970; DEMETRIADES-SHAH et al., 1990). In this kind of analysis, features already included in zero-order spectra are enhanced in the first and second-derivatives, which are the most commonly used in this type of approach. This spectral processing technique intensifies the main features, by reducing the background signals that do not add new information to the zero-order spectra (TALSKY, 1994; HEDLEY; MUMBY, 2002). Moreover, the derivative analysis is advantageous compared to other techniques, because the derived spectra are independent of continuous offset, resulting in a reduction of bi-directional effects on a wide range of wavelengths (UHL et al., 2013). In this work, the first-derivative applied by finite approximation was estimated for all spectra according to Equation 6.16. First-derivatives were used to inspect the consistency of a few features, feasible to be detected only in some of the zero-order spectra.

$$\left. \frac{d\rho_{bottom}}{d\lambda} \right|_i = \frac{\rho_{bottom}(\lambda_i) - \rho_{bottom}(\lambda_j)}{\lambda_j - \lambda_i} \quad (6.16)$$

where  $\lambda_i$  and  $\lambda_j$  are consecutive bands, respecting the order  $\lambda_i < \lambda_j$ .

### 6.2.5.2. Spectral Angle Mapper analysis

Spectral Angle Mapper (SAM) is a supervised classification technique based on the shape of reflectance curves, as a function of the geometric similarity between two spectra (KRUSE et al., 1993). In this approach, the reflectance spectra are treated as vectors and their difference is measured as the arc-cosine of the scalar product between

them (Equation 6.17). For this reason, it is not sensitive to the differences in magnitude between the spectra, but only the spectral shape.

$$d_{SAM} = \cos^{-1} \left[ \frac{\sum_{i=1}^N \text{spectra1}_i \text{spectra2}_i}{\left[ \sum_{i=1}^N \text{spectra1}_i^2 \right]^{1/2} \left[ \sum_{i=1}^N \text{spectra2}_i^2 \right]^{1/2}} \right] \quad (6.17)$$

where *spectra1* and *spectra2* are the reflectance curves to be compared, both measured at band *i*. SAM was applied to all spectra and  $d_{SAM}$  values were used to create a SAM matrix, formed by the differences between each pair of spectra.

### 6.2.5.3. Multivariate statistics

Cluster analysis was performed to group sites according to the biological information (abundance of benthic categories) as well as their spectral information. In the last case, the spectral information encompassed the retrieved bottom reflectance using the third approach of the water column correction (with modeled  $a_{total}$  and  $b_{bp}$ ), and also their associated SAM matrix, considering it as a similarity matrix. Unlike the bottom reflectance spectra by their own, the SAM matrix is not affected by differences in amplitude between the reflectance curves, but only by their spectral shape. For this reason, the same grouping was not necessarily expected when using the reflectance spectra or SAM matrix. All cluster analyses were processed with the amalgamation rule of Ward's method and using Euclidean distance.

### 6.2.5.4. Data mining

Data mining is defined as the process of discovering patterns in the data, with the capacity to highlight useful information from large database, in any type of data or system (HAN; KAMBER, 2006; WITTEN et al., 2011). Some algorithms frequently used in data mining and learning machine are based in decision trees. As a result of its application, a decision tree is produced, which indicates rules for the discrimination between the groups previously defined. It means that from a huge data base, decision tree algorithms select which information is relevant for the classification and in which thresholds that information should be used. The C4.5 algorithm (QUINLAN, 1993) is an example of decision-tree classifiers and is available in the free software Weka 3.10

(<http://www.cs.waikato.ac.nz/ml/weka/>). It has been applied to remote sensing data with successful results (e.g., SILVA et al., 2008).

This technique was applied with the aim to identify if diagnostic bands were presented in the bottom reflectance spectra, so that the benthic communities could be separated according to the spectral information. For the data mining application, bottom reflectance was restricted to wavelengths between 450 and 650 nm, since this spectral region is where the main absorption peaks of pigments occur and where lower uncertainties regarding the water column correction are expected to be found. The normalization of the spectra in the range of 450 to 650 nm by mean and standard deviation preceded the analysis. To avoid negative values, an offset value equal to 2.83 was added to all spectra. This offset value corresponded to the absolute minimum obtained for all sites for the normalized spectra (450 to 650 nm). The normalization procedure was applied to consider only the possible diagnostic features in the analysis, and to avoid including the influence of the spectral magnitude of  $\rho_b$ . Besides of the individual bands, some reflectance ratios were also included in the analysis. The bands obtained from the normalized spectra had a 10 nm bandwidth and were centered at: 455, 465, 475, 485, 495, 505, 515, 525, 535, 545, 565, 575, 585, 595, 605, 615, 625, 635 and 645 nm. Band ratios considering all of the possible combinations using these bands were also calculated. This bandwidth was chosen following recommendations of Fyfe (2003), who appointed that optimal bands used for the differentiation of seagrasses should be reasonably narrow, varying from 5 to 15 nm breadth. In the total, 411 values were used for each site when applying the data mining analysis: 201 narrow 1 nm bands from 450-650 nm plus 19 wider 10 nm bands and 191 band ratios.

The spectral data mining analysis allowed the identification of spectral features that were associated to two benthic classes that were separated in the cluster analysis. Smaller groups were not taken into account since the number of samples included in some of them was reduced (e.g., two sites for some groups). A criterion used for the grouping analysis was based on the abundance of red substrate types. Among all sites, 4 of them were excluded of this analysis. PA2-1 and ARCH-9 were desconsidered because the red coverage type was absent in them. ARCH-11 and ARCH-12 were not included because the performance of the water column correction algorithm used to retrieve bottom reflectance was low for wavelengths longer than 600 nm.

### 6.2.5.5. Band depth

The continuum removal processing was applied to all spectra between 585 and 700 nm in ENVI 4.7 environment. This normalization rescales data in a value interval between 0 and 1 (KOKALY; CLARK, 1999). It is calculated dividing the reflectance at a certain wavelength in the absorption feature by the value of the hull at that wavelength (CLARK; ROUSH, 1984). After applying the continuum removal to the bottom reflectance between 585 – 700 nm, band depth ( $BD$ ) was estimated as:

$$BD = CRR(585) - CRR(675) \quad (6.18)$$

being  $CRR(585)$  and  $CRR(675)$  the continuum removed reflectance at 585 and 675 nm, respectively. The band centered at 585 nm was found to be in a position of relative maximum. Whereas the 675 nm band is where the maximal absorption of chl-*a* occurs, and therefore, a minimum in bottom reflectance was seen in the spectra.

The  $BD$  was related to the coverage of benthic types that had chl-*a* through Pearson, correlation, considering the abundance of: red substrate type; green substrate type; brown substrate type; red + green + brown substrate types; and red + green + brown substrate types + live coral. In this case, substrate types with lower coverage than 5 % were not neglected.

## 6.3. Results and discussion

### 6.3.1 Bio-optical characterization

The CDOM absorption coefficient showed a high variation between 0.0014 to 0.3485  $m^{-1}$ . The maximum value almost doubles the highest found in other coral reef areas (Table 5.6). Chl-*a* concentration, in the other hand, presented a variation between 0.06 to 1.27  $mg\ m^{-3}$ , comparable with those reported in other coral reefs (Table 5.2). According to the *in situ* IOPs, the ACRB can be characterized as Case-2 waters, since the absorption coefficient of detritus plus CDOM are not correlated with the phytoplankton absorption coefficient, even if the samples are analyzed separated for coastal and external waters ( $R^2 = 0.0244$  for all waters;  $R^2 = 0.0037$  for coastal waters;  $R^2 = 0.0247$  for external waters). This means that besides of the local phytoplankton production, external sources may also contribute to the variability in the optical properties of the water column at the ACRB. In the collected samples the total

absorption was dominated by phytoplankton particles, CDOM, or a mixture of them, while detritus represented less than 50% and was not dominant at any site, as can be seen in the ternary diagram (Figure 6.1). Note that this diagram represents the dominance of the absorption coefficients and not their absolute values. In 65% of the cases, CDOM was the COA with the highest contribution to absorption at 440 nm. In the coastal areas, it is expected for CDOM not to be solely related to the biological activity of phytoplankton, but also come from terrestrial runoff or benthic inputs from seagrass and corals (MOBLEY et al., 2004). The pattern of the sediment distribution indicates some degree of terrestrial contribution in the coastal arc, since they are dominated by siliciclastic sand and mud (LEIPE et al., 1999; DUTRA et al., 2006). The sediments transported by rivers to the coastal zone are mainly distributed perpendicular to the shoreline (SILVA et al., 2013). However, the along-shore currents and topography of the coastal arc forms also an efficient hydrodynamic and geomorphological barrier for the offshore transport of the suspended materials. For this reason, the continental influence is minor upon the external arc, where sediments are dominated by pure carbonates (DUTRA et al., 2006). This means that CDOM in the ARCH and PAB areas should come mainly from the benthic local production while in the coastal arc, terrestrial material is also received. Other worldwide coral reef areas have also shown CDOM dominating the water absorption properties, with its high concentration attributed to a decay in the benthic biota and to tide exchanges controlling its temporal variation (ZANEVELD; BOSS, 2003; MOBLEY et al., 2005). Figure 6.2 shows that CDOM and phytoplankton pigments did not follow a distribution according to the distance to the coast. Nevertheless, high detritus absorption was found only in the coastal arc. The source of detritus in the external arc is mainly originated from the local biological community and the highest values are associated to resuspension dynamics, especially caused by the passage of polar fronts, which are more frequent during the austral winter. During the summer, as in the case of this work, the water column should actually be more vertically stable due to the less frequent arrivals of cold fronts to the ACRB, keeping the suspended sediments low.

The depths at the sampling sites and stations varied between 0.3 and 22.5 m, but the water samples were always collected at surface. Analyzing the absorption coefficients obtained *in situ*, it is possible to observe that their distribution does not respond to the

depth of the location where the samples were taken. This suggests that vertical processes are less important than the horizontal. The water samples were collected above the reefs, at inter-reef areas or around the Archipelago.

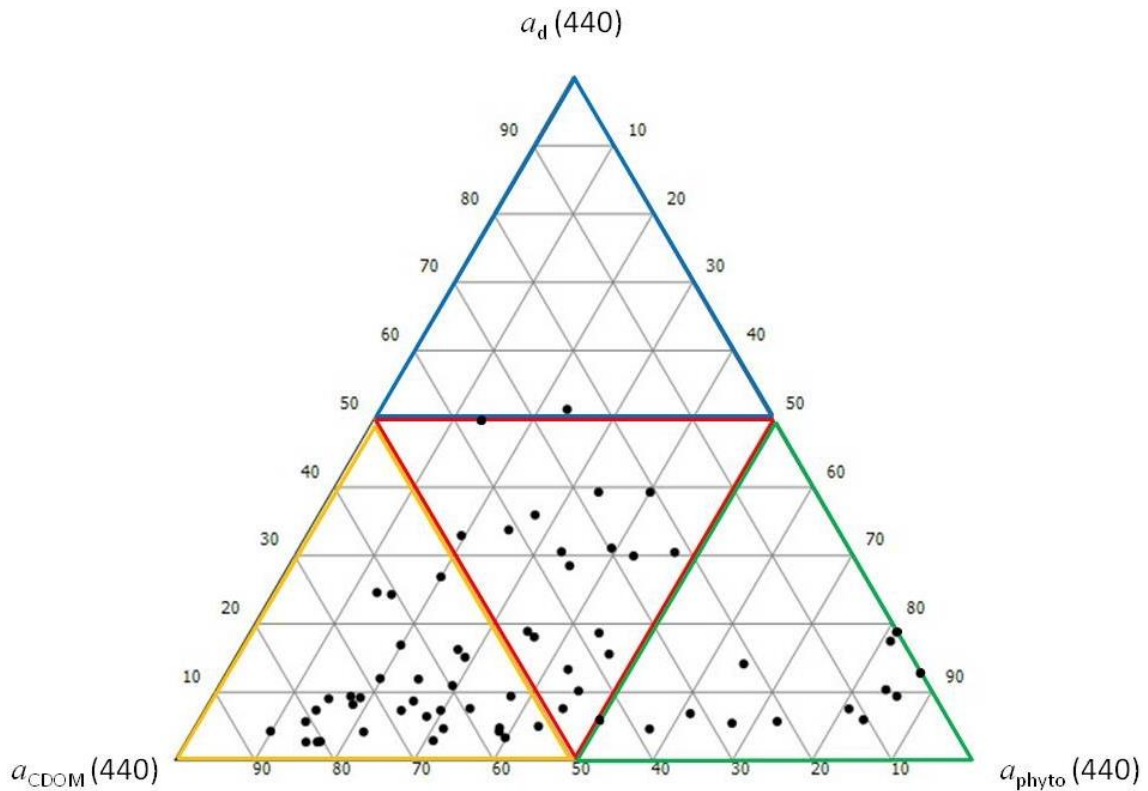


Figure 6.1 – Ternary diagram representing the percentage of the absorption coefficients of each optical constituent (CDOM, detritus and phytoplankton) at 440 nm, referred to the total absorption. Samples in the internal green triangle are dominated by phytoplankton absorption; in the yellow triangle are dominated by CDOM absorption; in the blue triangle, by detritus absorption; and in the red triangle at the middle of the diagram corresponds to the mixture between all constituents.

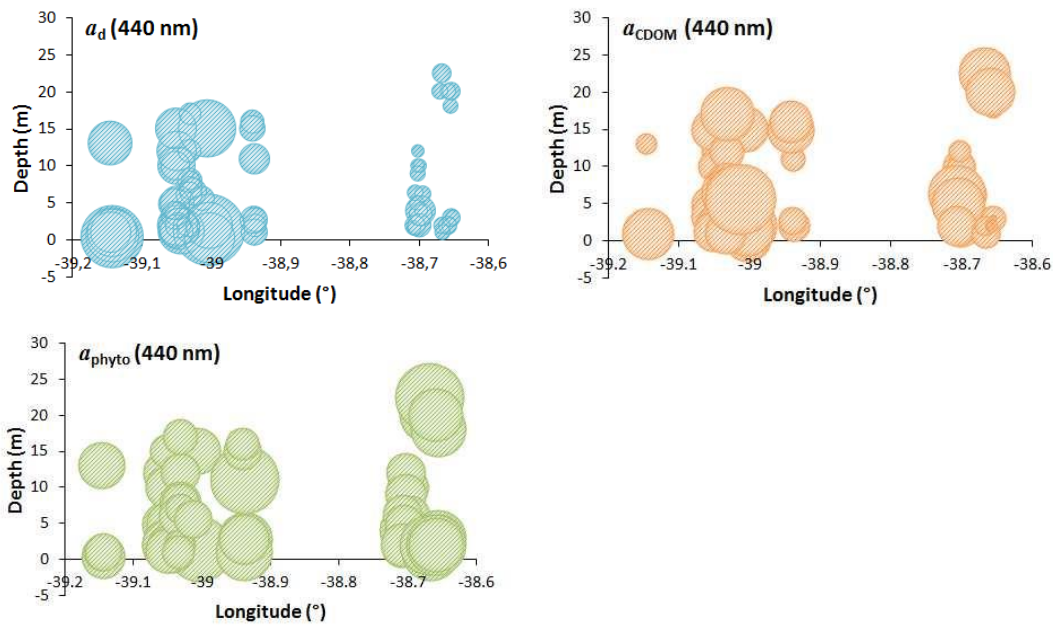


Figure 6.2 – Absorption coefficients at 440 nm obtained *in situ* as a function of longitude (in the axis x) and the depths of the sites in meters (in the axis y). The area of the circles is directly proportional to their value. Upper left:  $a_d$ . Upper right:  $a_{CDOM}$ . Down:  $a_{phyto}$ .

In such a small scale in which some samples were taken (around 60 to 200 m distant), a considerable variation in the absorption and backscattering coefficients was observed (Figures 6.3 to 6.5). This emphasizes the idea that a unique attenuation coefficient used to apply the water column correction in an entire scene, for satellite applications, could be inappropriate, and thus, an algorithm including the horizontal heterogeneity should be used. Hence, the use of algorithms that retrieve IOPs simultaneously, could be the best approximation to obtain the bathymetry and bottom reflectance for environments with high horizontal environmental heterogeneity. These findings however, are contrary to those found by Holden and LeDrew (2008). The authors proposed that the assumption of horizontal homogeneity could be valid and suggested the use of a single attenuation coefficient applied to the entire satellite image, when they studied a coral reef environment in Fiji, in the South Pacific. The choice of the best method will actually depend on the environmental characteristics of each area.

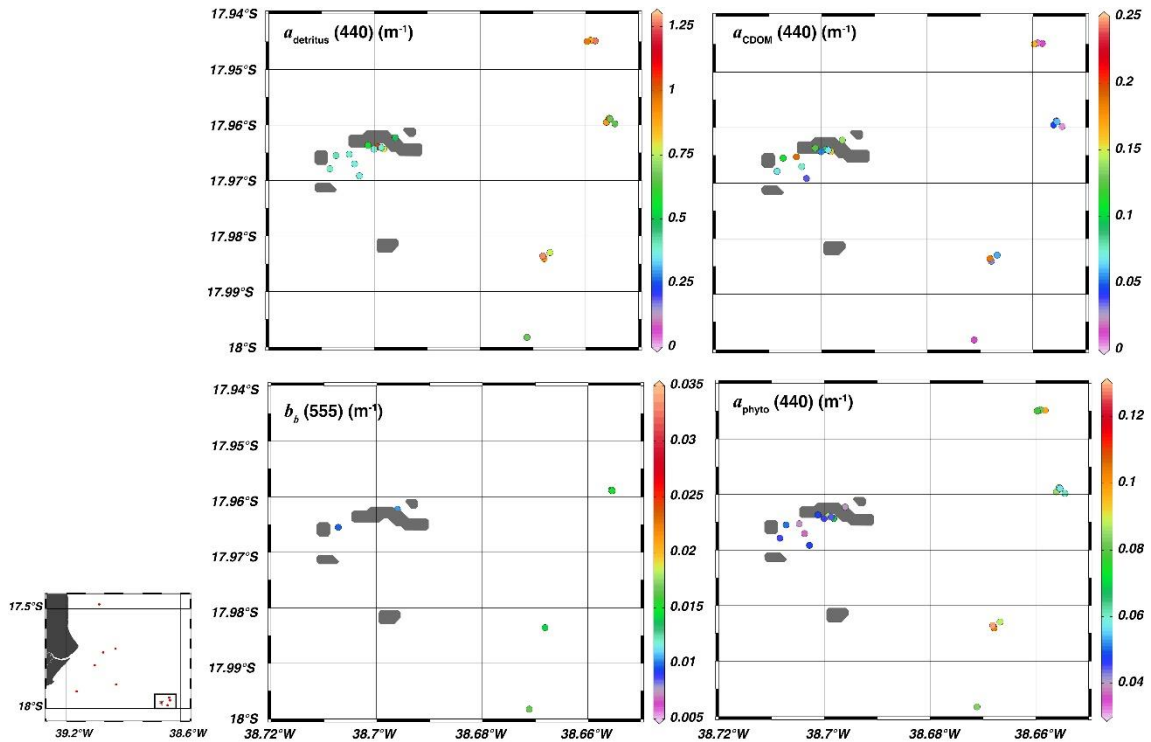


Figure 6.3 – Absorption coefficients measured in the field at all stations and sites in the ARCH and PAB reefs:  $a_{detritus}(440)$  (upper left);  $a_{CDOM}(440)$  (upper right);  $a_{phyto}(440)$  (lower right);  $b_{bp}(555)$  (lower left), measured at stations in the ARCH and PAB reefs. At the side of each figure, a colorimetric scale represents either absorption or backscattering values in  $m^{-1}$ . The islands are represented in grey.

### 6.3.2. Retrieved bottom reflectance

In this work, three approaches were used to retrieve the bottom reflectance. In all cases, Maritorena et al.'s model was applied, but the values used for the inputs varied. The best results both in magnitude and shape of the bottom reflectance spectra, as well as the modeled deep water reflectance, were obtained using the absorption and backscattering coefficients retrieved by Lee et al.'s inversion scheme using measured above-water radiometry. Figure 6.6 shows some examples of the bottom reflectance retrieved through the three approaches applied at different locations. Using the first approach, the bottom reflectance showed the largest variability compared to the expected behavior. Such variability was manifested in the high values obtained towards the blue and red end of the visible spectra, in some extremes cases even showing an exponential behavior in this spectral region (e.g., ARCH-12 in Figure 6.6). Using modeled  $R_{\infty}(0^-)$

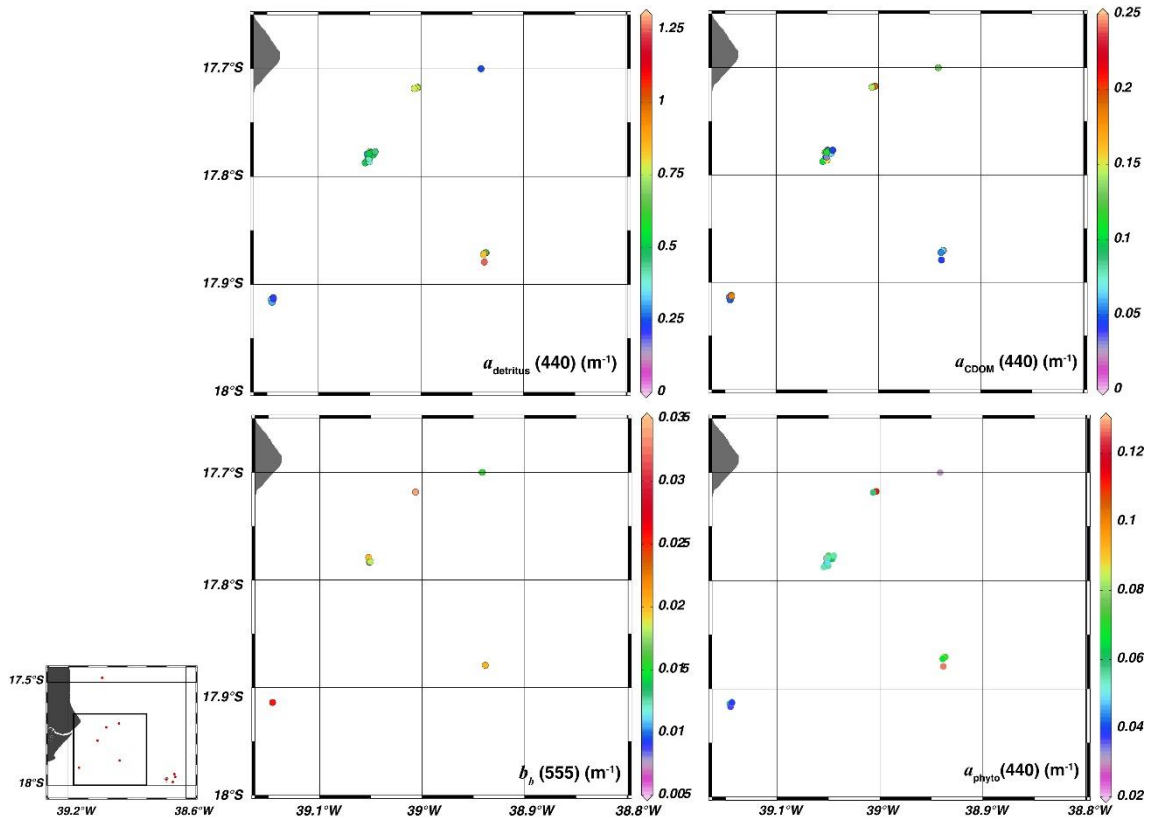


Figure 6.4 – Absorption coefficients measured in the field at all stations and sites in PL and PA reefs:  $a_{detritus}(440)$  (upper left);  $a_{CDOM}(440)$  (upper right);  $a_{phyto}(440)$  (lower right);  $b_b(555)$  (lower left), measured at the stations in PL and PA reefs. At the side of each figure, a colorimetric scale represents either absorption or backscattering values in  $m^{-1}$ .

the results were improved at some sites (e.g., ARCH-10), but the bottom reflectance still showed anomalies towards the blue bands, either as increases or as negative values. Clearly, high increases towards the blue bands are due to an artifact of the model application.

The only difference between these approaches was in the  $R_{\infty}(0^-)$  used. Measured deep water reflectance was generally higher than the modeled and the main differences were observed especially for bands shorter than 500 nm (Figure 6.7). Two main reasons can explain this discrepancy. The first is that the assumption of no bottom contribution to the surface reflectance could be invalid in some situations depending on the OAC concentration, and particularly for the blue and beginning of the green spectral regions,

where light penetration is expected to be higher compared with longer wavelengths. The depths of the points used as “optically deep waters” varied between 7 to 22 m. On the other hand, for the examples cited in Figure 6.6, the maximum  $z_{90}$  values expected for these points were 8.54 and 10.35 m, which are much shallower than the bottom depths of these points (15 and 20 m, respectively). The second source of variability between measured and modeled  $R_{\infty}(0^-)$  could be caused by some overestimation in the above-water radiance measured by the ASD Fieldspec, as reported by RUDORFF et al. (2014). Despite of this, although the modeled  $R_{\infty}(0^-)$  was lower than measured, this reduction was still not enough to lead some of the bottom reflectance spectra to the correct shape, in which case remaining an increase in the blue or, on the contrary, the modeled

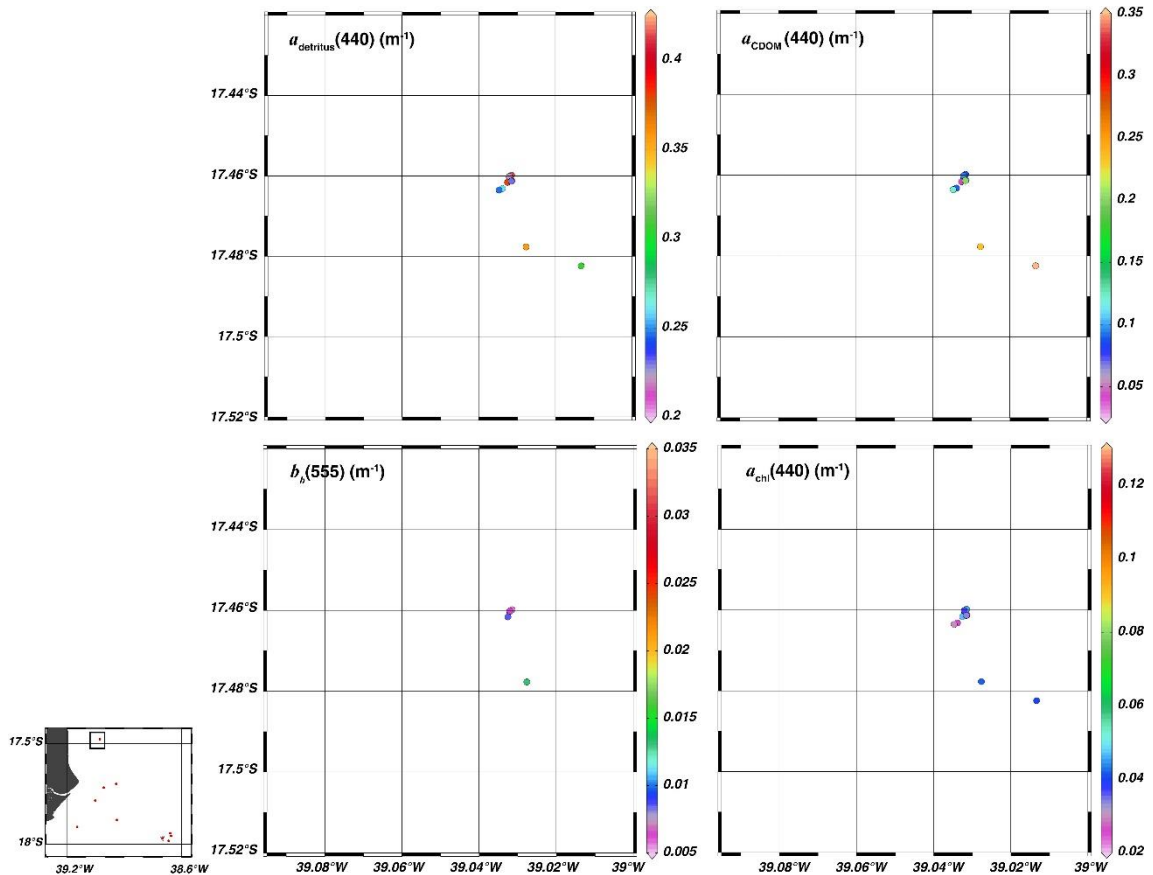


Figure 6.5 – Absorption coefficients measured in the field at all stations and sites in the TIM reef:  $\alpha_{detritus}(440)$  (upper left);  $\alpha_{CDOM}(440)$  (upper right);  $\alpha_{phyto}(440)$  (lower right);  $b_{bp}(555)$  (lower left), measured at the stations in the TIM reef. At the side of each figure, a colorimetric scale represents either absorption or backscattering values in  $m^{-1}$ .

$R_{\infty}(0^-)$  was sometimes so low that the algorithm retrieved negative values. Hence the second approach was also not satisfactory to obtain accurate bottom reflectance.

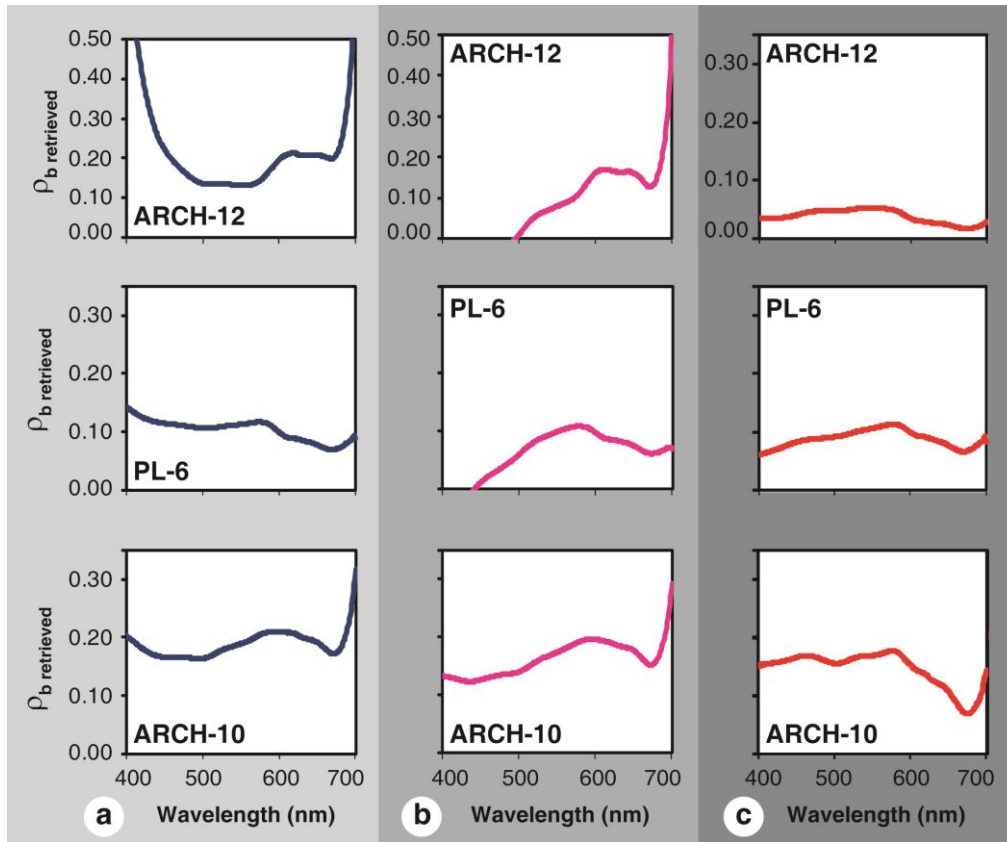


Figure 6.6 – Retrieved bottom reflectance (adimensional) as a function of wavelength (nm), Applying the three approaches. (a): using  $a$  and  $b_b$  coefficients measured *in situ* and  $R_{\infty}(0)$  measured in waters with similar OAC concentration; (b): using  $a$  and  $b_b$  coefficients measured *in situ* and modeled  $R_{\infty}(0)$  (pink); (c): using modeled  $a$  and  $b_b$  coefficients and  $R_{\infty}(0)$  (red). The graphs correspond to different stations: ARCH-12, PL-6 and ARCH-10.

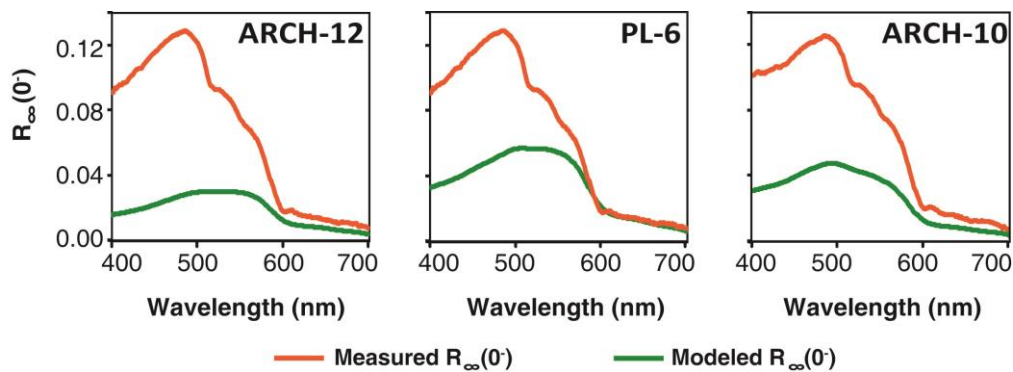


Figure 6.7 –  $R_{\infty}(0)$  modeled using  $a$  and  $b_b$  coefficients measured *in situ* (green), and  $R_{\infty}(0)$  measured in waters with similar OAC concentration (orange), as a function of wavelength (nm). The graphs correspond to different stations: ARCH-12, PL-6 and ARCH-10.

Among the three approaches, and contrary to the expected, the last one, which did not use measured coefficients as input to obtain  $\rho_b$ , showed the best performance. On the one hand, there are always some uncertainties associated with the *in situ* measurements, especially of  $a$  and  $b_b$ . Hence, this can be a source of error responsible, at least in part, for the anomalous behavior of the bottom reflectance. In an endeavor to evaluate if errors in the estimates could be caused by these anomalies, some tests were performed considering an overestimation of 20% simultaneously in all measurements ( $z$ ,  $a_{phyto}$ ,  $a_{CDOM}$ ,  $a_d$ ,  $b_{bp}$ ) and re-estimating  $R_\infty(0^-)$  using the new values to apply the second approach. Even in this situation, the retrievals showed anomalous behavior towards the red and blue spectral ends, in waters with high CDOM concentration. It is thus suggested that other sources of error still remain besides the uncertainties in the bio-optics measurements. As mentioned before, the Fieldspec measurements tend to overestimate the water-leaving radiance. When using the diffuse attenuation measured in the field, even if its estimation was perfectly accurate, the algorithm will still not adjust well because of the overestimation in the surface reflectance, causing biases in the retrieved bottom reflectance. The inversion/optimization scheme retrieves values for both the coefficients and bathymetry, seeking to minimize the overall error between measured and modeled values. Although the constituents and bathymetry obtained by the inversion model are also subjected to uncertainties, these errors tend to be compensated with those in the reflectance measurements made using Fieldspec and retrieving a reasonable bottom reflectance. Even though the combination of both inversion and forward forms of the algorithms seem to work well to retrieve the bottom reflectance, the inversion way can only be applied to hyperspectral data, and the radiometric information needs to be available up to 850 nm, at least.

While the shape of the retrieved bottom reflectance spectra varied considerably within the three approaches, for the ARCH-10 and PL-6 sites, their magnitude were similar. On the other hand, for ARCH-12 sites the magnitude of the reflectance spectra was much higher for the first two approaches (Figure 6.6). Note that in these cases the “y” axis reaches up to 0.50, and only to 0.35 for the third approach. Considering the mean value of each spectrum as an indicator of amplitude variations, the third approach showed a range of variability of 600 % between the highest (PA2-2, magnitude = 0.0377) and lowest (ARCH-12, magnitude = 0.226) spectra (Figure 6.8).

In the spectral region between approximately 500 to 600 nm, the retrieved bottom reflectance seemed to be less affected by either one of the water column correction approaches. This spectral region is where the bottom has its highest contribution to the surface reflectance, and at the same time it has the lowest differences in the parameters used as input for the approaches. On the contrary, the retrievals at the blue and red spectral regions seemed more variable according to the inputs used in the models. Comparing the two first approaches, the main differences in the retrievals were found for the blue wavelengths, due to the higher differences between the modeled and measured  $R_{\infty}(0^-)$  in this spectral region. Among the second and third approaches, the differences in the retrieved bottom reflectance at the blue region were caused basically by differences in  $a_d + a_{CDOM}$  and  $a_{phyto}$ . On the other hand, at the red spectral region where major attenuation occurs, caused predominantly by water molecules, some differences in the absorption or backscattering due to other constituents have small impact in the total attenuation. At this region, the differences in the bottom reflectance retrievals were caused mainly by differences in the depth determinations, due to the high light attenuation. Hence, even a little variance in depth can largely alter the optical path impacting the retrieved bottom reflectance in the red spectral region.

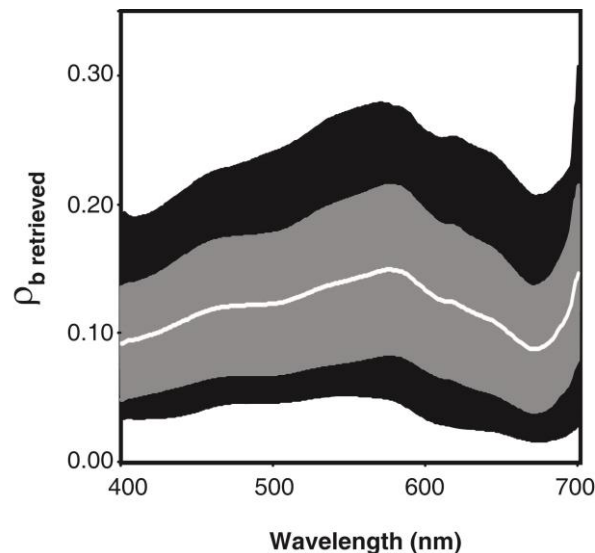


Figure 6.8 – Retrieved bottom reflectance (adimensional) as a function of wavelength (nm) using the third approach with the parameters retrieved using Lee et al.' inversion scheme (1999): average value between all sites (white line); mean  $\pm$  standard deviation (gray area); maximum-minimum of the retrieved bottom reflectance at all sites (black area) (N=20).

### 6.3.3. Benthic community composition

The analyzed benthic communities were, in general, dominated by algae, being algal turfs the predominant type present in 80% of the sites with more than 15% of coverage (Figure 6.9). Brown and green algae were also abundant, reaching maximum percentages of coverage of 65.8 and 33.7 %, respectively. Although live coral was also abundant, their coverage did not exceed 41 % at any site and at only 40 % of the sites more than 15 % of coverage by some type of coral was registered. *Millepora* sp. and *Mussismilia* sp. were the most representative coral genera. The less abundant classes were Seagrass (present only at one site), Sponge and Zoanthid, both with coverage between 1 to 27 %. Bleached coral was the less abundant class, with a bare coverage of 1.1 % maximum. TIM-7 was the only site where it was possible to identify cyanobacteria in the photographs, with 6.7 % coverage.

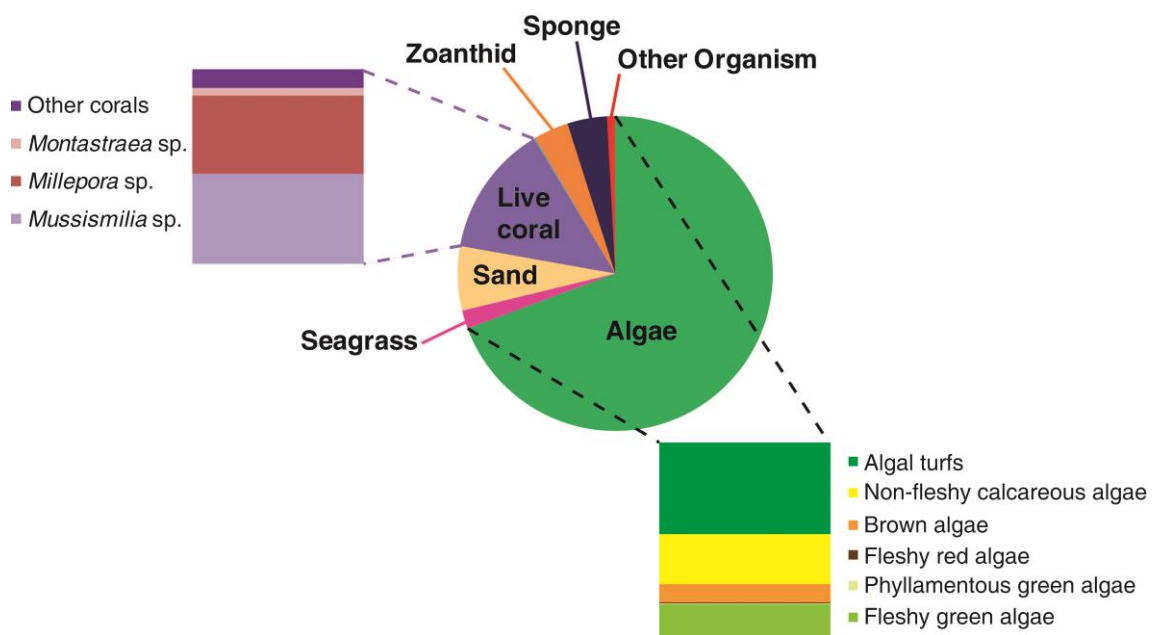


Figure 6.9 – Relative composition of benthic communities in the ACRB considering the average of abundance between all sites. In violet scale, the composition of live coral class is showed (left). In green scale, the proportions of each category to the algal class are represented (down).

All sites showed communities composed by different proportions of bottom types. In some cases, the differences among the sites were subtle, but none of them had exactly

the same benthic community as the other (Figure 6.10). All the points had more than 10 % coverage of one type of algae or turf, at least. Even when two sites showed similar dominance of algae e.g., PL-7 and PL-9, the proportions of the different algal types were not the same between them. Contrary to other studies in coral reefs, in this study no site was represented by a unique pure substrate, for example, of brown algae, green algae, live coral, etc. The *in situ* above-water remote sensing reflectance collected in a realistic framework for remote sensing applications, showed that the heterogeneity of the benthic community sampled within the IFOV of the sensor, implies in a great challenge to identify and separate each of the bottom types contained in each site. Since the depths were different for the distinct sites, the IFOV varied between 1.2 to 9.9 m<sup>2</sup>, and therefore, the area of the benthic community considered in each spectrum was also different. Figure 6.11 shows the underwater pictures taken at different sites and illustrate the variability between sites and the complexity in each of them. One can clearly observe the differences between the community compositions of the different sites.

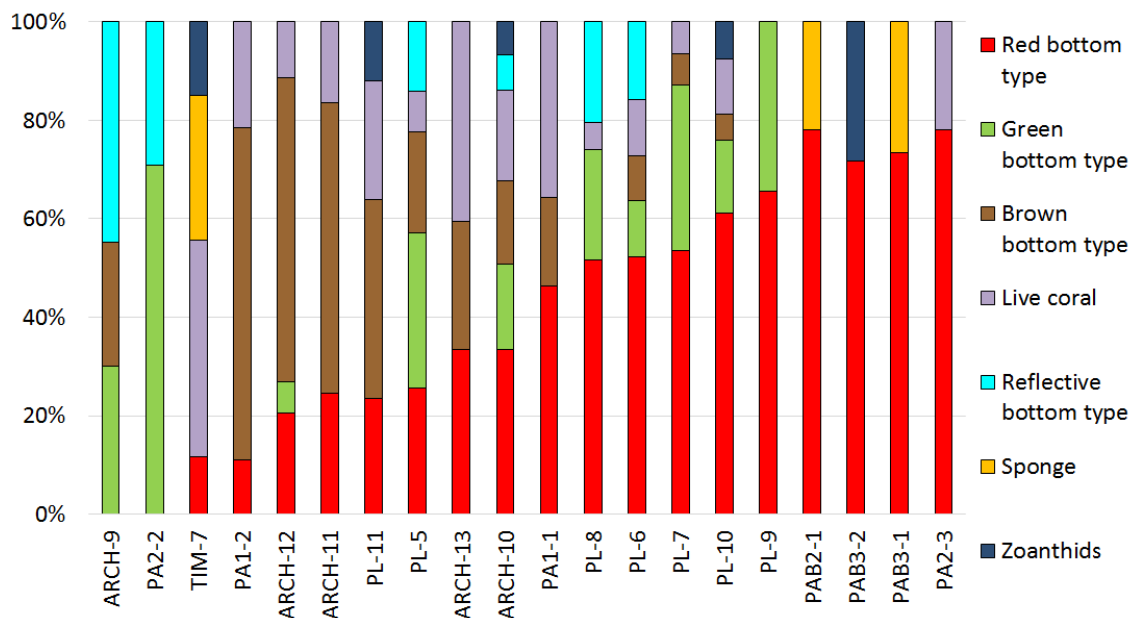


Figure 6.10 – Relative percentage of coverage of each category to the benthic communities for the 20 sites analyzed in the ACRB.

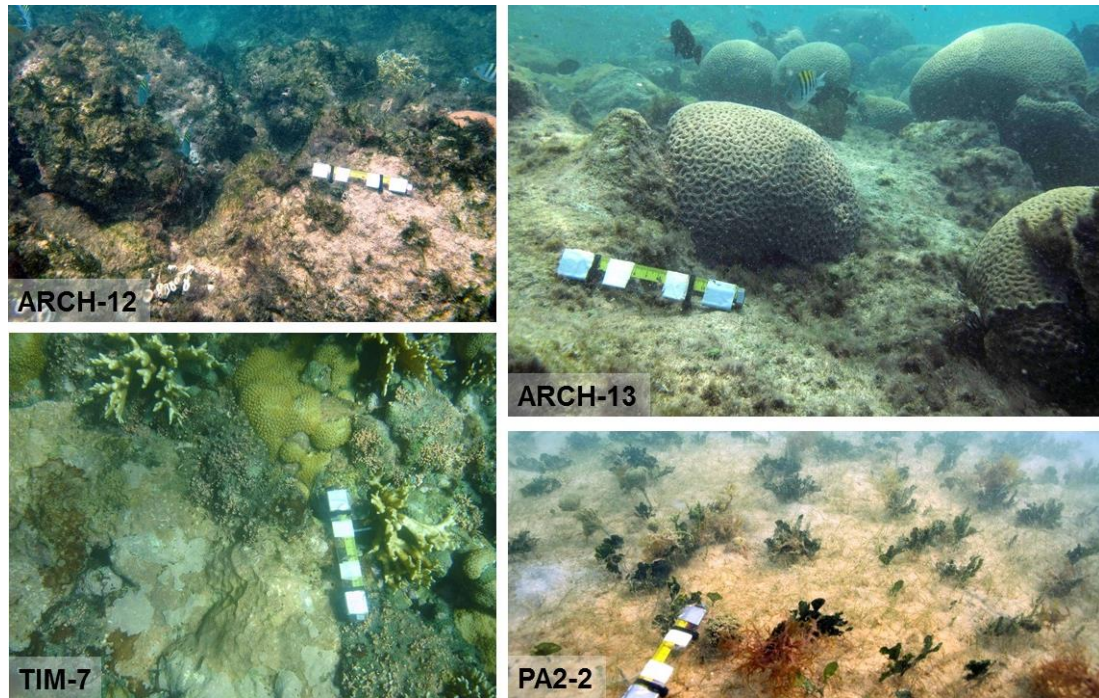


Figure 6.11 – Photographs of the benthic community taken at four sites within the ACRB during the field campaign of 2013/March at the same time that above-water radiometric measurements were done. ARCH-12 (Upper left); ARCH-13 (Upper right); TIM-7 (Lower left) and PA2-2 (Lower right).

Other coral reefs worldwide have shown larger patches of pure benthic classes than for the ACRB, and their richness and diversity were also reported to be higher. Several forms of coral that are frequently found in other regions (e.g., SW Pacific, SCOPELETIS et al., 2010) were completely absent or scarce in the ACRB, such as soft and tabular corals. Furthermore, in the ACRB the number of coral and algae species registered in the visited sites was lower compared to other reefs elsewhere.

#### 6.3.4. Analyzing the bottom reflectance in light of the benthic community

Hochberg et al. (2003) measured 13,100 bottom reflectance spectra of several classes of pure bottom type (seagrass, different types of algae and coral, sand and mud) in the Atlantic, Indian and Pacific Oceans. They found that the bottom reflectance showed spectral features common to all of the bottom types, but exhibited variations in the magnitude. The relative shape of these substrates was rather biogeographically maintained, showing low values at the blue and green bands, caused by the absorption of photosynthetic and photoprotective pigments (BIDIGARE et al., 1990; DOVE et al.,

1995; SALIH et al., 2000). At the red spectral region, the reflectance curves presented higher values, explained by the lower absorption and/or the presence of active fluorescence (MAZEL, 1995). Chlorophyll-*a* absorption may be readily seen with a depression in the spectra near 675 nm, and high reflectance towards the near-infrared can be seen at 700 nm for algae types. With the exception for carbonate sand, all bottom types had a low reflectance averaged over the entire visible spectra, generally falling in the range 0–30 %, and all of them have either peaks or shoulders near 600 and 650 nm. In this work, the “real” measured bottom reflectance was not available to validate the estimates. It is worth noting though, that even if under-water measurements of bottom reflectance without interference of the water column had been available, some simulations would have been needed to obtain the expected reflectance at the community level. Moreover, the overall retrieved bottom reflectance obtained from the third approach of the water column correction showed spectral shapes consistent with the previous descriptions observed in other works (e.g., HOCHBERG et al., 2003) (see Figure 6.12). This is: the low values between 400 to 500 nm; a peak between 575 to 625 nm; a depression around 675 nm, well conserved at all sites, and an increase towards the end of the red region. ARCH-12 and ARCH-11 were the only sites that did not show an increase towards 700 nm. A plausible explanation for this is that the retrieved depths by the Lee et al.’s inversion algorithm were 0.2 and 1.15 m, respectively for both sites. This implies an underestimating of 95 % and 67 % because the real depths were of 0.2 and 1.15 m, respectively. That is to say, that the actual optical path for the longer wavelengths was high in both cases. When using the modeled depths as input for the forward model, the optical path was underestimated and then, the algorithm was not able to simulate the expected increase for the longer wavelengths. Both forms, however, either using modeled or measured depths as input, performed well in 90 % of the cases for the entire visible spectrum and in 100 % of the cases for wavelengths shorter than 600 nm. In most cases, environmental information such as depth and even the bio-optical properties, were not necessary to obtain  $\rho_{bottom}$ . This means that the inversion/optimization scheme of Lee et al.’s algorithm, followed by the forward way can be applied successfully to retrieve the bottom reflectance up to 600 nm, for sites shallower than 5 m, even in Case-2 waters.

Using reflectance curves published in Hochberg et al.'s work (2003) as reference, the spectra of all sites were inspected to identify the typical features of each pure bottom type. Two or three reflectance peaks were expected to be observed in the presence of any type of algae, between 600 to 650 nm. Some peaks could be identified in this spectral region at almost all sites (either in the zero-order and/or first-derivative spectra), but their positions were dislocated in respect to the reference spectra (Figures 6.12 and 6.13). Several simulations of bottom reflectance were performed in WASI software using reference spectra of bottom types obtained from Maritorena et al. (1994).

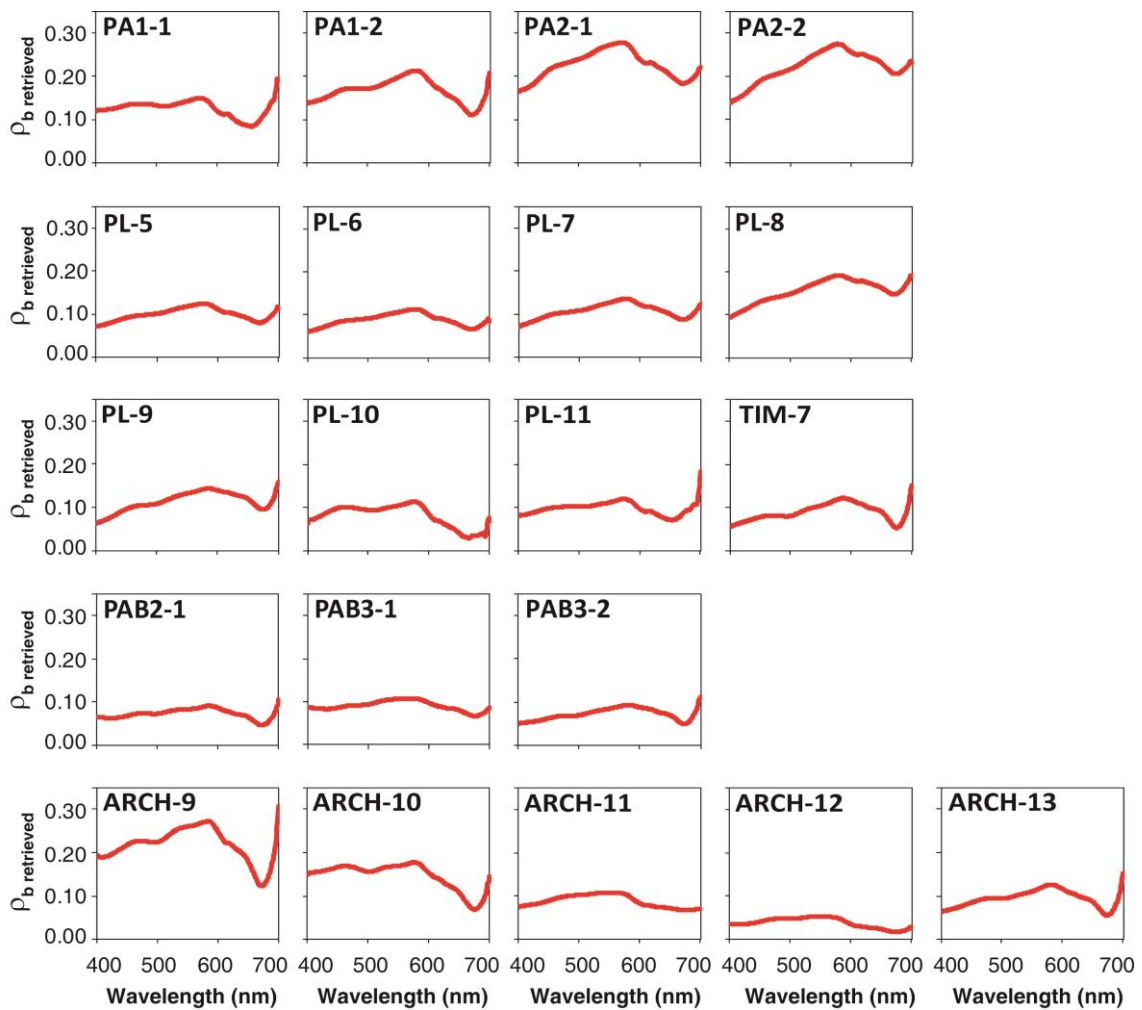


Figure 6.12 – Retrieved bottom reflectance (adimensional) as a function of wavelength (nm), using parameter values from the inversion scheme of Lee et al. (1999).

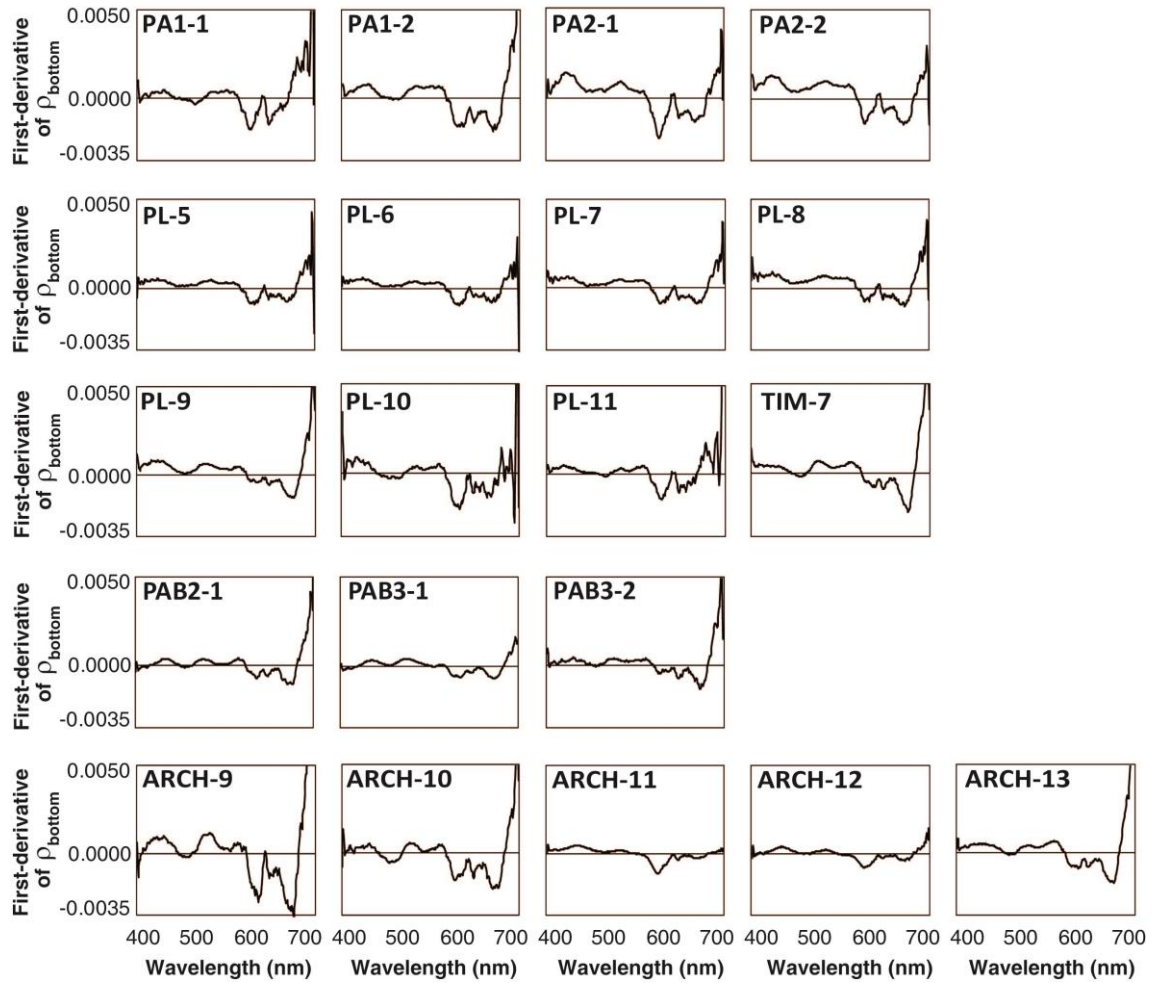


Figure 6.13 – First-derivative of the retrieved bottom reflectance (adimensional) as a function of wavelength (nm). Retrieved bottom reflectance was estimated using parameters values from the inversion scheme of Lee et al. (1999).

These simulations included two or three types of macroalgae, in different proportions: *Boodlea* sp. representative of green algae, an average of *Sargassum* sp. and *Turbinaria* sp. for brown algae and an average of *Porolithon onkodes* and a *Corallinacea* for red algae. In the bottom reflectance of these compositions it is possible to identify four main peaks that are maintained, but their position can change according to the percentage of each type (Figure 6.14). If other taxa were included (e.g., live coral, sponge), even more variability in the feature locations should be expected arising from the presence of other pigments. Hence, the displacements of the features found here do not contradict those found in the previous works. In the region between 600 to 630 nm, only phycocyanin has an absorbance peak. Around 640 nm, there is a region with low absorption considering the main pigments at the same time (Figure 6.15). The presence of a slight

reflectance peak in the bottom reflectance (more evident in the first-derivative) may be due to this lack of pigment absorption. On the other hand, the presence of absorption features near 600-630 nm may also suggest the presence of phycocyanin and/or chlorophyll-*b* in the sample. Additionally, phycocyanin shows a peak of fluorescence centered at 640 nm, which could contribute to a slight increase in the reflectance in this region.

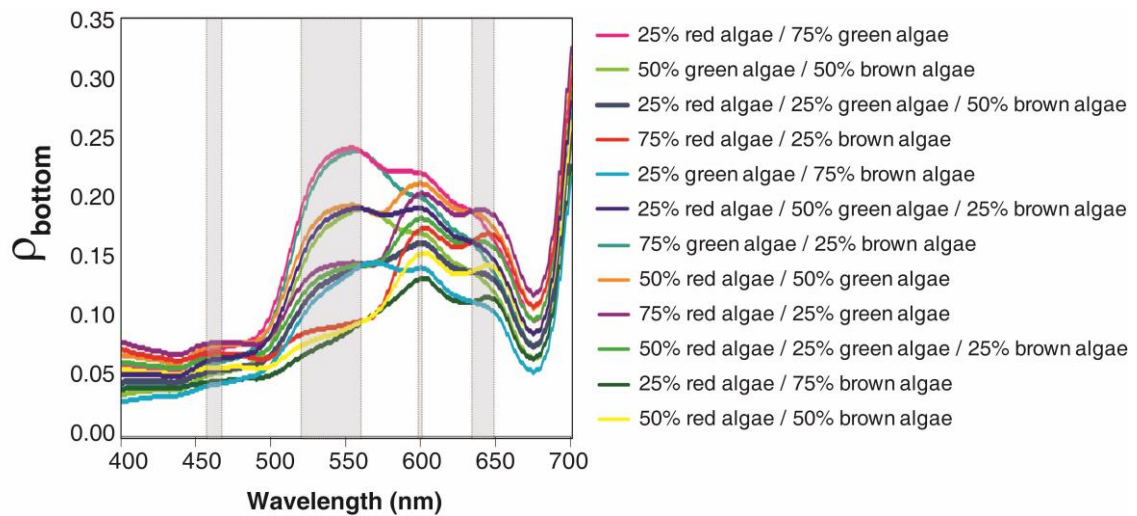


Figure 6.14 – Bottom reflectance simulated in WASI for combinations of different proportions of red, green and brown algae, from reflectance curves in Maritorena et al. (1994).

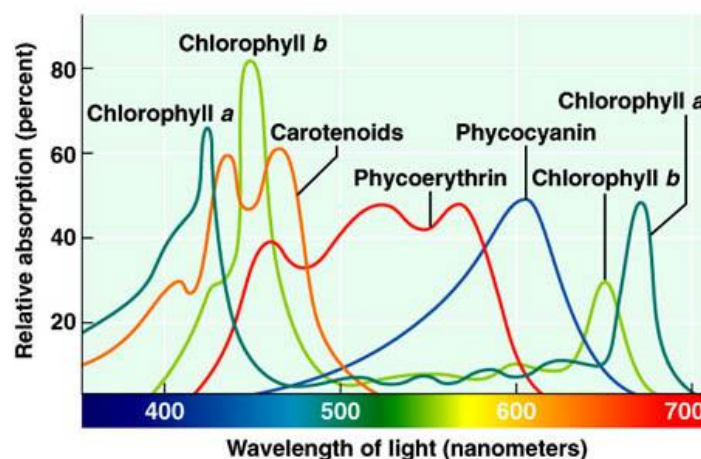


Figure 6.15 – Spectra absorption (in %) of the main pigments encountered in benthic communities versus wavelength (in nm).

Source: <http://www.citruscollege.edu/lc/archive/biology/Pages/Chapter06-Rabito.aspx>

Some spectra showed a slight increase at the first blue wavelength (before 420 nm) (e.g., sites ARCH-9, PAB2-1, PAB3-1). This behavior was also previously observed for several pure bottom types (e.g., algal turf, calcareous algae, brown and green algae), whose reflectance spectra were measured underwater, close to the targets (HOCHBERG et al., 2003). In a reflectance curve simulated based on the presence of five zooxanthellae pigments, this increment can also be expected (HOCHBERG et al., 2003). An atypical behavior, not reported previously, was observed in the retrieved bottom reflectance curves, which consisted in a depressed shoulder centered at 600 nm. In some cases the mentioned feature was almost imperceptible in the zero-order spectra, but noticeable only in the first-derivative. Noteworthy that in the water column correction, instead of using as inputs the measured absorption coefficients from the *in situ* measurements, the modeled coefficients were used, which in turn, considered solely the effects of the spectral absorption of chlorophyll-*a*. Hence, the “anomalous” feature could actually correspond to some pigments present in the water column that were not corrected by the Lee et al.’s algorithm. However, when observing the absorption spectra measured *in situ*, this absorption feature was not present. Hence, this absorption peak had to be caused by pigments present in the benthic community. Some pigments such as phycocyanin and chlorophyll-*b* have a typical absorption peak around 600 nm, much higher in the first case, which can be responsible for this feature in the bottom reflectance spectrum. Chlorophyll-*b* is present in green algae, while phycocyanin is found in both cyanobacteria and red algae (SATO et al., 2001; SIMIS et al., 2005). All sites had some presence of either red or green algae substrates. But even when their percentage of coverage was low, it could be possible that the absorption around 600 nm could have been caused by cyanobacteria, even though not detected in the benthic community through the picture sampling. Cyanobacteria occur frequently in coral reefs associated to benthic communities, as microbialites, in symbiosis with sponge, as epiphytes of seagrass or algal turf, or as microbial mats (CHARPY et al., 2012).

Another absorption feature, detectable mostly in the zero-order spectra and in all of the first-derivative, was located between 450 to 500 nm. In the paper of Hochberg et al. (2003) it is possible to identify a slight absorption peak centered at 500 nm, mainly associated to calcareous and turf algae. In this work, the intensity of this feature had no relation with the red substrate abundance. Nonetheless, carotenoids, chlorophyll-*b* and

phycoerythrin are pigments with high absorption in this region. As mentioned before, green algae synthesize chlorophyll-*b*. Phycoerythrin is commonly found in red algae (HEDLEY; MUMBY, 2002). In return, carotenoids are widely included in several substrates: green, brown and red algae, zooxanthella, coral tissues, sponges (FOX; WILKIE, 1970; ZAGALSKY; HERRING, 1977; CZECZUGA, 1983; HEDLEY; MUMBY, 2002). The presence of these types of substrates in the analyzed benthic communities would explain the referred absorption peak.

Most of the spectra also showed a small positive peak between 684 and 687 nm, but only in the first-derivative. This feature was observed as a narrow band and could correspond to fluorescence by chl-*a*, present in all vegetal cells and which were present in all sites either in forms of algae, seagrass, turf or in the zooxanthells associated to corals (HARDY et al., 1992).

In general, the bottom reflectance spectra obtained over the benthic communities of the Abrolhos Bank were consistent with the expected for the categories that composed each of the sites, based on previous measurements of the individual classes (e.g., MARITORENA et al., 1994; HOCHBERG; ATKINSON, 2000; HOCHBERG et al., 2003). Some features maintained perfectly their position in the  $\rho_b$  spectra, as for example the depression at 675 nm. At this wavelength only Chl-*a*, which is a pigment common to most of the bottom types, shows a strong narrow absorption band. Other features, on the contrary, varied in their position and bandwidth. This shift can be explained by the overlapping absorption bands of other pigments between 400 to around 650 nm. Nevertheless, a question that is still to be responded is that, even though the bottom reflectance seemed to respond well to the biological composition of the seabed, revealed by the spectral features observed the in curves, is it really possible to differentiate subtle discrepancies in the community proportion of the benthic sites analyzed in the ACRB, based solely in the bottom reflectance spectra?

Analyzing the sites according to the similarities in the benthic community composition in a cluster analysis, the sites in the extreme groups showed the most different community compositions (Figure 6.16). In one side, sites PAB3-1 and PAB2-1 without red bottom type were together; and in the other extreme, ARCH-9 and PA2-2, which only had red bottom types and sponges were joined. Comparing the order of the

grouped sites, they responded to a gradient governed mainly by the percentage of coverage of red bottom type, and additionally, of brown substrate in a finer scale. Looking at the broad grouping (with two main groups), they were established according to the red bottom type abundance, in which all sites with less than 50 % abundance or no red substrate presence, formed the same group (G1). G1 was composed by 11 sites: PA2-2 ARCH-9, ARCH-10, PL5, ARCH-13, PA1-1, TIM-7, ARCH-11, ARCH-12, PA1-2 and PL11. Sites with higher red substrate abundance belonged to the second group (G2, 9 sites). Sites in G2 were: PL-7, PL-9, PL-6, PL-8 PL-10, PA2-3, PAB3-2, PAB3-1 and PAB2-1. Establishing a threshold criterion of 1 in the linkage distance, the G1 group can be refined in 3 sub-groups (G1-a,b,c). G1-a was composed by two sites without red substrate (PA2-2 and ARCH-9); G1-b was formed by five sites with low coverage of red bottom type and low or no coverage of brown substrate, and with communities quite equivalent in their bottom type composition (ARCH-10, PL-5, ARCH-13, PA1-1 and TIM-7); G1-c included four sites dominated by brown cover type (ARCH-11, ARCH-12, PA1-2 and PL-11).

Two main groups were also formed either by the bottom reflectance or SAM matrix, however with some differences among the groups according to type of input data. Comparing the dendrograms of both benthic communities and SAM matrix, the separability of the sites was higher when considering the biological information, rather than only the spectral shape of  $\rho_b$ , as can be seen in the linkage distance scale (Figures 6.16 to 6.18). The  $\rho_b$  magnitude also added information for the discrimination of the groups, evidenced in the linkage distance axis. However, the groups formed by benthic composition and radiometric information were not the same. This is to say that spectral information does not respond exclusively to the bottom composition, in which case, environmental information still remains in the retrievals of bottom reflectance, or, these targets are not spectrally differentiable. Only some sites were grouped together both by their magnitude and spectral shape and by their benthic community composition. They were ARCH-9, ARCH-10, PA1-1 and PA2-2 on one side, and PL-6, PL-7, PL-9 and PAB3-2 by the other side.

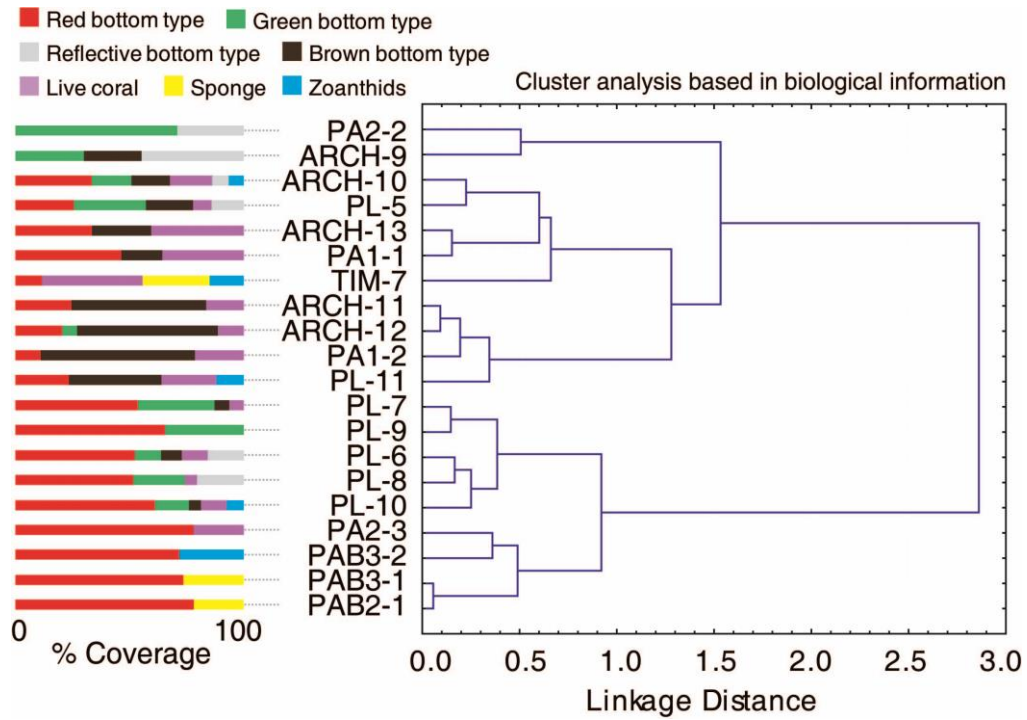


Figure 6.16 – Cluster analysis for the coverage of benthic communities (right). At the side of the graph, colored bars represent the percentage of coverage of each benthic category (left).

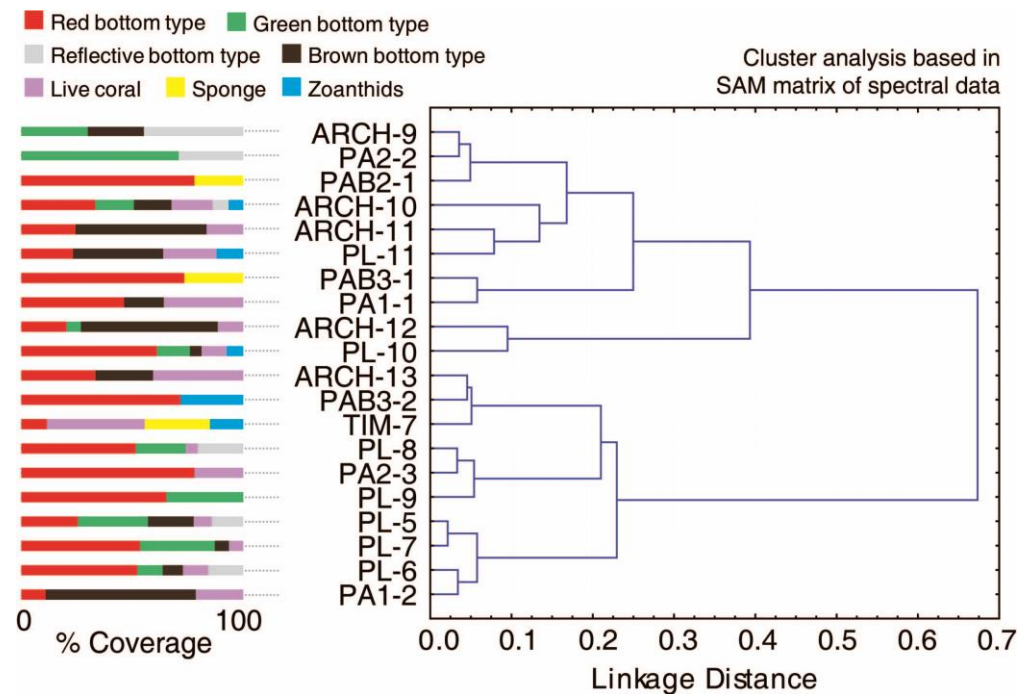


Figure 6.17 – Cluster analysis for the SAM matrix applied to bottom reflectance spectra (right). At the side of the graph, colored bars represent the percentage of coverage of benthic categories at each site (left).

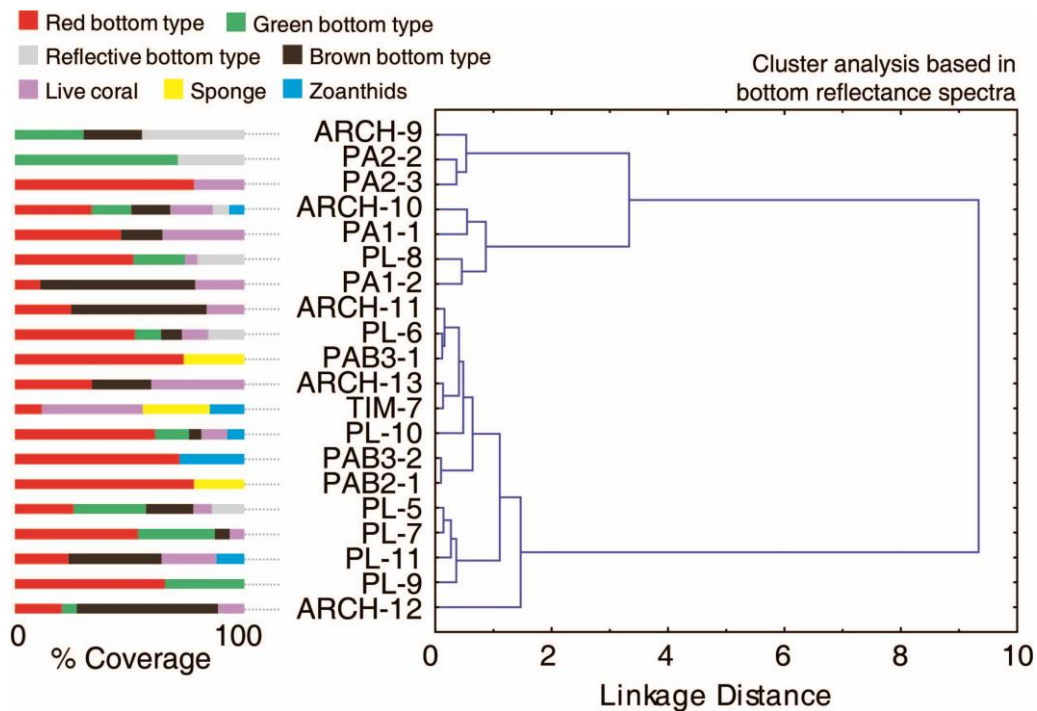


Figure 6.18 – Cluster analysis for bottom reflectance in all visible region (right). At the side of the graph, colored bars represent the percentage of coverage of benthic categories in each site (left).

Nevertheless, observing the benthic composition among these groups, they presented large differences and no point in common in some cases. Note, for example, the benthic communities in PA2-2 (covered by a high reflective bottom type and green bottom type) and PA1-1 (covered by live coral, brown and red substrate types). These bottom types that were grouped together are ecologically different, but were confused with their reflectance spectra.

To identify the bands that were effective to separate the groups in the cluster analysis, data mining was applied to normalized  $\rho_b$  spectra. Because of the number of samples and groups used in the data mining approach, it pointed out the identification of diagnostic bands used to discriminate between high (more than 50 %) and low abundance of red bottom type. The decision tree constructed from the C4.5 algorithm had a size of 5, with 3 leaves (Figure 6.19). It was based on bands centered at 594 and 515 nm. Sites with high percentage of abundance of red substrate type were characterized by high reflectance at these two bands. However, this is contrary to the expected, because the absorption of Chl-*a* and phycoerythrin is high in the range

between 515 and 594 nm. The percentage of correctly classified groups was just 50 % and the confusion was high (Table 6.1). This means that the classification based on both spectral bands worked as a random classifier and had no physical meaning. An important thing was that the number of sites considered was low, only 20. A greater quantity of sites is needed for a robust identification of diagnostic bands or spectral regions. The present analyses, however, revealed that this failed attempt suggests that there are no typical spectral features so strong to be common to the same group allowing a satisfactory spectral classification of the bottom coverage, despite of the small sampling size. Uhl et al. (2003) corroborate with this result when they state that “spectral signatures of algal groups were so close to each other that a correct assignment was unreliable and, moreover, spectral unmixing was unfeasible”.

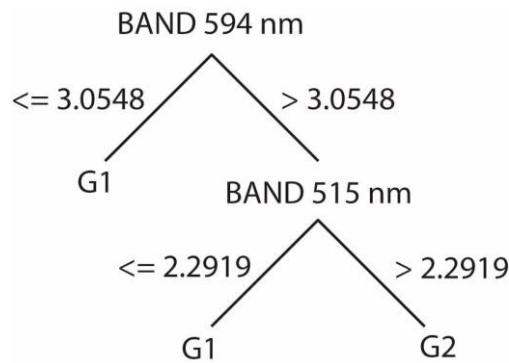


Figure 6.19 – Decision tree obtained from data mining processing for normalized bands between 450 and 650 nm and different band ratios (left). G1 corresponded to group 1 identified in the cluster analysis of the benthic communities and was characterized by low coverage of red substrate type. G2 was the second group with more than 50 % of red substrate type.

Table 6.1 – Confusion matrix for the cross-validation after the decision tree creation.

		Assigned group		
		G1	G2	
Real group	G1	1	6	7
	G2	2	7	9
		3	13	16

It should be taken into account that some features are shared by different bottom types. In the Hocheberg et al.'s work, they used 61 to 1,377 reflectance spectra worldwide spread to estimate mean values for the identification of typical and conserved features. However, some spectral variability may still be observed among measured reflectance spectra for the same bottom type. Fyfe (2003) identified intraspecific differences in the reflectance pattern of seagrasses among years, seasons and habitats. Even when the presence of pigments is evolutionally conserved, their synthesis and the concentration within individuals can vary not only between species, but also intraspecifically or temporally within the same individual. The production of pigments depends on the reproductive and maturative stages, genetic variation, health of the individual, diurnal cycle, season of the year, nutritional state, stressful conditions, and environmental conditions, such as light intensity (HEDLEY; MUMBY, 2002; UHL et al., 2013).

Additionally to pigment concentration, structural factors can also affect the reflectance spectra. In seagrass, for example, the arrangement and abundance of the leaf internal air channels called lacunae vary considerably among species and are likely to have an important influence on the reflectivity of the leaves (FYFE, 2003). In algae species the morphology, thickness of the stalk and cellular structure affect the relationship between pigment densities and the absorption spectra (RAMUS, 1978; VOGELMANN; BJÖRN, 1986; HANNACH, 1989). Also, in algae light absorption in the visible region is not only caused by photosynthetic pigments, but also includes absorption by non-photosynthetic tissues (e.g., proteins, nucleic acids) (CLAYTON, 1971). Non-pigmented absorption may exceed that of photosynthetic pigments in the blue wavelengths, whereas most of the absorbed red light may be channeled to photosynthesis (ENRIQUEZ et al., 1994).

Considering all this variability in the reflectance of benthic targets, it is not surprising to perceive that the quantity and position of diagnostic bands vary so much among the different works, even though when the aim was the separability of pure classes. The possible factors responsible for this range of variability may be pointed out as: the sensor used, sensor position (*in situ*, on-board an aircraft or orbital platform), spatial resolution of the sampled sites, bottom type categories considered or the geographic study area. Just to illustrate, some of the spectral  $\rho_b$  bands previously appointed in other works are:

- Bands within the respective intervals of 500 – 530, 450 – 550 and 680 – 740 nm, used for the discrimination between corals and macroalgae (MYERS et al., 1999).
- Bands centered at 506 – 566, 582 – 686 and 654 – 674 nm used to discriminate between sand, algae, bleached and healthy coral (HOLDEN; LEDREW, 1999)
- In the first-derivative spectra, a band centered at 596 nm to discriminate between live, recently dead and old dead categories. At 550 nm to separate between live and dead coral. A gradient between ~ 515 – 572 nm to discriminate between live and dead coral (CLARK et al., 2000).
- Spectral reflectance with 16 or 13 wavelengths either using orbital or *in situ* data, for the separability of coral, sand and algae (the position of all these bands were not mentioned) (HOCHBERG; ATKINSON, 2000)
- Bands centered at 522 – 574 and 637 – 700 nm for the separation between seagrasses species (FYFE, 2003)
- Bands positioned at 406, 430, 454, 467, 480, 499, 507, 529, 540, 577, 602, 608, 643 and 684 nm for the classification of brown fleshy algae, green fleshy algae, red fleshy algae, calcareous non-fleshy algae, turf non-fleshy algae, bleached hermatypic coral, blue hermatypic coral, brown hermatypic coral, soft/gorgonian coral, seagrass, terrigenous mud and carbonate sand (HOCHBERG et al., 2003)
- Bands common to both and CASI reflectance: 406, 450, 535, 539, 554, 580, 584, 592, 614, 630, 645, 665 and 682 nm for the discrimination between macroalgae species (ANDRÉFOUËT et al., 2004).
- The first-derivative of the 558 nm band to separate between stages of coral colonies (MUMBY et al., 2004).
- Narrow bands centered at 555, 650, 675 and 700 nm to use the Leaf Area Index for the discrimination between seagrass (YANG et al., 2010).

The Band Depth (BD) was the last analysis applied in the present work to associate the spectral data with the bottom types containing chl-*a*. The BD between the maximum peak around 600 nm and the minimum at 675 nm is usually used as proxy of chl-*a* concentration in studies by remote sensing. Insofar chl-*a* concentration increases, the spectral degree between 600 and 675 nm also increases, and thus, the band depth is directly proportional to chl-*a* content. Here, on the other hand, band depth was inversely correlated with the percentage of coverage of Red+Brown+Green substrate types (Table 6.2). The absorption peak centered at 675 nm was a feature conserved at all spectra, caused by the chl-*a* content present in all communities. Contrary to the other portions of the visible spectra, at this wavelength there was no overlapping absorption caused by other pigments. On the other hand, at 585 nm there is an overlap of absorption by phycoerythrin and phycocyanin. The presence of phycoerythrin in red substrates could thus mask the difference between reflectance at the BD wavelengths, i.e., 600 and 675 nm. Cyanobacteria also could occur in some bottom types, in which case phycocyanin would be present. Controlled experiments in laboratory could corroborate this hypothesis of the co-occurrence of other pigments reducing the band depth. For this, reflectance spectra should be measured above different substrates taken from the seabed, in which a detailed identification of all the components would need to be performed. High-Performance Liquid Chromatography (HPLC) from bottom components should also be done to relate the reflectance with the presence and concentration of pigments in the different benthic communities and validate the possible presence of phycocyanin.

Table 6.2 – Pearson correlation index between band depth and different substrate type coverage: Green substrate type, Brown substrate type, Red substrate type, Green+Brown+Red substrate types, Green+Brown+Red substrate types + Live coral. Significant value is highlighted (N=20;  $p < 0.05$ ).

	Green substrate type	Brown substrate type	Red substrate type	Green + Brown + Red substrate types	Green + Brown + Red substrate types + Live coral
BD	-0.306	0.058	-0.186	-0.503	-0.337

Without question, a larger set of sampling sites to be included in new campaigns over the Abrolhos bank, to complement this study, is strongly recommended.

Previous works using spectral measurements in coral reef bottom types have worked with spectra which were either collected underwater, close to the target, or measured in samples collected out of the water. In these cases, the water column effect was not included in the measurements or minimized and, in general, they did not deal with much spectral complexity, because samples were pure with only one species or, a maximum of two species simultaneously. In this work, measurements were done above the benthic substrates in a more realistic framework, including benthic and environmental complexities, due to the water column effect that had to be corrected and the seabed heterogeneity. Within the Case-2 waters of the ACRB, the studied submerged benthic communities were not separable by hyperspectral  $\rho_b$  information. This does not mean that there are no complex communities able to be separated by bottom reflectance spectral data. But it does represent a counterexample showing that if a study is based solely in radiometric data, errors in the association with the biological community can occur. In some situations, alterations in the benthic coverage may not be captured exclusively by remote sensing. Hence, habitat changing indicators based exclusively in remote sensing data should not be considered as real alterations without field validations. Effective monitoring programs should necessarily include both complementary approaches: remote sensing and field campaigns. Even with some limitations and a limited quantity of sampled sites, this chapter depicts a real situation, within the best conditions as possible, without atmospheric interferences. Bottom reflectance is potentially useful for the discrimination of pure bottom types in shallow areas. Nonetheless, in more complex submersed communities, where several types of bottom with similar spectral behavior coexist, spectral information seems insufficient for subtle discriminations.

In addition to spectral data, remote sensing can provide other types of information. For example, active remote sensing such as LIDAR seems promissory for ecological studies. Benthic mapping by LIDAR instruments on board airplanes can be produced in very high resolution (e.g., 6 cm grid). This refined data can be used to reproduce the structural complexity of the reef, which can be used together with spectral information for change detection and diversity studies in coral reef habitats.



## **7 REMOTE SENSING DATA FOR CORAL REEF MAPPING IN THE ACRB**

### **7.1. Introduction**

Remote sensing represents an efficient and complementary tool for field studies. As for terrestrial areas, in reef ecosystems it provides data acquisition with the best cost-benefit relation, because it allows synoptic monitoring in extensive areas, including places with difficult access (MUMBY et al., 1999). Besides of the wide spatial coverage, orbital data can also provide temporal information to evaluate changes and succession dynamics in coral reefs. According to Hamel and Andréfouët (2010), different approaches may be applied using remote sensing data for coral reef ecological studies. He considered a direct use to obtain information about the benthic coverage, habitat localization, diversity of patches and habitats, geomorphology of the seabed and reef structures, bathymetry and ocean circulation. The authors also considered the indirect use of remote sensing with auxiliary data obtained in the surroundings of these environments. This includes the utilization of meteorological-oceanographic data, for example: SST, significant wave height, sea surface height, turbidity, chlorophyll concentration, CDOM absorption, wind speed and direction, aerosol optical thickness, precipitation rates, incoming solar radiation and cloud coverage. Such indirect use may also include terrestrial information, such as land-use coverage maps, hydrographic basin structure and urban growth maps. Therefore, remotely obtained data is useful for an integrated ecosystem analysis in different scales of ecological analysis.

Mapping of reef habitats can provide important information for the management of these ecosystems, both to examine reef structure and resource inventory and also for the estimation of ecological functions and biodiversity (YAMANO, 2013). Remote sensing coral reef mapping started with the launch of the LANDSAT satellite series, since the 1970's (SMITH et al., 1975). Research developed using orbital and aerial information have continued following technological advances with new sensors and processing data methods (KUTSER et al., 2006).

In the evaluations of mapping performance, two factors are considered. First, the accuracy and second, the detail level in which maps are created, typically expressed as the number of thematic classes. High thematic resolution is frequently needed for realistic ecological studies about reef processes (SCOPÉLITIS et al., 2010). This is

because it is improbable that simple typologies allow representing adequately the complexity of the processes that are found in this type of environment. The level of detail of a map of substrate types does not depend only on the sensor and quality of an image (ANDREFOUET; WANTIEZ, 2010). But also it can depend on the characteristics of the reef, the availability of auxiliary environmental variables (that can only be obtained *in situ*), as well as the imagery processing techniques used, image interpretation, and even, the user expertise (ANDRÉFOÛET, 2008; WABNITZ et al., 2008). In coarse classifications, the typical classes that are usually considered are of pure bottom types, as for example, sand, coral, algae and deep water. In more detailed studies, mixtures of different substrate types should also be considered (BENFIELD et al., 2007, BERTELS et al., 2008, KNUDBY et al., 2010), but as it was seen in Chapter 6, some benthic communities can be spectrally confusable and this spectral ravel represents a limitation in the number of classes that can be effectively used.

Bertels et al. (2008) highlighted that comparisons of map accuracies, between different coral reefs, is not trivial in most cases. Foremost because reef structures in different geographic regions generally have different geomorphological and biological characteristics, leading to the identification of different benthic classes. These classes can have different spectral signatures resulting in different separability properties, which affect the classification accuracy. Hence, studies performed in different regions are not completely comparable due to the disparity between the mapped areas. However, several studies comparing the accuracy of coral reef maps in different regions have still been carried out (LIM et al., 2009). Reviewing literature, there is a general pattern that follows the sensor resolutions and processing methods for the different mapping results. As the sensor resolution increases and the processing methods are more sophisticated, more accurate and detailed the maps are expected to be.

Maps created using multispectral sensors with intermediate spatial resolution (10 to 30 m), as for example, the *Advanced Spaceborne Thermal Emission and Reflection Radiometer* (ASTER/TERRA), HRV/SPOT, TM/LANDSAT and *Enhanced Thematic Mapper Plus* (ETM+/LANDSAT), showed low-medium accuracy, varying from 30 to 75 %, depending on the number of classes (KNUDBY et al., 2007). In a coarse classification, accuracies frequently range between 60 to 74 % (GREEN et al., 2000,

CALL et al., 2003). When using more than 10 classes, accuracy was lower, around 30% (MUMBY; EDWARDS, 2002).

Two main reasons can explain these results. In first place, the confusion between classes. This topic was addressed in Chapter 6 using hyperspectral data. When multispectral information is considered, the situation can be even worse, since the positions of the spectral bands are not optimized for bottom type discrimination (HOCHBERG; ATKINSON, 2003; CALL et al., 2003). Also, multispectral sensors generally have relatively large pixel sizes considering the heterogeneity of these ecosystems. The interaction between the spatial resolution of the sensor and the size of benthic patches will control sub-pixel mixtures that will occur in the images. The level of spectral mixture affects even more the classification accuracy, depending on the benthic types involved (HEDLEY et al., 2004). Thus, intermediate spatial resolution sensors (10 - 30 m) are more appropriate to study reefs only with pure bottom types, although this situation is not the most frequent (MUMBY et al., 2004). However, orbital data of the LANDSAT satellite series is still a useful tool to evaluate coverage changes in coral reef substrates at a medium level through temporal studies, since they have the longest data base with records for more than 30 years (DUSTAN et al., 2001).

Currently, the availability of sensors with better spectra and spatial resolutions has improved mapping accuracy in these complex ecosystems. It has been recognized that high spatial and spectral resolution data can provide more detailed information about the reef (MUMBY et al., 1997). Very high spatial resolution sensors such as IKONOS or QuickBird, with nominal resolutions of 4 and 2.4 m, respectively, and other aircraft sensors with spatial resolution around 1 m (e.g., CASI), have been successfully applied for coral reef mapping in different regions worldwide spread (ANDRÉFOUËT et al., 2003; LOUCHARD et al., 2003). Higher spatial resolution allows the better discrimination of substrates (LOUCHARD et al., 2003), and supports a higher number of classes to map. These high spatial resolution sensors have allowed to map benthic substrates reaching accuracy between 80-88 %, when using 8 or 9 classes (KNUDBY et al., 2010). In 2009 the WorldView-2 (WV02) satellite was launched with better resolutions than its predecessor multispectral sensor Quickbird. WV02 orbital sensor has high spatial resolution (2 m) and better spectral resolution than other multispectral orbital sensors (8 multi-spectral bands) with similar spatial resolution. Despite its

potential for target discrimination, there are only a few works published using this sensor for coral reef mapping (COLLIN; PLANES, 2012).

The first works regarding the mapping of benthic substrates from satellite images, applied pixel-based automatic classification methods (MUMBY; EDWARDS, 2002, SCOPÉLITIS et al., 2010). Using multispectral images with high spatial resolution, Andréfouët et al. (2003) and Mishra et al. (2006) applied these classification techniques to map 3 to 15 thematic classes. Some other works also applied semi-supervised techniques or multi-steps classification schemes, which are more sophisticated techniques than a simple automatic classification. As examples, works of Bertels et al. (2008) and Bouvet et al. (2003) can be mentioned. In their work, image segmentation was initially performed. Subsequently, the segments were grouped based on spatial and spectral analyses or from decision rules defined by statistical parameters.

Recently, the *Object-Based Image Analysis* (OBIA) was used to process high spatial resolution images with reef environments. This technique increased mapping accuracy 80 to 90 % when using 4 to 10 classes (BENFIELD et al., 2007, SCOPÉLITIS et al., 2010). This application allows the integration of different data bases, enabling the extraction of more robust conclusions about changes in the extension, localization and spatial patterns of benthic resources along time (LUCIEER, 2008). Scopélitis et al. (2010) developed a classification scheme based on field expertise and knowledge using visual photointerpretation. This methodology allowed including 45 classes of the structure of the coral community, being the most detailed thematic map documented in literature regarding orbital remote sensing in coral reefs. The definition of these classes allowed distinguishing substrates according to the percentage of live coral and all the variety of morphologies of coral and substrate present in the area. In a comparison between different techniques used to produce bottom maps, those based on the expertise of the photointerpreter were the most accurate. This shows that substantial improvements in the thematic resolution can be obtained if efforts are invested in the familiarization with the study area and interpretation of patterns in the image with local knowledge.

In the ACRB, only one work has explored the use of remote sensing data to map submerged benthic substrates (MOREIRA, 2008). This work focused in the *Pedra de*

*Leste* (PL) reef, belonging to the coastal arc. ETM+/LANDSAT and synthetic QuickBird images were used. The ETM+/LANDSAT image provided a map with accuracies between 45 – 55 % considering four classes (Sand; Palythoa; Zoanthids; Deep reef); while six classes (Sand; Sand+Halimeda; Palythoa; Dictyota; Phyllamentous algae; Mixed) were used for QuickBird mapping with an accuracy varying between 40 and 73 %. In the surrounding of the Archipelago and over the *Parcel dos Abrolhos*, however, no mapping of the bottom substrate has yet been done. In this area, all reefs are submerged, and the *chapeirões* occur isolated to each other, without merged tops, differently from the coastal arc. The aim of the present chapter was to perform the first coral reef habitat mapping in the *Parcel dos Abrolhos*, belonging to the ACRB, Brazil, using data from the WorldView-2 orbital sensor. For this, the object-based image analysis (OBIA) was applied to the WV02 image collected on 2012/02/14 to produce a high resolution bottom type map.

## **7.2. Materials and Methods**

### **7.2.1. Pre-processing of the WV02 scene**

#### **7.2.1.1. Geometric correction**

Together with the WorldView-2 images, files containing coefficients called *Rational Polynomial Coefficients* (RPC) are delivered. These coefficients can be used in the absence of adequate control points collected *in situ* (Ground Control Point – GCP). The image was georeferenced using the numeric model Rational Function, available in PCI software, which uses RPC for the correction.

#### **7.2.1.2. Atmospheric correction**

In a following step, atmospheric correction was applied to the WV02 image. The purpose of this step in the pre-processing scheme of remote sensing imagery is the reduction or elimination of atmospheric effects. This step is important especially for aquatic environments considering the low signal reflected by water, which amplifies the sensor noise. The performance of the algorithms applied to obtain the bathymetry and bottom reflectance retrievals, depends on the accuracy of the values of reflectance used as input. Hence, a good atmospheric correction is essential to obtain accurate bottom type maps. The correction converts digital numbers (DN) to physical quantities, for example, to surface reflectance. The atmospheric correction was performed in PCI

Geomatica 2013 using the ATCOR2 package. The input for the model is the raw image with DN values, the software converts them to  $L_{TOA}$  and then, applies the atmospheric correction to obtain the output, which is surface reflectance ( $\rho_w$ ). For the conversion from DN to  $L_{TOA}$  (in  $W m^{-2} sr^{-1} \mu m^{-1}$ ), the software uses the absolute calibration factor ( $K_{BAND}$ , in  $W m^{-2} sr^{-1} count^{-1}$ ), and the effective bandwidth ( $\Delta\lambda_{BAND}$ , in  $\mu m$ ). Values of  $K_{BAND}$  and  $\Delta\lambda_{BAND}$  coefficients for each band are included in the IMD file delivered together with the image.

The ATCOR2 model assumes a Lambertian surface, is restricted to sensors with small swath angles and takes into account adjacency effects, which caused by backscattering of bright targets on neighboring pixels. The model works with atmospheric catalogues that contain radiative transfer functions through MODTRAN-2 and SENSAT-5 models, stored in Look-Up-Tables (RICHTER, 1996). ATCOR2 was used to correct the WV02 satellite imagery assuming a flat terrain, maritime aerosol type and tropical condition. Visibility and adjacency effects were set at 43 and 0.18 km, respectively. Visibility was obtained from the aerosol optical thickness at 547 nm ( $AOT_{547}$ ) of the MODIS-Aqua image obtained on the same day of the WV02 image (collected on 2012/02/14 at 10:06 local time). A window of 9x9 pixels was defined in the  $AOT_{547}$  image centered at the central coordinate of the WV02 image. The mean value of these pixels was estimated and converted to a visibility value using the model proposed by Vermote et al. (2002) (Equation 7.1, Figure 7.1). The performance of the atmospheric correction was evaluated by extracting samples in the deepest areas, where no bottom signal was expected to contribute to the surface reflectance.

$$Visibility (km) = 3.9449 / (AOT_{550} - 0.08498) \quad (7.1)$$

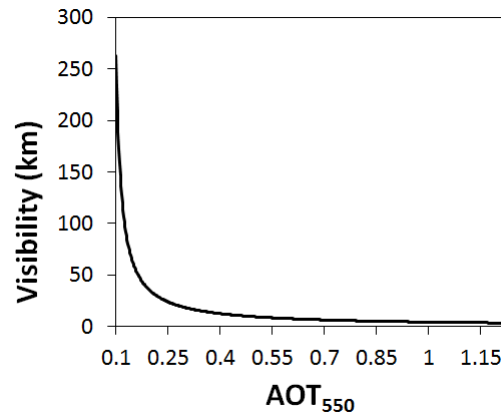


Figure 7.1 – Visibility (in km) as a function of Aerosol Optical Thickness (at 550 nm) according to Vermote et al.’s model (2002).

### 7.2.1.3 Sunlint correction

In remote sensing images with high spatial resolution (e.g., of IKONOS, Quickbird or Worldview2 sensors, with 4, 2.4 or 2 m, respectively) collected over water bodies, sunlint is observed as a rugosity effect in the surface. This effect causes confusion to detect submerged features and has to be adequately treated. The method proposed by Hedley et al. (2005) was adopted to perform sunlint correction in the WV02 scene. This method considers that water-leaving radiance in the Near Infrared (NIR) region is negligible and so any signal remaining after the atmospheric correction must be due to sunlint (KAY et al., 2009). The method assumes a linear relation between the signals of bands in the infrared and the visible regions, because the real index of refraction is nearly equal for NIR and visible bands (MOBLEY, 1994). For its application, some samples collected above areas displaying a range of sunlint effects and over homogeneous sub-surface spectral brightness are required and the regression of each visible band versus the NIR band has to be performed. Equation 7.2 formally describes such correction.

$$\rho'_{w,i}(0^+) = \rho_{w,i}(0^+) - slope_i(\rho_{w,NIR}(0^+) - MIN_{NIR}) \quad (7.2)$$

where the suffix  $i$  refers to the signal in the visible region,  $\rho'_{w,i}(0^+)$  is the above-water sunglint corrected reflectance in band  $i$ ,  $\rho_{w,i}(0^+)$  is the above-water reflectance in band  $i$ ,  $slope_i$  is the regression slope of band  $i$  against the NIR band,  $\rho_{w,NIR}(0^+)$  is the above-water reflectance in the NIR region, and  $MIN_{NIR}$  corresponds to the minimum value of the samples in the NIR band. Only bands at the visible region can be corrected by this method.

For both assumptions to be valid, two other postulations are necessarily presupposed: (i) the wavebands are perfectly aligned, (ii) signals in the visible and NIR bands are collected at the same time, and (iii) the spatial resolution of the visible and NIR bands are the same. Although the spectral bands of the WV02 sensor are not perfectly aligned in space and some delay exist between bands, a significant correlation between the visible and NIR bands in the sampled pixels over deep waters still remain. Figure 7.2 shows the scatter plots of the reflectance sampled over deep waters at the visible bands against the NIR bands. The WV02 sensor has two bars of detectors. In each of them, three visible and one NIR bands are disposed. Better adjustments were observed between the NIR and visible bands that are in the same bar of detectors. The equations used to perform sunglint correction in each band are listed in Table 7.1. The performance of sunglint correction was evaluated visually and according to the spectral behavior of the samples extracted at different locations of the scene and contaminated by sunglint distortion.

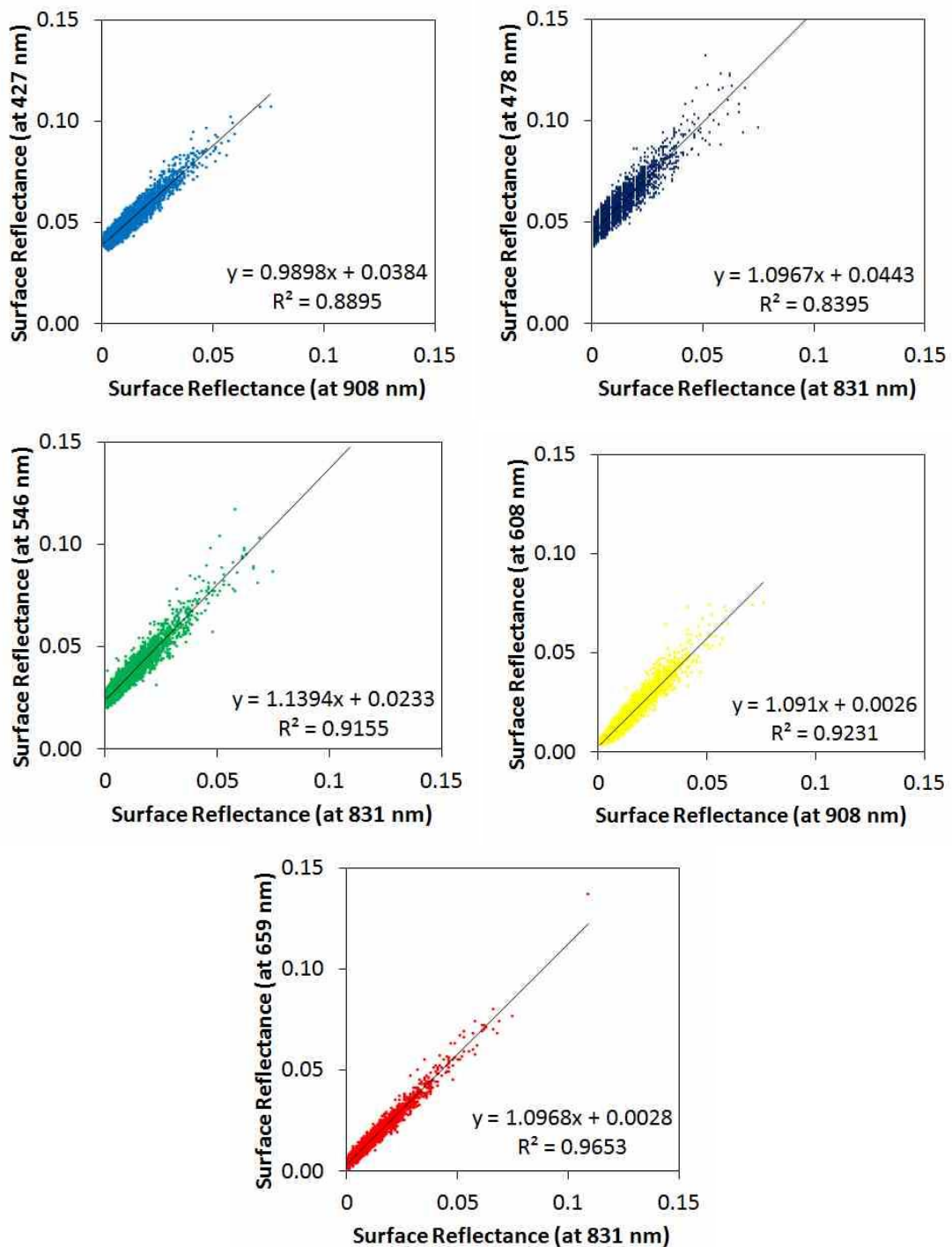


Figure 7.2 – Scatterplot of surface reflectance values at the visible bands against reflectance in the NIR region from samples extracted in deep waters. Each plot refers to one spectral band of the WV02 sensor: 427 nm (Upper left), 478 nm (Upper right), 546 nm (Middle left), 608 nm (Middle right), and 659 nm (Lower left).

Table 7.1 – Equations used to perform sunglint correction in each band, based in Hedley et al.’ model (2005).

Band centered at (nm)	Equation
427	$\rho'_{w,427}(0^+) = \rho_{w,427}(0^+) - 0.9898(\rho_{w,908}(0^+) - 0.001)$
478	$\rho'_{w,478}(0^+) = \rho_{w,478}(0^+) - 1.0967(\rho_{w,831}(0^+) - 0.0009)$
546	$\rho'_{w,546}(0^+) = \rho_{w,546}(0^+) - 1.1394(\rho_{w,831}(0^+) - 0.0009)$
608	$\rho'_{w,608}(0^+) = \rho_{w,608}(0^+) - 1.091(\rho_{w,908}(0^+) - 0.001)$
659	$\rho'_{w,659}(0^+) = \rho_{w,659}(0^+) - 1.0968(\rho_{w,831}(0^+) - 0.0009)$

#### 7.2.1.4. Water column correction

The Maritorena et al. (1994) algorithm was chosen to correct the water column effect in the WV02 image. Only the five bands shorter than 700 nm were corrected. The algorithm was applied following the same procedure as described in chapters 5 and 6 (using Equation 7.3). First, the above-water reflectance was used to determine  $R_{\infty}(0^-)$  and  $R(0^-)$ , using both surface reflectance in deep and shallow areas ( $\rho_{\infty}$  and  $\rho_w$ , respectively) (Equation 7.4).

$$\frac{R(0^-) - R_{\infty}(0^-)}{e^{-2K_d z}} + R_{\infty}(0^-) = \rho_{b \text{ retrieved}} \quad (7.3)$$

$$R_{\infty}(0^-) = \frac{\rho_{\infty}(0^+)}{0.5 + 1.5\rho_{\infty}(0^+)} \quad , \quad R(0^-) = \frac{\rho_w(0^+)}{0.5 + 1.5\rho_w(0^+)} \quad (7.4)$$

Besides  $R(0^-)$ , the algorithm also uses  $K_d$ ,  $z$  and  $R_{\infty}(0^-)$  as inputs. The  $K_d$  used for each band, was obtained from measured *in situ* data. Since this parameter was not available for each pixel on the image, the average value of  $K_d$  obtained at the ARCH

and PAB stations during the summers of 2012 and 2013, was used to represent the entire scene. Hyperspectral  $K_d$  data was simulated to the multispectral bands of the WV02 sensor using ENVI v.4.8 (Table 7.2).

Table 7.2 –  $K_d$  ( $\text{m}^{-1}$ ) obtained around PAB and ARCH stations in the ACRB during the summer of 2012 and 2013 for the five bands of WV02 in the visible region.

<b>Band centered at (nm)</b>	<b><math>K_d</math> (<math>\text{m}^{-1}</math>)</b>
427	0.144
478	0.115
546	0.142
608	0.329
659	0.384

Samples of pixels ( $N = 4,112$ ) of the below-water reflectance image were extracted in deep-water areas and the average between them was estimated. This value was used for the  $R_\infty(0^-)$  in Equation 7.3. The curve of the deep water samples used is shown in Figure 7.3. Deep areas were selected in the image based on a bathymetry map provided by the International Conservation Organization of the Abrolhos Bank.

All pixels where the retrieved depth was deeper than 12 m or where the water column correction algorithm retrieved  $0 > \rho_{bottom} > 1$  were masked out. This depth threshold was defined for two reasons. First, according to findings discussed in Chapter 5, the uncertainties of the retrieved bottom reflectance are higher in areas deeper than 10 m, for non-clear waters. Second, the uncertainties in the retrieved bathymetry are lower up to 12 m for most types of waters (Stumpf et al., 2003).

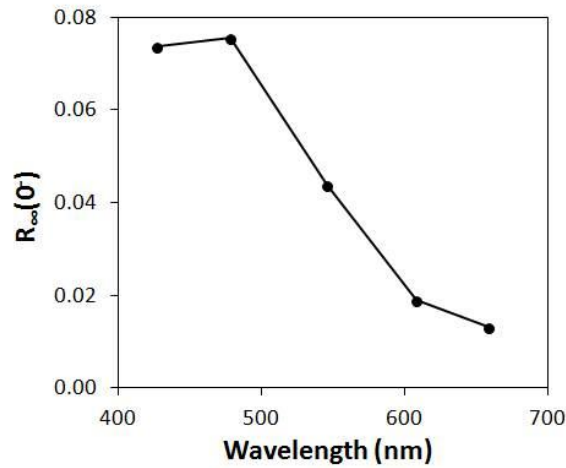


Figure 7.3 – Average of  $R_{\infty}(0)$  corrected for sunglint and extracted over deep waters within the WV02 image.

#### 7.2.1.5. Bathymetry map

Bathymetry data for each pixel of the image is a requirement to retrieve bottom reflectance using Maritorena et al.'s algorithm (1994). However, this detailed information of  $z$  was not available and bathymetry was obtained from remote sensing data using the algorithm proposed by Stumpf et al. (2003) (Equation 7.5).

$$z = \beta_1 \frac{\ln(n\rho_{w,i})}{\ln(n\rho_{w,j})} - \beta_0 \quad (7.5)$$

where  $\beta_1$  is a tunable constant to scale the above ratio;  $n$  is a constant for small areas, which is chosen to assure both that the logarithm will be positive under any condition and that the ratio will produce a linear response with depth, usually varying between 500 and 1,500 (500 for the present work); and  $\beta_0$  is the offset for a depth of 0 m. Using two bands  $i$  and  $j$  ( $i < j$ ) that have different  $K_d$ , as the logarithm values change with depth, the ratio also changes. As the depth increases, while the reflectance of both bands decreases, the logarithm of  $\rho_{w,i}$  will decrease proportionally faster than the logarithm of  $\rho_{w,j}$  and then, the ratio will increase. Contrary to other algorithms, the one used here can be applied over non-homogeneous bottom types since the ratio compensates for

variations in the bottom reflectance. Coefficients  $\beta_1$  and  $\beta_0$  are obtained from a regression between  $(\ln(n\rho_{w,i})/\ln(n\rho_{w,j}))$  against real  $z$  values measured in some pixels where field information was available.

In this work, field information of  $z$  at 135 points well distributed over the WV02 scene was provided by the Brazilian Navy. Such information was delivered in Universal Transverse Mercator Projection, Datum Corrego Alegre and previously transformed to tidal height at 0 m. Two treatments had to be performed to the data set before using. First, depths were corrected for the tidal height variation of the day and time of the WV02 image. As no tidal gauge data was collected in the Archipelago by that time, the predicted tidal height for the closest port (Ilheus Port) was used (1.39 m). Second, geographic coordinates were converted to the Projection of Universal Transverse Mercator, Datum WGS-84, to be compatible to the WV02 image. Once these corrections were performed, the points were separated in two pools of sets, one of them used for calibration and the other for model validation. Due to the total of points was scarce for both procedures, a cross-validation technique was applied. For that, the points were separated in different sets of calibration (70% of the points) and validation (30% of the points), in which points were randomly assigned for either one. For each set of calibration-validation points, the  $\beta_1$  and  $\beta_0$  coefficients were estimated, and adjusted for both steps (calibration and validation).

The Stumpf et al. (2003) algorithm adapted for the WV02 image and study area is expressed in Equation 7.6. The  $\beta_{1,0}$  coefficients,  $n$  value and band combination presented in this equation, produced the best adjustment (Table 7.3).

$$z = 56.279 \frac{\ln(500\rho_{w,478})}{\ln(500\rho_{w,546})} + 59.9808 \quad (7.6)$$

Table 7.3 –  $\beta_1$  and  $\beta_0$  coefficients used for the calibration of the bathymetry map,  $R^2$  and RMSE obtained for different data sets. Bold numbers represent mean values between the sets.

$\beta_1$	$\beta_0$	$R^2$	RMSE
56.896	-61.040	0.4608	3.2006
52.485	-55.141	0.3952	3.2926
54.117	-57.162	0.3899	3.5331
43.294	-43.779	0.3265	3.1327
62.140	-67.373	0.4378	3.5501
56.646	-60.291	0.3748	3.6372
59.876	-64.482	0.4498	3.3314
56.997	-60.844	0.3728	3.7123
60.078	-64.720	0.3845	3.6517
60.261	-64.976	0.3852	3.5979
<b>56.279</b>	<b>-59.9808</b>	<b>0.39773</b>	<b>3.46396</b>

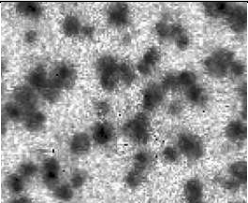
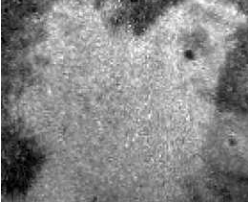
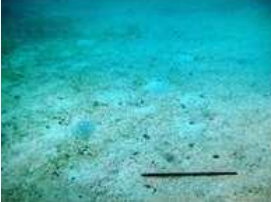
## 7.2.2. Bottom mapping in the *Parcel dos Abrolhos*, ACRB

After applying the water column correction to the WV02 image the band at 478 nm had the greater quantity of valid pixels (67.75%) compared with the other bands. For this reason, the classification scheme used to produce the bottom type map of the ACRB was applied only to the 478 nm band. Even though spectral information was lost using only one band, the adopted criterion was to prioritize the spatial extension of the bottom map over the quantity of classes able to be discriminated at 478 nm.

### 7.2.2.1. Definition of classes

Four classes were considered based on image interpretation, as well as observations and findings gained from the field work. The classes were: Sand; Macroalgae+Sand; Reefs; and Inter-reef areas. The reef areas encompassed different benthic communities located above the chapeirões, with a mixture of classes present in different percentages: coral, macroalgae, sponge, calcareous algae and Zoanthids. The inter-reef areas were located around the chapeirões and included Sand, Sediments, Macroalgae, Algal Turf and Rhodoliths in different proportions (Table 7.4). Macroalgae class was dominated by different types of algae (brown, red or green) and in some cases included exposed sand or rocks in low proportion. Sand areas in some cases included also sparse algae or seagrass.

Table 7.4 – Illustration of the thematic classes used for the bottom mapping in the *Parcel dos Abrolhos*, ACRB.

Thematic class	Sample				Context	
	WV02 at 478 nm	Photos				
Reef						Dark gray / black compact areas, with size varying around 60 and 200 pixels with roundish shape
Inter-reef area						Light to medium gray, mixed colored pixels, extensive matrix with some dark patches (reefs) inside.
Macroalgae						Dark gray areas limiting sand or inter-reef areas. Variable shape.
Sand						Clear homogeneous areas, with variable shapes, delimited by darker extensions of inter-reef areas or macroalgae

### **7.2.2.2. Processing of the WV02 scene**

OBIA has a high potential to integrate different techniques of processing, retrieval and analyzing multi-resolution data from various sensors (BLASCHKE et al., 2008). This technique starts with a segmentation that is defined as an aggregation of high level of detail (pixels), producing usable objects. Once the objects are defined, the second step is to apply a rule-based classifier to make explicit the required spectral and geometrical properties, as well as, the spatial relations for advanced class modeling. Contrary to a classical image classification, the OBIA is an interactive and cyclic process, open for accommodating different categories of target classes, from specific domains, with different semantics, etc

### **7.2.2.3. Segmentation**

eCognition software uses three parameters to perform segmentation that can be defined by the user: (i) Scale Parameter that determines the size of objects; (ii) Shape, which is a trade-off between shape and color, i.e., the lower the value, the higher is the influence of color in the process; and (iii) Compactness, that produces more compact objects, as higher its value is.

The WV02 image presented a gray scale gradient in the entire scene, and some discontinuities were observed to be related possibly to some calibration distortions. This was because the same features showed different reflectance values according to their position in the image. Also, different classes showed different sizes, so that, the same spatial scale was not appropriated for the segmentation of all features. On the other hand, processing time of segmentation was more than 10 hours for the entire scene, even using only one spectral band. For these reasons, the image was subdivided in four parts and segmentation was performed in several steps. Several tests were performed in each subset with different reflectance thresholds, Scale Parameter and Shape, according to characteristics of classes in each subset. The performance of the tests was visually inspected and analyzed (Figure 7.4).

The segmentation rules that showed the best results in the different subsets were:

- Multi-resolution segmentation was run to isolate sand or inter-reef areas. For that, a superior threshold for reflectance values was located

between 0.16 - 0.19 depending on the subset. The Scale Parameter varied between 50 and 100.

- Then, a multi-resolution segmentation was run to isolate small reefs. A inferior threshold for reflectance values was 0.18 - 0.15 depending on the subset. Scale Parameter varied between 10 and 50. Always, in each subset, superior threshold defined to isolate sand segments was higher than inferior threshold used for reef areas.

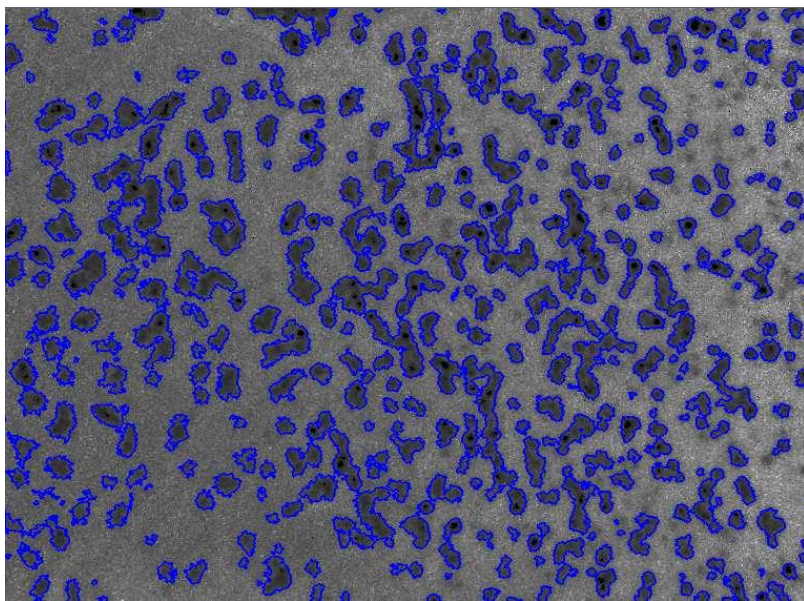


Figure 7.4 – Result of the segmentation process that was considered satisfactory, in a subset image of a portion of the *Parcel dos Abrolhos*. The figure shows reefs defined as different objects after segmentation (in blue).

#### 7.2.2.4. Classification

The classification process was not performed using an automatic algorithm, but rather using objects that were assigned manually to different classes according to their reflectance values and size, based in visual inspection of the image. As in the segmentation process, a multi-step classification was also adopted and different thresholds were defined sequentially in different portions of the subsets, according to the neighborhood of the different objects. Reflectance values were the highest for sand areas, intermediate for inter-reef areas and macroalgae and the lowest for reef areas and

thresholds were defined according to behavior of each feature in subsets. Maximum reflectance values in inter-reef areas were found in the center of the scene, coincident with the shallowest area in the bathymetric map. In some occasions, a threshold in the object size of this class was also delimited, being higher than 50 pixels and lower than 300 for reef areas. After the classification process, a low-pass filter with a 3x3 window was used to remove the salt-pepper effect in some parts of the map.

#### **7.2.2.5. Mapping validation**

Information of the benthic communities was collected at 39 sites, which were used for the map validation. These locations were sampled during both surveys in 2012 and 2013. They were distributed northern and southern of the Santa Barbara Island (the largest of the ACRB) and above the *Parcel dos Abrolhos* located eastward to the Archipelago. However, 5 of them were masked after applying the water column correction due to their proximity to land areas. Thus, 34 sites were actually used for the validation of the bottom type map. The accuracy assessment of the bottom type map was performed through a standard confusion matrix (CONGALTON; GREEN, 1999). Accuracy of the user, producer and Kappa index were calculated.

### **7.3. Results and discussion**

#### **7.3.1. Performance of the pre-processing steps**

##### **7.3.1.1. Atmospheric correction**

ATCOR2 module in PCI software performs internally with first a conversion from DN to radiance. Within this step, a radiometric correction is also done. The absolute radiometric calibration factors ( $K_{BAND}$ , in  $W m^{-2} sr^{-1} count^{-1}$ ) and the effective bandwidths ( $\Delta\lambda_{BAND}$ , in  $\mu m$ ) used for such conversion are continuously updated by the Digital Globe company through calibration tests done in highly reflective surfaces in the Earth, and the correct values to be used in each scene are delivered together with the remote sensing data. These calibration tests have to be constantly done because the detectors of the orbital sensor suffer degradation over time. Figure 7.5a shows the spectral curve of DN values above deep waters. Peaks at 659 and 831 nm are observed because of the relative discalibration between the spectral bands. After DN is transformed to radiance units, one may observe an increase at 427 nm and decrease at

659 and 831 nm, showing that the spectral radiometric correction performed well (Figure 7.5b).

The radiance spectral curve inspected above deep waters shows high values at the blue region, where Rayleigh scatterings dominates, increasing exponentially towards the shorter bands. After atmospheric correction, the surface reflectance shows a reduction at the beginning of the visible region (427 nm), compensating for the atmospheric Rayleigh scattering. However, some higher values were still observed after atmospheric correction at the longer bands of the WV02 sensor. This may reveal an imperfect correction of the model. The ATCOR2 model was actually not developed to be applied for water bodies. The Maritime aerosol model that can be selected for such correction was developed to be applied in the boundary layer over oceans and continents under a prevailing wind from the ocean, but it still is not so well adapted for the retrieval of water-leaving radiance.

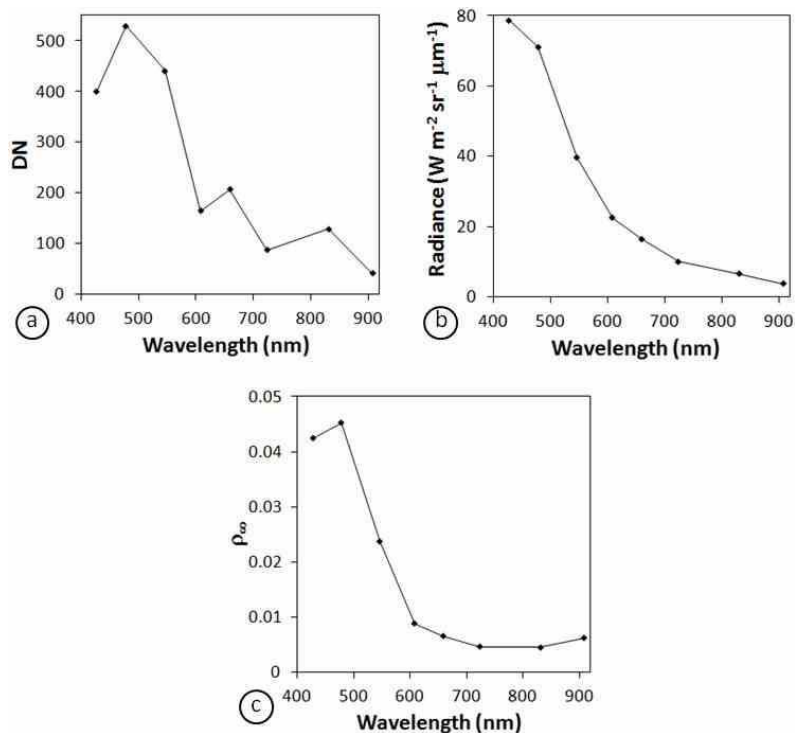


Figure 7.5 – Mean values extracted from the WV02 image in deep waters, as a function of wavelength (nm): digital number (DN) in a 16-bits scale, dimensionless (a); radiance in  $W m^{-2} sr^{-1} \mu m^{-1}$  (b); and surface reflectance of deep waters ( $\rho_{\infty}$ ), dimensionless (c).

Several orbital sensors such as MODIS-Aqua, SeaWiFS and MERIS, with low spatial resolution, have specific atmospheric model routines that are operationally implemented in specific software. They have been developed to be applied specifically in oceanic areas and have been evaluated to derive ocean-color products by the Atmospheric Correction Working Group (ACWG) established by the International Ocean-Color Coordinating Group (IOCCG) for that purpose (IOCCG, 2010). Nevertheless, those algorithms were developed for Case-1 waters, and they fail in Case-2 waters mainly due to the incorrect assumption of zero water-leaving radiance at the NIR region and due to the high CDOM absorption at the shorter bands. In the case of sensors with intermediate or high spatial resolution (30 m or less), the situation is even worst. No algorithm to correct atmospheric effects performing well in aquatic environments is operational for these sensors. These sensors with better spatial resolution have been used routinely to study coastal waters, river plumes and coral reef areas (MUMBY; EDWARDS, 2002; BOUVET et al., 2003; ANDRÉFOUËT et al., 2003; SARANGI et al., 2004; PURKIS, 2005; PALANDRO et al., 2008; RUDORFF et al., 2011, PHINN, et al., 2012; among many others) and atmospheric corrections to retrieve reasonably good surface reflectance values are required.

In the present work, during the WV02 imagery, some reflectance measurements were done near the Abrolhos Archipelago. Only three locations were sampled on the same day, and the depth of these points varied between 3.8 and 10.2 m. Comparisons between the surface reflectance collected *in situ* and by the orbital sensor are shown in Figure 7.6. Larger errors between both types of measurements i.e., satellite and *in situ*, were observed for the shorter bands (up to 608 nm), with mean uncertainties between 46 and 63%. These errors were not random, but rather revealed consistent biases of an overestimation of the *in situ* measurements compared to the satellite remote sensing reflectance. Despite of all the limitations aforementioned regarding the atmospheric correction algorithms applied to water body environments, the water surface remote sensing reflectance obtained from the satellite WV02 image showed a behavior consistent with the *in situ* measurements. Hence, the correction applied in the present work was well done. It is important, however, also to note that differences in the reflectance estimates are not caused exclusively by atmospheric interference. Differences in the configuration of sensors, signal-to-noise relation and size of the area

integrated by both types of data i.e., satellite and *in situ*, are other factors responsible for these biases.

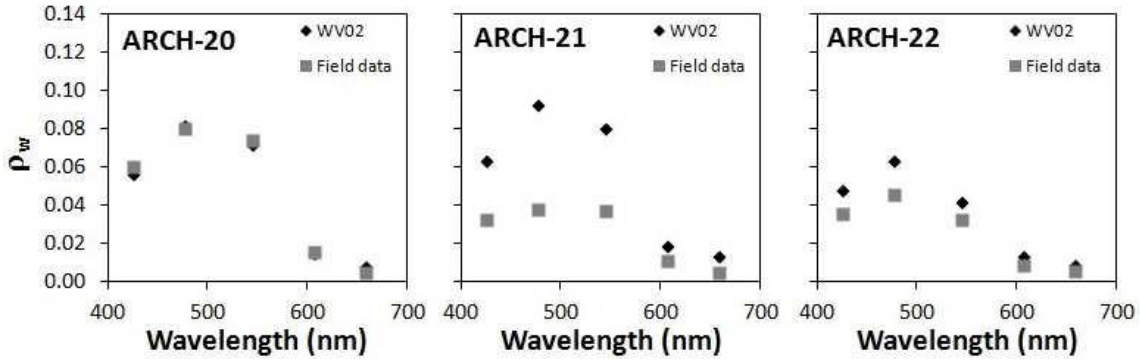


Figure 7.6 – Water reflectance ( $\rho_w$ ) as a function of wavelength (nm) collected *in situ* (gray squares) and extracted from the WV02 image (Black diamonds), in three different sites around the Archipelago (ARCH-20, ARCH-21 and ARCH-22).

### 7.3.1.2. Sunlint correction

The sunlint effect seen in the surface reflectance image was removed after the application of the Hedley et al. (2005) algorithm through Equation 7.5. Rugosity effect in the water surface was eliminated, bottom features were enhanced and submerged targets could be better discriminated. Around the Archipelago, sunlint effect was not so significant, possibly because the islands make a physical barrier for wind and waters were calmer in this region. However, above the chapeirões, eastward from the islands, the sunlint effect was high, making difficult the identification of the bottom types before applying the correction of such effect. In terms of the reflectance values, the sunlint correction caused an overall reduction in all bands and there was no anomalous artifact in the spectral behavior (Figure 7.7). The standard deviation also decreased, as the color was homogenized, since bright pixels containing specular reflection were obscured.

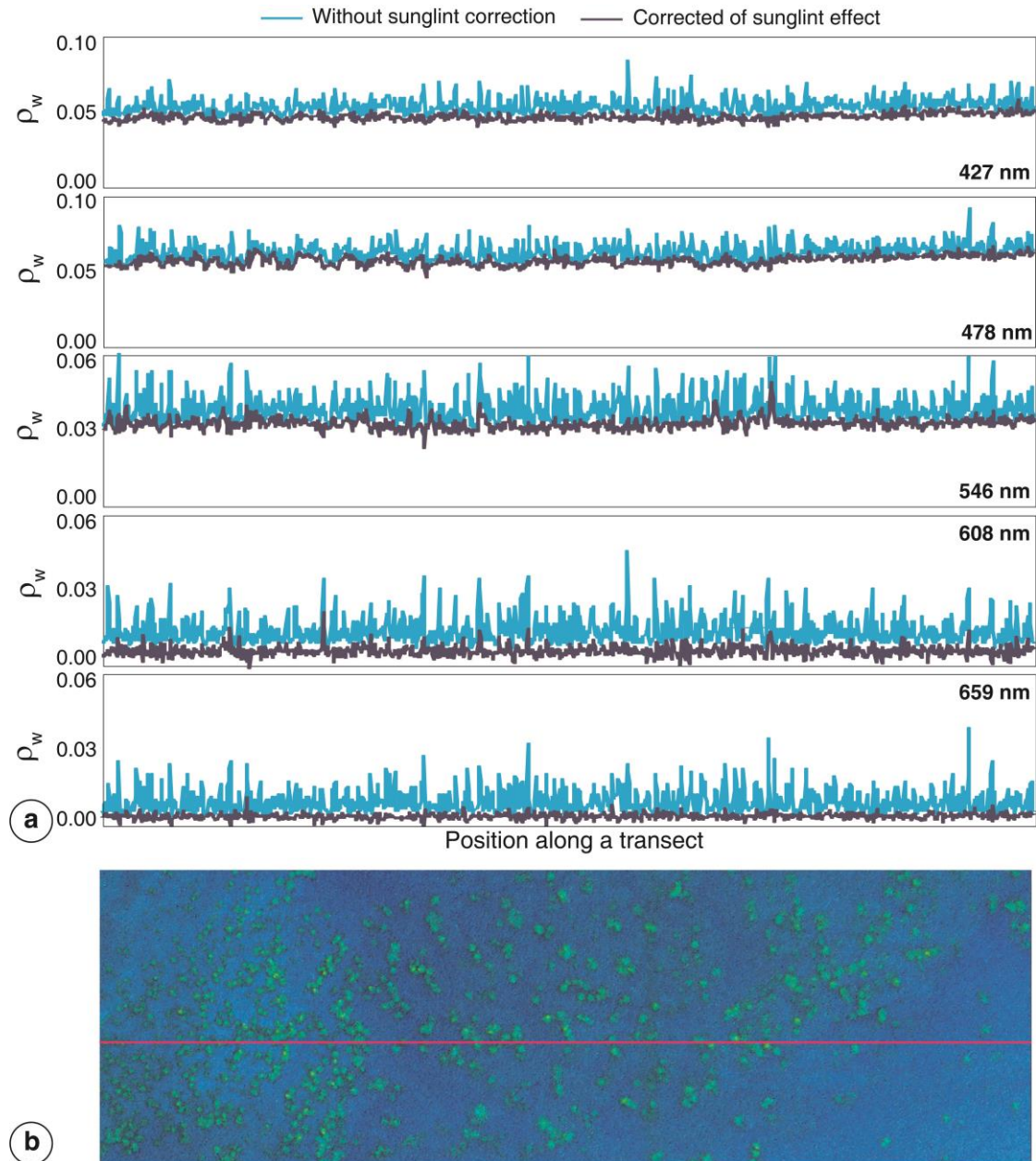


Figure 7.7 – Water reflectance ( $\rho_w$ ) before and after application of sunglint correction for the different bands of the WV02 sensor (a) along a transect (in red) above the *Parcel dos Abrolhos* in the WV02 image (b). The portion of the WV02 image is showed in a quasi-true color composition (R: 659 nm; G: 546 nm; B: 478 nm)

After the sunglint correction, some stripes were evident in the image (Figure 7.8). An image without radiometric correction, collected by a pushbroom imager, normally presents some vertical strips caused by calibration distortions among the detectors of the sensor. The application of such correction causes the banding and streaking to virtually disappear in the image, but once it is performed, the radiometric corrections are not

reversible. The image here used was already radiometrically corrected. However, some problems in this irreversible processing could be enhanced after the sunglint correction. The streaking effect is not an artifact of this correction, but it was already dissembled in the image and evidenced after the sunglint correction.

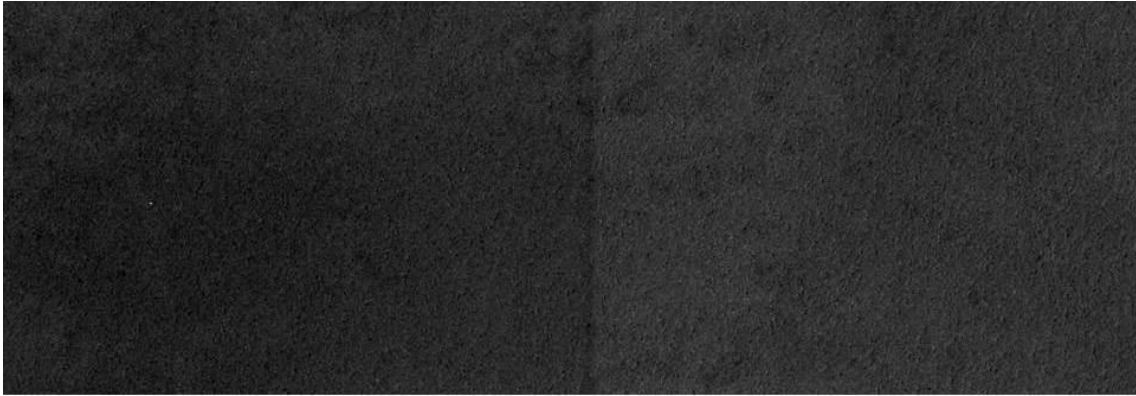


Figure 7.8 – Vertical stripes in the WV02 image at 478 nm, enhanced after sunglint correction.

### 7.3.1.3. Bathymetry map

The bathymetric map obtained from the application of Stumpf et al. (2003) algorithm to the WV02 scene is shown in Figure 7.9. All points deeper than 12 m were masked and are displayed in black. A low pass filter with a window size of 3x3 was applied to this map only for visualization purposes with noise reduction. Note that vertical stripes in several portions of the map are seen as well as some discontinuities in depth.

In general, based on a visual inspection, the map showed a good representation of the topography of the area. The bathymetry shows a shallower central area vertically extended in the map that corresponds to the *Parcel dos Abrolhos*. Inside the *Parcel dos Abrolhos*, a large number of *chapeirões* is distributed with depths varying between 0.1 and 6.5 m (Figure 7.10- point 2). In the center of some *chapeirões* the model retrieved invalid values. It is possible that some portions of shallow *chapeirões* were exposed during the WV02 causing these erroneous retrievals. Another possibility could be the presence of waves and foam at some tops of the reefs that could not be eliminated through the sunglint correction. In fact, Bertels et al. (2008) applied an algorithm to retrieve bottom depth from a hyperspectral image and appointed that in some parts of the reef crest it was not possible to retrieve depth where breaking waves were responsible for the total reflection of light.

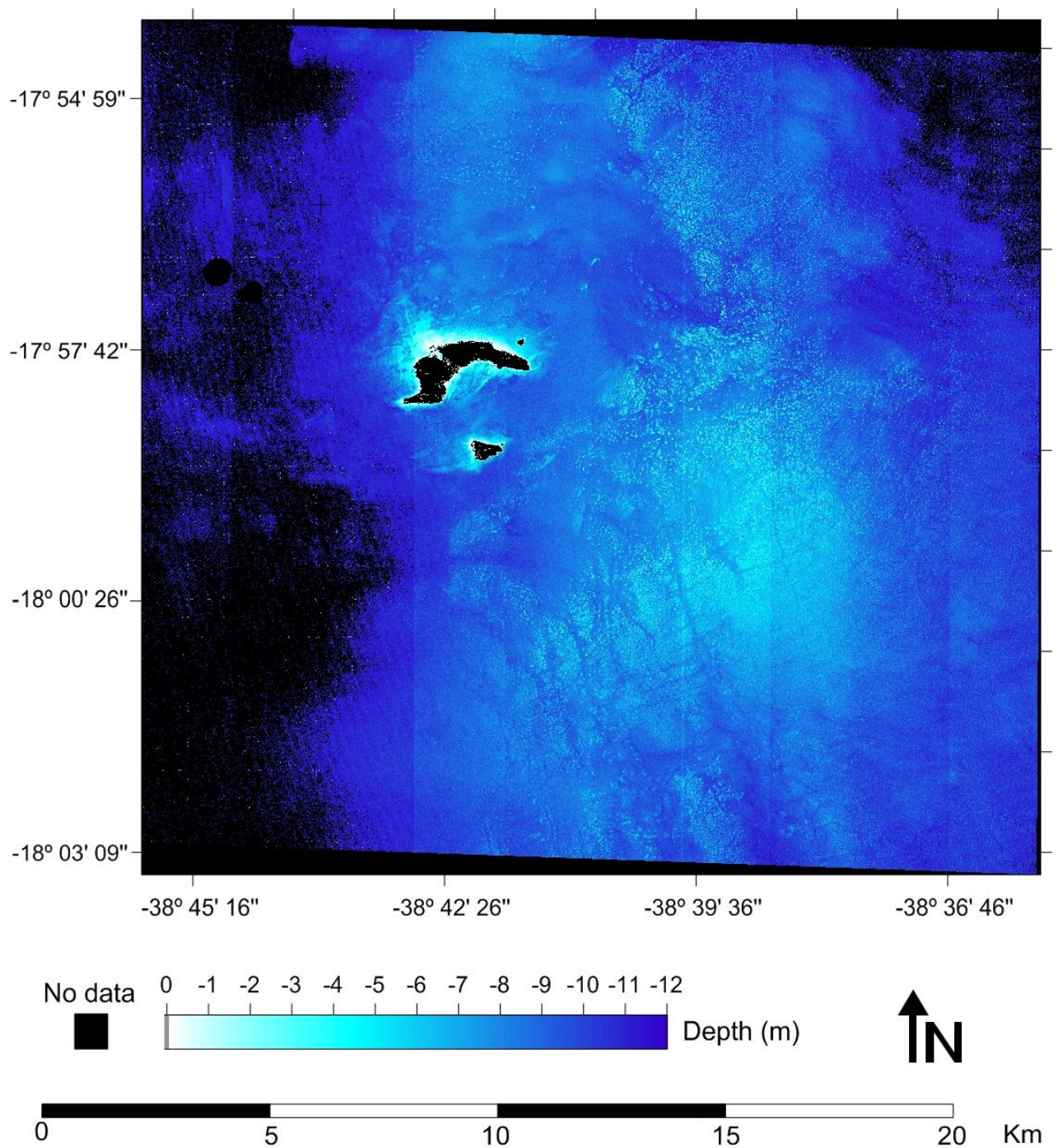


Figure 7.9 – Bathymetric map of the Archipelago and *Parcel dos Abrolhos*, in the ACRB, Brazil, obtained through the application of the Stumpf et al. (2003) algorithm to a WV02 scene. Depths shown in the map vary between 0 and 12 m and are represented in blue scale. No data and land areas are represented in black.

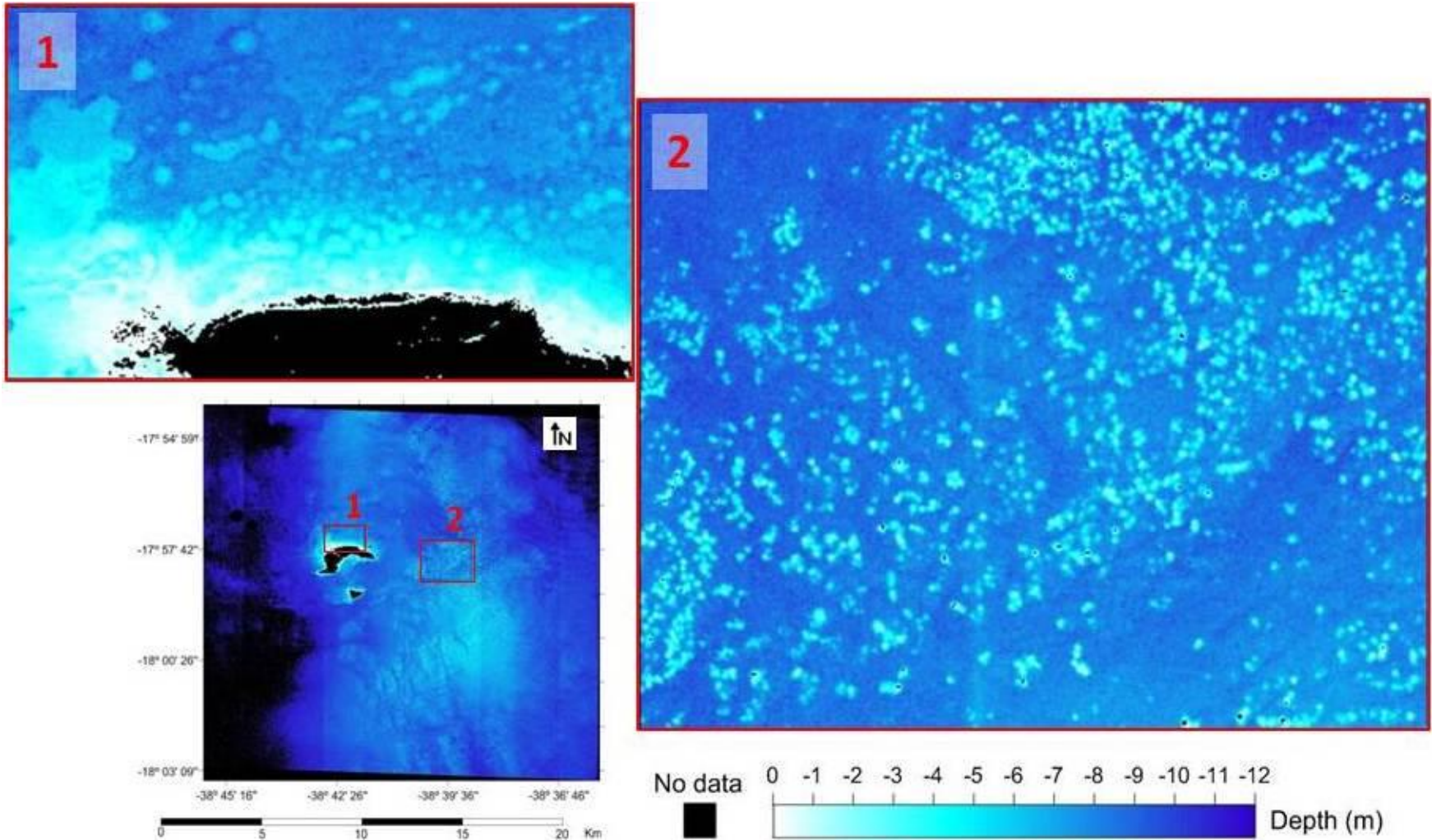


Figure 7.10 – Bathymetric map of the Archipelago and *Parcel dos Abrolhos*, in the ACRB, Brazil (Down left). Number 1 and 2 represent zooms focusing the Northern Archipelago (Number 1), and above an area with a large amount of isolated chapeirões in the *Parcel dos Abrolhos* (Number 2).

Between the *Parcel dos Abrolhos* and the islands, a deeper channel is observed, with depths around 12 m and where no *chapeirões* are present. The deepest parts of the scene are located in the westernmost portion and towards the northeast. Around the islands, in a smaller spatial scale, depths showed variations from 2 to 11 m, indicating an abrupt gradient. Even though the Stumpf et al. (2003) algorithm is considered insensitive to changes in bottom reflectance, in this work some discrepancies were observed when accounting for this type of variation in the substrate. Figure 7.10 - point 1 shows a clear example of this situation. Some clear circles are perceived as 2 to 3 m shallower than the surrounding areas. However, these features are actually located at the same depth with data collected in the field, and differences in the retrieved depth may be caused by contrasted differences in the bottom reflectance. Inside the circles, the substrate is highly reflective dominated by sand, while macroalgae dominated substrates that encircle these areas.

Using different sets of 41 validation points, shallower than 12 m, the bathymetry model showed a low to medium adjustment (mean  $R^2$  equal to 0.43, RMSE 2.09) (Table 7.5). Besides the variations in bottom reflectance that could be responsible for the low performance in some parts of the map, errors in geopositioning could also be another source of error. The WV02 has a spatial resolution of 2 m and the bottom in this area is very patchy and heterogeneous, where *chapeirões* and other already mentioned features have small sizes. On the other hand, the mean error for the *in situ* collections of points using standard GPS range approximately at  $\pm 5$  m. This means that the measured point could correspond to a window size of at least 3x3 pixels. Errors in bathymetry inevitably were propagated to the bottom reflectance retrievals. Other surveys to estimate accurate bathymetry data are indispensable to reduce uncertainties in the water column correction procedure. LIDAR imagery would be desirable due to its ability to produce a detailed grid of information in a reduced spatial scale, even to a centimeter scale.

Table 7.5 –  $\beta_1$  and  $\beta_0$  coefficients,  $R^2$  and RMSE obtained for the validation of different data sets of the bathymetric map. Bold numbers represent mean values between sets.

$\beta_1$	$\beta_0$	$R^2$	RMSE
0.2835	6.915	0.3313	1.983
0.3486	7.291	0.4470	2.016
0.3688	6.536	0.4417	1.856
0.3710	6.499	0.6030	1.769
0.4004	6.300	0.3226	2.312
0.4643	5.718	0.4782	2.085
0.3317	7.315	0.2991	2.341
0.4893	5.390	0.5040	1.994
0.4838	5.580	0.4568	2.253
0.4861	5.723	0.4494	2.326
<b>0.40275</b>	<b>6.3267</b>	<b>0.43331</b>	<b>2.0935</b>

#### 7.3.1.4. Water column correction

The overall performance of the water column correction was poor, especially for the bands longer than 600 nm. Most of the pixels at 608 and 646 nm had bottom reflectance retrieved values either lower than 0 or higher than 1. The best results were obtained at 478 nm. This band had the lowest quantity of invalid pixels that had to be masked, as the water column effect is the lowest due to the high light penetration, evidenced by the lowest  $K_d$  for this band (Table 7.2).

Considering only the 478 nm band, the water column correction performed well in some portions of the image, enhancing the bottom features (Figure 7.11a-b). On the other hand, in other parts of the image the water column correction limited the use of those areas for the bottom type mapping, due to the low quantity of valid pixels retrieved by the model (Figure 7.11c-d). In Chapter 5 the importance of this step for the mapping of submerged substrates was deeply discussed. Despite that the Maritonena et al.'s algorithm (1994) showed the best results between the tested methods in Chapter 5, the performance of its application was still not satisfactory for the entire WV02 scene. Uncertainties in the  $K_d$  and depths used as inputs of the model are the main reasons accounting for this underperformance. It was observed that the water column within the ACRB area presents important heterogeneities in small spatial scales. Hence, the utilization of a unique attenuation coefficient for the entire scene was certainly responsible for the retrieval of the invalid values of bottom reflectance. On the other hand, the bathymetry map used as input had a RMSE of 2.09 m. One must take into

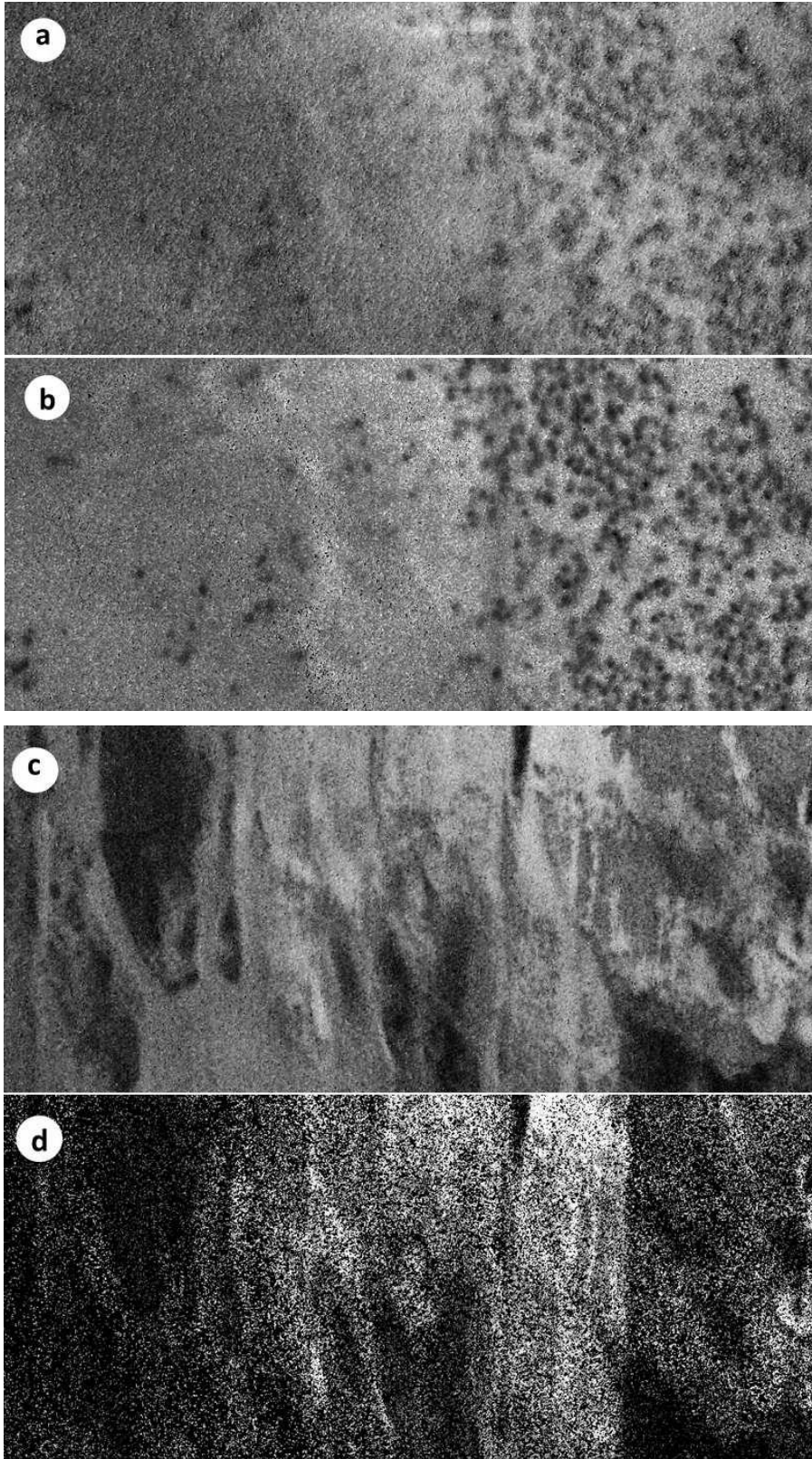


Figure 7.11 – WV02 image at 478 nm in different portions of the ACRB: above the *Parcel dos Abrolhos* (a and b) and westward the Archipelago (c and d). Both portions are showed before water column correction were performed (a and c) and after correction of this effect (b and d).

account that this was the first work to map the *Parcel dos Abrolhos* area in the ACRB. The lack of a detailed bathymetric grid with a spatial resolution compatible with the WV02 image, made necessary the utilization of an algorithm to retrieve bottom depth from the image itself, which inevitably subjects the data to higher uncertainties.

The main challenge for the submerged bottom mapping presented in this work, was undoubtedly the water column correction procedure. Unsuccessful retrievals of bottom reflectance in several WV02 bands relied in the lack of adequate input data. A possible solution to compensate for the errors in the depths used in the model input, could be the use a high resolution bathymetry map derived from LIDAR surveys across the ACRB. However, this could not compensate for the heterogeneities in the water column attenuation, which will still remain as a challenge. Another possibility could be the utilization of hyperspectral image, for which the Lee et al.'s inversion scheme (1999) can be applied, so that  $a$  and  $b_b$  coefficients can be retrieved in each pixel. One might suggest however, that even though the Lee et al.'s inversion scheme is proposed for hyperspectral image, since the WV02 has a better spectral resolution than other high spatial resolution orbital sensors with an adequate position of the bands for water quality studies (bands at 427, 478, 546, 608, 659, 724, 831 and 908 nm) the correction could be adapted for WV02 bands. Hence, further works should explore alternatives to adapt inversion schemes to multispectral data to improve the water column correction performance which is essential for bottom type mapping.

### **7.3.2. ACRB Mapping**

Figure 7.12 depicts the bottom type map produced from the WV02 scene obtained on 2012/02/14, and the total area of each class, as well as their cover percentage, are shown in Table 7.6. The inter-reef class was the most abundant, totalizing 129 km<sup>2</sup> that correspond to 73 % over the total of the mapped area, followed by reefs, sand and macroalgae classes. It does not mean that macroalgae were restricted only to 4.39 % of the area, but that they were the dominant group in these areas. In fact, macroalgae were also present in the other three classes of bottom type and this group is probably the most representative in all substrates of the ACRB. Inter-reefs areas are relevant from the ecologic point of view since rhodoliths beds are located in this areas (AMADO-FILHO

et al., 2012). Inter-reefs areas, sand patches and reefs were the main features found in the study area and matches with findings showed by AMADO-FILHO et al. (2012).

Despite of the low quantity of points for the validation and the confusion between sand and inter-reef areas, the reefs could be easily mapped even using one spectral band. This work shows the first map in the *Parcel dos Abrolhos* and Archipelago where the distribution of the reefs and the quantification of the area occupied by them were shown. The isolated reefs were spatially distributed in patches with different abundance among them. To facilitate the identification of these interspersed patches, Figure 7.13 shows their location according to a visual inspection. From the Archipelago towards the east, after the deep channel a broad area with high concentration of reefs disposed in shape of arc can be observed (Patch 1) (Figure 7.14). Inside this arc, reefs were larger compared to other parts of the map and several of them were so close to each other that they seemed to be merged. Southwestward to this arc there was a narrow channel with scarce *chapeirões* that encircles patch 1 (Patch 2). The area southern to Patch 2, which is Patch 3, was characterized by spaced small reefs, followed by another area where *chapeirões* were once again very frequent (Patch 4). Some thin cracks with a NW-SE direction were also present in Patch 4. Another area with scarce reefs was Patch 5, and in the southeastest portion, another patch with a lot of reefs was identified as Patch 6. From the islands to the northern sector, an area with large reefs scarcely distributed and inter-spaced with macroalgae and sand was identified as Patch 7. In the northeast portion of the map, small reefs were homogeneously distributed in low frequency (Patch 8).

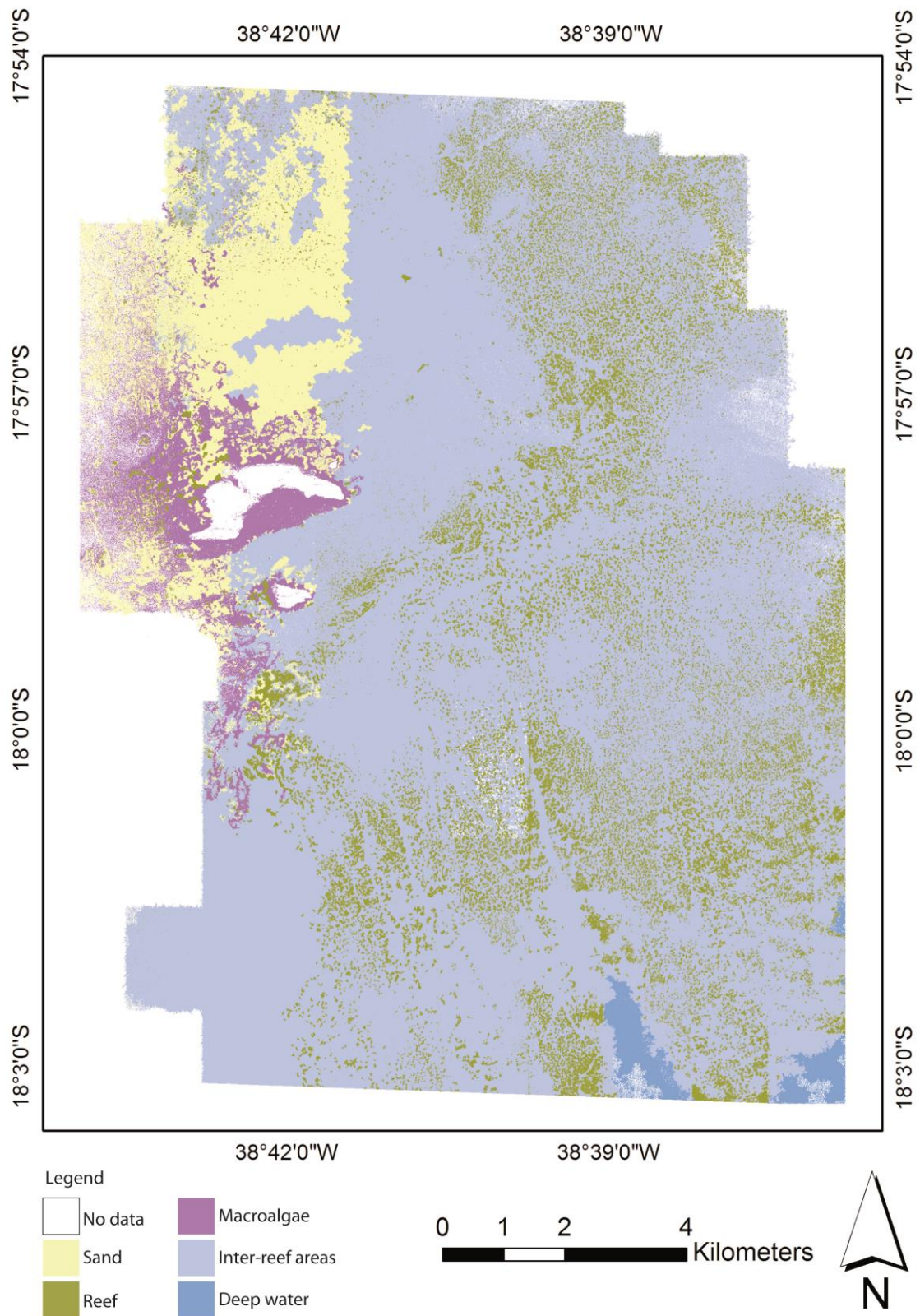


Figure 7.12 – Bottom type map of the ACRB produced from the WV02 image. The "No data" class includes also land areas.

Table 7.6 – Area and percentage of occupation of each class of bottom type.

	Reef	Inter-reef areas	Macroalgae	Sand	Deep water
Area (km <sup>2</sup> )	21.93	129.63	7.79	15.78	2.14
Area (percentage)	12.37	73.13	4.39	8.9	1.2

The accuracy achieved for the bottom type map was high, with an overall accuracy of 88.23 % and a Kappa index of 0.81 (Table 7.7). It is important to recall that errors in geopositioning could also be present associated to the *in situ* GPS records of the geographical coordinates, which could lead to mismatches in the map validation, reducing accuracy. The main confusions were between reef and inter-reef areas and between macroalgae with reef or sand. These discrepancies between the mapped and ground-truth data were observed mainly in the proximities of the Archipelago, where most of the classes were present. On the contrary, above the *Parcel dos Abrolhos*, reef and inter-reef areas were easily separated, for both reflectance values as for the size of features.

Some sites that were used for the validations were registered in 2013, whereas the imagery was collected in 2012. Thus, this information was used for the accuracy assessment of the maps under the premise that the benthic coverage of these sites was invariant along one year (between 2012 and 2013). According to Andréfouët et al. (2003), this could be questionable based on the history of the site and type of perturbations. Nevertheless, the area mapped in this work may be considered stable in a temporal scale of one year. No direct human impacts are observed there, since it is comprised in a protected area where tourism is controlled and extractive activities are forbidden. Furthermore, no natural hazards were observed between 2012 and 2013, causing coral bleaching or massive mortality events. Thus, it is reasonable to use the entire set of validation sites (of 2012 and 2013) in the accuracy assessment of the WV02 mapping.

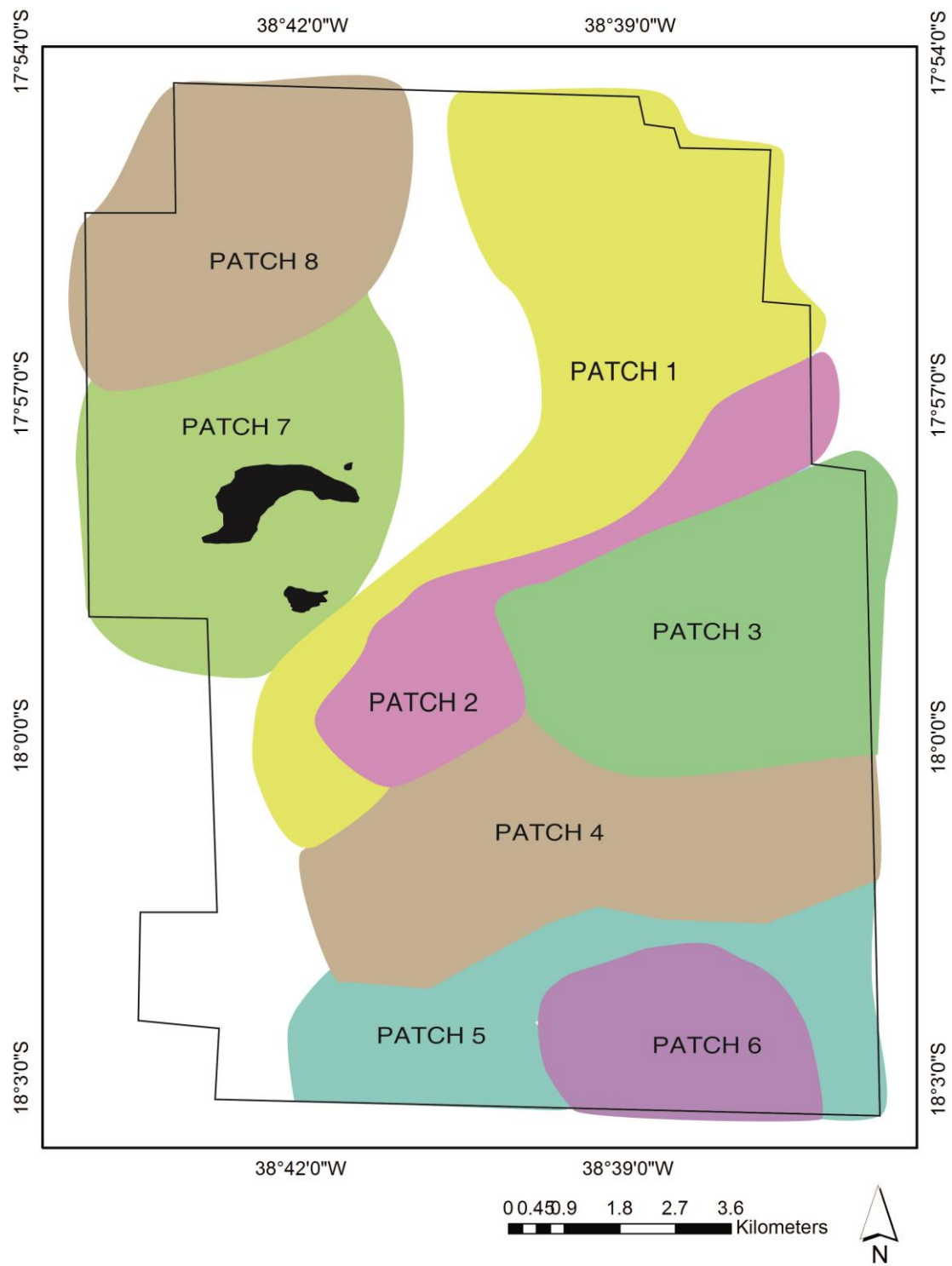


Figure 7.13 – Patches with different patterns of spatial distribution of coral reefs in the ACRB.

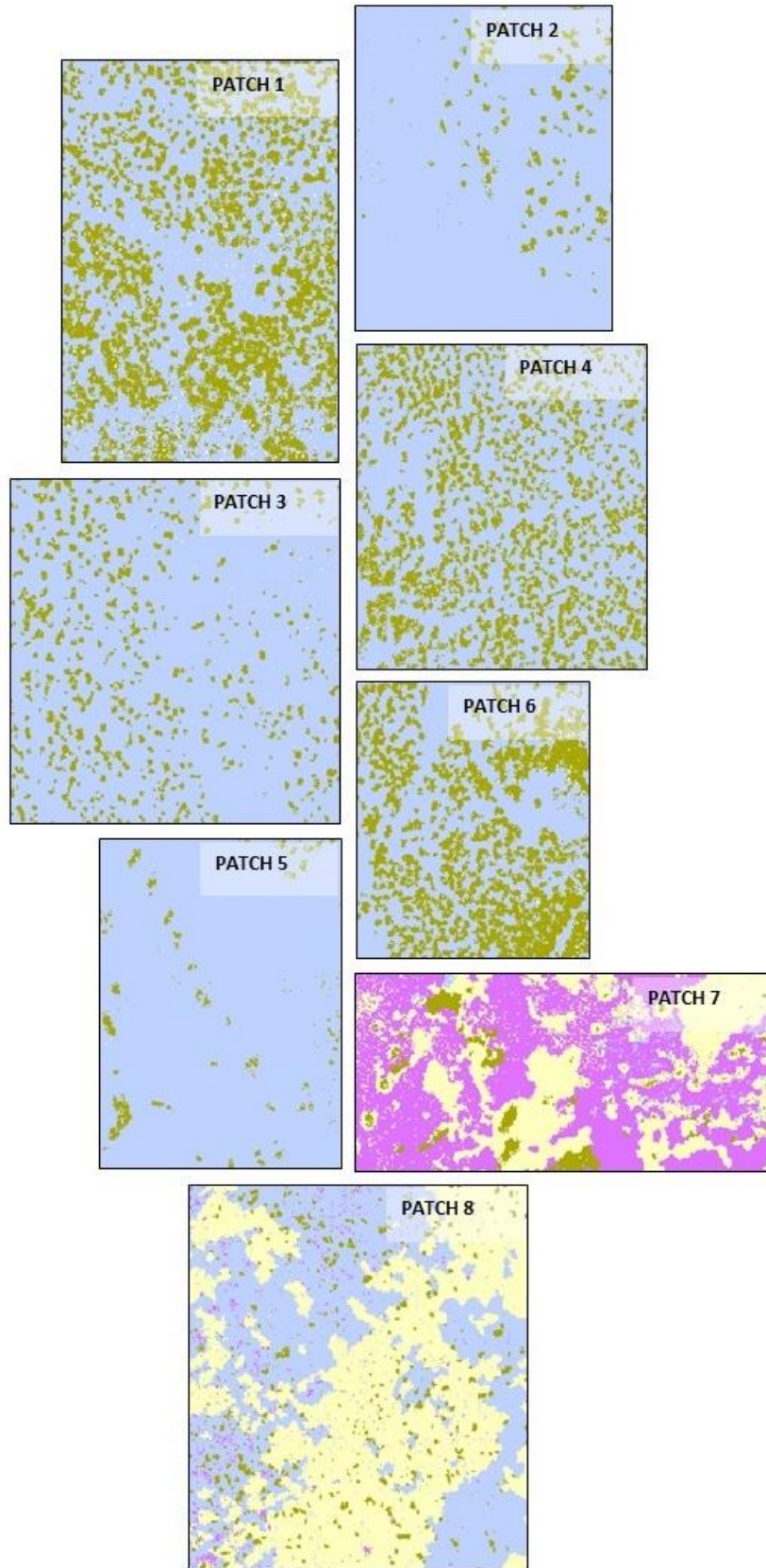


Figure 7.14 – Zooms over different portions of the bottom type map of the ACRB, that correspond with different spatial patterns of reef distribution.

Table 7.7 – Confusion matrix for the classified WV02 image. The overall accuracy and Kappa index are also provided.

		Real Substrate				Row Totals	Producer accuracy
		Reef	Sand	Inter-reef	Macroalgae		
Assigned class	Reef	14	0	1	0	15	93.33%
	Sand	0	1	0	0	1	100.00%
	Inter-reef	0	0	2	0	2	100.00%
	Macroalgae	2	1	0	13	16	81.25%
Column Totals		16	2	3	13	34	
User accuracy		87.5%	50.0%	66.7%	100.0%		
Overall accuracy:		88.23%					
Kappa index:		0.81					

In the North of the islands, approximately in the center of the map, a disruption in the sand class was observed. This abrupt delimitation of the class does not seem a natural feature, but an artifact of the imagery, since there is no sharp change in bathymetry. Observing the bathymetric map, a vertical stripe was coincident with the delimitation of the sand class, thus, a radiometric problem could probably be responsible for this discontinuity. During our two field works, this wide area of sand, northern to the Archipelago, was not visited and there are no records of the bottom type, both for training or validation. This area was classified as sand according to the higher reflectance values compared with the neighbor inter-reef areas to the east and similar reflectance values found in specific features (“randall zones”) that were visited near the islands. Other areas with interesting features that were mapped in the northwest of the scene, also could not be validated in this work due to the lack of validation points. A greater quantity of validation points, better distributed in the entire scene is required for a more robust validation. Literature shows a wide variety in the number of validation points used to create confusion matrixes, varying from 35 to more than 500 sites (e.g., PURKIS, 2005; BENFIELD et al., 2007; CALL et al., 2003; ANDRÉFOUËT et al., 2003; ANDRÉFOUËT; DIRBERG, 2006; FEARNIS et al., 2011). According to Congalton (1991) at least 50 validation points for each class are required for the accuracy assessment. However, Andréfouët (2008) mentioned the difficulty for researchers in remote reef areas to follow an accuracy assessment scheme comparable to

those conducted at sites with easy access and historical knowledge, especially where works are conducted for the first time. Many works have actually been developed for decades in the ACRB. However, generally these works have been conducted focusing on ecological dynamics in punctual areas both in the coastal and external arcs, but they lack of a broad spatial representation of the ecosystem. From the point of view of remote sensing requirements in terms of field sampling, the ACRB could be considered almost unexplored. New validation data in the ACRB should follow recommendations of Andréfouët (2008) and be collected in transects to diminish the errors caused by misclassification or mis-geopositioning. The spectral ravel of benthic communities in the ACRB (discussed in Chapter 6), the quantity of points used for validation and the availability of only one spectral band after the low performance of the water column correction, were responsible for the simplicity in the definition of only 4 classes of bottom type. It is expected that a more exhaustive inspection in the field, visiting different sites in the study area, will provide not only a more robust accuracy assessment, but also the accomplishment of a more detailed map, with a higher number of classes.

A particular feature detected in the scene corresponded to randall zones or haloes, which are areas around coral patches that are kept clear of vegetation by herbivorous fish or invertebrates such as sea urchins (RANDALL, 1965; MCMANUS et al., 2000). These zones have ecological interest since they can provide evidence of the status of the reefs. In reefs under intensive fishing pressure, haloes tend to disappear or be strongly reduced, accompanied by macroalgae growth close to the reef. On the contrary, in pristine environments or where fishing is highly controlled, broad haloes around the reefs are expected to be observed. Figure 7.15 shows these features in the WV02 image and in field photographs taken at sites around the Archipelago. Because of the contrast in the reflectance between sand, reef and macroalgae, and the spatial dynamics of these areas, even using one unique band and given the spectral confusion of benthic classes, randall zones can be easily identify by remote sensing. A large number of randall zones were found in the northern, western and southern sectors from the islands. The entire WV02 scene is located in the Abrolhos National Marine Park where fishing activities are forbidden. Hence the temporal monitoring of randall zones by remote sensing can bring information about the controls of herbivorous fish populations and the

effectiveness of fishing restrictions in this area. Reefs located in the center of randall zones are different from the *chapeirões* found in the *Parcel dos Abrolhos*. In the *Parcel*, the inter-reef matrix is deep and the reefs are disposed in columns, such that there is a rapid increase in depths at the sides of the reefs, while the reefs belonging to patches 7 and 8 (according to the zonation presented in Figure 7.13) are shallower and depths increases more gradually towards the surroundings.

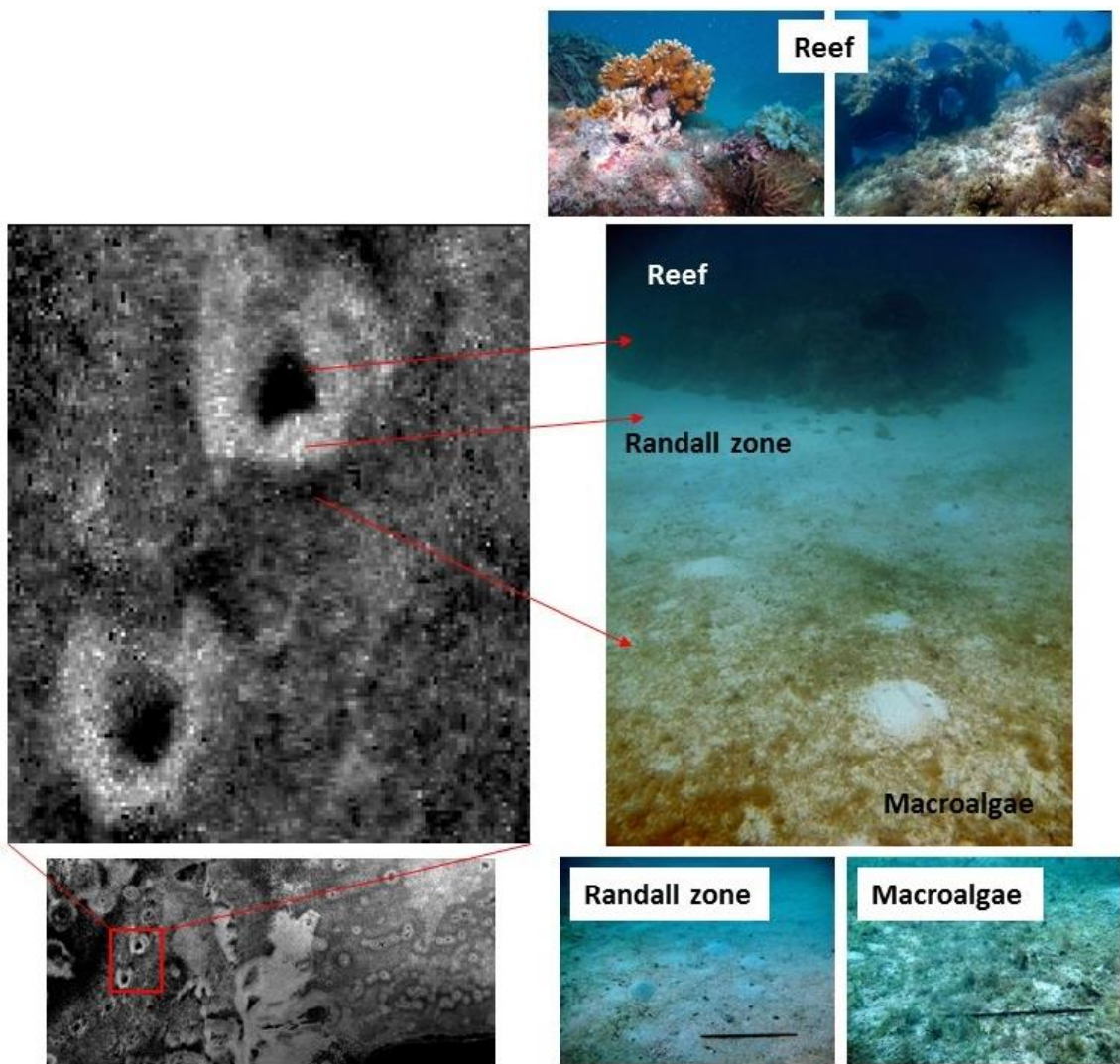


Figure 7.15 – Portion of the WV02 image at 478 nm northern to the islands (Lower left). The red square is observed in a zoom for a better identification of features (Upper left). The same feature identified in the image is showed in a subaquatic picture (Middle right). The three parts of these features (Reef, Randall Zone and Macroalgae) are more detailed in pictures on the lower and upper right.



## **8 CONCLUDING REMARKS, RECOMENDATIONS AND FINAL CONSIDERATIONS**

Bottom type maps over a broad quantity of coral reef environments have been produced worldwide using remote sensing data. Despite the potential of optical images to provide information of the seabed, some limitations caused by environmental factors, such as the water column effect, and by the target characteristics itself, expressed in the spectral complexity of the benthic communities, were addressed in this work. The deep knowledge of these limitations is required to draw proper conclusions, either about the ecosystem functionality or for the delineation of adequate management plans in these environments.

The first challenge to extract information of submerge targets, studied in this work, was the water column effect. Water column correction is a required step to compensate for the differences in depths between different portions of an image and the heterogeneities of the OACs present in the water column. The first methods proposed in literature were the simplest and easiest to apply, using solely band ratios as inputs and outputs of the model. Despite their limitations, they are still the most frequently used algorithms. More complex algebraic algorithms have been developed to estimate the bottom reflectance in shallow environments, but they require the use of *in situ* field data for adequate retrievals. Nevertheless, they are the only methods capable of estimating bottom reflectance. For this reason, improvements and validations of this group of algorithms should be encouraged. Most of the recent algorithms have been based on matching the pixel spectra with simulated spectra from a library. While these algorithms produce satisfactory results, their output is a categorical map and their performance is dependent on the availability of realistic bottom reflectance data sets built in the library. Basically, the choice of the method to apply is dictated by the availability of the input data and the desired outcome in terms of the output variable (e.g., reflectance ratios, categorical maps or bottom reflectance) and the accuracy based on the scientific study envisioned.

Among all the methods developed up to date, none is really capable of correcting for the water column effect properly in the entire visible spectrum. Uncertainties in retrieving the bottom reflectance from above-water spectra increase proportionally with depths and the concentration of optically active water constituents. In clear waters with low

CDOM concentration, the uncertainties augmented towards the red spectral bands. While in environments with high CDOM concentration, uncertainties increased both towards the blue and the red spectral ends. Even in the best conditions of clear waters and shallow depths, the uncertainties in the bottom reflectance retrievals were still not completely independent of depth as they were also depended on the wavelength, and bottom type of the substrate. The algorithms applied in the present work, minimized the differences between similar bottom types located at different depths. In all cases, some knowledge of the water column constituents, as well as depths and the spectral behavior of the substrate, was required to act as an input during the application of a method or to evaluate its performance. In cases where above-water hyperspectral information was available, Lee et al. (1999) inversion method was an alternative that performed well retrieving bottom reflectance up to 600 nm, in areas shallower than 5 m. This method is advantageous since it allows to retrieve both depth and bio-optical information for each spectrum to be corrected. When working with an image, this means that all this information is retrieved for each of the pixels. Lee et al. (1999) inversion method also compensate for biases associated with the instrument used to collect radiance measurements, which explained in part, its good performance when applied to *in situ* hyperspectral data. In the ACRB, the correction of the water column effect represented the main challenge when using above-water spectra to study the benthic communities or to map the sea bottom. Waters in the ACRB were characterized as Case-2 waters (at least for the summer campaigns analyzed in the present work), and showed strong spatial heterogeneities, which demanded accurate measurements of absorption and backscattering coefficients, as well as depths, to obtain accurate bottom reflectance spectra. The adaptation of the Lee et al. inversion technique to be applied to multispectral data for high resolution satellite applications, should be encouraged for further works. LIDAR surveys, complementary to the WV02 information, are desirable to be obtained in the study area, which can help in different steps, either to be used as input in the forward model to retrieve bottom reflectance or for the validation of bathymetry retrievals derived from optical remote sensing data.

The second challenge faced in this work was the spectral entanglement of benthic targets. Spectral information of the benthic communities that could be considered ideal in the point of view of remote sensing, was used in the present study. This information

was collected over sites with shallow depths (lower than 5 m), without atmospheric interferences, because radiometry was collected *in situ*, over the entire visible spectra with narrow bands. Bio-optical information at each site was also collected at the same time of the radiometric measurements. Despite that the environmental noises contained in the collected reflectance spectra were effectively reduced applying filters and correction schemes, and that reasonable bottom reflectance values up to 600 nm were possible to retrieve, the benthic communities in the ACRB with subtle differences in coverage were not possible to be spectrally separated. This implies that monitoring programs may demand more frequent field surveys, since remote sensing could not capture subtle changes in the coverage of benthic classes. The number of samples analyzed was too low for a robust identification of diagnostic bands or spectral regions that allowed a finer differentiation on the level of biological communities. However, even if some spectral features were found using a larger pool of data, they should not be so intensively present in any spectra, due to the spectral mixture intrinsic to the benthic communities. Depending on the characteristics of the benthic communities inhabiting the coral reefs, as well the optical properties of the water column, the utilization of a large number of thematic classes to perform a bottom type map using remote sensing data could entail to low mapping accuracies.

In this work, the bottom characteristics of the *Parcel dos Abrolhos* within the ACRB, was inspected for the first time using high spatial resolution remote sensing data. Due to the spectral confusion of the benthic communities and the low performance of the water column correction applied to the WV02 image, a reduced number of thematic classes was chosen for the bottom type mapping. The isolated reefs covered an area of approximately 22 km<sup>2</sup> that corresponded to 12.4% of the total area. Chapeirões were distributed almost in all the studied area, formed by patches of different bottom types, covering different areas. Macroalgae was the most abundant class in the scene, and was concentrated around the Archipelago and inter-reef areas. A greater quantity of ground points are needed for a more robust map validation and should be collected in further works, covering all the area imaged by the WV02 sensor at the ACRB.

The present work was a first attempt to explore the potential of remote sensing applications to map the bottom types of the coral reefs of the ACRB using high resolution imagery. High challenges were pointed out, mainly associated to the water

column correction and spectral mixture of the benthic communities. The main recommendations pointed out are the improvements of water column correction models adapted for multispectral high resolution imagery and a greater effort of field campaigns in the Abrolhos Coral Reef Bank to characterize the spectral properties of the benthic assemblages and their typical distribution, as well as a finer characterization of the water column properties, (including winter campaigns), and a fine resolution bathymetry map that may be provided by LIDAR surveys. Building a comprehensive *in situ* data base covering the ACRB, further works may improve benthic type mapping using high resolution imagery for ecosystem functioning studies, to monitoring environmental changes and for management strategies of the National Park.

## REFERENCES

- ACKLESON, S.G.; KLEMAS, V. Remote-sensing of submerged aquatic vegetation in lower Chesapeake Bay. A comparison of LANDSAT MSS to TM imagery. **Remote Sensing of Environment**, v. 22, n.2, p. 235–248, 1987.
- AMADO-FILHO, G. M.; MOURA, R. L.; BASTOS, A. C.; SALGADO, L. T.; SUMIDA, P. Y.; GUTH, A. Z.; FRANCINI-FILHO, R. B.; PEREIRA-FILHO, G. H.; ABRANTES, D. P.; BRASILEIRO, P. S.; BAHIA, R. G.; LEAL, R. N.; KAUFMAN, L.; KLEYPAS, J. A.; FARINA, M. THOMPSON, F. L. Rhodolith Beds Are Major CaCO<sub>3</sub> Bio-Factories in the Tropical South West Atlantic. **PLoS ONE** v. 7, n. 4, p. e35171. doi:10.1371/journal.pone.0035171, 2012.
- ANDRÉFOÜET, S. Coral Reef Habitat Mapping using Remote Sensing: A User vs Producer Perspective. Implications for Research, Management and Capacity Building. **Journal of Space Science**, v. 53, p.113-130, 2008.
- ANDRÉFOÜET, S.; DIRBERG, G. **Cartographie et inventaire du système récifal de Wallis, Futuna et Alofi par imagerie satellitaire Landsat 7 ETM+ et orthophotographies aériennes à haute résolution**. 10 Noumea, IRD, 2006, 53p.: Sci. Mer; Biol. Mar.Report Conventions.
- ANDRÉFOÜET, S.; GUZMAN, H. Coral reef distribution, status and geomorphology biodiversity relationship in Kuna Yala (San Blas) archipelago, Caribbean Panama. **Coral Reefs**, v. 24, p. 31-42, 2005.
- ANDRÉFOÜET, S.; KRAMER, P.; TORRES-PULLIZA, D.; JOYCE, K.E.; HOCHBERG, E.J.; GARZA-PEREZ, R.; MUMBY, P.; RIEGL, B.; YAMANO, H.; WHITE, W.H.; ZUBIA, M.; BROCK, J.C.; PHINN, S.R.; NASEER, A.; HATCHER, B.G.; MULLER-KARGER, F.E. Multi-site evaluation of IKONOS data for classification of tropical coral reef environments. **Remote Sensing of Environment**, v. 88, p. 128–143, 2003.
- ANDRÉFOÜET, S.; WANTIEZ, L. Characterizing the diversity of coral reef habitats and fish communities found in a UNESCO World Heritage Site: The strategy developed for Lagoons of New Caledonia. **Marine Pollution Bulletin**, v. 61, n. 7, p. 612-620, 2010.
- ANDRÉFOÜET, S.; ZUBIA, M.; PAYRI, C. ; Mapping and biomass estimation of the invasive brown algae *Turbinaria ornata* (Turner) *J. Agardh* and *Sargassum angarevense* (Grunow) Setchell on heterogeneous Tahitian coral reefs using 4-meter resolution IKONOS satellite data. **Coral Reefs**, v. 23, p. 26–38, 2004.
- BEJARANO, S.; MUMBY, P.J.; HEDLEY, J.D.; SOTHERAN, I. Combining optical and acoustic data to enhance the detection of Caribbean forereef habitats. **Remote Sensing of Environment**, v. 114, n. 11, p. 2768-2778, 2010.
- BENFIELD, S.L.; GUZMAN, H.M.; MAIR, J.M.; YOUNG, J.A.T. Mapping the distribution of coral reefs and associated sublittoral habitats in Pacific Panama: a

comparison of optical satellite sensors and classification methodologies. **International Journal of Remote Sensing**, v. 28, n. 22, p. 5047-5070, 2007.

BERNER, T. Coral-reef algae. In: Z. DUBINSKY (Ed.). **Ecosystems of the World 25: Coral Reefs**. Amsterdam: Elsevier, 1990. p. 253–264.

BERTELS, L.; VANDERSTRAETE, T.; VAN COILLIE, S.; KNAEPS, E.; STERCKX, S.; GOOSSENS, R.; DERONDE, B. Mapping of coral reefs using hyperspectral CASI data; a case study: for data, Tanimbar, Indonesia. **International Journal of Remote sensing**, v. 29, n. 8, p. 2359-2391, 2008.

BIDIGARE, R. R., ONDRUSEK, M. E., MORROW, J. H.; KIEFER, D. A. In vivo absorption properties of algal pigments. **Proceedings of Ocean Optics X**, SPIE Orlando, FL: SPIE v. 1302, p. 290–302, 1990.

BIERWIRTH, P.; LEE, T.; BURNE, R. Shallow sea floor reflectance and water depth derived by unmixing multispectral imagery. **Photogrammetric Engineering and Remote Sensing**, v. 59, n. 3, p. 331-338, 1993.

BLASCHKE, T.; LANG, S.; HAY, G. **Object-based image analysis: spatial concepts for knowledge-driven remote sensing applications**. Springer, 2008. 817p. Lecture Notes in Geoinformation and Cartography.

BOTHA, E.J.; BRANDO, V.E.; ANSTEE, J.M.; DEKKER, A.G.; SAGAR, S.; Increased spectral resolution enhances coral detection under varying water conditions. **Remote Sensing of Environment**, v. 131, p. 247-261, 2013.

BOUVET, G.; FERRARIS, J.; ANDRÉFOUËT, S. Evaluation of large-scale unsupervised classification of New Caledonia reef ecosystems using Landsat 7 ETM+ imagery. **Oceanologica Acta**, v. 26, n. 3, p. 281-290, 2003.

BRANDO V.E.; ANSTEE, J.M.; WETTLE, M.; DEKKER, A.G.; PHINN, S.R.; ROELFSEMA, C. A physics based retrieval and quality assessment of bathymetry from suboptimal hyperspectral data. **Remote Sensing of Environment**, v. 113, n. 4, p. 755-770, 2009.

BRICAUD, A.; MOREL, A.; PRIEUR, L. Absorption by dissolved organic matter of the sea (yellow substance) in the UV and visible domains. **Limnology and Oceanography**, v. 26, n. 1, p. 43-53, 1981.

BROCK, J.C.; PURKIS, S. The Emerging Role of LIDAR Remote Sensing in Coastal Research and Resource Management. **Journal of Coastal Research**, p. 1-5, 2009.

BROCK, J.C.; WRIGHT, C.W.; CLAYTON, T.D.; NAYEGANDHI, A. LIDAR optical rugosity of coral reefs in Biscayne National Park, Florida. **Coral Reefs**, v. 23, n. 1, p. 48-59, 2004.

BRUCE, T.; MEIRELLES, P.M.; GARCIA, G.; PARANHOS, R.; REZENDE, C.E., MOURA, R.L.; FRANCINI-FILHO, R.; CONI, E.O.C.; VASCONCELOS, A.T.; AMADO FILHO, G.; HATAY, M.; SCHMIEDER, R.; EDWARDS, R.; DINSDALE,

E.; THOMPSON, F.L. Abrolhos Bank Reef Health Evaluated by Means of Water Quality, Microbial Diversity, Benthic Cover, and Fish Biomass Data. **PloS ONE**, v. 7, n. 6, p. e36687, 2012. doi:10.1371/journal.pone.0036687, 2012.

CALL, K.A.; HARDY, J.T.; WALLIN, D.O. Coral reef habitat discrimination using multivariate spectral analysis and satellite remote sensing. **International Journal of Remote Sensing**, v. 24, n. 13, p. 2627-2639, 2003.

CHARPY, L.; CASARETO, B.E.; LANGLADE, M, J. SUZUKI, Y. Cyanobacteria in Coral Reef Ecosystems: A Review. **Journal of Marine Biology**, v. 2012, 2012.

CIRAOLO, G.; COX, E.; LA LOGGIA, G.; MALTESE, A. The classification of submerged vegetation using hyperspectral MIVIS data. **Annals of Geophysics**, v. 49 p. 287-294, 2006.

CLARK, C.D.; MUMBY, P.J.; CHISHOLM, J.R.M.; JAUBERT, J.; ANDREFOUET, S. Spectral discrimination of coral mortality states following a severe bleaching event. **International Journal of Remote Sensing**, v. 21, n. 11, p. 2321-2327, 2000.

CLARK, R. N.; ROUSH, L. T. Reflectance spectroscopy: Quantitative analysis techniques for remote sensing applications. **Journal of Geophysical Research: Solid Earth (1978–2012)**, v. 89, n. B7, p. 6329-6340.

CLAYTON, R.K.. **Light and Living Matter: A Guide to the Study of Photobiology 1: The Physical Part**. New York: R.E. Krieger Pub. Co., 1971.

COLLIN, A.; PLANES, A. 2012, Enhancing coral health detection using spectral diversity indices from WorldView-2 imagery and machine learners. **Remote Sensing**, v. 4, n. 10, p. 3244-3264, 2012.

CONGALTON, R. AND GREEN, K. **Assessing the accuracy of remotely sensed data: Principles and practices**. New-York: Lewis Publishers, 1999. 137 p.

CONGALTON, R.G., A review of assessing the accuracy of classification of remotely sensed data. **Remote Sensing of Environment**, v. 37, n. 1, p. 35-46, 1991.

CONGER, C.L.; HOCHBERG, E.J.; FLETCHER, C.H.; ATKINSON, M.J. Decorrelating remote sensing color bands from bathymetry in optically shallow waters. **Geoscience and Remote Sensing, IEEE Transactions on**, v. 44, n. 6, p. 1655-1660, 2006.

CONNELL, J. H. Disturbance and recovery of coral assemblages. **Coral reefs**, v. 16, n. 1, p. S101-S113, 1997.

CONNELL, J.H. Diversity in tropical rain forests and coral reefs. **Science**, v. 199, n. 4335, p. 1302-1310, 1978.

CZECZUGA, B. Muxatoxanthin, the dominant carotenoid in lichens of the *Xanthoria* group. **Biochemical Systematics and Ecology**. v.11, n. 329, 1983.

DAWES, C. J. **Marine botany**. 2. ed. John Wiley & Sons, 1998.

DEKKER, A.G.; PHINN, S.R.; ANSTEE, J.; BISSETT, P.; BRAND, V.E.; CASEY, B.; FEARN, P.; HEDLEY, J.; KLONOWSKI, W.; LEE, Z.P.; LYNCH, M.; LYONS, M.; MOBLEY, C.; ROELFSEMA, C. Intercomparison of shallow water bathymetry, hydro-optics, and benthos mapping techniques in Australian and Caribbean coastal environments. **Limnology and Oceanography: Methods**, v. 9, p. 396-425, 2011.

DIGITAL GLOBE. **Radiometric Use of WorldView-2 Imagery**. DigitalGlobe®, Inc. 2010. Technical Note.

DOVE SG, TAKABAYASHI M, HOEGH-GULDBERG, O. Isolation and partial characterization of the pink and blue pigments of pocilloporid and acroporid corals. **The Biological Bulletin**, v. 189, n. 3, p. 288-297, 1995.

DUSTAN, P.; DOBSON, E.; NELSON, G. Landsat Thematic Mapper: Detection of Shifts in Community Composition of Coral Reefs. **Conservation Biology**, v.15, p. 892-902, 2001.

DUTRA, L.X.C.; KIKUCHI, R.K.P.; LEO, Z.M.A.N. Effects of Sediment Accumulation on Reef Corals From Abrolhos, Bahia, Brazil. **Journal of Coastal Research**, p. 633-638, 2006.

ELDVIDGE, C.D.; DIETZ, J.B.; BERKELMANS, R.; ANDRÉFOUËT, S.; SKIRVING, W.; STRONG, A.E.; TUTTLE, B.T.; Satellite observation of Keppel Islands (Great Barrier Reef) 2002 coral bleaching using IKONOS data. **Coral Reefs**, v. 23, n. 1, p. 123-132, 2004.

ENRIQUEZ, S., AGUSTI, S., DUARTE, C.M., Light absorption by marine macrophytes. **Oecologia**, v. 98, p. 121–129, 1994.

FEARN, P.R.C.; KLONOWSKI, W.; BABCOCK, R.C.; ENGLAND, P.; PHILLIPS, J. Shallow water substrate mapping using hyperspectral remote sensing. **Continental Shelf Research**, v. 31, n. 12, p. 1249-1259, 2011.

FLATAU, P.J.; FLATAU, M.; ZANEVELD, J.R.V.; MOBLEY, C.D. Remote sensing of bubble clouds in sea water. **Quarterly Journal of the Royal Meteorological Society**, v. 126, n. 568, p. 2511-2523, 2000.

FLATAU, P.J.; JACEK PISKOZUB, J.; ZANEVELD, J.R.V. Asymptotic light field in the presence of a bubble-layer. **Optics Express**, v. 5, n. 5, p. 120-124, 1999.

FOUGNIE, B.; FROUIN, R.; LECOMTE, P.; DESCHAMPS, P. Y. Reduction of skylight reflection effects in the above-water measurement of diffuse marine reflectance. **Applied Optics**, v. 38, n. 18, p. 3844–56, 20 jun. 1999.

FOX, D.L.; WILKIE, D.W. Somatic and skeletally fixed carotenoids of the purple hydrocoral *Allopora californica*. **Comparative Biochemistry and Physiology**, v. 36, p. 49–60, 1970.

FRANCINI-FILHO, R.B.; MOURA, R.L. Dynamics of fish assemblages on coral reefs subjected to different management regimes in the Abrolhos Bank, eastern Brazil. **Aquatic Conservation: Marine and Freshwater Ecosystems**, v. 18, n. 7, p. 1166-1179, 2008.

FYFE, S.K. Spatial and temporal variation in spectral reflectance: Are seagrass species spectrally distinct? **Limnology and Oceanography**, v. 48, n. 1, p. 464-479, 2003.

GAGNON, A.C.; ADKINS, J.F.; FERNANDEZ, D.P.; ROBINSON, L.F. Sr/Ca and Mg/Ca vital effects correlated with skeletal architecture in a scleractinian deep-sea coral and the role of Rayleigh fractionation. **Earth and Planetary Science Letters**, v. 261, n. 1, p. 280-295, 2007.

GEGE, P. **The Water Colour Simulator WASI**. User manual for version 4. DLR Internal Report IB 564-01/12. 2012. 94 p.

GOODMAN, J.A.; LEE, Z.; USTIN, S.L. Influence of atmospheric and sea-surface corrections on retrieval of bottom depth and reflectance using a semi-analytical model: a case study in Kaneohe Bay, Hawaii. **Applied Optics**, v. 47, n. 28, p. F1-F11, 2008.

GOODMAN, J.A.; USTIN, S.L. Classification of benthic composition in a coral reef environment using spectral unmixing. **Journal of Applied Remote Sensing**, v. 1, n. 1, p. 011501-011501-17, 2007.

GORDON, H.R. Radiative Transfer in the Ocean: A Method for Determination of Absorption and Scattering Properties, **Applied Optics**, 15, 2611-2613, 1976.

GORDON, H.R. Simple Calculation of the Diffuse Reflectance of the Ocean. **Applied Optics**, v. 12, n. 12, p. 2803-2804, 1973.

GORDON, H.R., MOREL, A. **Remote Assessment of Ocean Color for Interpretation of Satellite Visible Imagery, a Review**, Lecture Notes on Coastal and Estuarine Studies, 4; Springer-Verlag, New York. 1983. 114 p.

GORDON, H.R.; BROWN, O.B. Influence of bottom depth and albedo on the diffuse reflectance of a flat homogeneous ocean. **Applied Optics**, v. 13, n. 9, p. 2153-2159, 1974.

GORDON, H.R.; BROWN, O.B. Irradiance reflectivity of a flat ocean as a function of its optical properties. **Applied Optics**, v. 12, n. 7, p. 1549-1551, 1973.

GORDON, H.R.; MCCLUNEY, W.R. Estimation of the Depth of Sunlight Penetration in the Sea for Remote Sensing. **Applied Optics**, v. 14, n. 2, p. 413-416, 1975.

GOULD, R.W.; ARNONE, R.A. Optical water mass classification for ocean color imagery. In: INTERNATIONAL CONFERENCE, CURRENT PROBLEMS IN OPTICS OF NATURAL WATERS, 2., 2003, St. Petersburg, Russia. **Proceedings...** St. Petersburg, 2003.

GREEN, E.P.; MUMBY, P.J.; EDWARDS, A.J.; CLARK, C.D. **Remote sensing handbook for tropical coastal management**. Paris: UNESCO. 2000. 316 p.

HAMEL, M. A.; ANDRÉFOUËT, S. Using very high resolution remote sensing for the management of coral reef fisheries: review and perspectives. **Marine Pollution Bulletin**, v. 60, n. 9, p. 1397–405, 2010.

HAMYLTON, S. An evaluation of waveband pairs for water column correction using band ratio methods for seabed mapping in the Seychelles. **International Journal of Remote Sensing**, v. 32, n. 24, p. 9185-9195, 2011.

HAN, J., KAMBER, M. **Data mining, Concepts and techniques**. 2. ed. San Francisco, USA: Elsevier, 2006. 743 p.

HANNACH, G. Spectral light absorption by intact blades of *Porphyra abbotiae* (Rhodophyta): Effects of environmental factors in culture. **Journal of Phycology**, 25, 522-529, 1989.

HARDY, J. HOGE, F., YUNGEL, J., DODGE, R. Remote detection of coral bleaching using pulsed-laser fluorescence spectroscopy. **Marine Ecology Progress Series**, v. 88, p. 247, 1992.

HEDLEY, J.D.; MUMBY, P.J.; JOYCE, K.E.; PHINN, S.R.; Spectral unmixing of coral reef benthos under ideal conditions, **Coral Reefs**, v. 23, n. 1, p. 60-73, 2004.

HEDLEY, J. D.; MUMBY, P. J. Biological and remote sensing perspectives of pigmentation in coral reef organisms. **Advances in Marine Biology**, v. 43, p. 277-317, 2002.

HEDLEY, J. ROELFSEMA, C. M., PHINN, S.R., MUMBY, P.J. . Environmental and Sensor Limitations in Optical Remote Sensing of Coral Reefs: Implications for Monitoring and Sensor Design. **Remote Sensing**, v. 4, n. 1, p. 271-302, 2012.

HEDLEY, J.; ROELFSEMA, C.; PHINN, S.R. Efficient radiative transfer model inversion for remote sensing applications. **Remote Sensing of Environment**, v. 113, n. 11, p. 2527-2532, 2009.

HEDLEY, J.D.; HARBORNE, A.R.; MUMBY, P.J. Simple and robust removal of sun glint for mapping shallow-water benthos. **International Journal of Remote Sensing**, v. 26, n. 10, p. 2107-2112, 2005.

HOCHBERG, E. J.; ATKINSON, M. J. Spectral discrimination of coral reef benthic communities. **Coral Reefs**, v. 19, n. 2, p. 164-171, 2000.

HOCHBERG, E.J.; ATKINSON M.J.; APPRILL, A.; ANDRÉFOUËT, S. Spectral reflectance of coral. **Coral Reefs**, v. 23, n. 1, p. 84-95, 2004.

HOCHBERG, E.J.; ATKINSON, M.J. Capabilities of remote sensors to classify coral, algae, and sand as pure and mixed spectra. **Remote Sensing of Environment**, v. 85, n. 2, p. 174-189, 2003.

HOCHBERG, E.J.; ATKINSON, M.J. Coral reef benthic productivity based on optical absorptance and light-use efficiency. **Coral Reefs**, v. 27, n. 1, p. 49-59, 2008.

HOCHBERG, E.J.; ATKINSON, M.J.; ANDRÉFOUËT, S.; Spectral reflectance of coral reef bottom-types worldwide and implications for coral reef remote sensing, **Remote Sensing of Environment**, v. 85, n. 2, p. 159-173, 2003.

HOEGH-GULDBERG, O. Climate change, coral bleaching and the future of the world's coral reefs. **Marine and Freshwater Research**, v. 50, n. 8, p. 839 - 866, 1999.

HOEGH-GULDBERG, O.; MUMBY, P.J.; HOOTEN, A.J.; STENECK, R.S.; GREENFIELD, P.; GOMEZ, E.; HARVELL, C.D.; SALE, P.F.; EDWARDS, A.J.; CALDEIRA, K.L.; KNOWLTON, N.; EAKIN, C.M.; IGLESIAS-PRIETO, R.; MUTHIGA, N.; BRADBURY, R.H.; DUBI, A.; HATZIOLOS, M.E. Coral reefs under rapid climate change and ocean acidification. **Science**, v. 318, n. 5857, p. 1737-1742, 2007.

HOGUE, F.E.; VODACEK, A.; BLOUGH, N.V. Inherent optical properties of the ocean: Retrieval of the absorption coefficient of chromophoric dissolved organic matter from fluorescence measurements. **Limnology and Oceanography**, v. 38, n. 7, p. 1394-1402, 1993.

HOLDEN, H.; LEDREW, E. Spectral discrimination of healthy and non-healthy corals based on cluster analysis, principal components analysis, and derivative spectroscopy. **Remote Sensing of Environment**, v. 65, n. 2, p. 217-224, 1998.

HOLDEN, H.; LEDREW, E.; Hyperspectral identification of coral reef features. **International Journal of Remote Sensing**, v. 20, n. 13, p. 2545-2563, 1999.

HOLDEN, H.; LEDREW, E.; The scientific issues surrounding remote detection of submerged coral ecosystems. **Progress in Physical Geography**, v. 22, n. 2, p. 190-221, 1998.

HOLDEN, H.; LEDREW, E. An Examination of Variability in Vertical Radiometric Profiles in a Coral Reef Environment. **Journal of Coastal Research**, p. 224-231, 2008.

HOOKER, S.; MOREL, A. Platform and environmental effects on above-water determinations of water-leaving radiances. **Journal of Atmospheric and Oceanic Technology**, p. 187-205, 2003.

HUOT, Y.; BROWN, C.A.; CULLEN, J.J.; Retrieval of phytoplankton biomass from simultaneous inversion of reflectance, the diffuse attenuation coefficient, and Sun-induced fluorescence in coastal Waters. **Journal of Geophysical Research: Oceans (1978-2012)**, v. 112, n. C6, 2007.

IOCCG: **Remote Sensing of Ocean Colour in Coastal, and Other Optically-Complex, Waters**. SATHYENDRANATH, S. Ed. Reports of the International Ocean-Colour Coordinating Group, No. 3, IOCCG, Dartmouth, Canada. 2000. 140 p.

- IOCCG: **Atmospheric Correction for Remotely-Sensed Ocean-Colour Products**. WANG, M. Ed. Reports of the International Ocean-Colour Coordinating Group, No. 10, IOCCG, Darmtmouth, Canada. 2010. 78 p.
- ISOUN, E.; FLETCHER, C.; FRAZER, N. GRADIE, J. Multi-spectral mapping of reef bathymetry and coral cover Kailua Bay, Hawaii. **Coral Reefs**, v. 22, n. 1, p. 68-82, 2003.
- JERLOV, N.G. Optical studies of ocean water. **Rep. Swedish Deep-Sea Exp.**, v. 3, n. 1, p.1-69, 1951.
- KANNO, A.; TANAKA, Y. Modified Lyzenga's method for estimating generalized coefficients of satellite-based predictor of shallow water depth. **Geoscience and Remote Sensing Letters, IEEE**, v. 9, n. 4, p. 715-719, 2012.
- KAY, S.; HEDLEY, J.D.; LAVENDER, S. Sun Glint Correction of High and Low Spatial Resolution Images of Aquatic Scenes: a Review of Methods for Visible and Near-Infrared Wavelengths. **Remote Sensing**, v. 1, n. 4, p. 697-730, 2009.
- KINSEY, D. W. Metabolism, calcification and carbon production I: systems level studies. In: INTERNATIONAL CORAL REEF CONGRESS, 5., 1985, Tahiti, Moorea, French, Polynesia. **Proceedings...** Thaiti: Antenne Museum- EPHE, 1985. v. 4, p. 505–526.
- KIRK, J. T. O. **Light and photosynthesis in aquatic ecosystems**. Cambridge: Cambridge University Press, 1983. 401 p.
- KIRK, J. T. O. **Light and photosynthesis in aquatic ecosystems**. 3. ed. Cambridge: Cambridge University Press, 2011. 649 p.
- KIRK, J.T.O. The vertical attenuation of irradiance as a function of the optical properties of the water. **Limnology and Oceanography**, v. 48, n. 1; NUMB 1, p. 9-17, 2003.
- KLONOWSKI, W.M.; FEARNES, P.R.C.S.; LYNCH, M.J. Retrieving key benthic cover types and bathymetry from hyperspectral imagery. **Journal of Applied Remote Sensing**, v. 1, n. 1, p. 011505-011505-21, 2007.
- KNOPPERS, B., MEYERHOFER, M., MARONE, E., DUTZ, J., LOPEZ, R., LEIPE, T.,CAMARGO, R.. Compartments of the pelagic system and material exchange at the Abrolhos Bank Coral Reef, Brazil. **Archives of Fisheries and Marine Research**. v. 47, n.2/3, p. 285–306, 1999.
- KNUDBY, A.; LEDREW, E.; BRENNING, A. Predictive mapping of reef fish species richness, diversity and biomass in Zanzibar using IKONOS imagery and machine-learning techniques. **Remote Sensing of Environment**, v. 114, n. 6, p. 1230-1241, 2010.

KNUDBY, A.; LEDREW, E.; NEWMAN, C. Progress in the use of remote sensing for coral reef biodiversity studies. **Progress in Physical Geography**, v. 31, n. 4, p. 421-434, 2007.

KOBRYN, H.T.; WOUTERS, K.; BECKLEY, L.E.; HEEGE, T.; Ningaloo Reef: Shallow Marine Habitats Mapped Using a Hyperspectral Sensor. **PloS ONE**, v. 8, n. 7, p. e70105, 2013.

KOKALY, R. E.; CLARK, R. N. Spectroscopic determination of leaf biochemistry using band-depth analysis of absorption features and stepwise multiple linear regression. **Remote Sensing of Environment**, v. 67, n. 3, p. 267-287, 1999.

KRUSE, F.; LEFKOFF, A.; BOARDMAN, A.B.; HEIDEBRECHT, K.B.; SHAPIRO, A.T.; BARLOON, P.J.; GOETZ, A.F.H. The Spectral Image Processing System (SIPS) dinteractive visualization and analysis of imaging spectrometer data. **Remote Sensing of Environment**, v. 44, n. 2, p. 145-163, 1993.

KUTSER, T.; JUPP, D. L. B.; On the possibility of mapping living corals to the species level based on their optical signatures. **Estuarine, coastal and shelf science**, v. 69, n. 3, p. 607-614, 2006.

LEÃO, Z. M. A. N. **Morphology, geology and developmental history of the southernmost coral reefs of Western Atlantic, Abrolhos Bank, Brazil**. 1982, 218 p. PhD thesis. (Doctor of Philosophy) - Rosenstiel School of Marine and Atmospheric Studies, Miami, Florida.

LEÃO, Z. M. A. N. Abrolhos - O complexo recifal mais extenso do Oceano Atlântico Sul. In: SCHOBENHAUS, C.; CAMPOS, D.A.; QUEIROZ, E.T.; WINGE, M.; BERBERT-BORN, M. (Eds.) **Sítios Geológicos e Paleontológicos do Brasil**. 1999. Disponível em: Published online at <http://sigep.cprm.gov.br/sitio090/sitio090.htm>. Acesso em: 20 out. 2014.

LEE, Z.; CARDER, K.L.; CHEN, R.F.; PEACOCK, T.G. Properties of the water column and bottom derived from Airborne Visible Infrared Imaging Spectrometer (AVIRIS) data. **Journal of Geophysical Research: Oceans (1978–2012)**, v. 106, n. C6, p. 11639-11651, 2001.

LEE, Z.; CARDER, K.L.; MOBLEY, C.D.; STEWARD, R.G.; PATCH, J.S. Hyperspectral remote sensing for shallow waters: 2. Deriving bottom depths and water properties by optimization. **Applied Optics**, v. 38, n. 18, p. 3831-3843, 1999.

LEE, Z.; CASEY, B.; ARNONE, R.; WEIDEMANN, A.; PARSONS, R.; MONTES, M.J.; GAO, B.; GOODE, W.; DAVIS, C.O; DYE, J. Water and bottom properties of a coastal environment derived from Hyperion data measured from the EO-1 spacecraft platform. **Journal of Applied Remote Sensing**, v. 1, n. 1, p. 011502-011502-16, 2007.

LEE, Z.P.; CARDER K.L.; MOBLEY, C.D.; STEWARD, R.G.; PATCH, J.S. Hyperspectral remote sensing for shallow waters: 1. A semianalytical model. **Applied Optics**, v. 37, n. 27, p. 6329-6338, 1998.

LEE, Z.P.; CARDER, K.L.; ARNONE, R.A. Deriving inherent optical properties from water color: a multiband quasi-analytical algorithm for optically deep waters. **Applied Optics**, v. 41, n. 27, p. 5755-5772, 2002.

LEE, Z.P.; DARECKI, M.; CARDER, K.L.; DAVIS, C.O.; STRAMSKI, D.; RHEA, W.J. Diffuse attenuation coefficient of downwelling irradiance: An evaluation of remote sensing methods. **Journal of Geophysical Research: Oceans (1978–2012)**, v. 110, n. C2, 2005.

LEIPE, T.; KNOPPERS, B.; MARONE, E.; CAMARGO, R. Suspended matter transport in coral reef waters of the Abrolhos Bank, Brazil. **Geo-Marine Letters**, v. 19, n. 3, p. 186-195, 1999.

LIM, A.; HEDLEY, J. D.; LEDREW, E.; MUMBY, P. J.; ROELFSEMA, C. The effects of ecologically determined spatial complexity on the classification accuracy of simulated coral reef images, **Remote Sensing of Environment**, v. 113, n. 5, p. 965-978, 2009.

LOUCHARD, E.M.; REID, R.P.; STEPHENS, F.C.; CURTISS, O.; DAVIS, R.A.; LEATHERS, R.A.; DOWNES T.V. Optical remote sensing of benthic habitats and bathymetry in coastal environments at Lee Stocking Island, Bahamas: a comparative spectral classification approach. **Limnology and Oceanography**. v. 48, p. 511–521, 2003.

LUCZKOVICH, J.; WAGNER, T.; MICHALEK, J.; STOFFLE, R. Discrimination of coral reefs, seagrass meadows, and sand bottom types from space: A Dominican Republic case study. **Photogrammetric Engineering and Remote Sensing**, v. 59, n. 3, p. 385-389, 1993.

LUTZ, V. A.; SEGURA, V.; DOGLIOTTI, A. I.; GAGLIARDINI, D. A.; BIANCHI, A. A.; BALESTRINI, C. F. Primary production in the Argentine Sea during spring estimated by field and satellite models. **Journal of Plankton Research**, v. 32, n. 2, p. 181–195, 28 2010.

LYZENGA, D. Passive remote sensing techniques for mapping water depth and bottom features. **Applied Optics**, v. 17, n. 3, p. 379-383, 1978.

LYZENGA, D.R. Remote sensing of bottom reflectance and water attenuation parameters in shallow water using aircraft and Landsat data. **International Journal of Remote Sensing**, v. 2, n. 1, p. 71-82, 1981.

LYZENGA, D.R.; MALINAS, N.P.; TANIS, F.J. Multispectral bathymetry using a simple physically based algorithm **Remote Sensing, IEEE Transactions on**, v. 44, n. 8, p. 2251-2259, 2006.

MARITORENA, S. Remote sensing of the water attenuation in coral reefs a case study in French Polynesia. **International Journal of Remote Sensing**, v. 17, n. 1, p. 155-166, 1996.

MARITORENA, S.; MOREL, A.; GENTILI, B. Diffuse reflectance of oceanic shallow waters: influence of water depth and bottom albedo. **Limnology and Oceanography**, v. 39, n. 7, p. 1689-1703, 1994.

MAZEL, C. H. Spectral measurements of fluorescence emission in Caribbean cnidarians. **Marine Ecology Progress Series**, v. 120, p. 185-191, 1995.

MCMANUS, J.W.; MEÑEZ, L. A. B., KESNER-REYES, K.N.; VERGARA, S.G.; ABLAN, M.C. Coral reef fishing and coral-algal phase shifts: implications for global reef status. **ICES Journal of Marine Science: Journal du Conseil**, v. 57, n. 3, p. 572-578, 2000.

MICHALEK, J.L.; WAGNER, T.W.; LUZKOVICH, J.J.; STOFFLE, R.W. Multispectral change vector analysis for monitoring coastal marine environments. **Photogrammetric Engineering and Remote Sensing**, v. 59, p. 381-384, 1993.

MISHRA, D. R.; NARUMALANI, S.; RUNDQUIST, D.; LAWSON, M. High-resolution ocean color remote sensing of benthic habitats: a case study at the Roatan Island, Honduras. **Geoscience and Remote Sensing, IEEE Transactions on**, v. 43, n. 7, p. 1592-1604, 2005.

MISHRA, D.; NARUMALANI, S.; RUNDQUIST, D.; LAWSON, M. Benthic habitat mapping in tropical marine environments using QuickBird multispectral data. **Photogrammetric Engineering and Remote Sensing**, v.72, p. 1037-1048, 2006.

MITCHELL, B. G. Algorithms for determining the absorption coefficient of aquatic particulates using the Quantitative Filter Technique (QFT). In: R. W. SPINRAD [Ed.], **Ocean Optics X**. SPIE. 1990, p. 137-148.

MITCHELL, B.; KAHRU, M.; WIELAND, J.; STRAMSKA, M. Determination of spectral absorption coefficients of particles, dissolved material and phytoplankton for discrete water samples. In: (FARGION, G.S.; MUELLER, J. L. (Eds.). **Ocean optics protocols for satellite ocean color sensor validation** - revision 2 Greenbelt, MD: NASA. Goddard Space Flight Center. SIMBIOS Project , 2002. P. 39-60. , . NASA TM - 2000 - 209966.

MITCHELL, B.G.; KAHRU, M.; WIELAND, J.; STRAMSKA, M. Determination of spectral absorption coefficients of particles, dissolved material, and phytoplankton for discrete water samples. In: MUELLER, J.; FARGION, J.; MCCLAIN, C.R.(Eds). **Ocean optics protocols for satellite ocean color sensor validation**, revision 4, v.IV: inherent optical properties: instruments, characterizations, field measurements and data analysis protocols.. Greenbelt, Md: NASA. Goddard Space Flight Center. SIMBIOS Project, 2003. p. 125-153. NASA Technical Manual. 2003-211621.

MOBLEY, C. STRAMSKI, D, BISSET, W. P., BOSS, E. Optical modeling of ocean waters: is the Case 1-Case 2 classification still useful? **Oceanography**. v.17, n. 2, p.60-67, 2004.

- MOBLEY, C.D. Estimation of the remote-sensing reflectance from above-surface measurements. **Applied Optics** v.38, p.7442-7455, 1999.
- MOBLEY, C.D. **Light and water: radiative transfer in natural waters**. New York: Academic Press, 1994. 592p.
- MOBLEY, C.D.; SUNDMAN, L.K.; DAVIS, C.O.; BOWLES, J.H.; DOWNES, T.V.; LEATHERS, R.A.; MONTES, M.J.; BISSETT, W.P.; KOHLER, D.D.R.; REID, R.P.; LOUCHARD, E.M.; GLEASON, A. Interpretation of hyperspectral remote-sensing imagery by spectrum matching and Look-Up Tables. **Applied Optics**, v. 44, n. 17, p. 3576-3592, 2005.
- MOREIRA, P.P. **Mapeamento de habitats do recife de coral Pedra de Leste, Abrolhos, utilizando imagens orbitais QuickBird e Landsat7 ETM+**. 2008. f. 117 Dissertação (Mestrado em Sistemas Aquáticos Tropicais) - Universidade Estadual de Santa Cruz, Ilhéus, 2008.
- MOREL, A. Optical modeling of the upper ocean in relation to its biogenous matter content (case I waters). **Journal of Geophysical Research**. v.93, p.10749-10768, 1988.
- MOREL, A. Optical properties of pure water and pure seawater. In: JERLOV, N.G.; STEEMANN, N.E (Eds.). **Optical Aspects of Oceanography**. Academic Press: New York, USA, 1974, 24p.
- MOREL, A., GENTILI, B. A simple band ratio technique to quantify the colored dissolved and detrital organic material from ocean color remotely sensed data. **Remote Sensing of Environment**, v.113, n.5, p.998–1011, 2009.
- MOREL, A.; PRIEUR, L. Analysis of variations in ocean color. **Limnology and Oceanography**, v. 22, n. 4, p. 709-722, 1977.
- MUMBY, P.J.; CLARK, C.D.; GREEN, E.P.; EDWARDS, A.J. Benefits of water column correction and contextual editing for mapping coral reefs. **International Journal of Remote Sensing**, v. 19, n. 1, p. 203-210, 1998.
- MUMBY, P.J.; EDWARDS, A.J. Mapping marine environments with IKONOS imagery: enhanced spatial resolution can deliver greater thematic accuracy. **Remote Sensing of Environment**, v. 82, n. 2, p. 248-257, 2002.
- MUMBY, P.J.; EDWARDS, A.J. Water column correction techniques. In: ; GREEN, E.P.; MUMBY, P.J.; EDWARDS, A.J.; CLARK, C.D. (eds.). **Remote sensing handbook for tropical coastal management**. Paris: UNESCO, 2000. p. 121–128.
- MUMBY, P.J.; GREEN, E.P.; EDWARDS, A.J.; CLARK, C.D. Coral reef habitat mapping: how much detail can remote sensing provide? **Marine Biology**, v. 130, n. 2, p. 193-202, 1997.
- MUMBY, P.J.; GREEN, E.P.; EDWARDS, A.J.; CLARK, C.D. The cost-effectiveness of remote sensing for tropical coastal resources assessment and management. **Journal of Environmental Management**, v. 55, n. 3, p. 157-166, 1999.

MUMBY, P.J.; HEDLEY, J.D.; CHISHOLM, J.R.M.; CLARK, C.D.; RIPLEY, H.; JAUBERT, J. The cover of living and dead corals from airborne remote sensing. **Coral Reefs**, v. 23, n. 2, p. 171-183, 2004.

MYERS. M. R.; HARDY J. T.; MAZEL C. H. ; DUSTAN P. Optical spectra and pigmentation of Caribbean reef corals and macroalgae. **Coral Reefs**, v. 18, n. 2, p. 179-186, 1999.

NICODEMUS, F.; RICHMOND, J.; HSIA, J.; GINSBERG, I.; LIMPERIS, T.; **Geometrical considerations and nomenclature for reflectance**. Washington, DC: National Bureau of Standards (US), 1977.

PALANDRO, D.; ANDRÉFOUËT, S.; HU, C.; HALLOCK, P.; MÜLLER-KARGER, F.E.; DUSTAN, P.; CALLAHAN, M.K.; KRANENBUR, C.; BEAVER, C.R.; Quantification of two decades of shallow-water coral reef habitat decline in the Florida Keys National Marine Sanctuary using Landsat data (1984–2002). **Remote Sensing of Environment**, v.112, p. 3388–3399, 2008.

PHINN, S.R.; ROELFSEMA, C.M. MUMBY, P.J., Multi-scale, object-based image analysis for mapping geomorphic and ecological zones on coral reefs. **International Journal of Remote Sensing**, v. 33, n. 12, p. 3768-3797, 2012.

POPE, R.; FRY, E. Absorption spectrum (380–700 nm) of pure waters: II. Integrating cavity measurements. **Applied Optics**, v. 36, n. 33, p. 8710-8723, 1997.

PU, R.; BELL, S.; MEYER, C.; BAGGETT, L.; ZHAO, Y. Mapping and assessing seagrass along the western coast of Florida using Landsat TM and EO-1 ALI/HYPERION imagery. **Estuarine, Coastal and Shelf Science**, v. 115, p. 234-245, 2012.

PURKIS, S. A “Reef-Up” Approach to Classifying Coral Habitats From IKONOS Imagery. **Ieee Transactions On Geoscience and Remote Sensing**, v. 43, n. 6, p. 1375-1390, 2005.

PURKIS, S.J.; PASTERKAMP, R. Integrating *in situ* reef-top reflectance spectra with LANDSAT TM imagery to aid shallow-tropical benthic habitat mapping. **Coral Reefs** v.23, p.5–20, 2004.

QUINLAN, J. R. **C4. 5: Programs for machine learning**. Morgan Kaufmann, 1993.

RAMUS, J. Seaweed anatomy and photosynthetic performance: the ecological significance of light guides, heterogeneous absorption and multiple scatter. **Journal of Phycology**, v. 14, n. 3, p. 352-362, 1978.

RANDALL, J. E. Grazing effects on seagrasses by herbivorous reef fishes in the West Indies. **Ecology**, v. 46, p. 255–260, 1965.

RICHTER, R; Atmospheric correction of satellite data with haze removal including a haze/clear transition region. **Computers & Geosciences**, v. 22, n. 6, p. 6X-681, 1996.

- ROSENBERG, G., RAMUS, J., Ecological growth strategies in the seaweeds *Gracilaria foliifera* (Rhodophyceae) and *Ulva* sp. (Chlorophyceae): soluble nitrogen and reserve carbohydrates. **Marine Biology**, v. 66, n. 3, p. 251-259, 1982.
- RUDORFF, N.M, FROUIN, R, KAMPEL, M.; GOYENS, C.; MERIAUX, X.; SCHIEBER, B.; MITCHELL, B.G.; Ocean-color radiometry across the Southern Atlantic and Southeastern Pacific: Accuracy and remote sensing implications. **Remote Sensing of Environment**. v. 149, p. 13–32, 2014.
- RUDORFF, N.M.; KAMPEL, M..REZENDE, C.E. Spectral mapping of the Paraíba do Sul River plume (Brazil) using multitemporal Landsat images. **Journal of Applied Remote Sensing**, v. 5, n. 1, p. 053550-053550-19, 2011.
- SAGAWA, T.; BOISNIER, E.; KOMATSU, T.; MUSTAPHA, K.B.; HATTOUR, A.; KOSAKA, N.; MIYAZAKI, A. Using bottom surface reflectance to map coastal marine areas: a new application method for Lyzenga's model. **International Journal of Remote Sensing**, v. 31, n. 12, p. 3051-3064, 2010.
- SALIH, A., LARKUM, A., COX, G., KÜHL, M., HOEGH-GULDBERG, O., Fluorescent pigments in coral are photoprotective. **Nature**, v. 408, n. 6814, p. 850-853, 2000.
- SARANGI, R.K.; CHAUHAN, P., NAYAK, S.R. Detection and monitoring of *Trichodesmium* blooms in the coastal waters off Saurashtra coast, India using IRS-P4 OCM data. **Current Science**, v. 86, n.12, 2004.
- SATOH, S.; Ikeuchi, M.; Mimuro, M.; Tanaka, A. Chlorophyll *b* Expressed in Cyanobacteria Functions as a Light-harvesting Antenna in Photosystem I through Flexibility of the Proteins. **The Journal Of Biological Chemistry**. v. 276, p. 4293–4297, 2001.
- SCHOTT, J.R.; SALVAGGIO, C.; VOLCHOK, J. radiometric scene normalization using pseudoinvariant features. **Remote Sensing of Environment**, v. 26, n. 1, p. 1-16, 1988.
- SCOPELITIS, J.; ANDRÉFOUËT, S.; PHINN, S.; ARROYO, L.; DALLEAU, M.; CROS, A.; CHABANET, P. The next step in shallow coral reef monitoring: combining remote sensing and in situ approaches, **Marine Pollution Bulletin**, v. 60, n. 11, p. 1956-1968, 2010.
- SEGAL, B.; CASTRO, C.B., Coral community structure and sedimentation at different distances from the coast of the Abrolhos Bank, Brazil. **Brazilian Journal of Oceanography**, v. 59, n. 2, p. 119-129, 2011.
- SEGAL, B.; EVANGELISTA, H.; KAMPEL, M.; GONCALVES, A.C.; POLITO, P.S.; SANTOS, E.A. Potential impacts of polar fronts on sedimentation processes at Abrolhos Coral Reef (South-West Atlantic Ocean/Brazil), **Continental Shelf Research**, v. 28, n. 4, p. 533-544, 2008.

SEGAL-RAMOS, B., **Corais e comunidades recifais e sua relação com a sedimentação no Banco dos Abrolhos, Brasil**. 2003. Tese de doutorado, Universidade Federal do Rio de Janeiro, Rio de Janeiro.2003.

SILVA, A. S.; LEAO, Z.M.A.N.; KIKUCHI, R.K.P.; COSTA, A. B.; SOUZA, J. R. B. Sedimentation in the coastal reefs of Abrolhos over the last decades. **Continental Shelf Research**, v. 70, p. 159–167, 2013.

SILVA, M.P.S.; CAMARA, G.; ESCADA, M.I. S.; SOUZA, R.C.M. **Remote sensing image mining: detecting agents of land-use change in tropical forest areas**. São José dos Campos: INPE, 2008-07-16. (INPE ePrint sid.inpe.br/mtc-m17@80/2007/12.10.13.11). Disponível em: <<http://urlib.net/sid.inpe.br/mtc-m17@80/2007/12.10.13.11>>. Acesso em: 20 out. 2014.

SIMIS, S.G.H.; PETERS, S.W.M.; GONS, H.J. Remote sensing of the cyanobacterial pigment phycocyanin in turbid inland water. **Limnology and Oceanography**, v. 50, p. 237-245, 2005.

SMITH, R.; BAKER, K. Optical properties of the clearest natural waters (200-800 nm). **Applied Optics**, 20, 177-184, 1981.

SMITH, R.; BAKER, K. Analysis of ocean optical data. In: SLATER, P. N. (Ed.). **Ocean Optics VIII**, 1986. SPIE Proceedings.

SMITH, V.E.; ROGERS, R.H.; REED, L.E. Automated mapping and inventory of Great Barrier Reef zonation with Landsat. **Oceans**, v.7, p.775–80, 1975.

SPITZER, D.; DIRKS, R. BOTTOM. Influence on the reflectance of the sea. **International Journal of Remote Sensing**, v. 8, p. 279-290, 1987.

STRAMSKI, D.; BOOTH, C.R.; MITCHELL, B.G. Estimation of downward irradiance attenuation from a single moored instrument. **Deep Sea Research Part A. Oceanographic Research Papers**,v. 39, p.567-584, 1992.

STUMPF, R.P.; *HOLDERIED, K.*, SINCLAIR, K.H.M. Determination of water depth with high-resolution satellite imagery over variable bottom types. **Limnology and Oceanography**, v. 48, p. 547–556, 2003.

SUZUKI R, ISHIMARU T (1990) An improved method for determination of phytoplankton chlorophyll using N, N-dimethylformamide. **Journal of the Oceanographical Society of Japan**, v. 46, n. 4, p. 190-194, 1990.

SYDOR, M.; GOULD, R.W.; ARNONE, R.A.; HALTRIN, V.I. GOODE, W. Uniqueness in remote sensing of the inherent optical properties of ocean water. **Applied Optics**, v. 43, n. 10, p. 2156-2162, 2004.

TASSAN, S. Modified Lyzenga’s method for macroalgae detection in water with non-uniform composition. **International Journal of Remote Sensing**, v. 17, p.1601–1607, 1996.

- TEIXEIRA, C. E. P.; LESSA, G. C.; CIRANO, M.; LENTINI, C. A. D. The inner shelf circulation on the Abrolhos Bank, 18°S, Brazil. **Continental Shelf Research**, v. 70, p. 13–26, 2013.
- UHL, F.; OPPELT, N.; BARTSCH, I. Spectral mixture of intertidal marine macroalgae around the island of Helgoland (Germany, North Sea), **Aquatic Botany**, v.111, p.112-124, 2013.
- VALESINI, F.J.; HOURSTON, M.; WILDSMITH, M.D.; COEN, N.J.; POTTER, I.C. New quantitative approaches for classifying and predicting local-scale habitats in estuaries. **Estuarine, Coastal and Shelf Science**, v. 86, n. 4, p. 645-664, 2010.
- VANDERSTRAETE, T.; GOOSSENS, R.; GHABOUR, T.K. The use of multi-temporal Landsat images for the change detection of the coastal zone near Hurghada, Egypt. **International Journal of Remote Sensing**, v.27, p.3645–3655, 2006.
- VASILKOV, A.P.; GOLDIN, Y.A.; GUREEV, B.A.; HOGE, F.E.; SWIFT, R.N.; WRIGHT, C.W. Airborne polarized LIDAR detection of scattering layers in the ocean. **Applied Optics**, v. 40, n. 24, p. 4353-4364, 2001.
- VERMOTE, E.F.; VIBERT, S.; KILCOYNE, H.; HOYT, D.; ZHAO, T. **Suspended matter** - visible/infrared imager/radiometer suite algorithm theoretical basis document. Maryland: Raytheon Systems Company, Information Technology and Scientific Services, 2002. SBRS Document # Y2390.
- VILLAÇA, R.; PITOMBO, F.B. Benthic communities of shallow-water reefs of Abrolhos, Brazil. **Revista Brasileira de Oceanografia**, v.45, p.35-43, 1997.
- VOGELMANN, T.C.; BJÖRN, L.O. Plants as light traps. **Physiologia Plantarum**, v. 68, n. 4, p. 704-708, 1986.
- WAALAND, J.R.; WAALAND, S.D.; BATES, G.; Chloroplast structure and pigment composition in the red alga griffithsia pacifica: regulation by light intensity. **Journal of Phycology**, v. 10, n. 2, p. 193-199, 1974.
- WABNITZ, C.C.; ANDRÉFOUËT, S.; TORRES-PULLIZA, D.; MÜLLER-KARGER, F.E.; KRAMER, P.A. Regional-scale seagrass habitat mapping in the Wider Caribbean region using Landsat sensors: Applications to conservation and ecology. **Remote Sensing of Environment**, V.112, P. 3455–3467, 2008.
- WITTEN, I.H., FRANK, E., HALL, M.A. **Data mining. Practical machine learning tools and techniques**. 3. ed. Burlington, USA: Elsevier,., 2011. 629 p.
- YAMANO, H.; Multispectral Applications. In: GOODMAN, J.A.; PURKIS, S.J.; PHINN, S.R. (Ed.). **Coral Reef Remote Sensing**. Dordrecht: Springer, , 2013. p. 51-78.
- YANG, C.; YANG, D.; CAO, W.; ZHAO, J.; WANG, G.; SUN, Z.; XU, Z.; RAVI KUMAR, M.S. Analysis of seagrass reflectivity by using a water column correction algorithm. **International Journal of Remote Sensing**, v. 31, p. 4595–4608, 2010.

ZAGALSKY, P. F.; HERRING, P. J. **Philosophical Transactions of the Royal Society of London**. Series B, Biological Sciences, v.279, i. 964, pp. 289-326, 1977.

ZAINAL, A.J.M. New technique for enhancing the detection and classification of shallow marine habitats. **Marine Technology Society Journal**, v. 28, p. 68–74, 1994.

ZANEVLED, J.R.V; BOSS, E. The influence of bottom morphology on reflectance: Theory and two-dimensional geometry model. **Limnology and Oceanography**, v.48, p. 374-379, 2003.

ZHANG, C.; SELCH, D.; XIE, Z.; ROBERTS, C.; COOPER, H.; CHEN, G.; Object-based benthic habitat mapping in the Florida Keys from hyperspectral imagery, **Estuarine, Coastal and Shelf Science**, v. 134, p. 88-97, 2013.

ZIMMERMAN, R. C.; DEKKER, A.G. Aquatic optics: basic concepts for understanding how light affects seagrasses and makes them measurable from space. In: LARKUM, A.W.D; ORTH, R. J.; DUARTE, C. M. (Eds.). **Seagrasses: biology, ecology and conservation**. Netherlands Springer, 2006. p. 295- 301.



## APPENDIX A

### A.1 Lee et al.'s Inversion Method

Lee et al.'s algorithm proposes that remote sensing reflectance measured at the surface is the sum of water column and bottom contributions. In this algorithm, attenuation ( $k$ ) is given by the absorption and backscattering coefficients.

$$\rho^{RS}(0^-) = \rho_{\infty}^{RS}(0^-) \left( 1 - e^{\left[ -\left( \frac{1}{\cos \theta_s} + \frac{D_u^C}{\cos \theta_v} \right) k z \right]} \right) + \frac{1}{\pi} \rho_b e^{\left[ -\left( \frac{1}{\cos \theta_s} + \frac{D_u^B}{\cos \theta_v} \right) k z \right]} \quad (\text{A.1})$$

Absorption coefficient ( $a$ ) is the sum of phytoplankton ( $a_{phyto}$ ), pure water ( $a_w$ ), CDOM and detritus ( $a_g$ ) absorptions.  $a_w$  values can be obtained in Pope and Fry (1997).  $a_{phyto}$  can be expressed using a single-parameter model:

$$a_{phyto} = [a_0 + a_1 \ln P]P \quad (\text{A.2})$$

where  $P$  is  $a_{phyto}$  at 440 nm and  $a_0$  and  $a_1$  are empirical coefficients (LEE et al., 1999). The  $a_g$  can be estimated as:

$$a_g = G e^{[-0.015 \text{ nm}^{-1}(\lambda-440)]} \quad (\text{A.3})$$

where  $G$  corresponds to  $a_g$  at 440 nm.

The total backscattering coefficient ( $b_b$ ) can be considered as  $b_{bp} + b_{pure\ water}$ . In this equation,  $b_{pure\ water}$  corresponds to backscattering by water molecules and its values

can be taken from Morel (1974). The particle backscattering coefficient ( $b_{bp}$ ) can be expressed as:

$$b_{bp} = X \left( \frac{400}{\lambda} \right)^{0.5} \quad (\text{A.4})$$

where  $X$  is  $b_{bp}$  at 400 nm. The slope  $Y$  was estimated according to the Quasi-Analytical Algorithm (QAAv5) (Lee et al., 2002). In this,  $Y$  is a relation between  $\rho^{RS}(0^-)$  at 440 and 555 nm (Equation A.5).

$$Y = 2.2 \left\{ 1 - 1.2 e^{\left[ -0.9 \frac{\rho^{RS}(0^-)(440)}{\rho^{RS}(0^-)(555)} \right]} \right\} \quad (\text{A.5})$$

In the inversion scheme, an optimization technique minimizes the error ( $err$ ) between measured  $\rho^{RS}$  and modeled  $\hat{\rho}^{RS}$ . The values of  $P, G, X, \rho_b(550)$  and  $z$  that minimize  $err$  are considered as the real ones.

$$err = \frac{\left[ \sum_{400}^{675} (\rho^{RS} - \hat{\rho}^{RS})^2 + \sum_{750}^{830} (\rho^{RS} - \hat{\rho}^{RS})^2 \right]^{0.5}}{\sum_{400}^{675} \hat{\rho}^{RS} + \sum_{750}^{830} \hat{\rho}^{RS}} \quad (\text{A.6})$$

